LASER-SHOCK-DAMAGE OF IRON BASED MATERIALS

DISCLAIMER NOTICE

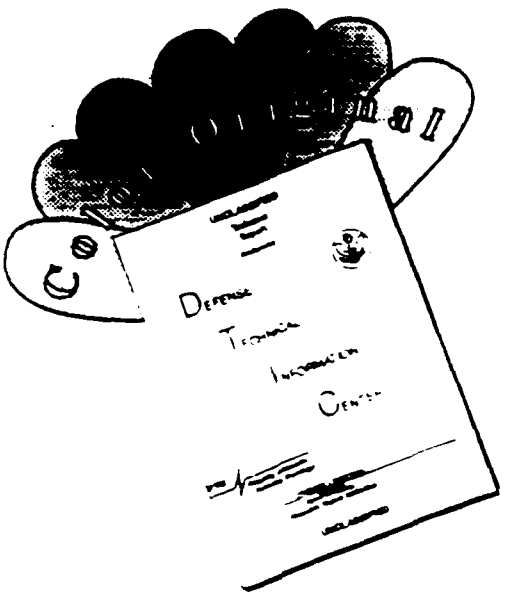

THIS DOCUMENT IS BEST QUALITY AVAILABLE. THE COPY FURNISHED TO DTIC CONTAINED A SIGNIFICANT NUMBER OF COLOR PAGES WHICH DO NOT REPRODUCE LEGIBLY ON BLACK AND WHITE MICROFICHE.

REPORT DOCUMENTATION PAGE

Form Approved
OMB No. 0704-0188

1. AGENCY USE ONLY (Leave blank)	2. REPORT DATE	3. REPORT TYPE AND DATES COVERED
	May 30, 1993	Final 1990-1993

4. TITLE AND SUBTITLE

LASER-SHOCK-DAMAGE OF IRON BASED MATERIALS

5. FUNDING NUMBERS

Grand AFOSR 90-0185

AFOSR-90-0185 2302/05

6. AUTHOR(S)

Jinn P. CHU, Grzegorz BANAS, Frederick V. Lawrence, James M. Rigsbee, and Hani E. Elsayed-Ali

7. PERFORMING ORGANIZATION NAME(S) AND ADDRESS(ES)

College of Engineering
University of Illinois

205 N. Mathews Ave.
Urbana, Illinois 61801

8. PERFORMING ORGANIZATION REPORT NUMBER

9. SPONSORING/MONITORING AGENCY NAME(S) AND ADDRESS(ES)

NA

Department of The Air Force
Structural Dynamics and Materials
Air Force Office of Scientific Research

Bolling Air Force Base, DC 20332-6448

10. SPONSORING/MONITORING AGENCY REPORT NUMBER

AFOSR-90-0185

11. SUPPLEMENTARY NOTES

The views, opinions and/or findings contained in this report are those of the author(s) and should not be construed as an official Air Force position, policy, or decision, unless so designated by other documentation.

12a. DISTRIBUTION/AVAILABILITY STATEMENT

Approved for public release; distribution unlimited.

12b. DISTRIBUTION CODE

13. ABSTRACT *(Maximum 200 words)*

The effects of laser shock processing on the microstructure and mechanical properties of the low carbon (0.04 wt.%C) and Hadfield manganese (1%C and 14%Mn) steels have been studied. Laser shock processing was performed with a 1.054 μm wavelength Nd:phosphate laser operating in a pulse mode (600 ps pulse length and up to 200 J energy) with power densities above 10^{11} W/cm^2. Shock waves were generated by volume expansion of the plasma formed when the material was laser irradiated. Maximum shock wave intensities were obtained using an energy-absorbing black paint coating without a plasma-confining overlay. Maximum modification of the material surface properties and favorable compressive residual stresses were achieved when laser shock processing induced deformation occurred without melting. Mechanical properties of materials such as surface hardness were greatly improved through modifying the microstructure by laser shock processing. High density arrays of dislocations (>10^{11}/cm^2) were generated in low carbon steel by high strain-rate deformation of laser shock processing, resulting in surface hardness increases of 30 to 80%. In austenitic Hadfield steel, laser shock processing caused extensive formation of ε-hcp martensite (35 vol.%), producing increases of 50 to 130% in surface hardness. The laser shock processing strengthening effect in Hadfield steel was attributed to the combined effects of the partial dislocation/stacking fault arrays and the grain refinement due to presence of the ε-hcp martensite. Surface and near surface compressive residual stresses due to plastic deformation by laser shock processing were measured in both steels. Comparisons of laser shock processing microstructure and properties were made with the lower strain rate processes of shot peening and cold rolling for both steels.

14. SUBJECT TERMS

Laser Shock Processing, plasma formation, metallic fatigue

15. NUMBER OF PAGES

155

16. PRICE CODE

17. SECURITY CLASSIFICATION OF REPORT	18. SECURITY CLASSIFICATION OF THIS PAGE	19. SECURITY CLASSIFICATION OF ABSTRACT	20. LIMITATION OF ABSTRACT
UNCLASSIFIED	UNCLASSIFIED	UNCLASSIFIED	UL

TABLE OF CONTENTS

SUMMARY

The effects of laser shock processing on the microstructure and mechanical properties of the low carbon (0.04 wt.%C) and Hadfield manganese (1%C and 14%Mn) steels have been studied. Laser shock processing was performed with a 1.054 μm wavelength Nd:phosphate laser operating in a pulse mode (600 ps pulse length and up to 200 J energy) with power densities above 10^{11} W/cm^2. Shock waves were generated by volume expansion of the plasma formed when the material was laser irradiated. Maximum shock wave intensities were obtained using an energy-absorbing black paint coating without a plasma-confining overlay. Maximum modification of the material surface properties and favorable compressive residual stresses were achieved when laser shock processing induced deformation occurred without melting.

Mechanical properties of materials such as surface hardness were greatly improved through modifying the microstructure by laser shock processing. High density arrays of dislocations (>10^{11}/cm2) were generated in low carbon steel by high strain-rate deformation of laser shock processing, resulting in surface hardness increases of 30 to 80%. In austenitic Hadfield steel, laser shock processing caused extensive formation of ε-hcp martensite (35 vol.%), producing increases of 50 to 130% in surface hardness. The laser shock processing strengthening effect in Hadfield steel was attributed to the combined effects of the partial dislocation/stacking fault arrays and the grain refinement due to presence of the ε-hcp martensite. Surface and near surface compressive residual stresses due to plastic deformation by laser shock processing were measured in both steels. Comparisons of laser shock processing microstructure and properties were made with the lower strain rate processes of shot peening and cold rolling for both steels.

1. INTRODUCTION

The effects of high intensity laser-pulse-generated shock waves on the microstructure and mechanical properties of iron-based alloys have been the focus of this study. Although the effects of laser-generated shock waves have been the subject of relatively few studies and are not quantitatively understood, these effects may be qualitatively predicted from the available laser studies *[1-14]* and from the much more extensive literature on explosively-generated shock waves (for example see *[15]*). Explosively-generated shock waves have been shown to induce dense arrays of dislocations, phase transformations and metastable phases, and internal flaws such as voids and microcracks. Although the laser-generated shock wave may fracture a material *[16-19]*, effects such as a high dislocation density have been shown to improve mechanical properties *[1-14]*.

In this study, shock waves are generated by the volume expansion of a plasma formed when the material is irradiated with a high power laser pulse. The microstructure and mechanical properties are altered due to interaction of the shock wave with the material. To control shock wave intensity and subsequently the degree as well as the nature of such microstructural/property changes in a material, it is critical to understand and control laser processing parameters such as power density. Because absorption of the laser energy and confinement of the plasma volume expansion are also critical to this process, modification of a material's surface through the use of energy-absorbing coatings and plasma-confining overlays are key processing parameters. Analyses of the effects of laser shock waves on microstructures and mechanical properties of iron-based alloys involved use of the following analytical techniques: optical and scanning electron microscopy (SEM) and surface profilometry for surface morphology studies, scanning Auger microprobe and SEM for chemistry studies, transmission electron microscopy for phase transformation and microstructure studies, micro- and nano-hardness measurements for

mechanical property studies, and X-ray diffraction for phase transformation and residual stress measurements.

1.1 Research Objectives

This study is directed toward a fundamental understanding of the effects of high intensity laser-pulse-generated shock waves on the microstructure and mechanical properties of iron-based alloys. Specific questions addressed include:

(1) As a function of the laser processing parameters, how do the energy-absorbing coating and plasma-confining quartz overlay affect absorption and transfer of the laser energy?

(2) Is there a threshold laser power density required to create significant surface deformation and generate a shock wave of significant intensity? Is there a relationship between power density and shock-induced deformation?

(3) What is the nature of the defects induced by laser shock wave? How do changes in material parameters (phase stability and crystal structure) change these defects?

(4) What is the relationship between the laser processing parameters and the shock-induced surface residual stress?

(5) What are the differences in the resulting microstructure/mechanical properties due to the laser shock processing, explosive-shock processing, conventional cold rolling and shot peening?

To study surface effects, quartz was selected as a plasma-confining overlay because of its good laser transmission property, and black paint as an energy-absorbing coating because of its low sublimation energy. Different combinations of these materials were utilized to maximize shock wave intensity and minimize surface melting. The shock wave intensity was interpreted as a surface indentation on the bulk specimen and an extent of deformation on the foil specimen. These results are discussed and compared with those from other laser and explosive shock wave studies. For the sake of comparison, both steel specimens after shot peening and cold rolling were prepared and examined.

1.2. Selection of Materials

This study concentrates on the effects of laser shock processing (LSP) of iron-based alloys. Single phase ferritic (low carbon steel) and austenitic (Hadfield manganese steel) alloys were selected as model systems because:

(1) They have relatively simple crystal structures and readily analyzed microstructures. To establish a fundamental understanding of the LSP effects, the materials selected are beneficial for this study

(2) Their different crystal structures and phase stability allow generation of various types of deformation-induced microstructures. The nature of microstructure/defects generated by LSP may be distinctly different, in the case of Hadfield steel there exists the potential for deformation-induced martensitic phase transformations.

(3) Extensive ancillary data is available for physical and mechanical properties. Availability of this data is important when describing the obtained results.

(4) Explosive-shock waves studies on the same materials are available and allow direct comparisons to be made. The extensive explosive-shock wave research includes a number of important findings on these ferrous alloys. The effects of shock waves are well documented so that the results from this study can be compared to obtain a better understanding of shock wave effects.

2. BACKGROUND

Since construction of the first ruby laser in 1960 by Maiman *[20]*, research and development efforts have rapidly led to a realization of the laser as an important means for materials processing. Laser material processing is widespread and generally divided into laser power density and interaction time regimes as shown in Figure 2-1 *[21, 22]*. Processes range

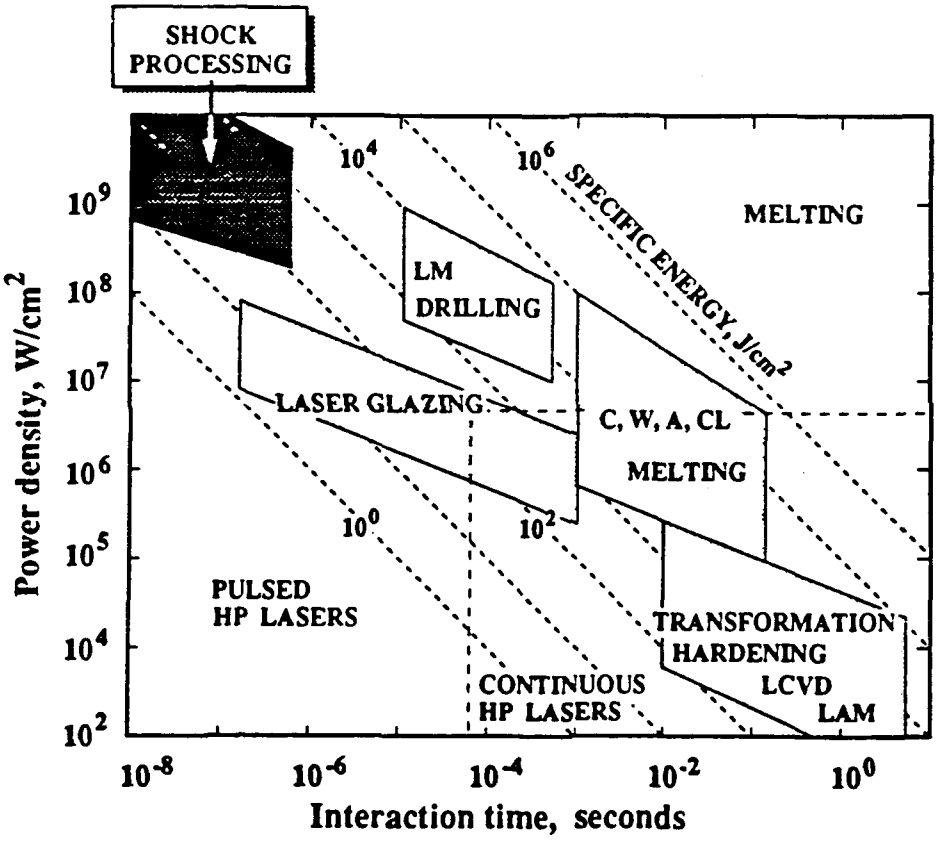

C - cutting, W - welding, A - alloying,
CL - clading, LM - laser machining,
LAM - laser aided manufacturing,
LCVD - laser chemical vapor deposition.

Figure 2-1 Operation regimes for various laser material processing *[21, 22]*.

from low power density/long interaction time transformation hardening to very high power density/short interaction time laser shock processing (LSP). Laser parameters for LSP require power density $\geq 10^9$ W/cm^2 and laser pulse duration $\leq 10^{-6}$ s.

Processing regimes such as transformation hardening have obvious industrial applicability and have been well studied. A review of laser materials processing is available in *[23]*. In contrast, LSP has been received much less attention and is neither well studied nor fundamentally understood, especially as related to its commercial usefulness. To date only one documented LSP industrial application exists *[24]*. In the early 1960's, the potential of LSP was recognized and initially explored by White *[25]* and Askar'yan *[26]*. Recently, due to the availability of gigawatt pulsed lasers, there is renewed interest in laser-shock-related research.

While laser-shock-related research began just two decades ago, a much greater number of studies exists, beginning in the 1940's, in the field of shock compression of solids by means such as explosion and flying-plate impact *[27]*. Those studies have developed a comprehensive understanding of shock wave formation and its effects on materials. As a result, shock wave techniques have been routinely utilized for industrial applications such as diamond synthesis and superconducting powder consolidation *[28]*. Therefore, from a materials science point of view, it is appropriate to recognize important findings of explosive shock-processing fields and to apply this knowledge to LSP for the sake of comparison and better understanding. Although in some ways LSP intrinsically is different from other shock processing (e.g., different shock generation sources and durations), some early studies have shown LSP materials exhibited similar microstructure and mechanical properties that have been observed in materials shocked by other methods *[1-10]*. This indicates that the deformation mechanism by LSP is somewhat analogous to that by the explosive-type shock wave.

2.1. Laser Shock Processing

For laser shock wave generation, a high-power laser pulse is used to irradiate the target material and only a very thin surface layer of target is heated because of a limited laser penetratio (typically ≤ 1 μm) in metals. Due to the rapid energy deposition ($\ll 1$ μs), thermal diffusion of energy from the irradiated area is limited to, at most, a few micrometers *[29]*. Subsequently, the heated material is vaporized and the vapor rapidly achieves very high temperatures at which electrons are ionized from the atoms and thus a plasma plume is formed. As a result of the sudden volume expansion during its formation, the plasma vapor recoils against the target surface and produces a high pressure, often referred to as a recoil pressure. Because of the presence of a recoil pressure, the plasma vapor is pushed away from the target and at the same time the pressure exerts a force very rapidly on the target, resulting in generation of a shock wave. To understand the concept of laser-generated shock waves in materials, it is instructive to start from the fundamentals of laser-material interactions.

2.1.1 Laser-Material Interactions

Two extreme situations may occur when a laser pulse is incident on the solid target. At very low intensities the laser light causes only a temperature rise by thermal conduction below the surface with no change of phase. If the laser intensity is very high, vaporization, ionization, and formation of a plasma take place at the surface. Between these extremes there is a wide variety of intermediate situations in which changes of phase, the pressure due to vaporization, thermionic emission and shock wave generation may occur. There are many factors affecting laser-material interaction: 1) Laser operation parameters (power density, laser pulse duration), 2) Thermal, optical and mechanical properties of the target material, 3) Temperature and pressure dependence *[30]*.

a. Laser Heating of Solids

Since the basic and dominant physical mechanism of laser-material interaction is heating *[31]*, it is important to understand how the material is heated by the laser. Before the plasma is formed in front of the irradiated material surface, the temperature rise in the material is determined by several factors such as the operational laser parameters: power density, pulse duration, etc., and the material's properties: surface reflectance, absorption coefficient, thermal diffusivity, etc. While heating of the materials by a pulsed laser constitutes a three-dimensional heat flow, in nano- and subnano-second laser processing regimes the short thermal diffusion distances and the large laser beam dimension essentially make the heat flow one-dimensional. The reason for one-dimensional heat flow is that the thermal gradients parallel to the surface are limited to many orders of magnitude less than those perpendicular to the surface *[32]*.

Surface Heating

Consider a laser pulse of uniform and constant power density normally incident on a material surface. The laser penetration into material is then described in a one-dimensional approximation by:

$$I(x) = I_0 (1 - R) e^{-\alpha x} \qquad (2\text{-}1)$$

where (I(x)) is the laser power density (in W/cm^2) penetrating to a depth (x) in the material, (I_0) the incident laser power density on the surface, (R) the material's surface reflectance, and (α) is the absorption coefficient. The material's surface reflectance is a material constant and varies with several factors such as surface finished condition, temperature, angle of laser incidence and wavelength of the laser. The absorption coefficient is defined as "a measure of the amount of normally incident laser energy absorbed after traversing a unit distance in the absorbing medium" *[33]*. The coefficient is a material and laser wavelength dependent constant *[33]*. By differentiating Eqn. (2-1), the amount of laser energy deposited in a small increment of depth Δx is obtained:

$$| \Delta I(x) | = I_0 (1 - R) \alpha e^{-\alpha x} \Delta x \qquad (2\text{-}2)$$

Thus the energy deposition is at a maximum at the surface, and decreases exponentially with depth. Most (> 90%) of the energy is deposited within a "skin layer", which is α^{-1} thick. For metals, α is typically in the range 10^4 - 10^5 cm^{-1} and the skin layer is thus 10^{-5} - 10^{-4} cm (or 0.1 - 1 μm) from the surface *[20]*.

Subsurface Heating

In metals, the absorption of laser energy occurs primarily by interaction between photons and electrons. After electrons absorb laser quanta they are raised to higher energy states *[20]*. The electrons will then very rapidly give up their energy in collisions with the vibrating lattice, in a time on the order of 10^{-12} seconds or less. The laser energy thereby transforms into lattice vibrations, which result in heating of the metal through ohmic losses *[34]*. Heating of the metal at depths below the skin layer takes place by means of thermal conduction. The depth of heat penetration (the thermal diffusion distance, D) at any time (t) after the laser energy deposits on the surface is given by *[35]*:

$$D = 2\sqrt{\kappa t} \qquad (2\text{-}3)$$

$$\kappa \equiv \frac{K}{C_v \rho} \tag{2-4}$$

where (κ) is the material's thermal diffusivity, (K) the thermal conductivity, (C_v) the specific heat, and (ρ) is the material density. The thermal diffusion distance is of a characteristic length that determines how much the temperature profile spreads out during the laser pulse. As an example, for an AISI 304 stainless steel with $\kappa = 0.054$ cm^2/sec irradiated with a 600-ps laser the heat will penetrate 0.11 μm deep by the end of the laser pulse *[20]*. This indicates that in practical cases where very short pulsed lasers are used the thermal diffusion distance in the material is limited to fractions of a micrometer into the material.

b. Surface Melting and Vaporization

For LSP and other laser processing such as metastable phase formation *[36]* and semiconductor annealing *[37]*, it is necessary to obtain melting or even vaporization of materials during processing. Therefore, the time required to achieve surface melting or vaporization for a given laser power density is of great interest and importance. Assuming such surface melting/vaporization can be accomplished while the laser-material interaction is in the "short time" or diffusion-free regime, then the time for such melting (t_m) and vaporization (t_v) are given by *[34]*:

$$t_m = \frac{\pi^3 \omega^4 K^2 T_m}{4 (1 - R)^2 I_o^2 \kappa} \tag{2-5}$$

$$t_v = \frac{\pi^3 \omega^4 K^2 T_v}{4 (1 - R)^2 I_o^2 \kappa} \tag{2-6}$$

where (ω) is the laser beam radius, (T_m) and (T_v) are the material's melting and vaporization temperature, respectively. Again, using 304-type stainless steel as an example irradiated with a laser power density of 10^{11} W/cm^2 and beam radius of 15 mm , one can obtain $t_m \approx 10^{-14}$ s and $t_v \approx 10^{-12}$ s. Therefore, it is possible to achieve or to avoid surface melting through a proper design of laser operation parameters such as power density.

In the first known time-resolved (0.1 psec resolution) imaging of laser annealed silicon, the images demonstrated surface melting and expulsion of molten silicon. The surface melting started as early as 0.1 ps and reached completion between 0.5 - 1 ps after the silicon surface had been irradiated by an 80 fs-laser pulse at 6.25×10^{12} W/cm^2 *[37]*. Another example is shown in a recent calculation for diamond thin film formation by the pulse laser irradiation on a carbon implanted copper substrate. The study revealed that the copper surface starts to melt 10 ns after being irradiated with a 30 ns-laser pulse at 1.8×10^8 W/cm^2 *[32]*. With the same irradiation the maximum surface temperature can be over 2,000 K and the melt depth can reach about 0.4 μm.

c. Plasma Formation and Expansion

Since the shock wave originates from the plasma formation during LSP, a general discussion of the physics of its formation will be given, along with some phenomenological examples, for a better understanding of the laser generation of a shock wave. In the laser power density regime (typically $\geq 10^9$ W/cm^2 *[38]*) where a plasma plume can be produced from the

target surface, the leading edge of laser pulse is absorbed by the surface layer, as described in the previous section, and then heats the material rapidly to the temperature at which it is vaporized into a gas phase. The early vapor-phase species that interact with the incident laser pulse are excited and ionized. For short wavelength lasers, an ionization event may be a bound-free transition involving absorption of a single photon; for long wavelength lasers, multiphoton absorption processes play a significant role *[39]*. Collisions among these ionized particles lead to a rise in the gas temperature and pressure. Thermal ionization, however, remains one of the mechanisms for the production of charged species at all stages of laser heating.

The process of evaporation and heating continues until the electron density of the partially ionized gas becomes high enough to allow heating of the gas by the inverse bremsstrahlung process. The inverse bremsstrahlung process is a laser absorption mechanism involving a photon absorption by a free electron in the presence of ions *[30]*. At this stage, the weakly ionized plasma gradually becomes coupled to the middle segment of the incident laser pulse, while the majority of the plasma is still partially transparent to the laser beam allowing direct laser heating of the target surface.

For sufficiently high laser power densities, the electron density of the plasma can reach a value that is high enough that the core of the plasma becomes opaque and the laser beam is no longer able to penetrate the plasma to reach the solid or liquid target surface. At this stage, nearly all of the still-incoming laser energy goes to heating of the plasma. Heating of the target surface occurs mainly by thermal conduction from the resultant hot plasma *[38]*. Experimentally, a variety of materials (Al, Sn, Cu, Teflon, carbon, and ebonite) studied by Basov et al. in 1969 were shown to have reduced surface reflectances (about one-tenth of the reflectances prior to plasma formation) as a result of high-temperature plasmas formed upon irradiation with a high-power laser ($\geq 10^9$ W/cm^2) *[40]*.

As laser heating of the plasma continues, the plasma region advances toward the laser, thus resulting in the growth of the plasma plume in a direction opposite to the laser. The heating rate of the plasma increases sharply at high electron densities by both the linear process of inverse bremsstrahlung and nonlinear processes such as formation of multiply ionized, high-kinetic energy species. Quantitative analysis of these ionized species is done using optical emission spectroscopy techniques (OES) *[41]*. Archbold and Hughes used OES to show the production of multiply ionized (C^+ to C^{4+}) carbon species in the carbon plasma emitted from graphite irradiated with laser power density around 10^{11} W/cm^2 *[42]*. In other studies, energetic charged particles were observed to escape the plasma ballistically *[41]*. Typically, the rapid plasma expansion occurs due to escape of these charged ballistic particles and their subsequent interaction with the laser beam. Such plasma expansion often begins about the time corresponding to the peak power density point of the laser pulse. The plasma expansion velocity is on the order of 10^6 to 10^7 cm/sec, depending upon factors such as the laser power density *[41,43]*.

As the plasma plume expands toward the laser, the energetic particles in the plasma become increasingly more energetic due to the previously mentioned heating mechanism, and more directional as the number of times a particle has been ionized increases. Consequently, the radial expansion of the plasma is characterized by greater concentrations of neutral and single ionized species, and the axial plasma expansion toward the laser exhibits mainly multiple ionized species *[38, 41]*. Once the plasma forms, its growth and heating continues at high temperature and densities, consuming most of the laser energy. Plasmas generated by the high power laser pulses are usually optically thick for the entire ultraviolet to infrared spectral range and the maximum plasma temperature is approximately 10^4 to 10^5 K *[38, 41]*.

The strong trapping and diffusion of radiation, together with the high density and temperature state of the plasma, create a high energy density plasma. As a result, the plasma formed can be sustained for periods much longer than that of the laser pulse. Depending on the density of the ambient gases and other factors such as laser pulse duration, this postpulse plasma lifetime may be anywhere from about 300 ns to more than 40 μs in length *[38]*. The first photographs of a plasma vapor plume emitted from a laser-irradiated carbon surface were presented by Ready *[44]*. The vapor plume existed almost a microsecond after completion of the laser pulse (<50 ns, ~10^{10} W/cm^2) and the corresponding velocity of the leading surface of the developing plume was estimated to be 2x10^6 cm/s. Later, Weichel et al. *[45]* and Veeser et al. *[46]* used streak camera techniques to record the plasma vapor plume formation. Weichel showed that the plume accelerated to 7x10^6 cm/s after an initial velocity of ~5x10^5 cm/s within 0.3 cm distance from the target surface for a laser power density of ~10^{10} W/cm^2 and pulse width of 50 ns on a graphite *[45]*. Veeser et al. showed the maximum plasma velocity is about 1.3x10^7 cm/s for ~10^{15} W/cm^2 power density and 50 ps on an aluminum target *[46]*.

2.1.2 Shock Wave Generation and Enhancement

a. Free Plasma Expansion

The high temperature and density of the laser-induced plasma are a direct result of the extremely high rate of heating made possible by the high-power laser pulse. The expansion of the main plasma becomes noticeable near the end of the laser pulse with the launching of a shock wave into the gas medium, if it exists, that surrounds the plasma and, by momentum conservation, another shock wave is formed and moves into the solid target, as seen in Figure 2-2 *[47]*. The gas region behind the plasma-side shock wave consists of the shock-heated ambient gas that followed by the expanding plasma. In the case of a vacuum environment, the shock-heated region may be the neutral gas species resulting from the escape of the fast ions. The observed luminous core of the post-pulse plasma that associates with the shock wave then decreases in size with time because of the cooling during the expansion *[38]*.

Formation of LSP-generated shock wave in target is discussed in a later section by adapting a model that has been well developed in the explosive shock wave field. Existence of a laser pulse generated shock wave in material was first shown by White *[25]* when a considerable increase in the elastic wave magnitude was detected on a black painted aluminum acoustic probe tip irradiated with a pulsed ruby laser (<500 μsec). In addition to the shock wave generation, as illustrated in Figure 2-2, there are some other effects associated LSP such as energy transfer from the hot plasma vapor into the surrounding atmosphere and the target by radiation and thermal conduction. Due to the extremely rapid interaction time, energy loss from the plasma to the target by thermal conduction is limited and energy radiated from the plasma is also negligible. At the vaporization temperature of tungsten, 5800 K, thermal radiation is on the order of 10^3 W/cm^2, which is small compared with a 10^9 W/cm^2 laser power density *[48]*.

b. Confined Plasma Expansion

To enhance the shock wave intensity into the target, Anderholm *[49, 50]* initially proposed that an overlay transparent to the laser wavelength (such as a quartz disk) be placed against the target surface to confine the plasma vapor volume expansion to the region between the target and overlay. Anderholm's studies and later studies by Yang et al. *[51, 52]* and O'Keefe et al. *[53, 54]* using this configuration on various targets demonstrated that the shock wave intensity was greatly enhanced. For example, irradiation of Al with a ~10^9 W/cm^2 power density and 20-50 ns laser pulse produced a shock wave pressure of 47 MPa for a bare foil (760 μm

thick) and 790 MPa for a Duco cement covered foil *[53]*. More recently Fabbro et al. *[55]* revealed that a difference of two orders of magnitude in shock wave intensity was obtained between confined and unconfined (no overlay or coating) configurations irradiated with a laser at $\sim 10^{10}$ W/cm^2 power density and 3 ns pulse. In their study the shock wave intensity was measured by the maximum velocity of an accelerated copper disk irradiated with the laser pulse. They found that with this confined configuration not only the magnitude of the shock pressure increased, but the shock duration as well, resulting in an increase in the momentum generated into the target. However, they also pointed out that the laser-induced fracture of the confining material at high power densities was the main mechanism limiting the shock wave generation in LSP.

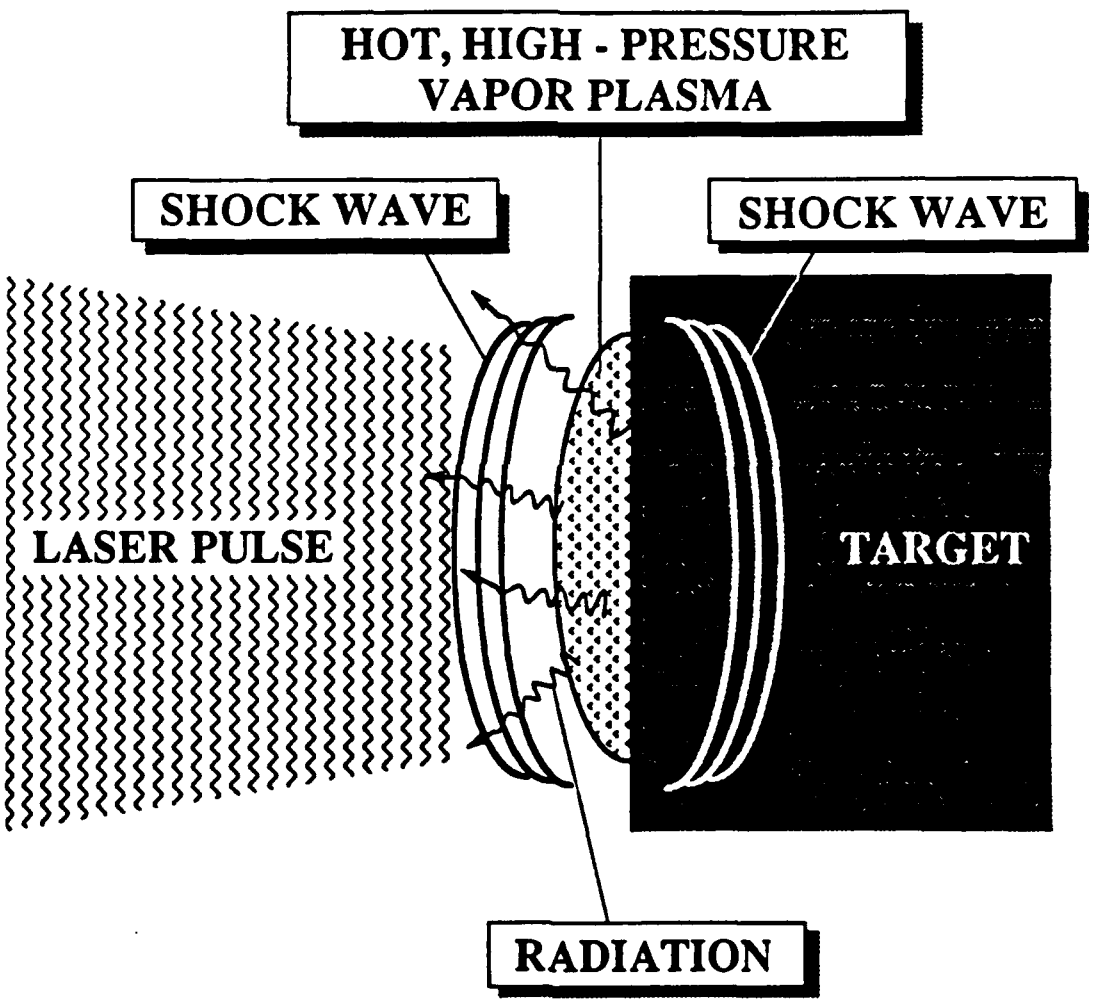

Figure 2-2 Generation of shock waves by a laser pulse *[47]*.

Absorption efficiency of laser energy by the target surface is also an important factor controlling shock wave intensity. Energy losses due to reflection from the target surface before plasma formation and absorption of the incident laser pulse by the surrounding gas environment will eventually result in a significant decrease in shock wave intensity. To alleviate or minimize energy loss to the surrounding environment, processing within a vacuum environment with a transparent overlay on the target is a viable solution. To reduce the energy losses, either a short wavelength laser should be used or the target should be coated with an energy-absorbing layer. Another advantage of using an absorbent coating is to protect the target surface from damage due to melting and/or vaporization as demonstrated by Fairand et al. *[6]*. The use of black paint as an energy absorbing coating was initially suggested by Fox *[56]* because of its low reflectivity and low sublimation energy. Comparing a water and black paint covered Al target to a target without any coating or confining overlay, both irradiated with the same ~10^9 W/cm^2 laser power density and 30 ns pulse, the measured pressure was 640 MPa and 50 MPa, respectively *[56]*.

2.1.3. Shock Wave Pressure Measurement

Since shock wave formation is a critical issue in LSP, several studies have attempted to measure the expanding plasma momentum quantitatively and to record or image the time history of shock waves under different surface conditions. Techniques include: use of pendulum *[57, 58]* and levitation impulse gauge *[59]* for momentum measurement, and quartz gauges *[48, 50, 51, 53, 55]*, streak camera *[45, 46]*, and, more recently, piezoelectric polyvinylidene fluoride (PVDF) transducers *[60]* and rear target surface reflectivity probing *[61, 62, 63]* for shock wave recording. Among these techniques, quartz gauges are most often used because pressure measurement is well established. On the other hand, PVDF transducers were invented about a decade ago and have been widely used in explosive shock wave field because they could function repeatedly under severe shock loading conditions and have the advantage of fast response nanosecond rise times *[64, 65]*.

2.1.4. Laser Shock Wave Modeling and Prediction *[55, 59]*

a. Free Plasma Expansion

In order to describe the expanding plasma momentum transfer to targets in the laser-induced plasma condition mentioned above, a mechanical coupling coefficient (C_m) has been introduced and it is defined as *[59]*:

$$C_m = \frac{P}{I} = \frac{J}{W_L} \qquad (2\text{-}7)$$

where (P) is the shock wave pressure (dyne/cm^2) at target surface, (I) is the incident laser power density (W/cm^2), J is the total momentum imparted to the target (dyne·sec), and (W_L) is the laser energy (J). Units of (C_m) are dyne/W or dyne·sec/J. Typical values of (C_m) are from 1 to 10 *[59]*. The momentum from laser light pressure due to its electromagnetic wave is usually relatively small and can be neglected *[66]*. Gregg and Thomas were the first to note that the (C_m) rapidly reached a maximum at the peak-coupling power density (I_{max}), and thereafter declining with increasing power density *[57]*. This is because at (I_{max}) dense plasma formation starts to mediate laser-material coupling. It was shown that (I_{max}) was dependent on pulse duration dependent *[59]*; for example, for a 600-ps laser, (I_{max}) was approximately 3×10^9 W/cm^2, whereas for a 22-ns pulse it was about 2×10^8 W/cm^2. However, no strong dependence of I_{max} on laser wavelength was noted in the range 0.25 - 10.6 μm *[59]*.

In recent work, Phipps et al. *[59]* summarized existing mechanical coupling coefficient data published by several research groups for metallic and nonmetallic materials in vacuum. By using a one-dimensional or planar plasma expansion model they showed that (C_m) follows an empirical equation that can be described by laser power density (I), wavelength (λ), and pulse duration (τ) over extremely broad ranges *[59]*:

$$C_m = b\,(I\lambda\sqrt{\tau})^n \qquad (2\text{-}8)$$

where (b) is a material dependent constant and (n) is -0.3 ± 0.03. In their study, the data from two types of materials, aluminum alloys and a variety of C-H type materials, were collected to evaluate this empirical trend. The latter included silica and carbon phenolic, carbon, rubber, and epoxy. They showed that the (b) value for aluminum alloys is 5.56 and for C-H type materials is 6.52. This laser-material scaling model yields an approximate prediction of the dependence of surface shock wave pressure upon laser power density, wavelength and pulse duration when no plasma confinement is used. Because the shock wave can be generated only when the plasma is formed, the Eqn. (2-8) is valid for laser intensities above the peak-coupling power density (I_{max}). Combining Eqns. (2-7) and (2-8), one can obtain the shock wave pressure at the surface for C-H type materials *[55, 59]*:

$$P = \frac{0.786\, I^{0.7}}{t\,\lambda^{0.3}\,\tau^{0.85}} \qquad (2\text{-}9)$$

where (P) is in unit of GPa, (I) in GW/cm^2, (λ) in μm, and (t) and (τ) in ns. In this equation, (t) is time duration of the pressure exerting on the target assuming triangle shapes of laser pulse and thus LSP-generated pressure pulse. Eqn. (2-9) demonstrates that higher laser power density, shorter wavelengths and pulse durations can attain a higher shock wave pressure. For a 1.06-μm laser wavelength, with a 0.6-ns pulse duration and power density of 100 GW/cm^2, the shock wave pressure is expected to reach as high as 0.2 GPa at the surface.

b. Confined Plasma Expansion

In the case where the laser-induced plasma is expanded in a confined geometry, Fabbro et al. developed an analytical model that describes three different stages involved in LSP *[55, 67, 68]*. The first stage which their work describes is for the period of time that the laser is heating the target and the plasma is formed. The resulting plasma is then heated to increase the internal energy inside the overlay-target interface. As shown in Figure 2-3 *[55]*, the heating of the plasma causes plasma expansion that serves to open the overlay/target gap, (L). Taking into account the overlay/target interface shock impedance the shock pressure can be obtained as:

$$P = \sqrt{\frac{Z\,I\,\alpha}{2\alpha + 3}} \qquad (2\text{-}10)$$

where (P) is in GPa, (I) in GW/cm^2, $\alpha \approx 0.1 - 0.2$ and (Z) is the overlay/target interface shock impedance in g/(cm^2·s) which is a function of the target (Z_t) and overlay (Z_o)

$$\frac{2}{Z} = \frac{1}{Z_t} + \frac{1}{Z_o} \qquad (2\text{-}11)$$

As indicated in Eqns. (2-9) and (2-10), for either free or confined geometry, the laser power density plays a significant role in achieving a high shock wave pressure. Nevertheless, Fabbro et al. showed that for similar laser operating conditions the shock pressure for a confined geometry will be 3.7 to 9.6 times larger than that for a non-confined one *[55]*.

The second stage, as described by Fabbro et al., begins after the laser is switched off and is characterized by an adiabatic cooling of the plasma that maintains the applied pressure over a period which is about 2 times that of the laser-pulse duration (τ). Such a post-pulse effect has been shown to enhance the impulse momentum that delivers the shock wave. At time $t = 1.8\tau$ the shock pressure decreases to half of that at time (τ) and at time 15.7τ the pressure drops by one order of magnitude. The plasma thickness at $t = 15.7\tau$ is 4 times greater than its thickness at time $t = \tau$. The third stage according to Fabbro et al. also concerns the adiabatic cooling of plasma, but during this period the exerted pressure is too small to generate any significant shock wave. Overall, they showed that very high efficiencies of laser-material coupling mechanism can be achieved by using the confined geometry, as compared to that of non-confined geometry. However, as mentioned earlier, they pointed out that because of the breakdown inside the overlay above some threshold laser power density, their model is valid for only certain LSP conditions (e.g., for a 3-ns 1.06μm laser pulse, the intensities must be below 2.5×10^{10} W/cm^2) *[55]*.

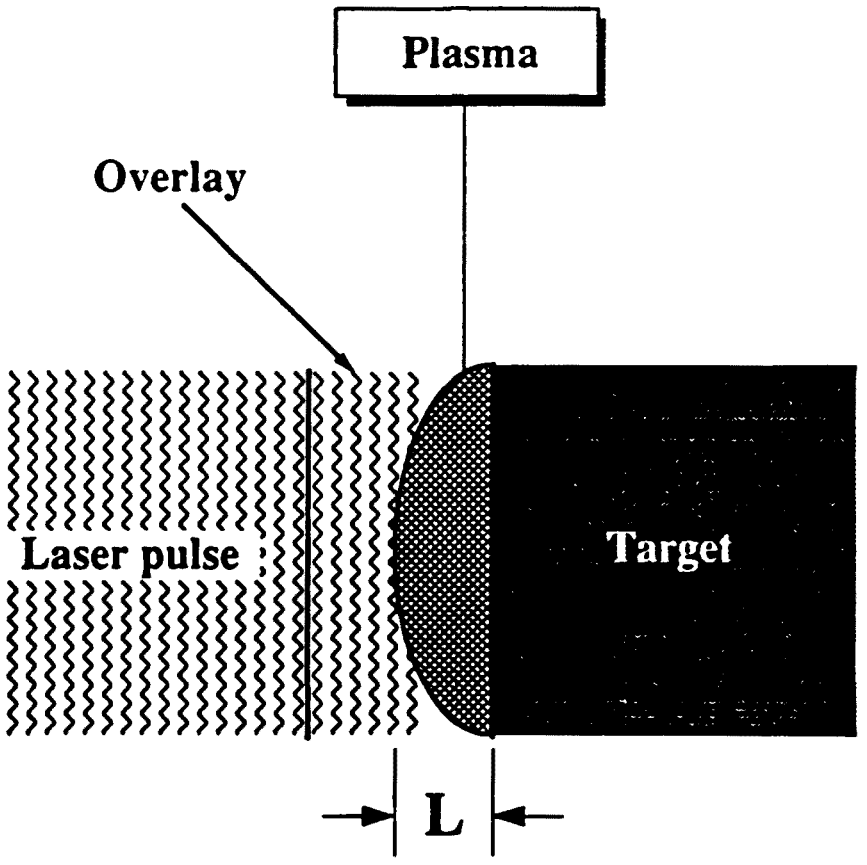

Figure 2-3 Confined plasma expansion in LSP *[55]*.

2.1.5. Effects on Microstructure and Properties of Materials

The first study of laser shock-induced microstructural alterations was performed by Metz and Smidt *[69]*. In their study, vacancy formation was observed in pure 50 μm-thick vanadium and nickel foils irradiated with a ruby laser at 1.5×10^8 W/cm^2 and 35-ns duration. Based on TEM observations, they estimated vacancy concentrations to be as high as 1 atomic percent (at.%). These concentrations were considered very high as compared to those observed in non-irradiated samples quenched from high temperatures (~10^{-2} at.%) and in explosively shocked samples (~10^{-3} at.%) *[69]*. However, in contrast to other LSP studies, Metz and Smidt's *[69]* showed laser-shocked samples exhibited little change in dislocation densities from unshocked samples.

In a later study, Fairand, Clauer, and their colleagues *[1-10]* at Battelle's Columbus Laboratory conducted systematic research on the effects of laser shock waves on the microstructures and mechanical properties of alloys (mainly aluminum and steel alloys). Experimental laser conditions used were 20 to 200 ns duration pulses, a 1.06-μm wavelength and power densities from 10^8 to 10^9 W/cm^2. Their results showed that beneficial mechanical property and microstructural changes are obtained by LSP. Significant results obtained in their research are summarized below *[1-10]*:

Mechanical properties were generally improved by LSP. These included increased microhardness (40% in 304 stainless steel), increased yield strengths (>30% of various Al alloys), and increased fatigue life (40X in an Al alloy). The increase in fatigue life appeared to result from significant surface compressive residual stresses introduced by the shock wave, while microhardness and tensile strengths were believed to be due to shock wave-generated dislocations.

Surface studies of LSP Fe-Si and Al alloys revealed that resolidified layers ranged from 5 to 50 μm thick and contained numerous resolidified droplets, craters, holes and shrinkage cracks. In microstructure studies, observed shock-induced slip and twinning in the Fe-Si alloy and tangled dislocation structures in the aluminum alloys were similar to that found for explosively shocked samples.

The concept of LSP for fatigue life improvement was first demonstrated by Fairand and Clauer *[7-10]*. Later studies by Fournier et al. on a nickel-based alloy *[13, 70]*, and more recently by Banaś et al. on a maraging steel *[14]* , have shown similar effects. Both of these later studies confirmed Fairand and Clauer's conclusions that increased fatigue strength was a consequence of surface compressive residual stresses generated by the laser shock waves. In fact, the research group of Fournier, Fabbro and their colleagues, showed that the significant compressive residual stresses extend up to 3 mm below the surface in an LSP nickel-based superalloy *[13, 70]*. They also observed a high density dislocation microstructure in a nickel-based superalloy and plastic deformation appeared to be strongly heterogeneous *[13, 67, 71]*.

The work by Banaś et al. *[14]* showed that LSP increased the hardness and fatigue strength of the heat affected zone of maraging steel weldments. Their microstructural results of the LSP material revealed an increased dislocation density and formation austenite as a result of surface melting. Other recent laser shock-related studies have shown that deformation twinning occurred in pure iron *[11, 72]* and that the hardnesses of Al, Ti, and steel increased by more than 50% *[12]*. From a materials science point of view, LSP studies to-date are insufficient to describe processing-property relationships. Indeed, this is one of reasons why LSP is not ready for the industrial applications.

2.2. Alternative Methods of Shock Wave Generation

Based on the microstructural studies of Fairand and Clauer *[1-10]* and other investigators *[13, 14, 71]*, propagation of laser-induced shock waves in a target material is analogous to that in explosively shocked materials. Therefore, it is appropriate and instructive to discuss laser-induced shock wave propagation using well understood and developed explosive-type shock wave models. In contrast to comparably few LSP studies, there have been numerous studies of the metallurgical effects of explosive shock waves. For a general picture of these studies, two early reviews by Leslie *[73]* in 1973 and Davison and Graham *[27]* in 1979 tabulated the results of many investigations on the effects of shock loading on various metals. Another review by Meyers and Murr focused on the types of defects generated in shock deformed metals *[74]*. Murr also reviewed broadly the microstructure-mechanical property relationships of several explosively shocked metals *[75]*.

2.2.1. Shock Wave Generation and Propagation

A model widely accepted in the explosive shock wave field states that the shock wave creates a mechanical impact on the target causing elastic or even plastic deformation. The shock wave results from the property of a material to transmit sound at a speed that increases with increasing pressure. Thus a compressional wave will gradually steepen until it propagates as a discontinuous disturbance -- or called shock wave *[76]*. Since any impact received by the material will propagate through it, even if the initial disturbance is elastic it moves at the speed of sound in the material. Once the amplitude of such disturbance reaches a critical value, the shear stress which it generates will lead to yielding of the material. Figure 2-4a shows how pressure, internal energy, and density are changed by the passage of the shock front *[28]*. The fundamental abrupt shock front characteristic of the shock wave is shown in Figure 2-4b. The wave velocity increases with the pressure, so that during propagation the high-pressure portion overtakes the low-pressure region ($U_{s2} > U_{s1}$), resulting the step front. This figure also shows that following the peak shock pressure a release wave, called rarefaction wave, occurs as the disturbance propagates into material and this wave lowers the pressure. It should be noted that rarefaction does not propagate as discontinuities as does the shock front.

Since propagation of a planar shock front is by far the simplest to treat, and since in most experiments the shock waves are planar, the conditions at shock wave front will be discussed assuming a one dimension configuration. As seen in Figure 2-4a, the shock front has a finite thickness and propagates with a velocity, U_s, called the shock velocity. In the high pressure region behind the shock front, the material is compressed and moves with a particle velocity, U_p, which is different from the shock velocity. The particle velocity ahead of the shock front in the undisturbed region is assumed to be zero. One can obtain the following expressions, from the concept of conservation of mass (2-12), momentum (2-13), and internal energy (2-14) at the shock front:

$$(U_s - U_p)\rho = U_s \rho_o \tag{2-12}$$

$$(P - P_o) = U_s \rho_o U_p \tag{2-13}$$

$$(E - E_o) = \frac{(P + P_o)(V_o - V)}{2} \tag{2-14}$$

where (P) is the shock pressure, (ρ) the material's density, (E) the internal energy, and (V) the volume (which is $1/\rho$). The subscript "o" denotes values for the unshocked region. By

rearranging Eqns. (2-12) to (2-14), the shock velocity and the particle velocity can be expressed by:

$$U_s = V_o \sqrt{(P - P_o)(V_o - V)} \tag{2-15}$$

$$U_p = \sqrt{(P - P_o)(V_o - V)} \tag{2-16}$$

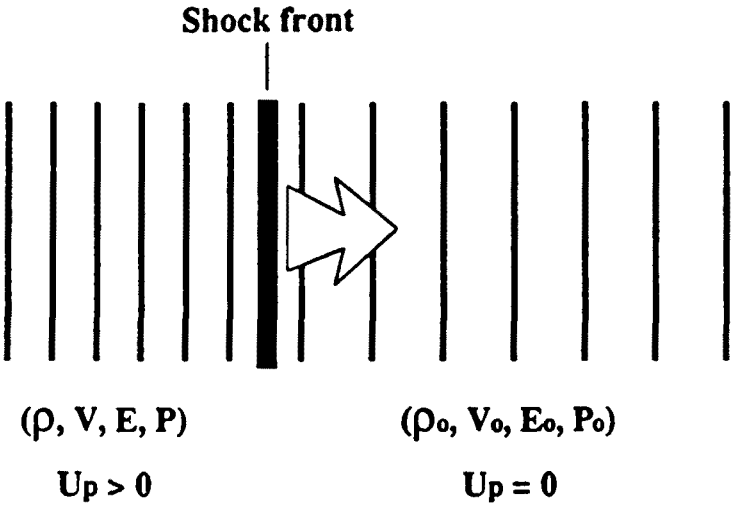

(a)

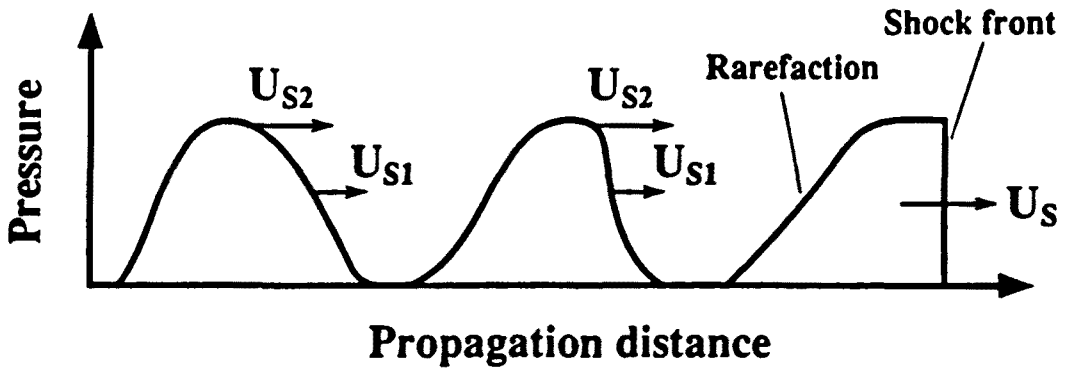

(b)

Figure 2-4 (a) Property changes in a shocked material. ρ is the density, V the volume, E the internal energy, and P is pressure. (b) Formation of a shock *[28]*.

Because it is difficult to measure experimentally (E) and even (P) and (V) directly for most materials, measurements of the shock velocity and particle velocity become important in order to understand shock wave phenomena. The techniques for those measurements have been well documented elsewhere *[27, 76]*. The measured shock velocity and particle velocity serve to establish (P) and (V) using Eqns. (2-15) and (2-16). The resulting P-V data can then be plotted as a Hugoniot curve for a given material, and it represents the loci of P-V states that are accessible by a shock transition. Figure 2-5 illustrates several examples of Hugoniot curves for a variety of metals *[28]*. Such dynamic equation-of-state curves are critical for designing shock loading experiments or applications, or for characterizing a shock wave propagating through a particular material.

Shock wave energy attenuation causes its effect on the material to slowly decrease and eventually vanishes, as it travels through the material. To understand the shock wave attenuation, it is necessary to consider behavior of the rarefaction wave when the shock front propagates. The rarefaction wave is known to have the property of accelerating particles in a direction opposite to the direction of propagation, resulting in a release of disturbance made by the shock front *[76]*. In addition, this rarefaction wave disperses with time. Consider a square wave propagating through a material, the shock front and rarefaction wave can then be replotted as a propagation distance vs time diagram, as seen Figure 2-6 *[76]*. The representation of the release wave in distance-time space gives rise to the name "rarefaction fan". The important features that should be noted are: 1) in the initial stage the shock front travels ahead of the rarefaction wave such that the shock wave propagates stably, although it is slower than the rarefaction wave; 2) eventually the shock front is caught by the rarefaction wave, resulting in attenuation of the shock wave.

2.2.2. General Effects on Microstructure and Mechanical Properties

a. Shear Stress Effects

To study microstructural alterations such as an increase in dislocation density, understanding the role of shear stress in the shocked material is important. Consider planar waves that can be generated by uniformly explosive loading on an infinite flat surface. The resulting particle motion will only be in the direction of wave propagation. Therefore, the plane wave produces a condition of uniaxial strain (deformation). Experimentally, the condition of uniaxial strain can be achieved by allowing the stress wave to propagate in a large flat plate. Taking pressure, P, as the hydrostatic component of stress and the material being isotropic, one can determine the maximum shear stress, τ_{max} *[77]*

$$\tau_{max} = \frac{3(1-2\nu)}{2(1+\nu)} P \qquad (2\text{-}17)$$

where (ν) is Poisson's ratio. As an example for iron, $\nu = 0.293$, the shear stress can be as high as 48% of the hydrostatic pressure. Since the hydrostatic pressures due to shock waves are often in the GPa range, the shear stress can easily reach a value high enough to generate defects such as dislocations *[77]*. For the metallurgical effects, the hydrostatic stress and shear stress are found to play different roles in contributing, for example, to the generation of dislocations, martensitic transformations, and twinning. Important microstructural effects controlled by the shear stress are dislocation generation, twinning, point defect generation, and formation of martensite. Hydrostatic stresses can affect point defect diffusion and generation of some phase transformations *[74]*.

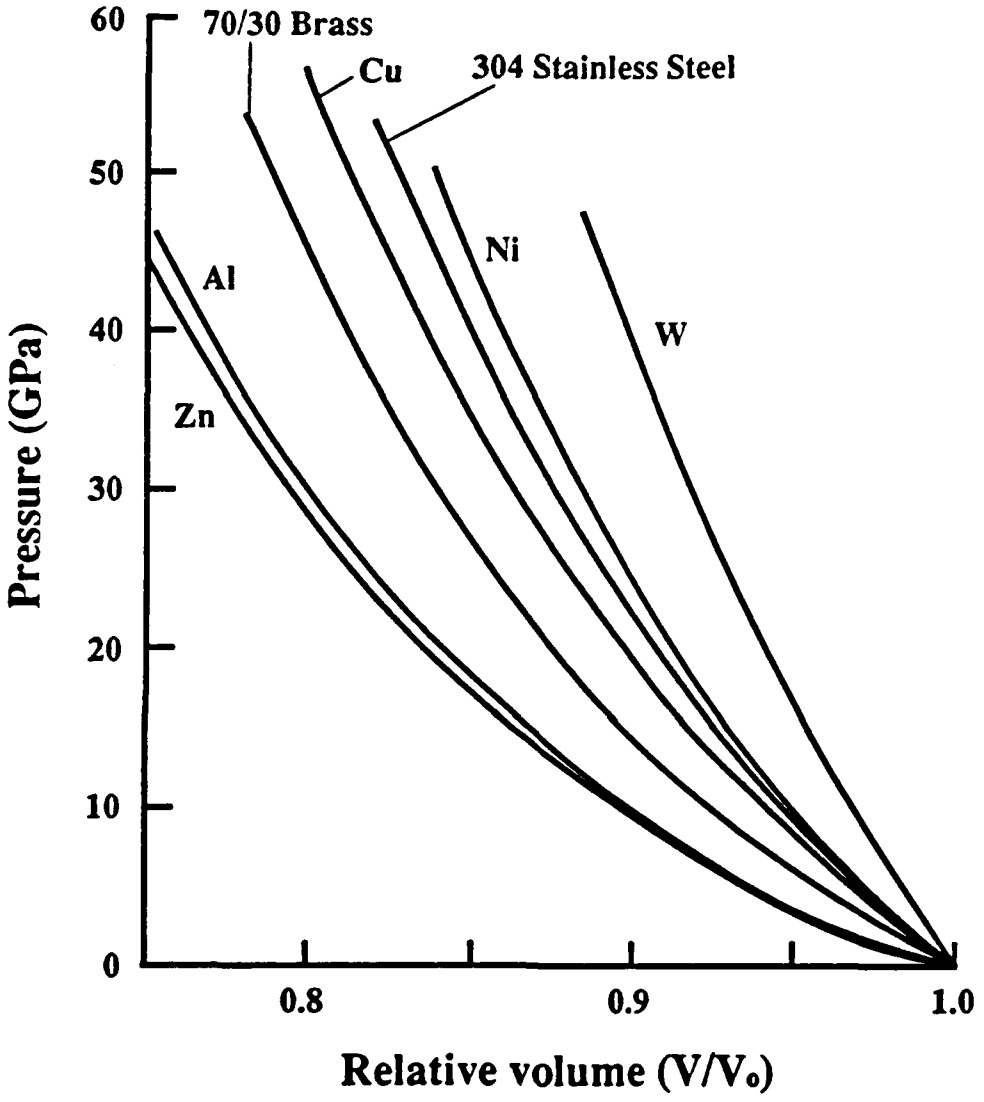

Figure 2-5 Hugoniot curves for various metals and alloys *[28]*.

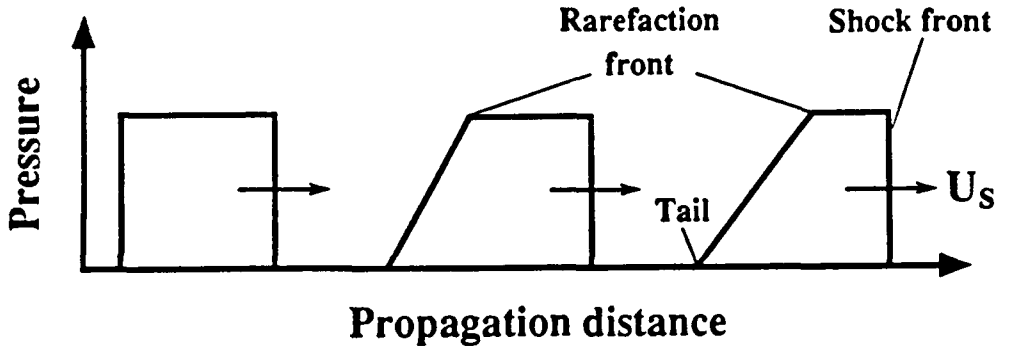

(a)

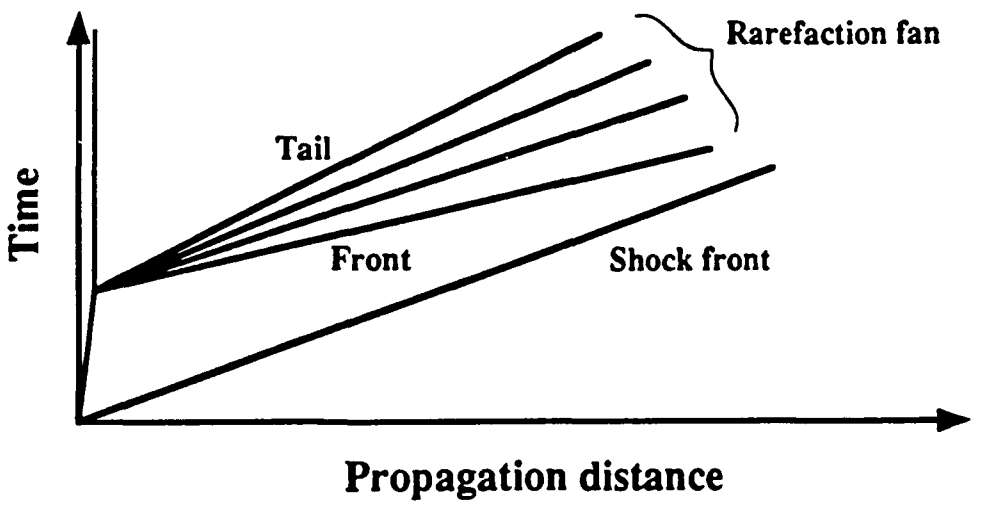

(b)

Figure 2-6 (a) Propagation of a square shock wave. (b) Formation of a rarefaction fan *[76]*.

b. Strain Rate Effects

Another important feature that the shock wave techniques possess is their high strain rate deformation. Since the shock wave can be supersonic, the induced deformation will be expected to be very fast. In LSP, for example, the speed of the shock wave was measured to be $2x10^6$ cm/s in an Al target irradiated with a 2 ns long ~10^{14} W/cm^2 power density *[78]*. This value is faster than the 3 to $6x10^5$ cm/s speed of sound in Al *[79]*. Explosive or impact-loaded shock wave processing create shock pulse durations with microsecond durations. Hence the deformations during LSP or other shock loaded processing are considered to occur at high strain rates (~10^5 to 10^7 s^{-1} *[80]*), as compared to those of conventional deformation processes such as rolling and tensile testing (~10^{-3} to 10^3 s^{-1}) *[77]*.

Because of large pressures and high strain rates, the resulting microstructures and physical properties differ, by comparison, with these obtained with lower strain rates. The diverse microstructural changes in shocked metals include extremely dense arrays of dislocations, dislocation cell structures, stacking faults, ε-martensite (in fcc materials), twins, point defects, and point defect clusters (particularly vacancy clusters). Reported microstructure changes include vacancy formation in nickel *[81]*; martensitic phases in iron *[82]* iron-nickel alloy *[83]*, and 304 stainless steel *[84]*; and twins in copper *[85]* and Hadfield steel *[86]*. Parameters affecting these microstructural changes can be divided into two classes: shock-wave parameters (shock pressure, pulse duration, rarefaction rate) and material parameters (grain size, existing microstructure, stacking-fault energy, and precipitates and other dispersoids) These parameters have been identified, and their effects have been extensively investigated on numerous materials in the explosive-type shock wave field.

c. Generation of Dislocations

Since dislocations are the feature most observed in the shocked materials, their generation and motion during the shock loading have become an important issue and somewhat controversial subject ever since the first model proposed in 1958 by Smith *[87]*. In the Smith model, the interface between the shocked and unshocked regions consists of an array of dislocations that accommodate the mismatch of the lattice parameters. This so-called Smith interface resembles an interface between two phases with different lattice parameters. Because dislocations at the Smith interface must travel with the shock front at velocities up to or even exceeding speed of sound in the material, supersonic and transonic dislocation movements have been proposed by Weertman *[88]*, although, so far, no direct experimental evidence exists to verify such a model. An alternative model has been presented by Meyers *[89]* in which the dislocations are homogeneously nucleated at or slightly behind the shock front but do not advance with it. In Meyers' model no supersonic dislocation movement is needed. However, to make an estimate of the dislocation density, dislocation motion, annihilation and multiplication at the rarefaction part of wave must be taken into consideration. To date, no model has been proposed and verified which successfully describes dislocation generation and motion in the materials subjected to shock waves.

2.2.3. Effects on Iron-Based Materials

A number of explosive shock studies have examined the microstructure and mechanical properties of iron-based materials. This section summarizes important results from studies of low carbon and Hadfield steels similar to those alloys used in this LSP study. The microstructural results and a summary of the mechanical properties' findings are described for both steels. This review provides a basic understanding of the principal microstructural features observed and allows comparisons to be made with this research.

a. Shock-modified Microstructure

Low Carbon Steels

Minshall reported α-phase iron undergoes a phase transformation to an unknown crystal structure when subjected to a 13 GPa shock pressure *[90]*. A later series of studies determined that the shock-induced phase is non-magnetic hcp ε *[91-93]*. In a study by Keeler and Mitchell it was shown that the α-to-ε phase transformation may take place at pressures as low as 5 GPa *[93]*, while most of the studies stated the transformation occurs at pressures between 13 to 16 GPa *[90-92]*. The effects of temperature *[92]* and alloying *[94-96]* on this shock-induced phase transformation were also studied. For instance, with sufficient additions of Ni and/or Mn the transformation pressure was substantially lowered and the transformation eventually changed to α→γ *[96]*. In low carbon steels shock waves were shown to induce a lath martensite microstructure, resembling the structure found in steels quenched from the high temperature austenite phase *[97]*.

As illustrated in a temperature-pressure iron phase diagram (Figure 2-7) *[74]*, the effect of pressure can be more clearly seen in light of Le Chatelier's principle. Because both hcp (ε) and fcc (γ) phases are more closely packed than the bcc (α) phase, a phase transformation

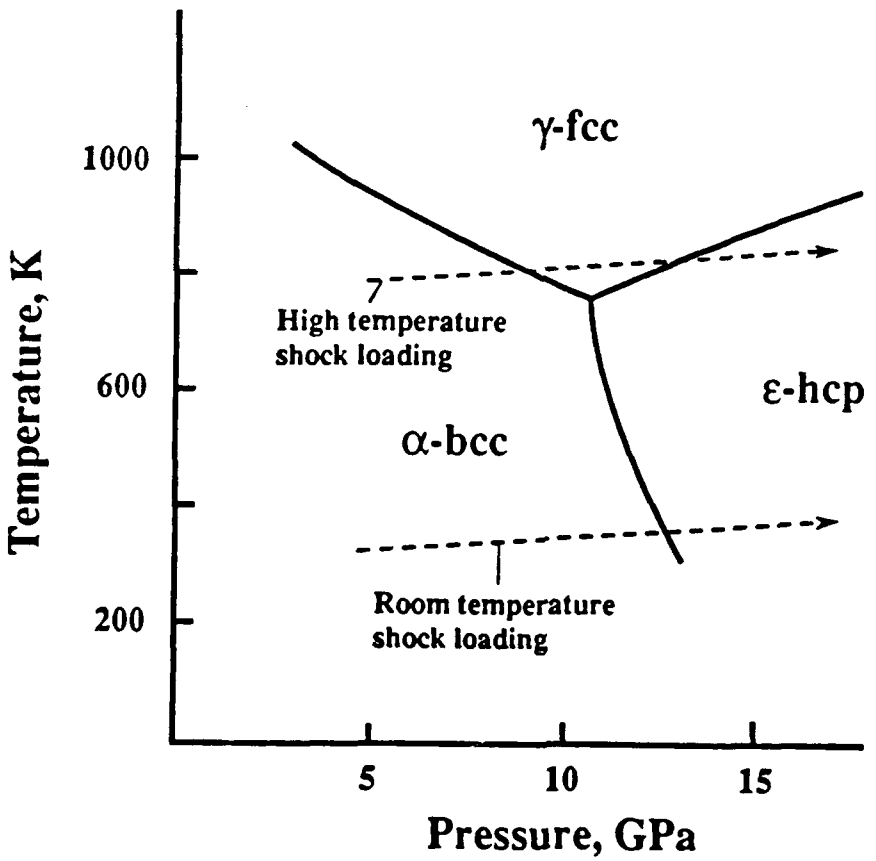

Figure 2-7 Temperature-pressure diagram for iron *[74]*.

resulting in a volume reduction is thermodynamically favored at high pressure. The shock transition pressure does not usually exceed the static pressure of transition, where static values are known. This is curious because the time available for transition is small and, since transitions are sometime slow in occurring under static pressure conditions, it might reasonably be assumed that they might not occur at all in a very short time, or that they might only occur at higher pressures. This suggests that a study of the kinetics of shock induced-phase transition is needed.

When the iron is shock-loaded at pressures not exceeding 13 GPa at room temperature, Leslie et al. showed that the dislocation configuration is similar to that developed by conventional deformation at low temperatures with comparatively straight screw dislocations forming on {110} planes in <111> directions *[98, 99]*. This is because in bcc metals the screw components of dislocations, upon deformation, move slower than edge dislocations at low temperatures or at high strain rates *[100]*. At this level of shock pressure in iron, Johnson and Rohde observed that deformation twinning was accompanied by a uniform dislocation microstructure *[101]*. They reported that the twinning was found at pressures from 0.3 to 1.6 GPa *[101]*. In such a range, the volume fraction of twins increased monotonically from zero to about 4%, while another study showed that at a higher shock pressure (30 GPa) the numbers of twins generated is an order of magnitude higher *[74]*. However, it was also noted that in a predeformed iron exhibiting reasonable densities of dislocations twinning did not occur *[102]*, suggesting that twin formation competes with the generation and motion of dislocations in shock-loaded iron *[74]*.

Hadfield Steel

Due to its unusually large work hardening characteristic, Hadfield manganese steel was one of the first alloys to be shock loaded *[73]*. Its ability to be strengthened by shock hardening has been exploited for commercial application in the railroad industry *[28]*. When deformed by conventional processing such as rolling, the observed rapid work hardening in Hadfield steel has been associated with the formation of deformation twins *[103-108]*, and α'-bcc *[109, 110]* and ε-hcp *[109-114]* martensites. In the explosive shock wave field, the nature of the microstructure and strengthening mechanism of the Hadfield steel are the subject of controversy *[86, 105, 116-118]*. For instance, while there was no α'- or ε-martensite was detected in samples shock loaded at 42.5 GPa by Roberts *[105]* and at 2 to 39.5 GPa by Champion and Rohde *[86]*, Filippov and Kodes observed both martensitic transformations at 50 GPa *[116]* and Dorph found ε-martensite at an unspecified pressure *[118]*. For the studies by Roberts *[105]* and Champion and Rohde *[86]*, the resulting microstructure was found to be typical of fcc alloys with comparatively low stacking-fault energies (such as gold and stainless steel), i. e., planar arrays of dislocations and twins on {111}. Furthermore, in addition to the shock pressure effect, Champion and Rohde found striking differences in twin densities for different pulse durations at 10 GPa *[86]*. Numerous twins were observed at 2 μs, while no twinning was present at 0.065 μs. They concluded that there must be a threshold time for twinning in shocked Hadfield steel. Similar effects of shock pulse duration on twinning formation have also been found in other iron-based materials by Murr and Staudhammer (AISI 304 stainless steel) *[119]* and by Stone et al. (AISI 1008 steel and Armco ingot iron) *[120]*.

b. Shock-modified Mechanical Properties

One of the explosive shock loading characteristics is its effects on the mechanical properties of materials. It may produce appreciable hardening of material with only negligible dimension changes. Figure 2-8 *[121]* shows hardnesses of iron after shock loading and rolling at different true strains. At equal strain, much greater hardening is produced by the explosive treatment than by rolling. This shock strengthening effect is attributed to the considerable high density defects microstructure and new phase generated during the explosive shock loading.

Such a strengthening effect can be explained by work-hardening considerations associated with more conventional modes of deformation. The strengthening model takes into account the substructures generated in the shocked materials such as dislocation density, twin spacing and defect concentration. As an example, a quantitative study of the hardness distribution due to the shock-induced dislocations and twinning in α-iron was performed by Ganin et al. *[122]*. In their study the hardness decreased with distance from the shocked surface. The decrease in hardness was associated with an increase in the average inter-twin spacing and a decrease in the average dislocation density. The relation between the hardness, H, and the parameters of the substructure is expressed by *[122]*:

$$H = H_0 + \frac{k}{\sqrt{\Lambda}} + a\,G\,b\sqrt{\rho} \qquad (2\text{-}18)$$

where (Λ) is the average inter-twin spacing, (ρ) is the average dislocation density, (H_0) is the hardness in an ideal material without any defects, (G) is the shear modulus, (b) is the scalar value of the Burgers vector, and (k) and (a) are the material's constants. In their study Ganin et al. found a linear relationship existed between $\sqrt{\rho}$ and Λ^{-1} in the shocked α-iron *[122]*, suggesting the dislocation density increase may be somewhat related to the twin boundaries.

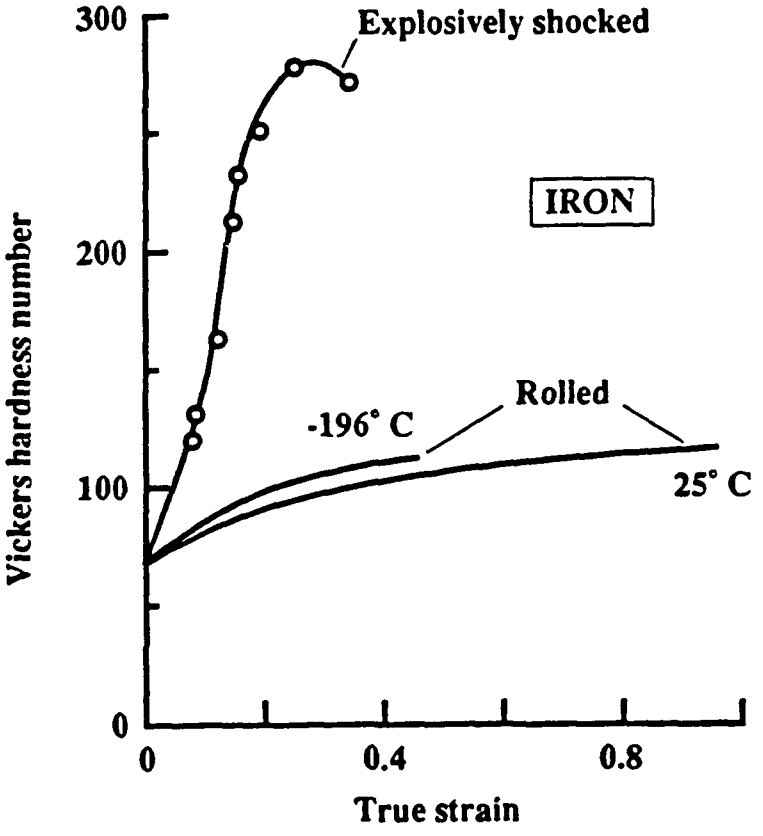

Figure 2-8 Hardness vs true strain for iron after explosive shock loading and rolling *[121]*.

3. EXPERIMENTAL PROCEDURES

3.1 Materials

For the microstructural and mechanical property study, the target materials used were low carbon steel (SAE 1010) and Hadfield manganese steel. They were heat treated and polished as described in the following sections. Types of overlay and coating materials used in this study will also be given. A schematic showing the overlay, coating, and target arrangement is illustrated in Figure 3-1. For processing optimization, AISI 304 stainless steel foil (25-μm thick) was used to measure deformation under different LSP conditions.

3.1.1 Low Carbon Steel

The starting material was 1.3 mm thick cold rolled low carbon steel (SAE 1010). The chemical composition of this material is shown in Table 3-1. Different disk-shaped specimens were prepared for the microstructure/property study (1.3 mm thick-15.2 mm diameter) and for shock pressure measurement (50 and 100 μm thick-9 mm diameter). The thick specimens were machined from as-received strips, followed by mechanical polishing down to 0.05 μm Al_2O_3. The thin specimens were made by cold rolling as-received strips to 150 μm, followed by chemical thinning to the final thickness of 50 and 100 μm. Chemical thinning was performed in a solution of 5 ml HF, 70 ml H_2O_2 and 25 ml deionized water. To insure low residual stresses prior to LSP, all specimens were vacuum annealed at 690°C for 1.5 hour followed by furnace cooling. X-ray diffraction indicated only a ferritic bcc (α) phase present in the as-annealed specimens.

3.1.2. Hadfield Manganese Steel

The hot rolled Hadfield manganese steel had an as-received thickness of 3.3 mm. The chemical composition of this material is listed in Table 3-2. The material was machined into 12.5 mm diameter disks and mechanically polished to 600-grit and then vacuum annealed at 700 °C for 0.5 hour followed by furnace cooling to minimize residual stresses. The specimens were next electropolished to remove at least the top 10 μm surface layer before being used for LSP. The chemical solution for electropolishing was 80 g of anhydrous Na_2CrO_4 in 400 ml acetic acid. X-ray diffraction revealed an fcc γ-austenite matrix with a very small volume fraction (<5%) of hcp ε-martensite after annealing.

3.1.3. Overlay and Coating Materials

In this study, fused quartz (SiO_2) was used as a transparent plasma-confining overlay and black paint was used as a sacrificial energy-absorbing coating. The thickness of the quartz transparent overlay was 3.1 mm, while that of black paint was either 10 - 15 or 40 - 50 μm. As will be shown, a 40 - 50 μm thick black paint provided continuous coverage and thus better protected surface from melting during LSP. Thus, unless otherwise specified, this thickness (40 - 50 μm) of black paint was used throughout the study. The chemical analysis of the black paint indicated that the organic component was an alkyd resin. The inorganic content is given in Table 3-3.

Several quality grades of quartz were initially used. The grades are rated by the surface finish, i. e. the higher the grade, the better polished the surface. The quartz used was supplied by Oriel Corporation, Stratford, CT and was commercial, optical, and laser quality fused quartz along with BK-7, a borosilicate crown glass. Transmission efficiency at the wavelength used in

this study was all in excess of 95%. Since several thicknesses (1.6 to 6.2 mm) of overlay used during early experiments resulted in no significantly different effect on the specimens, a 3.1-mm thickness overlay was used. Because even fine grade overlays such as laser quality quartz still suffered some degree of surface/bulk damages for the laser power densities used in this study, the overlay typically used was an optical quality quartz.

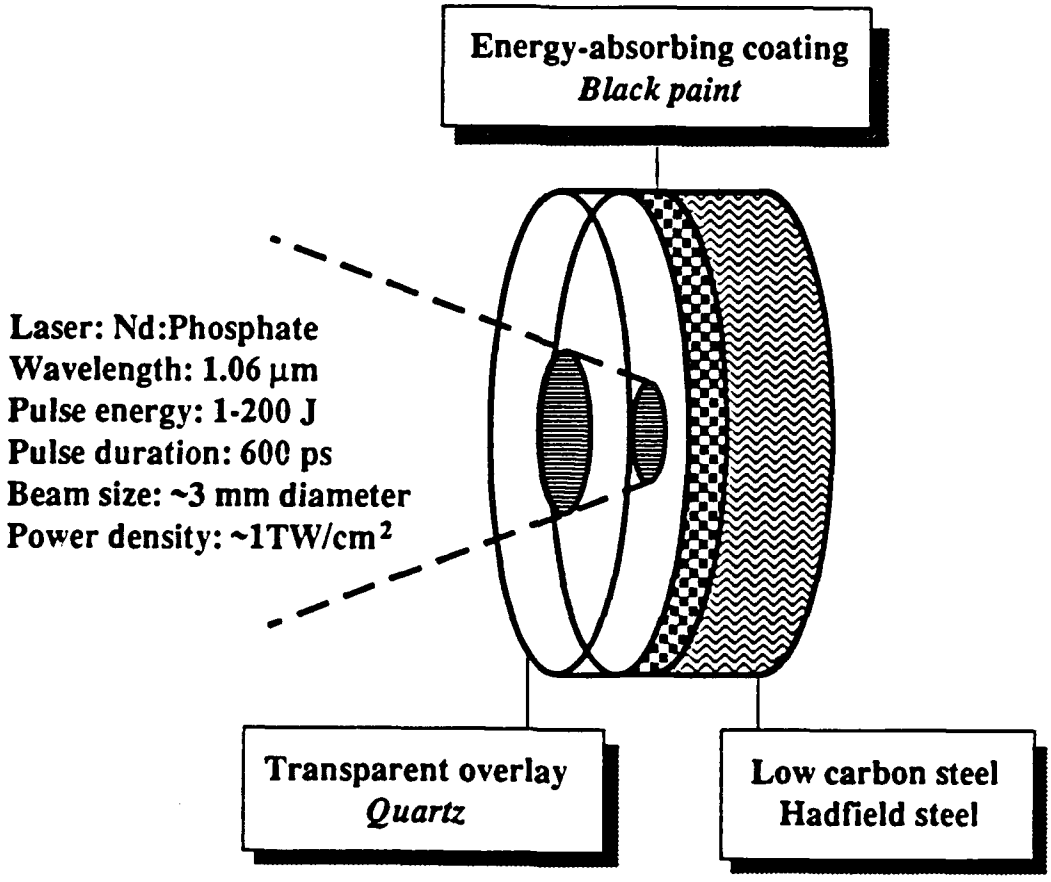

Figure 3-1 Laser and material arrangements used in this study.

Table 3-1 Chemical composition of SAE 1010 low carbon steel (in wt.%).

C	Mn	P	S	Si	Ni	Cr	Mo	Cu	Nb	Fe
0.04	0.45	0.007	0.012	0.04	0.01	0.02	0.01	0.05	0.056	Bal.

Table 3-2 Chemical composition of Hadfield steel (in wt.%).

C	Mn	P	S	Si	Ni	Cr	Mo	Cu	V	Al	Fe
0.97	13.83	<0.005	0.009	<0.01	<0.01	<0.01	<0.01	<0.01	<0.01	<0.01	Bal.

Table 3-3 Inorganic content of the black paint coating (in wt.%).

Si	Al	Fe	Ta	Sn
3.35	0.01	0.05	<0.01	<0.01

3.2. Laser Shock Processing

3.2.1. Laser System

The laser used in this study was a solid state Nd:phosphate (Nd:glass) laser in the Laboratory for Laser Energetics at the University of Rochester, NY. This laser has a wavelength of 1.054 μm and a pulse duration of 600 ps. The laser energies varied from 1 to 200 J. A typical laser beam intensity distribution on the target is shown in Figure 3-2a. The intensity curves were obtained by irradiated an infrared sensitive negative film placed at the target position with a low power density laser (typically <1 J laser pulse). Following digitizing of the developed film by a microdensitometer, the film density was converted into the laser power density using calibration curves. As shown in Figure 3-2b, the laser beam used in the study had a near-Gaussian intensity profile. The laser beam size in Figure 3-2b was measured to be approximately 3.5 mm at the full width at half maximum (FWHM) of the near-Gaussian intensity profile. The laser beam sizes were kept between 3.0 to 3.5 mm FWHM. Accordingly, the calculated power densities used in this study were ranged from 1.2×10^{11} to 4.7×10^{12} W/cm^2 for laser energies of 5 to 200 J.

3.2.2. Processing Chamber

Initially in this study, the processing chamber was evacuated to ~20 Pa (1.5×10^{-1} Torr) in order to alleviate environment breakdown problems. Later experiments were conducted in a

(a)

(b)

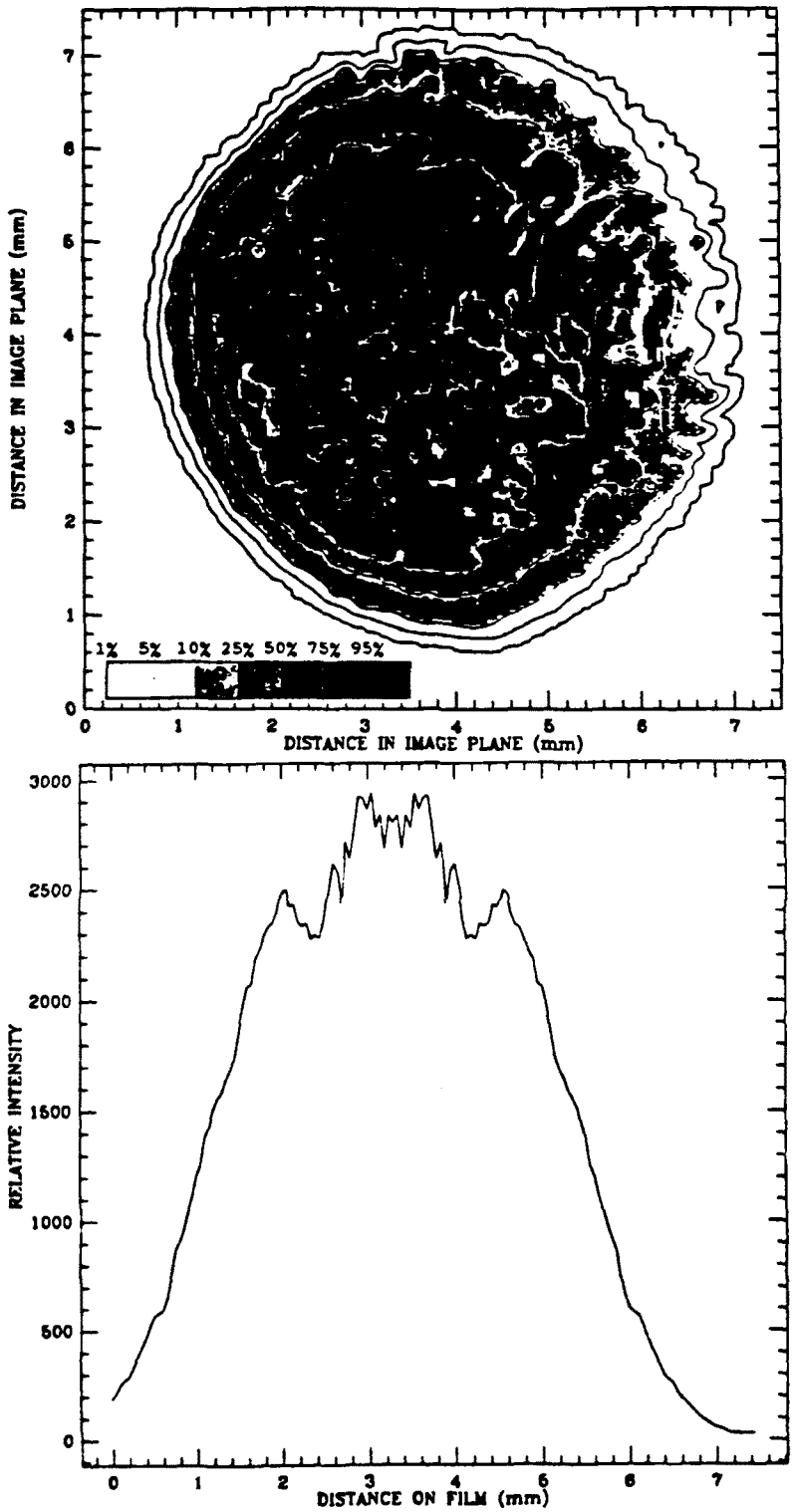

Figure 3-2 (a) An intensity distribution of the laser beam. (b) A line-scanned intensity profile taken from (a).

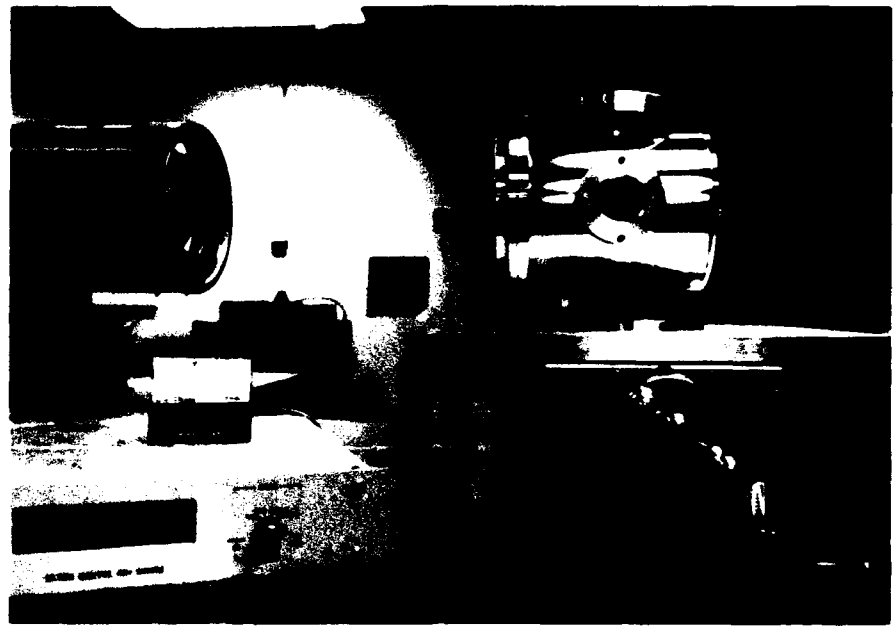

Figure 3-3 Photograph of the LSP processing chamber.

processing chamber with nominal vacuum of 2 MPa ($1.5x10^{-5}$ Torr). Although there was no direct evidence showing LSP-induced breakdown in the rough vacuum environment, shock wave-induced deformation on the specimen in high vacuum was greater than the rough vacuum case. The processing chamber was equipped with a 6-inch diffusion pump and a roughing pump in order to achieve and maintain the desired vacuum during LSP. A photograph of the chamber is shown in Figure 3-3, and a cross section diagram of chamber is illustrated in Figure 3-4. The laser beam entered the chamber through a Pyrex window that was periodically replaced when damage was visible. Viewing windows on the chamber were designed for in-situ observations. In the vacuum chamber the specimen target was held within a fixture and covered with an Al plate having a 6.3 mm diameter aperture for laser passage. In order to measure the deformation during LSP, the fixture was modified by removing the support behind the stainless steel foil thus the foil was deformed during LSP. A hollow aluminum block (14.5 mm in height with a 3.5 mm in diameter hole for the passage of laser) was used to separate the overlay and target foil. Measurement of the foil deformation will be described later.

3.3. Characterization

3.3.1. Plasma Formation

Observation of the plasma formation provided an additional approach for optimizing the LSP parameters. A 35-mm Cannon AE-1 camera equipped with a neutral density filter (ND = 0.3) and a macro lens was mounted onto one view port of the chamber. A 3-mm thick KG-5 color filter was used to absorb the specific 1.05 μm laser light. Plasma images were recorded on Kodak Ektar-25 color film with a camera f-stop setting between 22 and 32 and with the camera shutter open throughout the event of laser processing. To clearly view the plasma, a portion of the specimen fixture was removed.

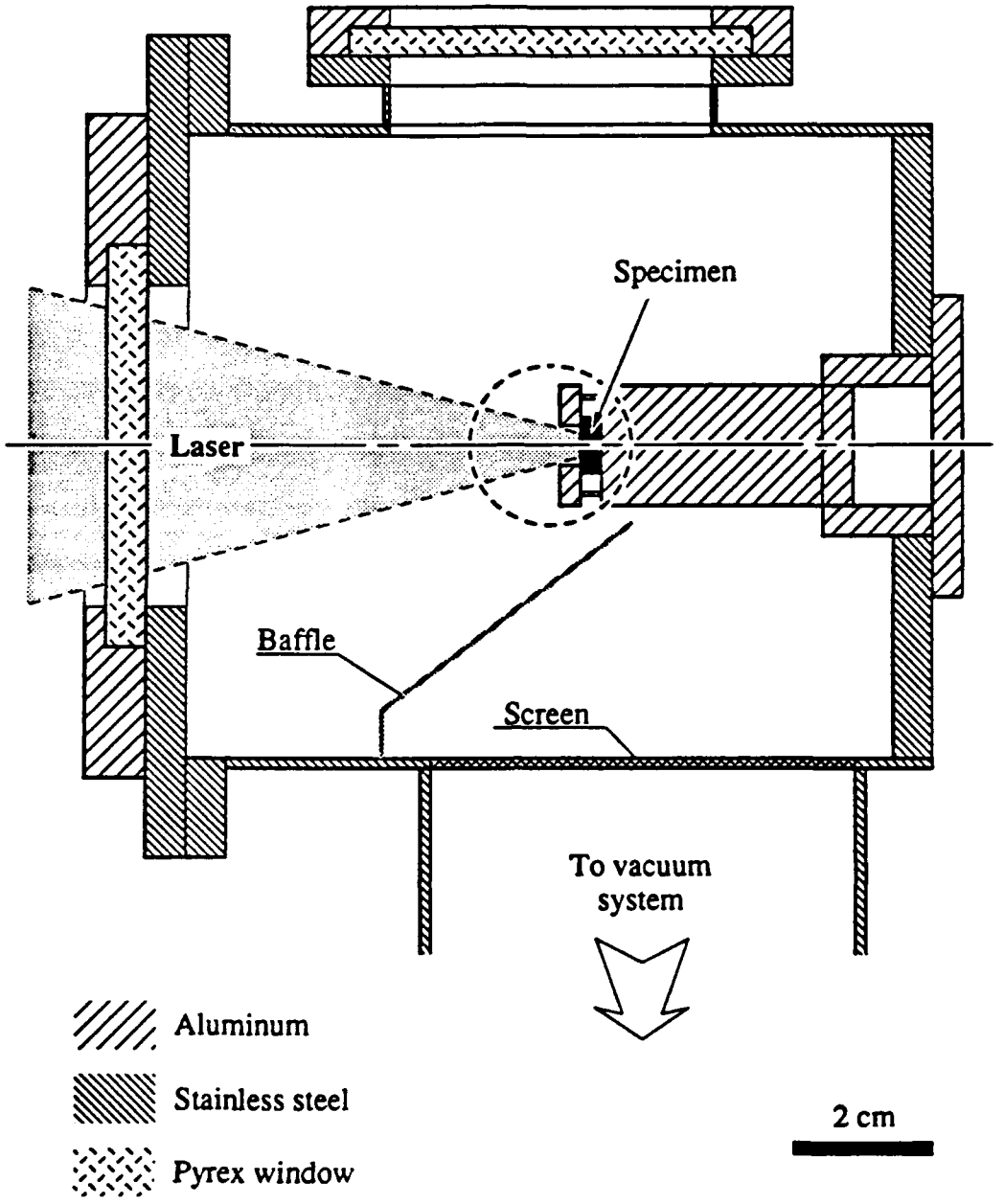

Figure 3-4 Cross sectional diagram of the LSP processing chamber.

3.3.2. Post-Processing Characterization

As illustrated in Figure 3-5, LSP specimens were subjected to various characterization techniques to determine the LSP effects on microstructure, chemistry, and mechanical properties. Analyses were performed both on the LSP surface and on specimen cross sections. If black paint coated, the shocked specimens were first rinsed with acetone followed by ultrasonic cleaning in ethyl alcohol.

a. Microstructure

Surface Profilometry

Tencor Alpha-Step and Veeco Dektak 3030 profilometers were used to record specimen surface profiles after LSP. Nominal stylus loading of 10 mg was used. To optimize experimental parameters, a value defined in this study as the extent of deformation (EOD) was measured by profilometry on the back surfaces of shocked 304 stainless steel foils. A typical back surface profile of a foil is shown in Figure 3-6a. EOD is defined as the tangent of the shock deformed region with respect to the unshocked region of the foil, as shown in Figure 3-6b. Higher laser-induced shock pressure resulted in higher measured tangents (and thus higher in EOD). The basic objective was to optimize the LSP parameters to maximize the value of EOD.

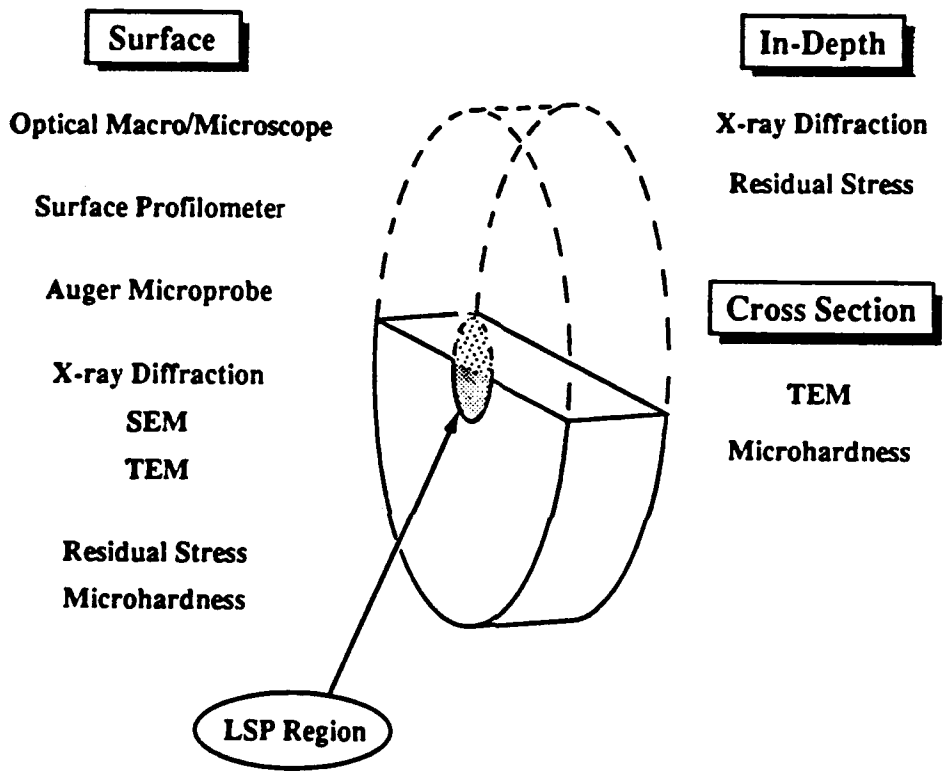

Figure 3-5 Characterization techniques used in this study.

X-ray Diffraction Study

LSP specimens were analyzed by a Rigaku D-Max X-ray diffractometer for determining crystal structural phase changes. The X-ray diffraction pattern was obtained using monochromatic Cu K_α radiation (45 kV and 20 mA). The measurement area was about a 25 mm square. For depth profile X-ray measurement, specimen surfaces were removed incrementally by electropolishing. The electropolishing solution used for Hadfield steel was given previously in section III.A.2. The volume fraction of phase change was calculated according to the method given in *[123]*; see Appendix A.

Surface Morphology

Scanning electron microscopy (SEM, ISI DS-130 and HITACHI S-800) was used for analysis of the surface morphology of LSP specimens. Before viewing in the SEM, the specimens were stripped of any black paint coating. To examine the LSP deformed surfaces, light etching was done using a 3% Nital solution for the low carbon steel and by electroetching for the Hadfield steel with the previously described solution.

Chemical Analysis

A Perkin Elmer PHI 660 scanning Auger microprobe was used for analyses of the surface chemistries. Because the LSP specimens that exhibited surface melting may have been

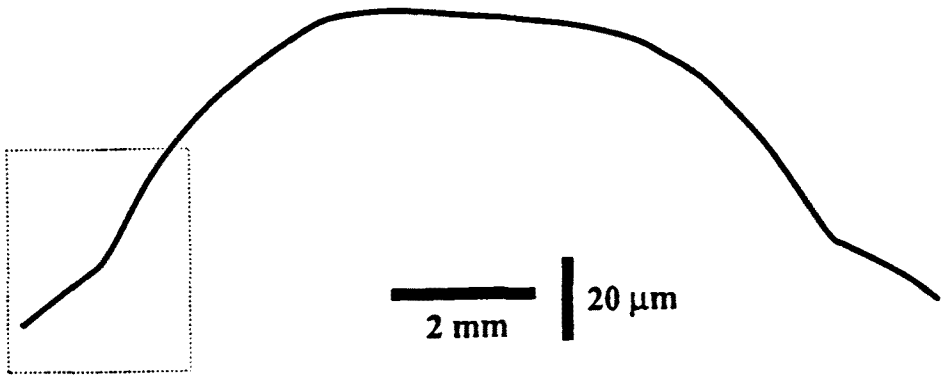

(a)

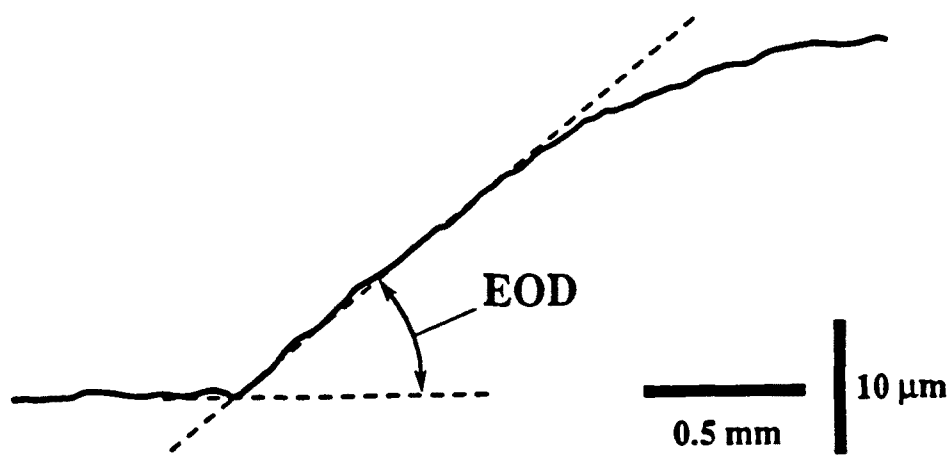

(b)

Figure 3-6 (a) A back surface profile of a LSP foil for EOD measurements. (b) Measurement of EOD in an enlarged profile of (a).

contaminated by the coating and/or overlay materials, the surface chemistries of these LSP specimens were determined by Auger microprobe analysis. Depth profile analysis was done by sputtering with Ar^+ at a sputter rate calibrated on SiO_2 of about 400 Å/min. Following the depth profile analysis, specimens were later examined by SEM to independently determine the total analysis depth. Results of this surface chemical analysis are presented in Appendix B.

Microstructure Analysis

Transmission electron microscopy (TEM, Philips EM400, EM420 and CM12) was done to examine the broad face and cross-sectional microstructures of several LSP specimens. For broad face examinations, 3 mm diameter TEM disks were cut from shocked specimens, mechanically polished with 600-grit SiC paper to a thickness of 100 to 150 μm, thinned to 50 - 60 μm by an electro-dimpling technique described in *[124]*, and finally perforated by atom milling. The polishing, thinning, and milling were done only on the side opposite the shock surface to preserve the shocked microstructures. For cross-sectional TEM examinations, specimen strips were cut from the thick (1.3 mm) LSP low carbon steel specimen and sandwiched into a 3-mm stainless steel tube with an epoxy vacuum glue for holding and fitting, as illustrated in Figure 3-7. The tube was then cut into about 1 mm thick slices and mechanically polished to about 125 μm followed by mechanical dimpling and atom milling. The perforated cross-section specimen was supported with a copper folding grid when examined in TEM. Since this specimen preparation could introduce defects and/or phase changes, the Hadfield steel specimens were not prepared for cross section TEM examinations

b. Mechanical Properties

Residual Stresses

The residual stresses of LSP specimen surfaces were measured by Technology for Energy Corporation located in Knoxville, TN using X-ray techniques. This method measured the average residual stresses at the surface in a layer up to ~0.013 mm deep layer, depending upon tilt angles. Cr K_α radiation was used and five tilt angles were used to get accurate stress readings: 0, 15, 25, 35, and 45° at $2\theta \approx 156°$ (hkl = 211) for low carbon steel and at $2\theta \approx 128°$ (hkl = 220) for Hadfield steel. The area of the LSP specimen exposed to the X-ray beam was approximately 3 mm in diameter. For the depth profile stress measurement, the specimen surface was removed incrementally by electropolishing. The electropolishing solution used for low carbon steel was 75 g anhydrous Na_2CrO_4 and 25 g flake-shaped CrO_3 in 250 ml acetic acid and 10 ml deionized water, while the solution for Hadfield steel was given previously. Stress relaxation due to surface removal was corrected according to the method given by *[125]*.

Hardness

Effects of LSP on the materials' hardness measurement were determined initially in this study using the nano-indentor facilities at Oak Ridge National Laboratory. Since similar results were obtained from Knoop microhardness measurements using light loading (30 g), as shown in Figure 3-8, the Knoop microhardness measurement was employed throughout the study, unless otherwise specified. LSP specimens were cut and the laser-shocked surfaces were plated with an electroless nickel-based coating for edge retention during polishing *[126]*. Final mechanical polishing was performed using 0.05 μm Al_2O_3. To determine whether polishing caused any hardening effects, an unshocked specimen was also prepared in the same fashion for comparison. Measurements were conducted on both LSP surfaces and transverse sections.

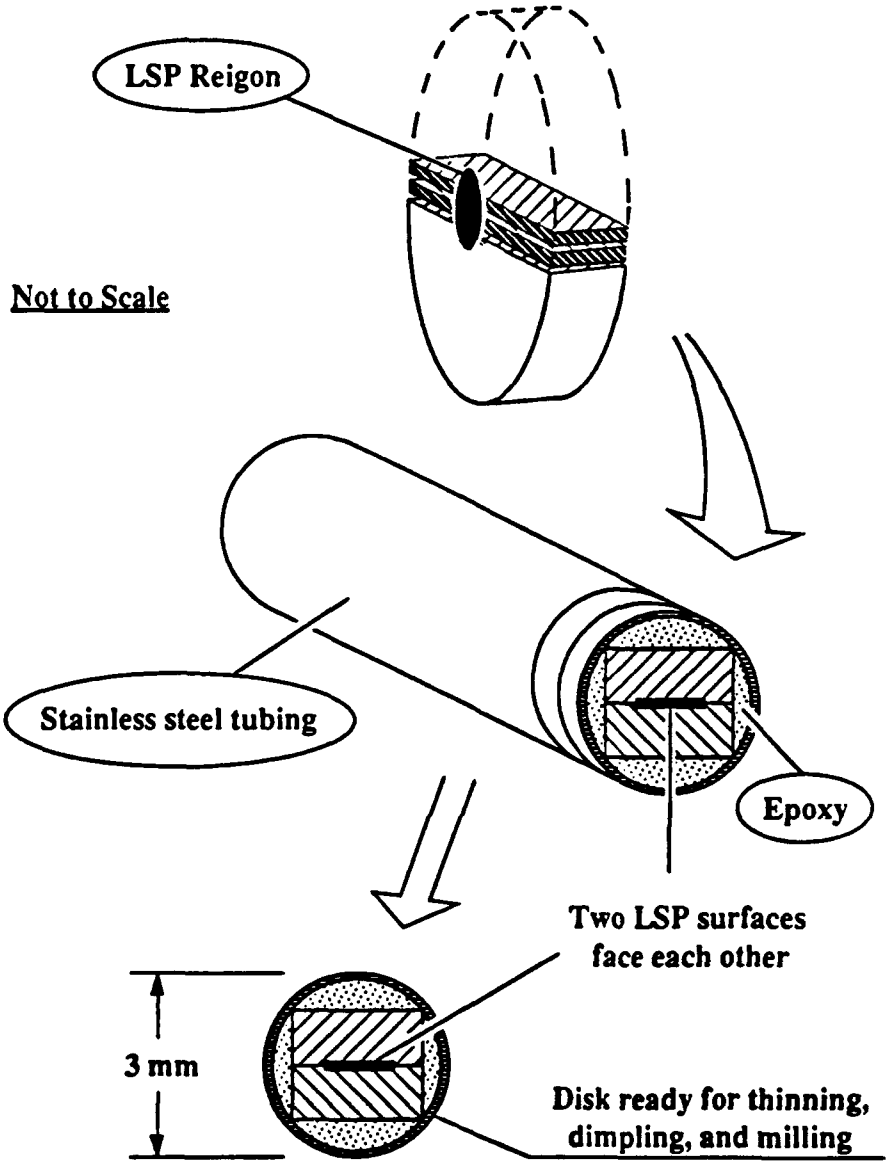

Figure 3-7 A specimen preparation technique for the cross sectional TEM examination.

3.4 Cold Rolling and Shot Peening

Parallel studies on the effects of different deformation processes involved cold-rolling and shot-peening specimens. The low carbon steel and Hadfield steel were cold rolled to a 63% and 51%, respectively, reduction in thickness. Shot peening was performed by Metal Improvement Company, Chicago, IL using the conditions in Table 3-4.

Table 3-4 Shot peening conditions for low carbon steel and Hadfield steel

Material	Shot size (mm)	Almen intensity (mm)	Coverage (%)
Low carbon	0.178	0.101 - 0.152A	100
Hadfield	0.598	0.254 - 0.305A	100

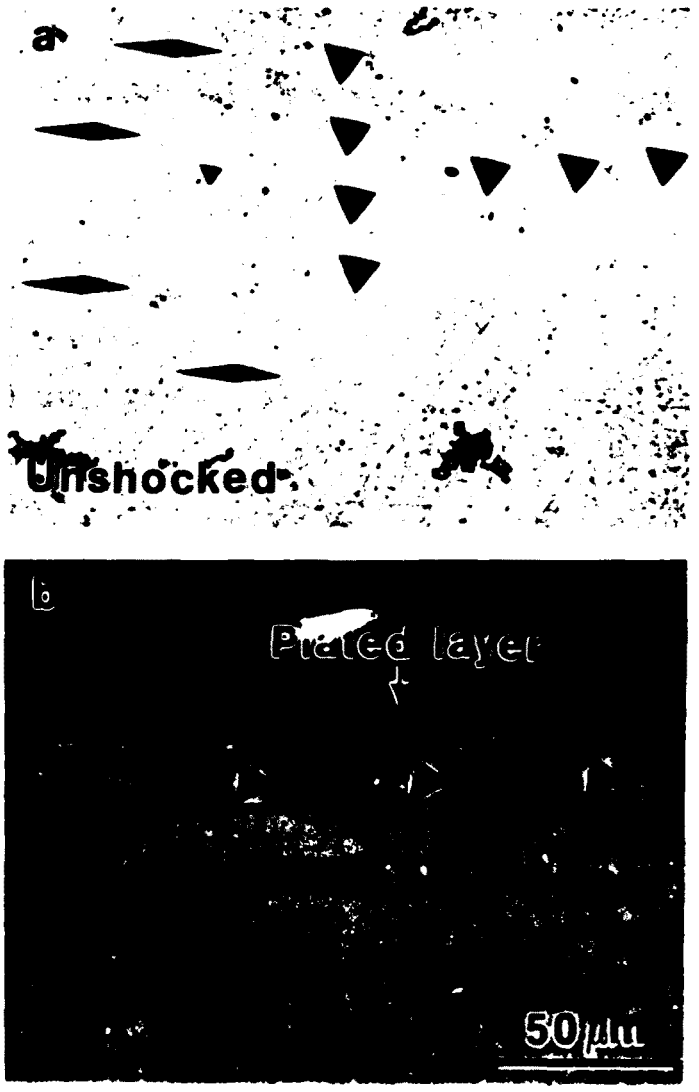

Figure 3-8 (a) Comparison of Nanoindentor and Knoop hardness indentations. (b) Transverse hardness measurement on a plated specimen.

3.5. Shock Pressure Measurements

Polarized polyvinylidene fluoride transducers (Ktech Corp., Albuquerque, NM) with a 2 mm x 2 mm active area, were used to measure the pressure generated by the laser-shock-wave. These gauges offer many unique features for measuring shock compression profiles *[173]*, such as: (1) self-powered operation, (2) large stress range, (3) high output signal, (4) unobtrusive nature, and (5) a stress-rate dependent output signal. The stress-rate dependency of the output signal and the very rapid loading and unloading pulses cause large amplitude current spikes with durations of tens of nanoseconds, separated by intervals of zero current while the stress sensed by the gauge is constant.

The experimental setup used to determine the nature of the of the shock wave created by the impingement of the laser beam on the black paint (sacrificial layer) is shown in Fig. 3.9. The 25 μm thickness PVDF transducer was bonded to the epoxy mounting cylinder with "Hysol thin-film epoxy" with a typical bond-line thickness of 1 - 2 μm. The transducer was electrically insulated using a 12.5 μm thick Teflon film on both sides of the gauge. The transducer was used in the negative current orientation, meaning that compressive stresses should generate a negative voltage. No metallic target was used, but the laser beam impinged directly on the PVDF gauge which was either covered by a 30 μm to 45 μm thickness layer of black paint or was covered only by the mentioned Teflon electrical insulation.

The electrical measurement circuit consisted of a precision current-viewing-resistor (CVR) across the electrodes of the gauge which was connected in parallel to two 50 Ω low-loss coaxial cables. The output from the transducer was recorded by two Tektronix oscilloscopes (Model 7834 with 400 MHz bandwidth) connected to the circuit through 50 Ω terminations. The oscilloscopes were triggered by the electrical signal coming from the oscillator (Fig. 3.9). The required delay time (32 nsec in toto) was determined in an initial set of experiments using a beam-splitter and a photo diode: see Fig. 3.9. A delay box was later placed in the electrical signal path between the oscilloscope and the oscillator in order properly synchronize the scopes. The signals recorded by oscilloscopes were photographed and then digitized in order to perform the integration. The shock pressure variation with time was determined using a calibration curve supplied by the Ktech Corp.

3.6. Fatigue Testing

Figure 3.10 shows the specimen geometry which was used for fatigue testing. A central hole was drilled in each specimen. Two notches were then cut in the edges of the hole to force crack initiation there. Three sets of specimens (8 specimens for each set) were prepared: 1) Untreated, 2) Treated by shot peening (both sides of the gauge section was peened), and 3) Treated by LSP (the area around the hole was treated from both sides of the specimen). Specimens were tested to failure using a tension load cycle (R = 0.1) in a 20 kip MTS frame under load control. The wave form was sinusoidal and the test frequency was 15 Hz. Tests were conducted in ambient laboratory conditions; 20 °C, 35 %RH.

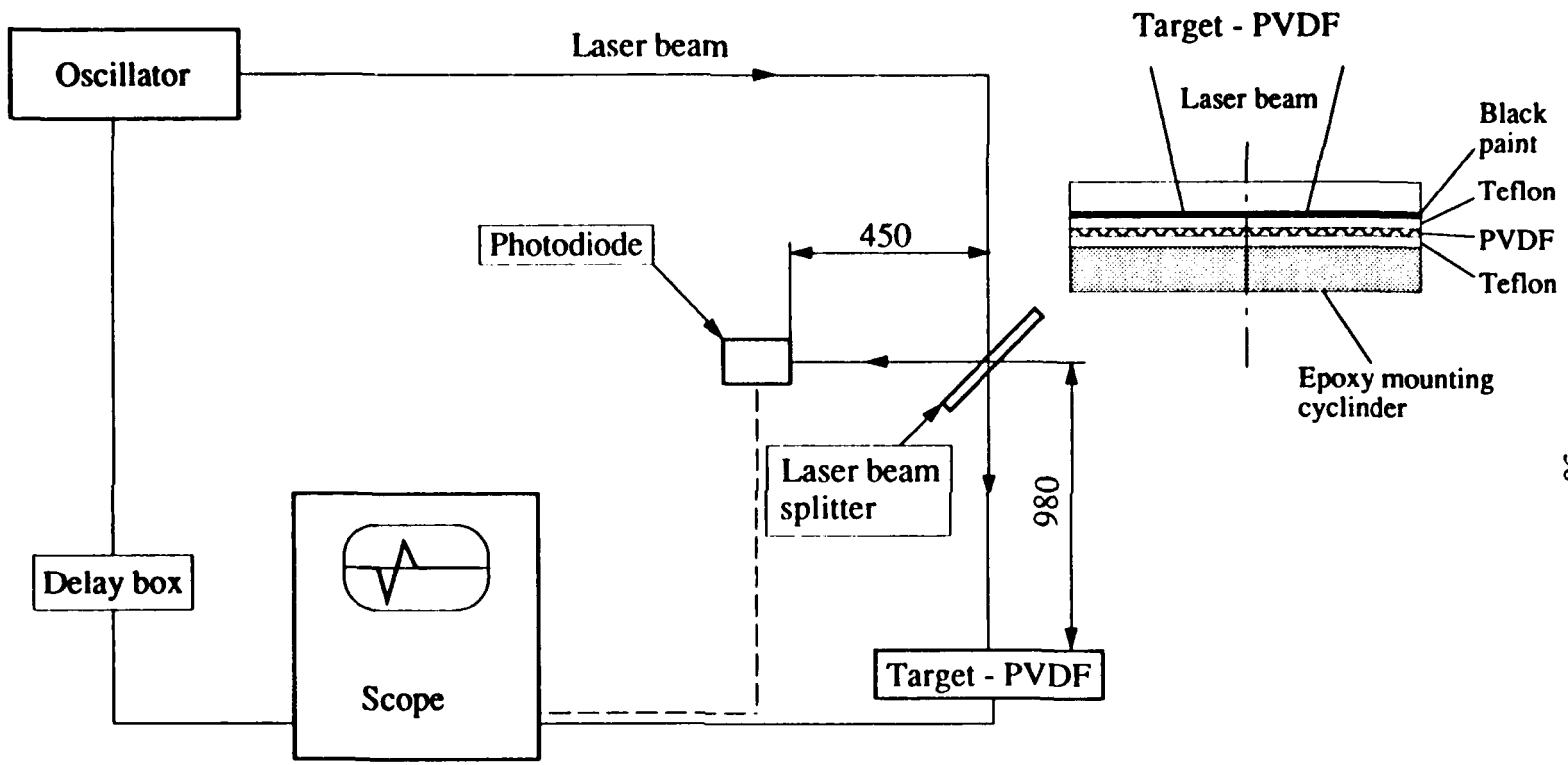

The length of laser path from oscilator to laser beam splitter -- ~ 80 m
The distance between laser trigger and scope is also about 80 m
The length of cable between target and scope -- 1 m
The same cable was used to connect scope with photodiode
980 - 450 = 530. This gives ~ 2 ns time difference (530 [mm]/300 [mm/ns])
The delay time was setup for about 32 ns using a delay box.

Fig. 3-9 Pressure measurements experimental set up.

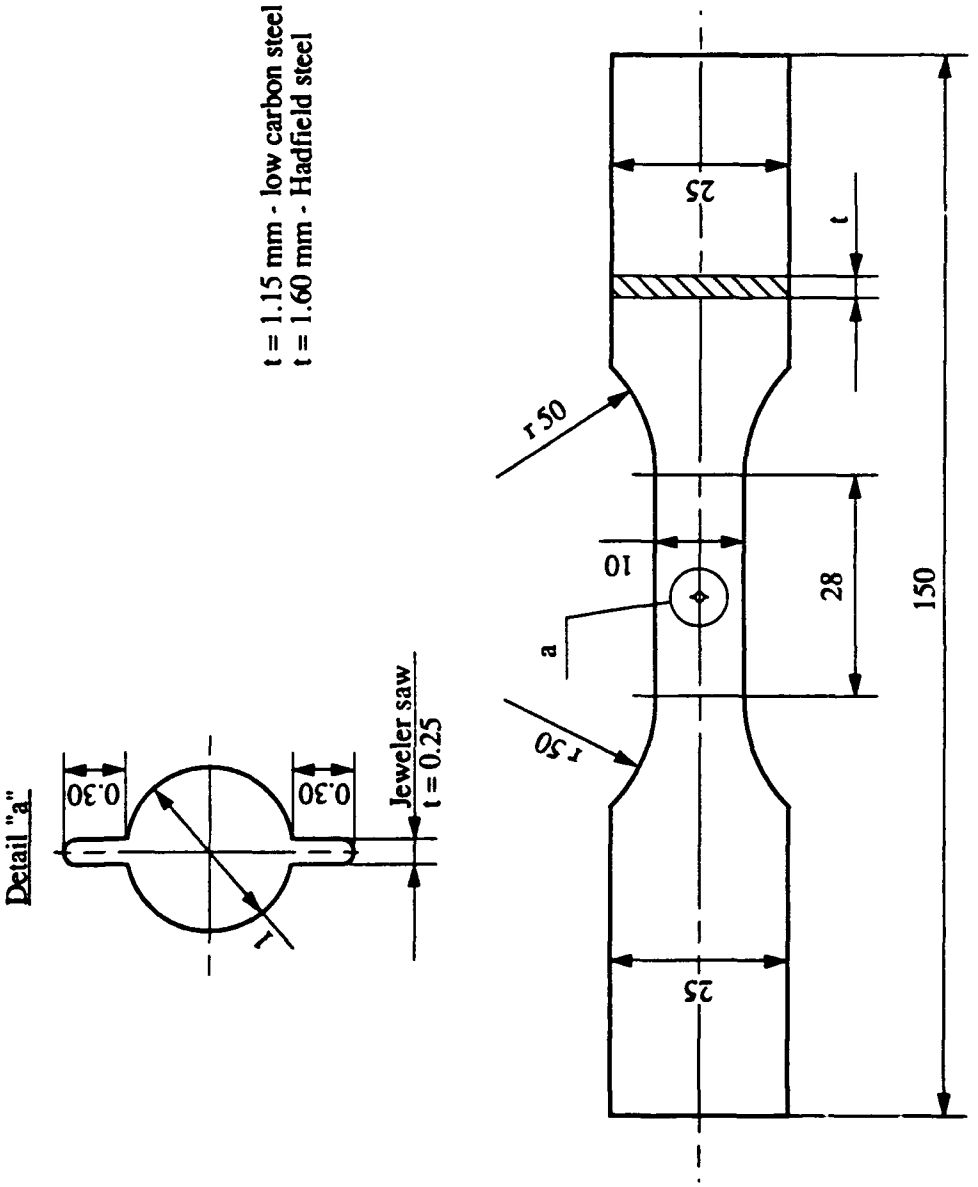

Fig. 3-10 Fatgiue test specimen.

4. RESULTS

The experimental results are divided into three main categories: direct plasma imaging, microstructural characterizations, and mechanical property evaluations. The laser energy is used in describing the laser power density effects since the size of laser-treated area (~3 mm diameter) was kept constant throughout the study. Abbreviations used hereafter are "LSP" for the laser shock processing and "BP" for the black paint coating.

4.1. Plasma Formation

To understand LSP effects on the surface morphologies, a comprehension of the laser-produced plasma is critical. Also, for better optimization of LSP parameters, these plasma formation images serve as direct evidence for the overlay breakdown phenomena. Processing variables affecting the plasma formation included the absence or presence of an overlay, coating and applied laser energy. The type of substrate target material was found to have no significant effect on the plasma formation in this study. The following describes key findings related to laser-produced plasma.

The series of photographs in Figure 4-1 shows images of events before, during and after LSP. In these and all following plasma images, the laser comes from the left side of the photograph. Figure 4-1a shows a 3.1-mm thick quartz overlay in contact with a Hadfield steel specimen before LSP. When the specimen was treated with a 108 J laser pulse, the plasma plume shown in Figure 4-1b formed on the laser side of the overlay and extended in the direction opposed to that of the incoming laser pulse. After LSP with 8.3 J, the overlay quartz fragmented with some pieces remaining in the fixture, Figure 4-1c. For LSP energies above ~30 J, the overlay was totally destroyed with no debris remaining in contact with the specimen. Fracture of the overlay likely resulted either from the laser-induced shock wave originating at the overlay/specimen interface or from laser-induced plasma formation on the laser side of the overlay itself.

4.1.1. Coating Effects

Photographs of the plasma in Figure 4-2 reveal the effects of a laser energy-absorbing BP coating on plasma formation. In the photographs, bare and coated Hadfield steel specimens were treated at the same level of laser energy without a quartz overlay. Top photograph shows a nearly 1 cm long plasma plume emitted from the bare specimen surface. The plasma formed on the metallic surface included a long, narrow, intense "jet" emitted along the laser axis. For the BP coated specimen, the overall plasma was much less intense. No "jet" feature was observed; see the bottom photograph. The difference in these plasmas indicates that the BP coating is effective for protecting the metal surface from significant plasma formation during LSP.

4.1.2. Pulse Energy Effects

Effects of laser energy on plasma formation can be seen from a series of photographs in Figure 4-3. In each case, the specimen is a BP coated stainless steel foil. For low energies (Figure 4-3a, 6.4 J), the laser produced a weak plasma plume on the specimen surface. This white plume formed just at the surface and did not expand too much in size. Increasing the laser pulse energy to 28 J (Figure 4-3b) increased the plasma size and intensity. In addition to this white plasma, a light purple plasma is visible in Figure 4-3b.

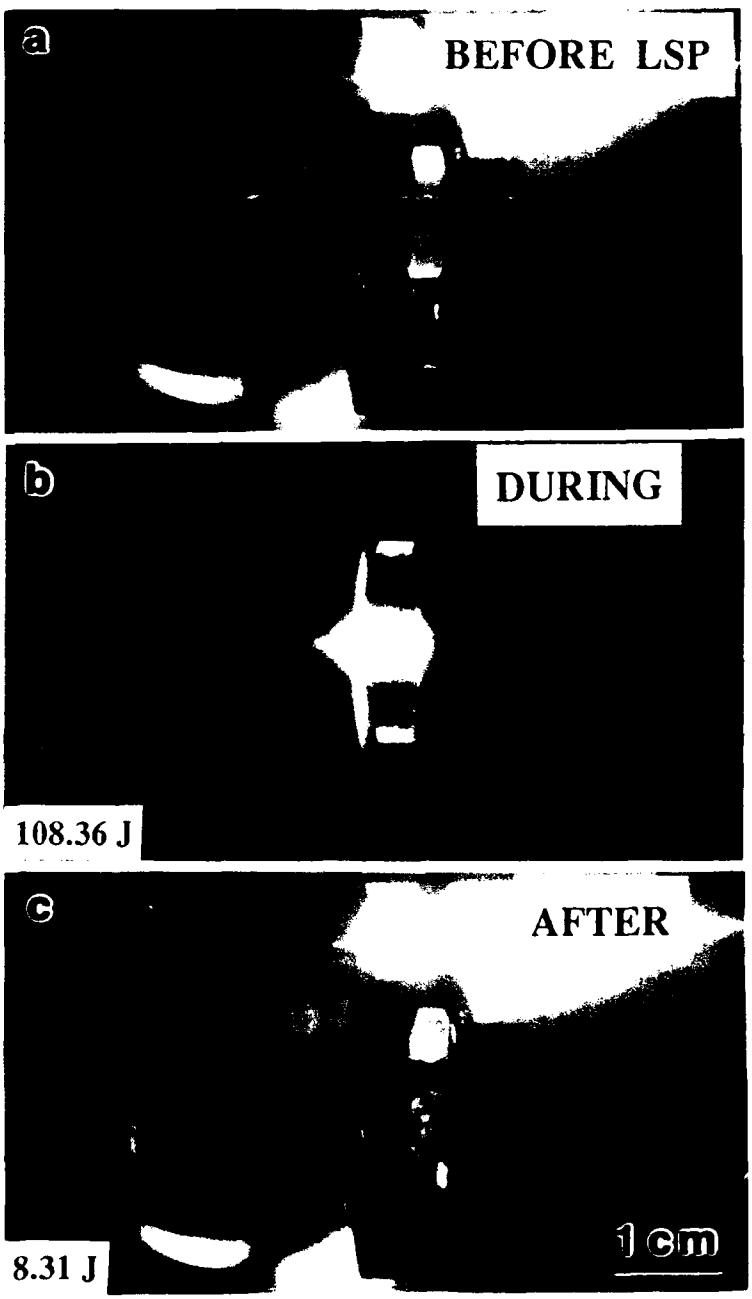

Figure 4-1 Photographs of events: (a) before, (b) during and (c) after LSP.

At 68 J, Figure 4-3c, the plasma further intensified with a much longer and more clearly defined "jet" and a much more visible purple/pink region away from the coated steel surface. However, in this coated surface case, the narrow plasma core was purple/pink, not like the bright white color on the metallic surface shown in Figure 4-2. These questions of plasma "color" are likely just observation of differences in intensity. For the 113 J pulse in Figure 4-3d, the plasma plume was so bright and thick that the background cover plate was occluded. Although the overall plasma did not expand in size and remained about 1.5 cm in length, the pink plasma became nearly white due to an increase in brightness. The long, narrow "jet" was even brighter and more clearly defined. Generally, the observed increase in plasma formation with increasing laser pulse energy is consistent with results presented in later sections explaining the energy effects on the shock-induced deformation of the targets.

Figure 4-2 Plasma formation on a bare specimen (top) and a BP coated specimen (bottom).

4.1.3. Overlay Effects

Effects of overlay on plasma formation are demonstrated in Figures 4-4 and 4-5. In both figures, BP coated stainless steel foils were used as specimen targets. To examine the overlay effect independently from the target, the overlay and target were separated by 6.5 mm using the setup described previously for measurement of the extent of deformation (EOD) of the foils. Figure 4-4 shows plasma images formed at different laser energies for a BK-7 overlay. When irradiated with a 6.1 J pulse, in Figure 4-4a, plasma regions formed on both sides of the overlay: on the laser side (left side) of the overlay the much more intense plasma was bright and white-

colored, while on the target side (right side) the plasma was light purple. On the basis of colors, the two plasmas may be different. However, the different colors may be an artifact of the very different intensities. In addition, the foil surface can be seen to be illuminated by the laser and, as the photographs in Figure 4-4 show, this illumination decreases with increasing laser energy.

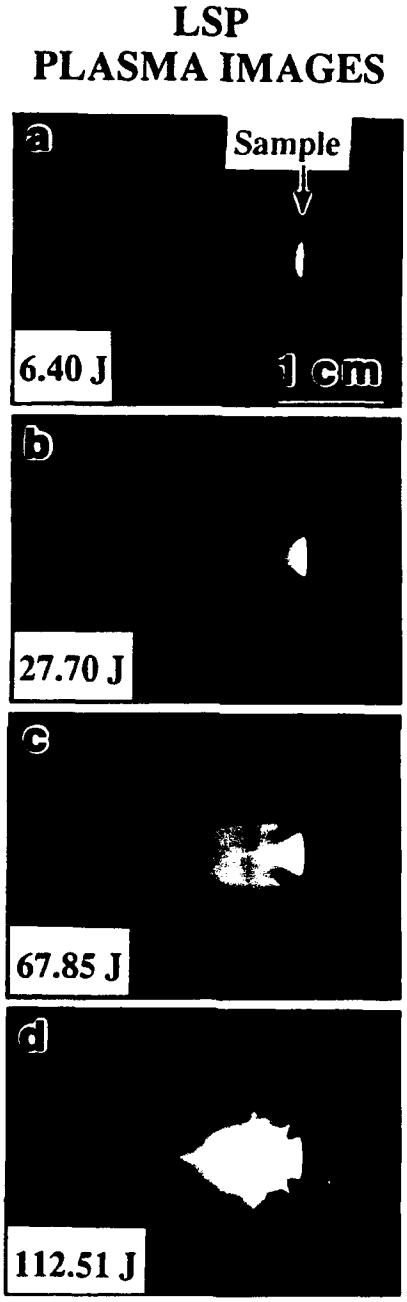

Figure 4-3 Effects of laser energy on plasma formation for BP coated specimens.

In Figure 4-4b, at 28 J, plasma regions were again observed on both overlay surfaces, although their appearances were different from those at low energy. The plasma on the laser side appeared to be brighter and longer, while the specimen side plasma became less intense and shorter. The specimen was illuminated by the laser but its brightness became dimmer as compared to that at low energy (Figure 4-4a). This effect can be attributed to greater absorption of the laser energy by the greater density plasma. At 44 J in Figure 4-4c, the plasma plume formed only on the laser side of the overlay surface. The laser side plasma plume was larger (approximately 8 mm long) and more intense than that for the 28 J pulse shown in Figure 4-4b. However, the specimen at 44 J was not illuminated at the surface, presumably because most of the laser energy was absorbed by the overlay plasma.

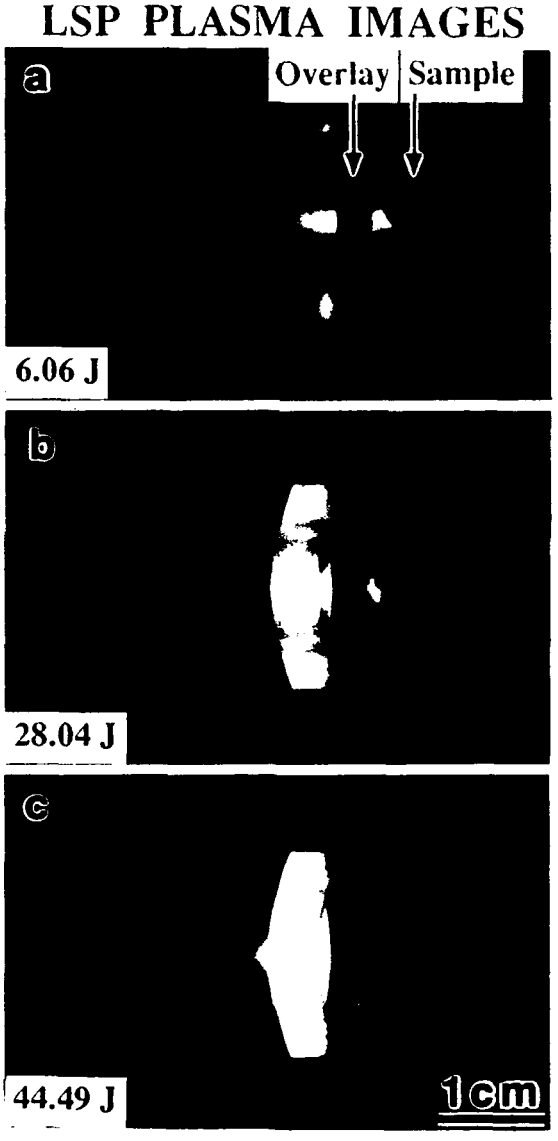

Figure 4-4 Effects of BK-7 overlay on plasma formation at different laser energies.

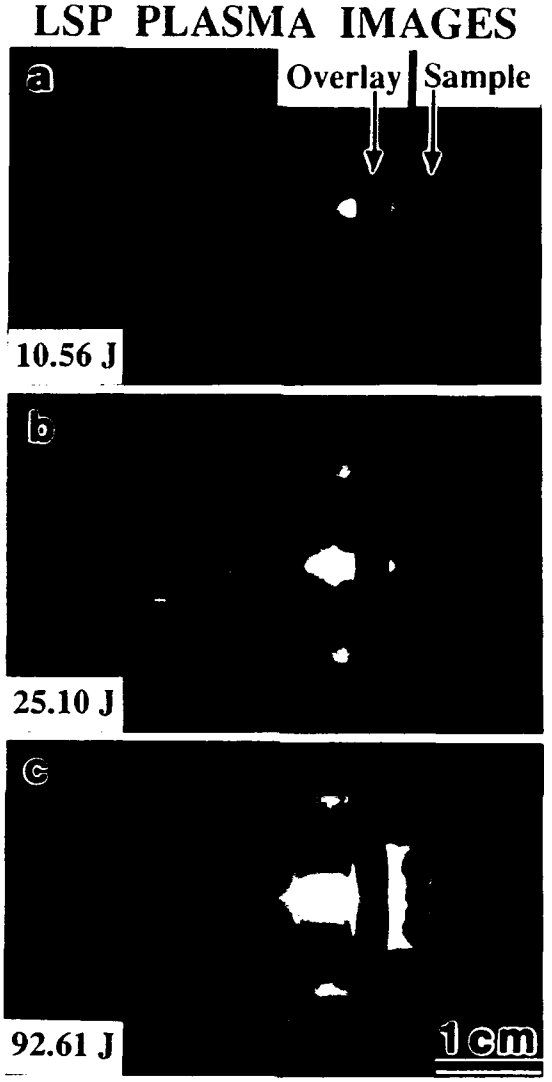

Figure 4-5 Effects of quartz overlay on plasma formation at different laser energies.

In Figure 4-5 the effect of the optical quality quartz overlay on plasma formation can be seen. At 11 J, Figure 4-5a, plasma regions formed on both sides of the overlay similar to the case described in Figure 4-4a. At 25 J, Figure 4-5b, the laser side plasma increased in intensity and developed a well-defined plume. Increased illumination of the specimen relative to the 11 J pulse suggests that the coated specimen was irradiated with more laser energy despite a more intensified overlay plasma. At a very high energy of 93 J, Figure 4-5c, the laser side plasma plume was very intense with a large, ~10 mm long plume. On the specimen side of overlay a broad, intense plasma region was formed. A particular striking feature was the illuminated ring-

like pattern on the coated specimen surface. The ring-like area consisted of a central dark region about 2 mm in diameter and a bright ring about 3.5 mm in diameter, and a low intensity outer ring. This ring-like feature may be a result of an interaction between the overlay and the high energy laser pulse.

These plasma observations were generally consistent with residual damage of the overlay materials after LSP. At laser pulse energies below about 10 J, the overlay surfaces were visibly clouded and cracked. At higher energies, both surface and internal damage (mainly cracks) was common. At energies above 80 J the overlay suffered catastrophic fracture. These observations of laser/overlay interactions suggest that a loss of effective laser energy and thereby a loss of shock wave pressure. This prediction is consistent with the post-LSP characterization results presented in later sections.

4.1.4. Summary of Plasma Formation

To summarize the plasma observation results, two important findings can be drawn: 1) The specimen coated with the BP was shown to form much less intense plasma than the metallic surface at the same level of laser energy. Intensity of plasma emitted from the coated surface became stronger as the laser energy increased. 2) When the overlay was used, the formation of plasma on the overlay surfaces was intensive. This overlay plasma intensified with increasing laser energy and, subsequently, the specimen received much less energy due to plasma absorption.

4.2. Surface Morphologies and Subsurface Microstructures

This section presents characterization results from the surface morphologies and the subsurface microstructures. Results include (1) optical photographs for macroscopic observation and surface profiles for measurement of surface roughness and indentations, (2) scanning electron micrographs of the surface morphology, (3) transmission electron micrographs for the microstructure and phase transformation study, and (4) X-ray diffraction results for the evolution of phase changes.

4.2.1. Macroscopic Observation and Surface Profilometry

a. Macroscopic Observation -- Energy and Overlay Effects

Photographs taken from the front and back sides of a 100 μm thick, BP coated, low carbon steel specimen LSP with 188 J (Figure 4-6b) show an indentation caused by the resulting shock wave. At lower laser energy of 30 J, no noticeable deformation on the back side of specimen was observed, as seen in Figure 4-7b. This suggests that a higher laser energy resulted in a higher shock intensity and more deformation at the target. In both figures (4-6a and 4-7a) the front sides of LSP specimens show two different processing affected zones: one about the size of the laser beam where the BP was almost completely removed and the other (about the size of the specimen-covering aperture) where some residual BP remains. As seen in Figure 4-6b, the size of the deformation on the specimen back surface was approximately that of the laser beam (as shown in Figure 3-2b). The measured step heights on the back surface (in Figure 4-6b) were in a range of 5 to 20 μm. The variation in step heights is presumably due to the inhomogeneous laser energy distribution.

To illustrate the effects of quartz overlay, photographs of two low carbon steel foils treated with different laser energies are presented in Figure 4-8. The back surface of overlay plus BP foils had a noticeable deformation at a low energy, 19 J, (in Figure 4-8a), but not at a high energy, 155 J, (Fig. 4-8b). For the high incident of laser energy, the lack of any protrusion may

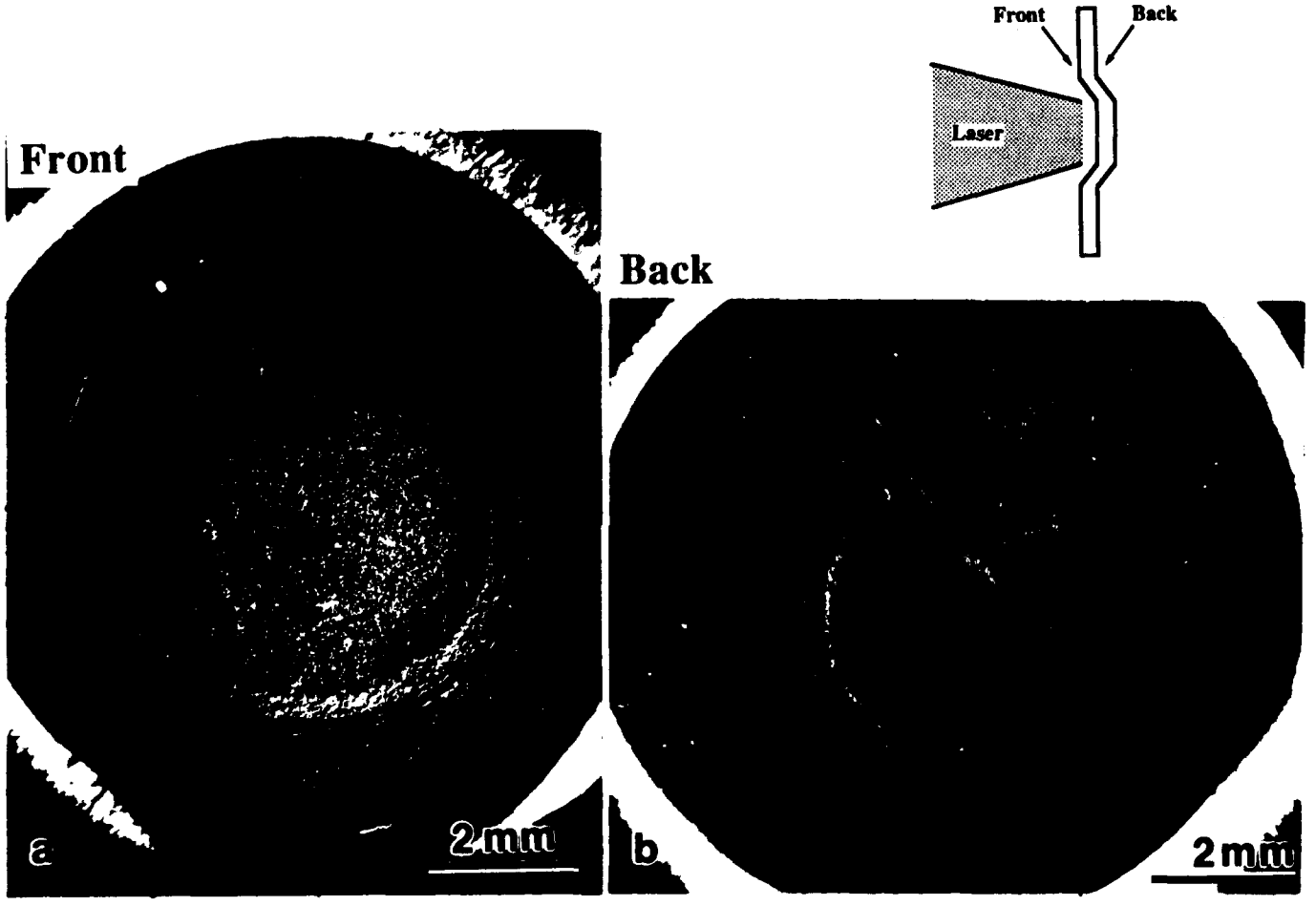

Figure 4-6 Photographs of a 100 μm thick low carbon specimen after LSP at an energy of 188 J with a BP coating and no overlay. (a) Front surface. (b) Back surface.

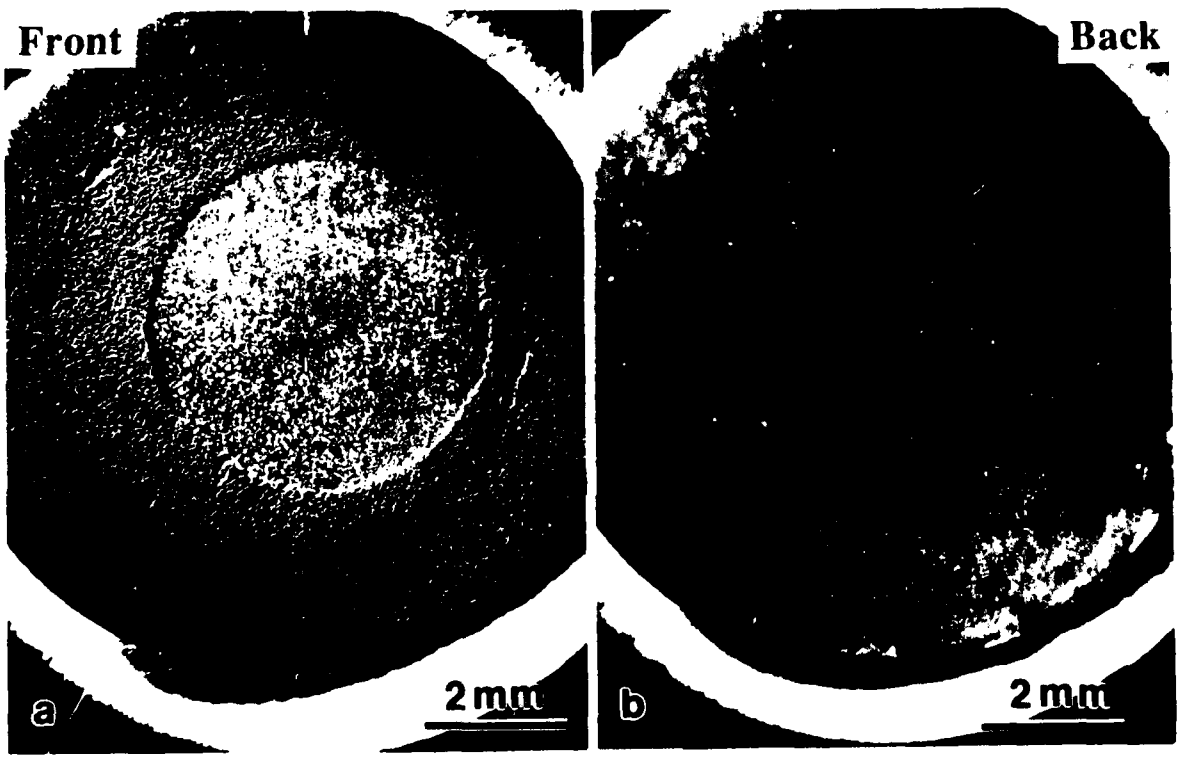

Figure 4-7 Photographs of a 100 μm thick low carbon specimen after LSP at an energy of 30 J with a BP coating and no overlay. (a) Front surface. (b) Back surface.

be because laser-induced fracture of the quartz overlay occurred before a shock wave sufficient to cause of deformation was formed. This is also supported by the evidence of quartz disintegration after LSP and the plasma observation where the overlay plasma became a dominant phenomenon at high laser energy.

b. Surface Profilometry

Overlay and Thin Coating Effects

Effects of the overlay and BP coating on LSP surface roughness are shown in the surface profilometry results of Figure 4-9. The low carbon steel specimens were treated with laser energies ranging from 167 to 178 J. In the case of coated specimens, the coating thickness was 10 - 15 μm and the coating was fully removed after LSP prior to the surface profiling. To differentiate from the later 40 - 50 μm BP coating, the 10 - 15 μm-thick layer is termed a thin coating. In Figure 4-9a, the specimen with a quartz overlay but no BP coating had a spike-like rough surface after LSP, as a result of severe melting. For the bare specimen without any overlay or coating, a similar rough surface resulting from melting is depicted in Figure 4-9b.

The effects of a BP coating on the surface roughness are illustrated in both Figures 4-9c and d. The most significant fact is that the BP coating protects the specimen from severe melting; compare Figures 4-9a and b with Figures 4-9c and d. This result is consistent with the plasma observation results in which the plasma formation on the coated surface was much less intense than that of the bare surface. Despite the use of the BP coating, however, the surface roughness of the coated surface was higher in comparison with that of the untreated specimen; see Figures 4-9c, d, and e. The observed slight curvature of the untreated surface was caused by mechanical polishing. From Figure 4-9, it can be concluded that the specimens without a laser-absorbing coating suffered surface melting, resulting in very rough surfaces. To avoid melting, the use of coating appeared to be a solution.

No Surface Melting -- Energy and Overlay Effects

To eliminate surface melting during LSP, a thick (40 to 50 μm) BP coating was applied. Surface profilometry results for these LSP specimens indicated no surface melting but surface indentations which are consistent with later SEM results. To obtain an overall picture, the surface profiles after removing the coating were more than 6 mm long. Further, the profile measurements all were done under the same conditions so that any energy variation effects within the measured region were minimized. Concerning the laser energy effects, Figure 4-10 depicts laser shock-induced surface indentations on the thick coated low carbon steel specimens treated at laser energies ranging from 5.9 to 111 J. Slight surface curvatures visible across the profilometer scans were due to the polishing effect. At 5.9 J energy no significant indentation was found on the surface. At 31 J energy an indentation started to form on the surface. The indentation appeared to be uneven; the left side of the indent was deeper than the right side. This uneven indentation was believed to be due to inhomogeneous distribution of the laser energy.

As the laser energy increased to 71, 98, and 111 J, the surface indentation became more pronounced, but still uneven. The deepest indentation was about 1.5 μm for the 111 J energy pulse. At this energy, the surface indentation clearly showed characteristics of "punch-in" deformation. Both edges of the indent showed formation of built-up noses as a result of being heaped outward to the peripheral edge from the center region during LSP. The edge build-up formed at energies as low as 31 J and became more pronounced as energy increased. Another interesting feature observed at 111 J was a surface protrusion at the center of the indented region. Overall, surface indentation depth increased with an increase of laser energy .

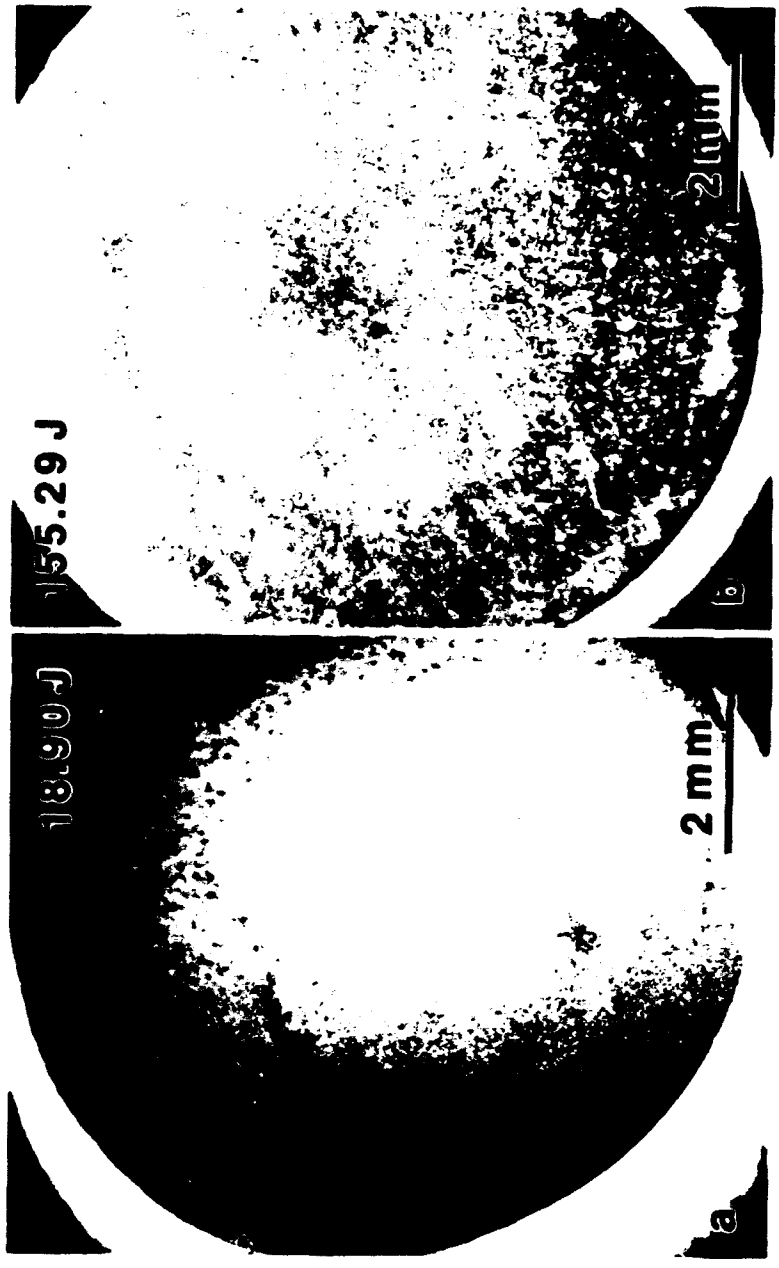

Figure 4-8 Photographs of 100 μm thick low carbon specimen back surfaces after LSP at an energy of (a) 19 J and (b) 155 J with an overlay plus BP.

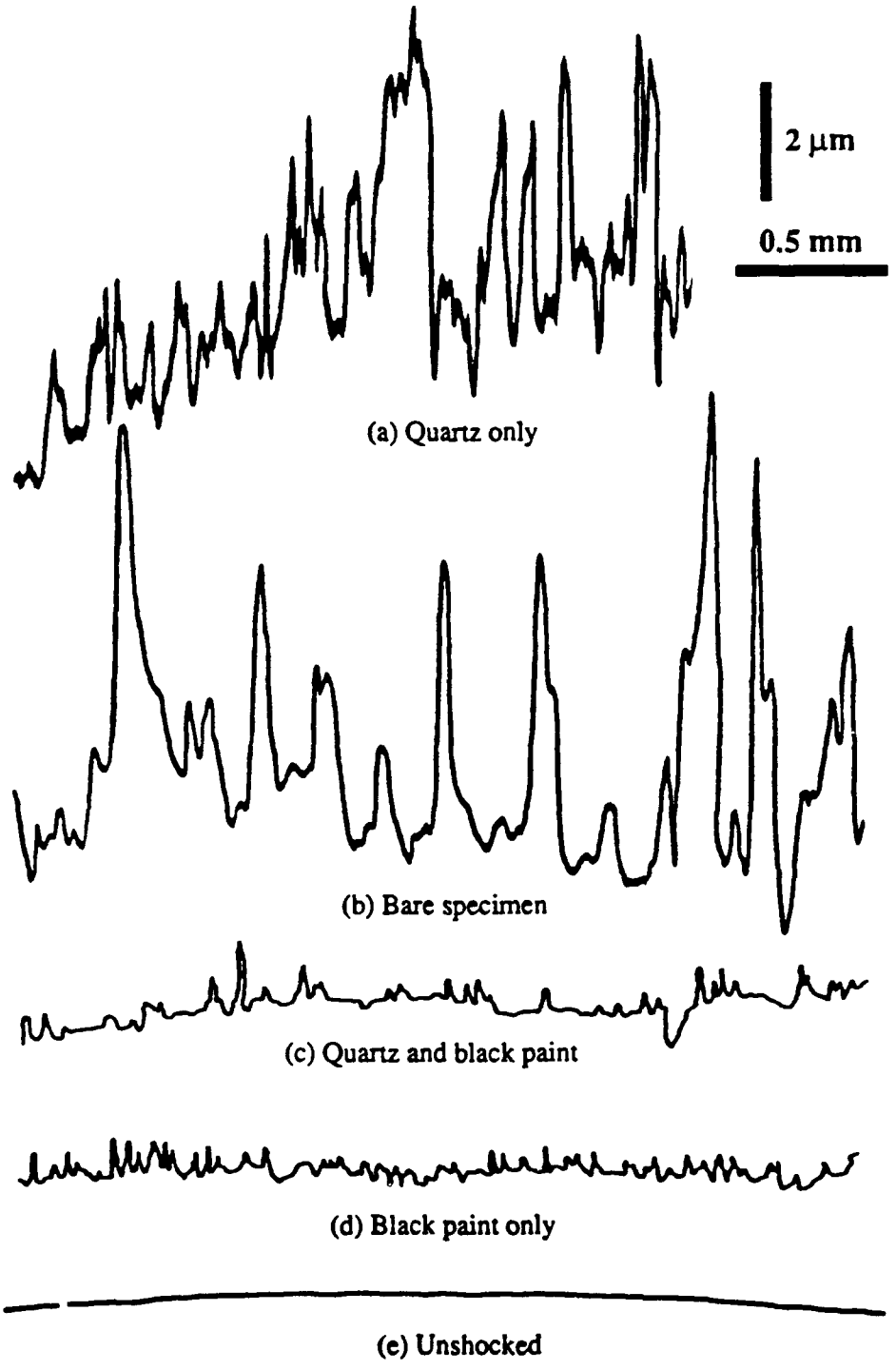

Figure 4-9 Surface profiles of LSP low carbon steel specimens for various surface conditions. All LSP specimens were treated at energies between 167 and 178 J.

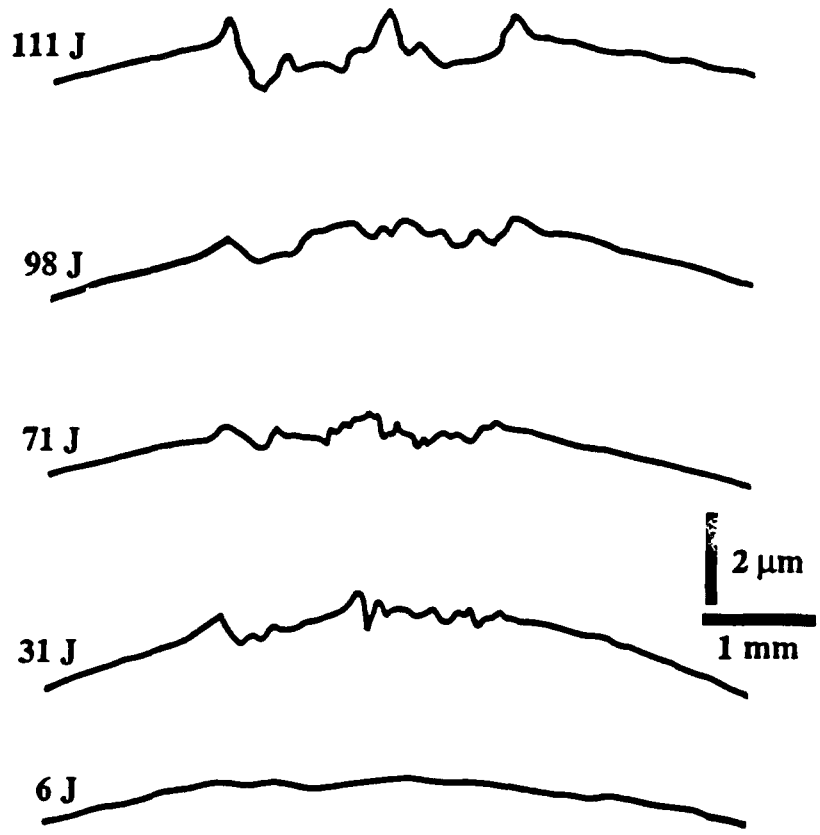

Figure 4-10 Surface profiles of low carbon steel specimens after LSP at energies ranging from 5.9 to 111 J. Specimens were coated with a thick BP during LSP.

A similar relationship between pulse energy and surface indentation was found for the Hadfield steel specimens. As shown in Figure 4-11, at 9.4 J no apparent surface indentation was observed, while at 104 J an indentation was nearly 3 μm deep. The rough surface for the 104 J Figure 4-11b case was due to shock-induced deformation, not melting. It is noted that the build-ups at the indent edges are similar to, but not as large as those for the low carbon steel specimen surfaces.

To see the overlay effect, the surface profiles in Figure 4-11c and d were obtained for quartz overlay plus BP coated LSP specimens. A small, smooth indentation was observed at 5.5 J, but not at 108 J. This is in agreement with laser energy absorption by a plasma formed at overlay that causes insufficient energy to generate a shock wave on the specimen surface for a measurable indentation to form. The shock-induced deformation at 5.5 J with an overlay was small, but still larger than that for the specimen treated with 9.4 J without an overlay (compare Figures 4-11a with c). This indicates that for low laser energies where the energy loss due to an overlay was not substantial, the overlay did enhance shock wave generation and thus specimen deformation.

To compare LSP with shot peening, a commercial surface treatment process, a surface profile measured from a shot peened Hadfield steel specimen is presented in Figure 4-11e. As seen in this profile, the shot peened specimen exhibited a considerably rougher surface, as compared to unmelted LSP surfaces. This rough surface is caused by the shot striking the sample and locally deforming the surface.

Estimation of Laser Energy Loss Due to Overlay

Since these results showed that use of a quartz overlay led to a significant laser energy loss during LSP, estimation of the energy loss was important in order to optimize the experimental conditions. Calculation of the energy loss assumed that the unsupported stainless steel foil was uniformly deformed by the laser generated shock wave. The extents of deformation (EOD) of the back surface of deformed foils were measured as the tangent of the shock deformed region with respect to the unshocked region of the foil, as shown in Figure 3-6b. In Figure 4-12 the EOD was plotted as a function of laser energy for foils with and without an overlay. In both cases the foils were coated with BP prior to LSP. In the case of no quartz overlay, Figure 4-12 shows more EOD when the foil was treated with higher laser energy. The EOD for foils with an overlay was constant for the entire energy range.

c. Summary of Macroscopic Observation and Surface Profilometry

Macroscopic observations and surface profiles of LSP specimens showed that energy loss in the quartz overlay was the dominant factor limiting specimen deformation. Energy loss became more significant as the laser energy increased. On the other hand, when an overlay was not used, the extent of deformation increased with increasing laser energy. A thick (40 - 50 μm) laser-absorbing BP coating protected the target specimen surface from severe melting during LSP.

4.2.2. Surface Morphology

a. Bare Specimen -- No Overlay and Coating

For LSP low carbon steel specimens without a quartz overlay or BP coating, surface melting and re-solidification accounted for the most common morphologies, as seen in Figures 4-

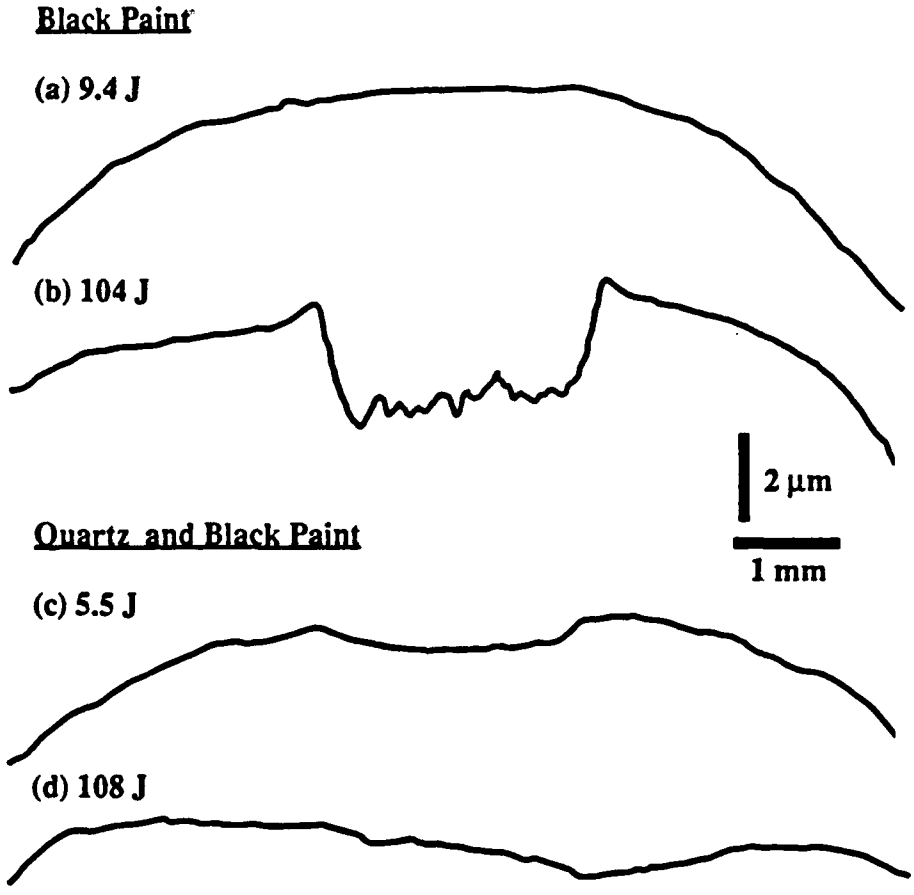

Figure 4-11 Surface profiles of Hadfield steel specimens after LSP at different energies and surface conditions. Thick BP coated only: (a) and (b); overlay and thick BP: (c) and (d).

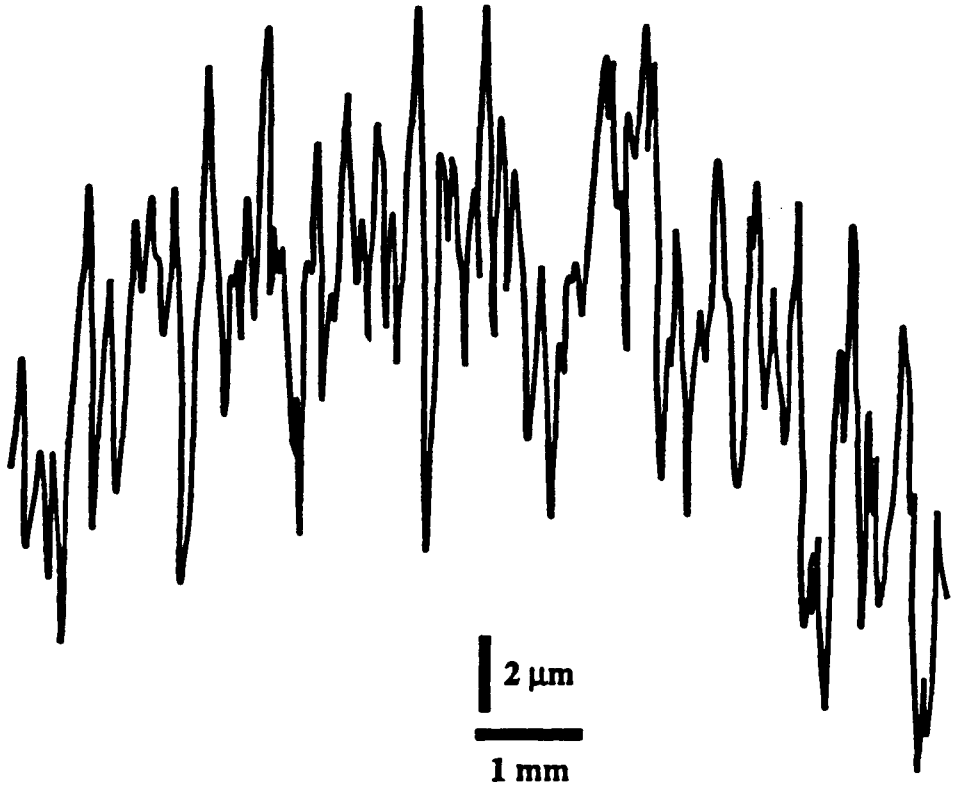

Figure 4-11 (continued) (e) Surface profile of a shot peened Hadfield steel specimen.

13 and 4-14. The morphologies most observed are craters, holes, solidified droplets, splash-like spills, and molten flowing layers. In both figures, specimens were treated with a laser energy of 149 J (Figure 4-13) and 190 J (Figure 4-14). At low magnification in Figure 4-13a, a ripple-like surface morphology is seen over the entire viewing area. At higher magnifications, a dimpled region (Figure 4-13b) and solidified droplets (4-13c and d) are revealed. Individual solidified droplet shown in the figures consisted of several solidified layers on top of each other. Further, in Figure 4-13c molten flowing layers are seen.

Different surface morphologies were observed in Figure 4-14 for a bare specimen subjected to a higher laser energy pulse. Figures 4-14b, c, and d correspond to regions b, c, and d in Figure 4-14a. It is apparent that the center laser treated region (Figures 4-14b and c) exhibited a different morphology from that of outer untreated region (Figure 4-14d). In the center treated region in Figure 4-14b, features such as solidified flowing layers were found to be similar to those observed in Figures 4-13c and d. A distinct feature, however, was noted as numerous craters and holes were formed in the region for 190 J (Figure 4-14b and c) energy pulse whereas droplets were present for 149 J pulse (Figure 4-13b, and c). This feature can be seen clearly at

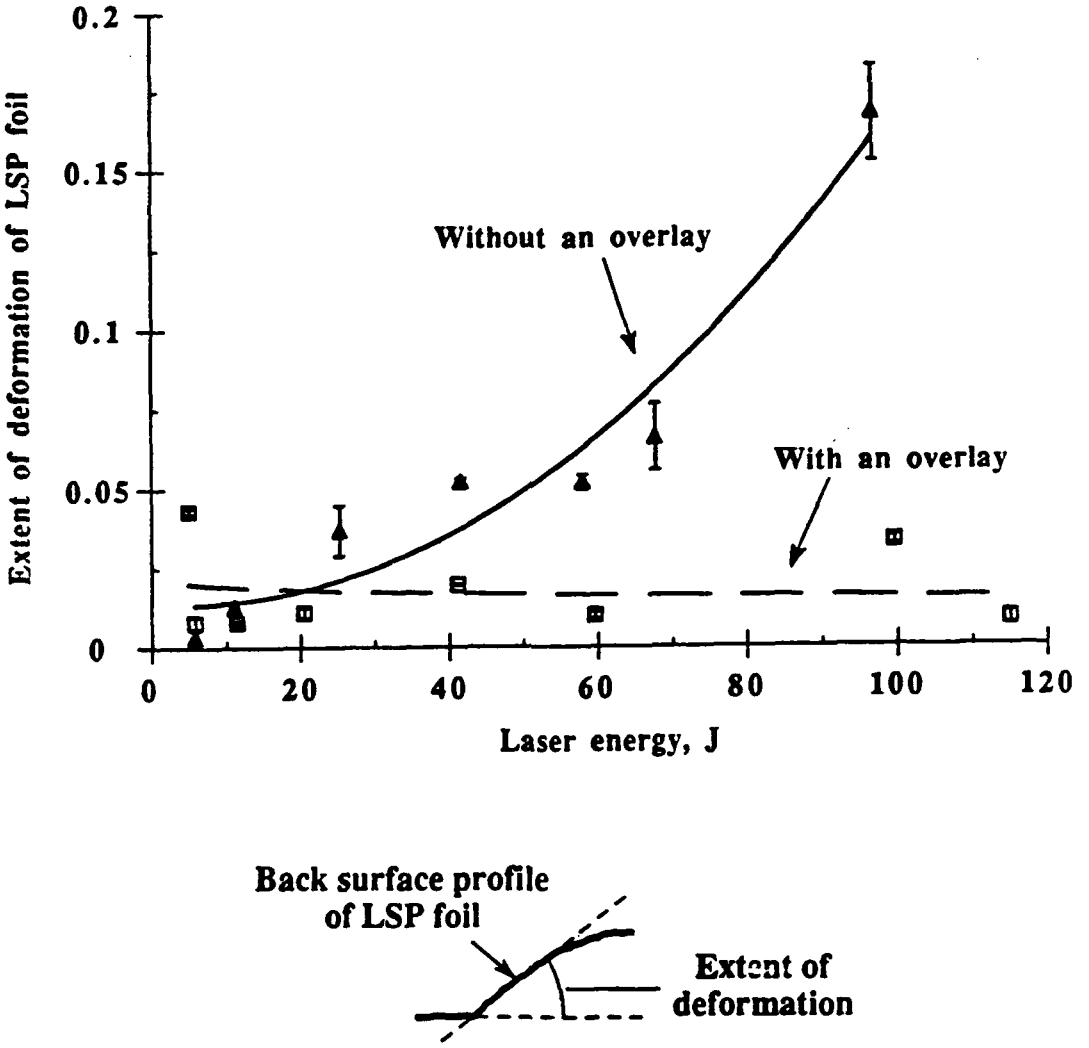

Figure 4-12 Extent of deformation of LSP foils as a function of laser energy with and without an overlay.

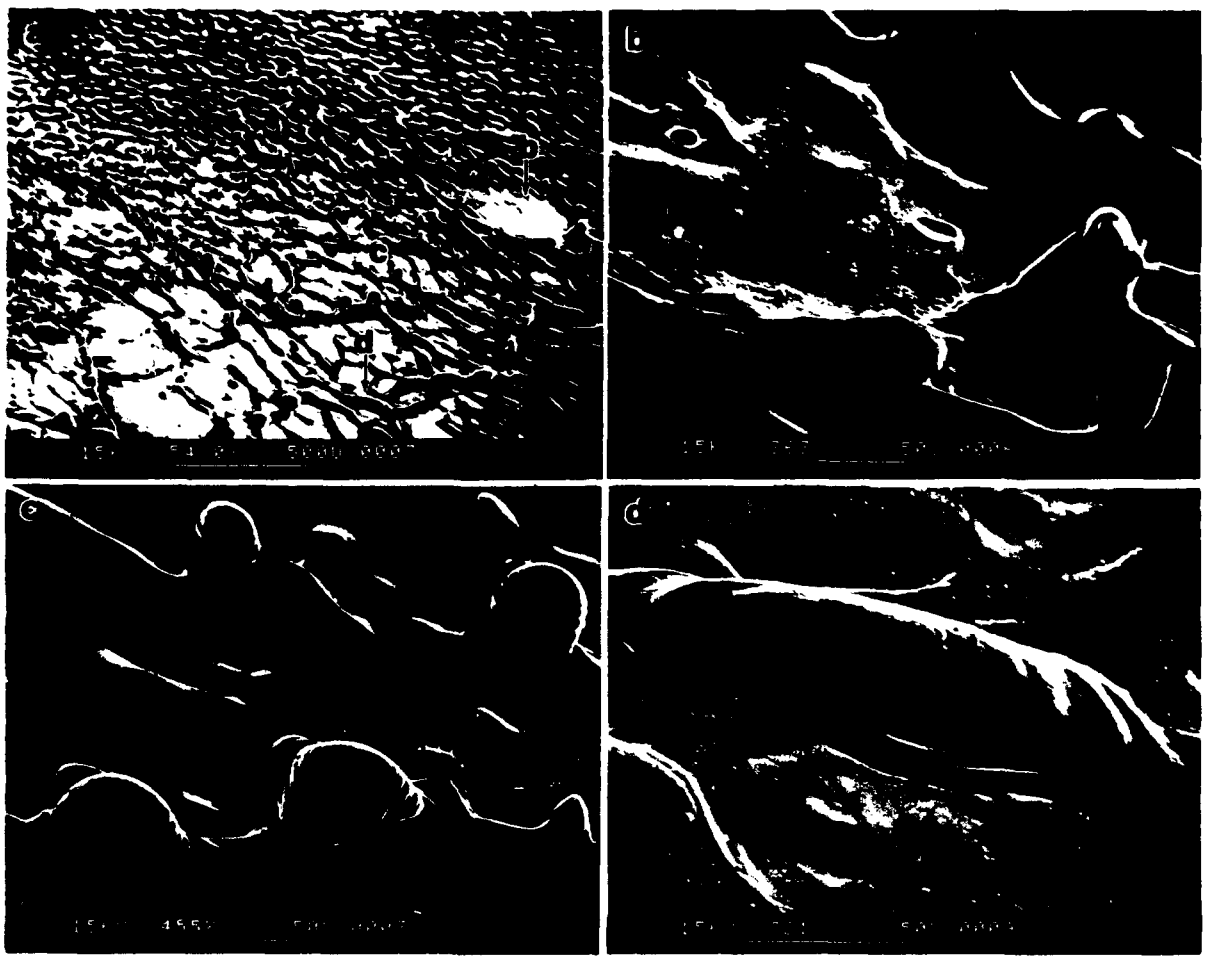

Figure 4-13 SEM micrographs of a low carbon steel specimen after LSP at an energy of 149 J without BP coating and overlay.

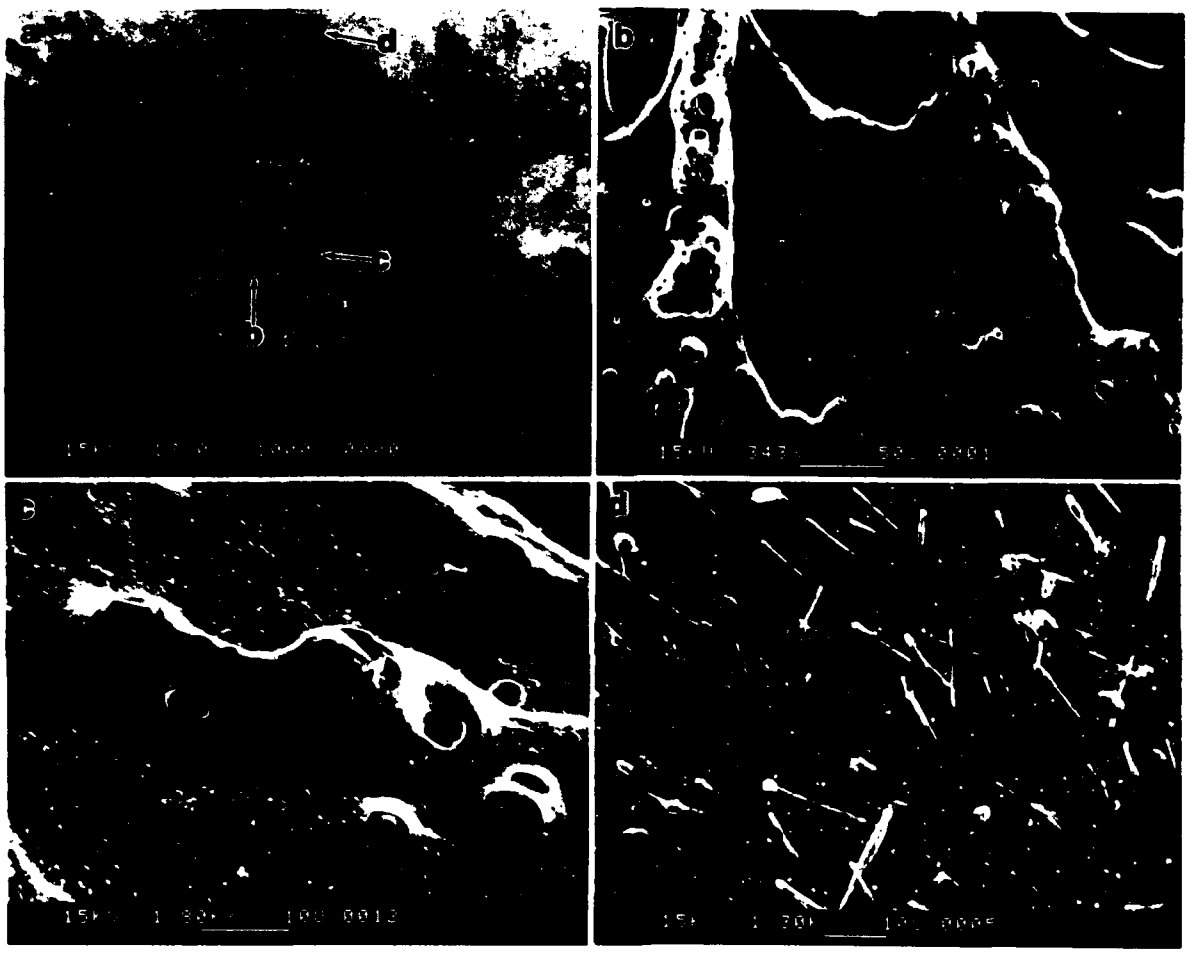

Figure 4-14 SEM micrographs of a low carbon steel specimen after LSP at an energy of 190 J without BP coating and overlay.

high magnification in Figure 4-14c. So, laser energy is an important factor in altering surface morphology. Further, for the 190 J energy pulse, a great number of solidified splash-like droplets were observed in the outer untreated region (Figure 4-14d). Existence of these droplets suggests that a pressure was exerted on the molten liquid, resulting in an expulsion of the molten liquid outwards creating the splash-like droplets.

b. Overlay Effects Without a Coating

Morphology effects of a quartz overlay without a coating can be seen in Figure 4-15 for a low carbon steel specimen treated with a laser energy of 166 J. Under these surface conditions, a surface morphology resulting from melting was commonly found. At low magnification, a view of the treated area reveals an explosion-like splash morphology (Figure 4-15a). The explosion-like splash may be the result of melted material expanding outwards under the formed plasma pressure between the overlay and the specimen. At high magnification in Figure 4-15b, small numerous droplets formed in a wake of whirlpool-like solidified structures.

Moreover, different surface features are seen within the LSP region (Figure 4-16). At low magnification in Figure 4-16a, two different morphologies adjacent to each other are observed. At higher magnification in Figure 4-16b and c these features can be distinguished; severe melting at the center (b) and droplets as well as flowing layers in the outer region (c). In Figure 4-16d much less melting was found in peripheral areas. Since the laser had a near-Gaussian intensity distribution, the laser energy in the center region was expected to be higher than that in the peripheral area. Therefore, the center surface suffered more melting than elsewhere. With the use of an overlay, the surface morphologies appeared to be more sensitive to the inhomogeneity of laser beam energy than other surface conditions.

c. Coating Effects

Partial Surface Melting

The effects of a BP coating on the specimens are presented in the two categories: partial specimen surface melting and no surface melting. For the LSP specimens coated with a thin layer of BP (10 - 15 μm), regardless of whether a quartz overlay was used or not, localized and scattered surface melting was found as a common feature as seen in Figure 4-17 for a low carbon steel specimen treated with a laser energy of 178 J. In this case, due to incomplete coating coverage, melting occurred in a scatter pattern with an average size of the melting spots of 10 to 20 μm. At the high magnification view shown in Figure 4-18a, the surface melting existed only to a limited extent and some initial surface's features (such as polishing scratches) were retained after LSP. This suggests that the BP sacrificial coatings absorbed much of the laser energy, and thus protected the shocked specimens from extensive surface melting. In this melting area, a number of various sized holes and craters were revealed at still higher magnification in Figure 4-18b. Formation of holes and craters may be caused by rapid cooling and solidification rates of the superheated shocked area after the hot plasma vapor plume decayed away.

No Surface Melting

For the LSP specimens coated with a thick layer of BP (40 - 50 μm), surfaces exhibited no melting at all in the SEM observations. In Figure 4-19, two low magnification views of chemically etched low carbon steel surfaces are presented. The specimen shown in Figure 4-19b was BP coated during LSP and treated with a laser energy of 108 J. The etched surface before LSP shown in Figure 4-19a indicated very few etch pits in the grains, while the etched LSP surface in Figure 4-19b revealed a number of etch pits in several grains. The pits that appeared

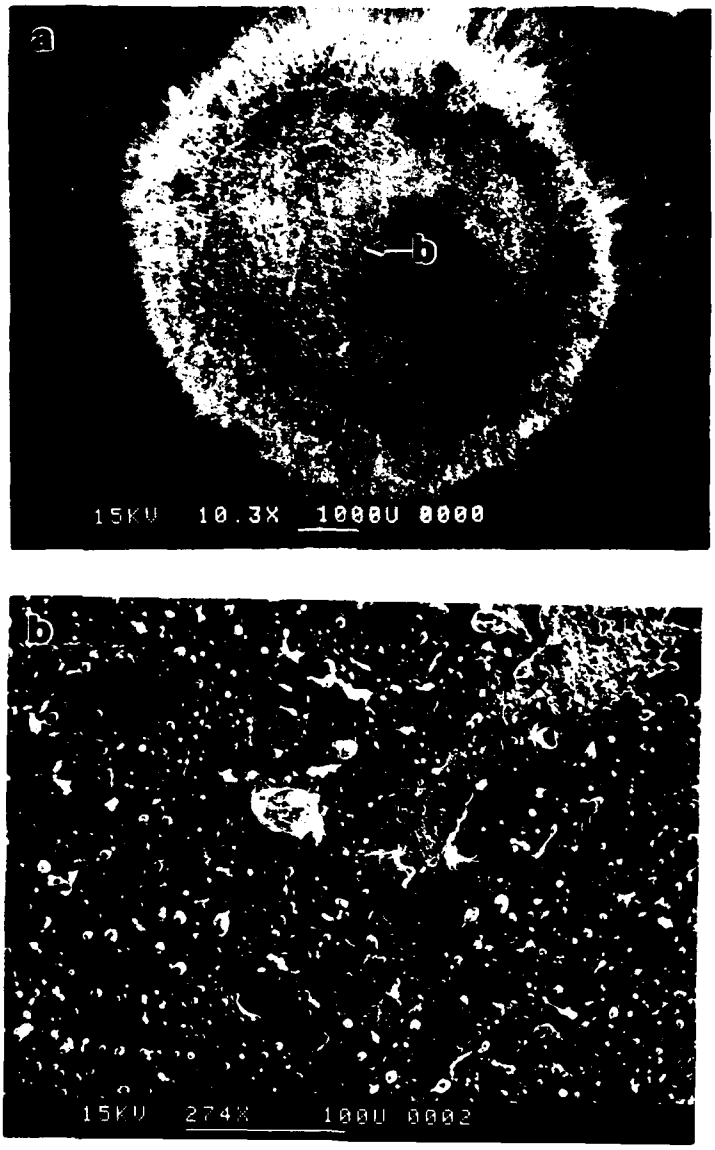

Figure 4-15 SEM micrographs of a low carbon steel specimen after LSP at an energy of 166 J with an overlay and no BP coating.

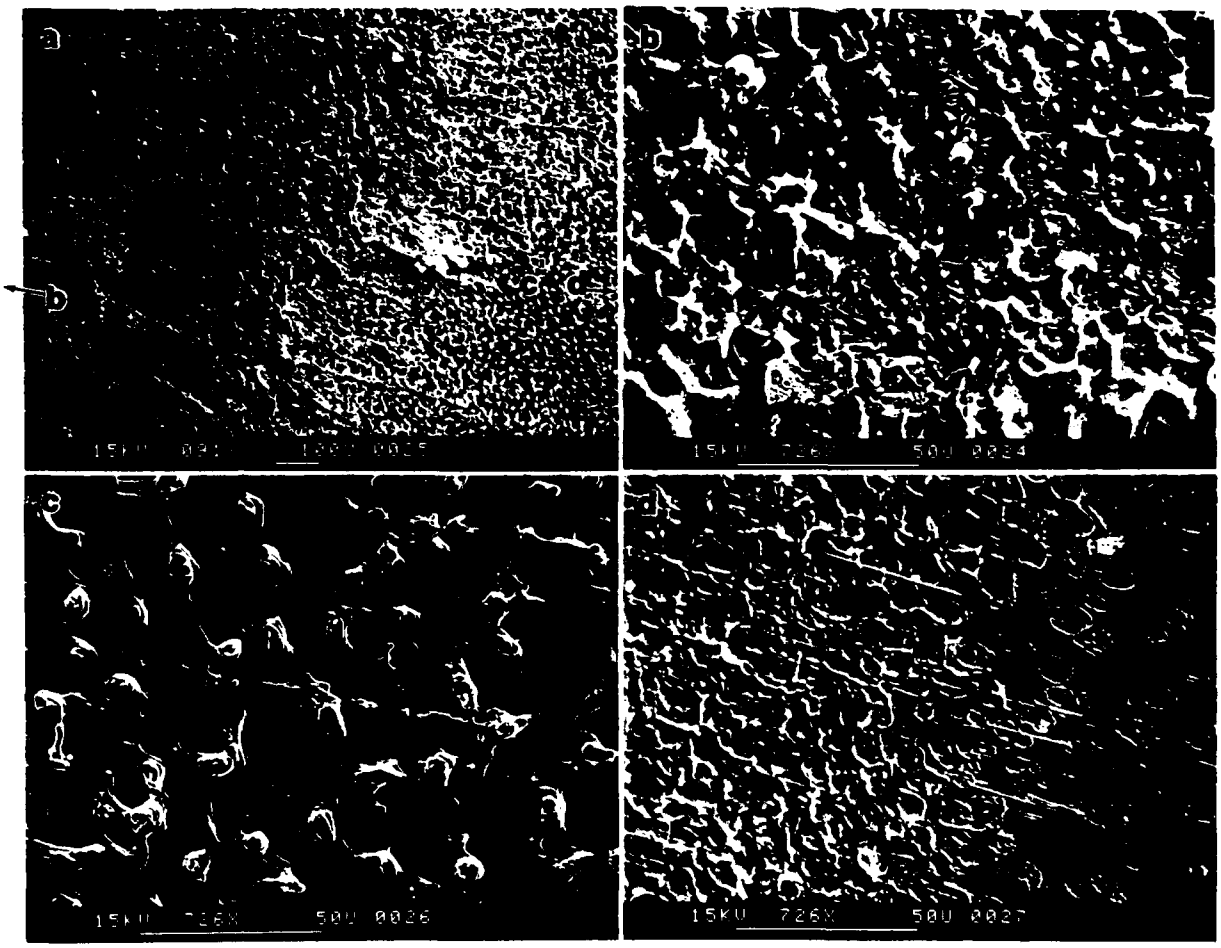

Figure 4-16 SEM micrographs of a low carbon steel specimen after LSP at an energy of 174 J with an overlay and no BP coating. (a), (c) and (d) at peripheral laser treated area; (b) center of laser treated area.

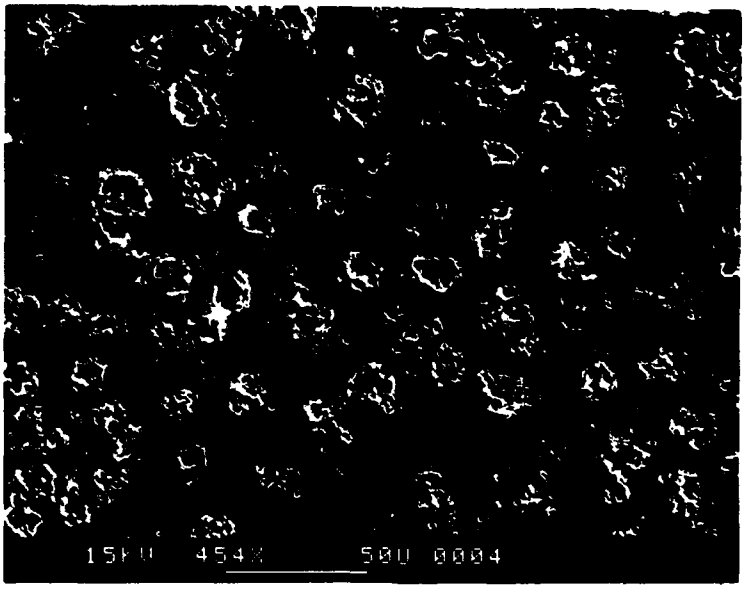

Figure 4-17 SEM micrograph of a low carbon steel specimen after LSP at an energy of 178 J with a thin BP coating and no overlay.

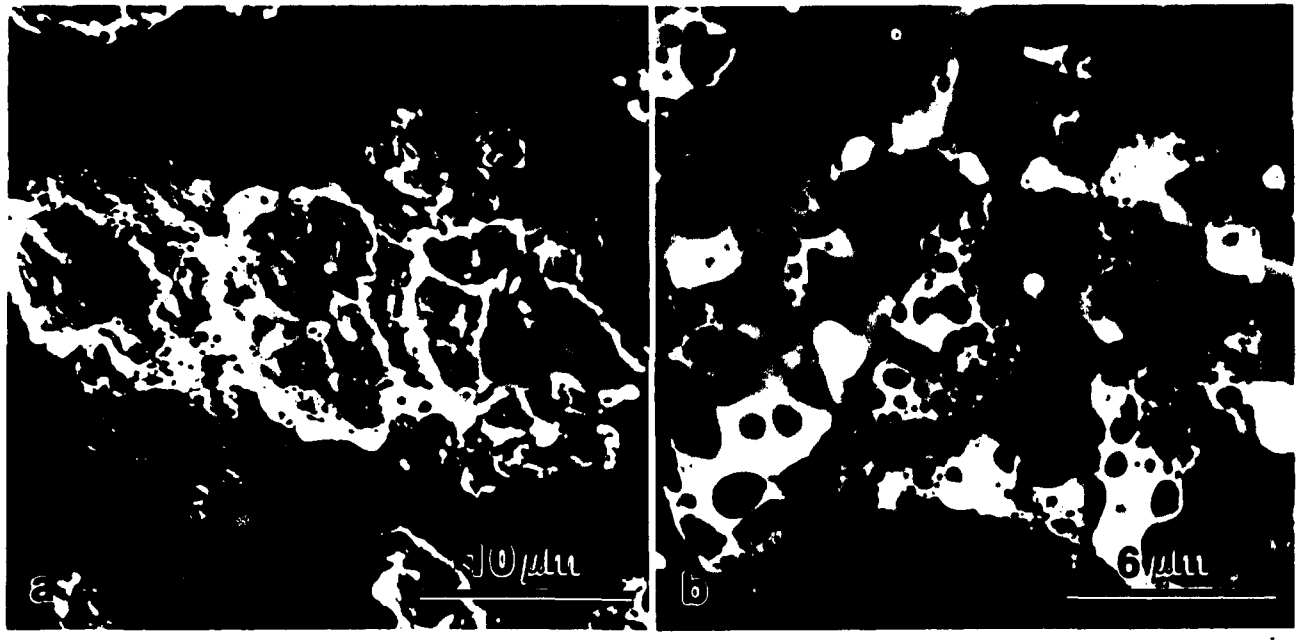

Figure 4-18 SEM micrographs of low carbon steel specimens after LSP at an energy of (a) 178 J and (b) 30 J with a thin BP coating and no overlay.

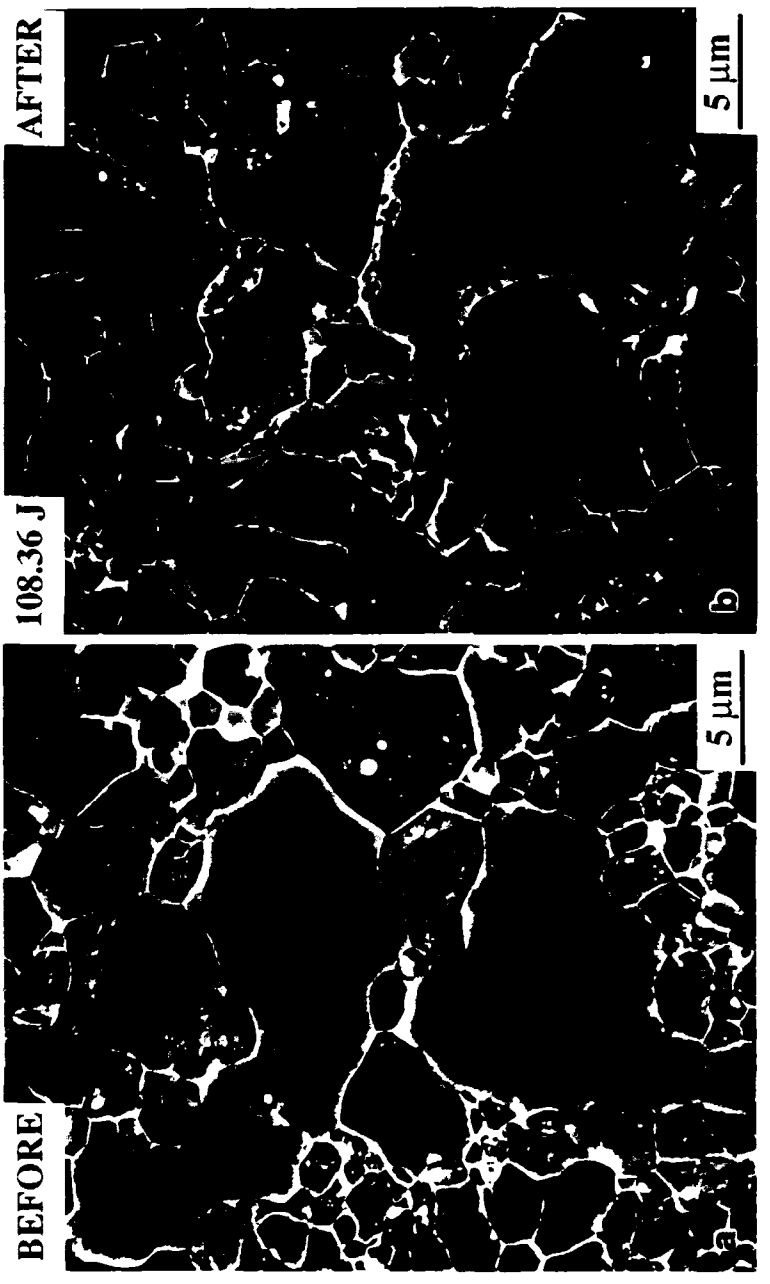

Figure 4-19 SEM micrographs of etched low carbon steel specimens: (a) Before LSP. (b) After LSP at an energy of 108 J with a thick BP coating and no overlay.

in the grains were dislocation etch pits. After LSP, an increase in the number of etch pits on the specimen surface indicates the specimen surface was deformed during LSP.

This is consistent with surface profilometry results. Also, Figure 4-19b shows no evidence of melting, suggesting that the thick BP coating served as a surface protection for the specimen from melting. At higher magnification in Figure 4-20, the dislocation etch pits are circular in shape. Coalescence of several small pits into large pits is also shown in this figure.

For the LSP Hadfield steel specimens, two SEM micrographs are shown in Figure 4-21. For comparison, the etched specimen surface before LSP is given in Figure 4-21a where grain boundaries were clearly visible. The LSP specimen surface in Figure 4-21b revealed deformation-induced slip lines within the grains. The specimen surface shown was lightly etched and then BP coated for LSP at 113 J. In addition to the slip lines, a macroscopic surface relief became obvious as a result of plastic deformation, as seen in Figure 4-21b. No surface melting occurred on the LSP surface (Figure 4-21b).

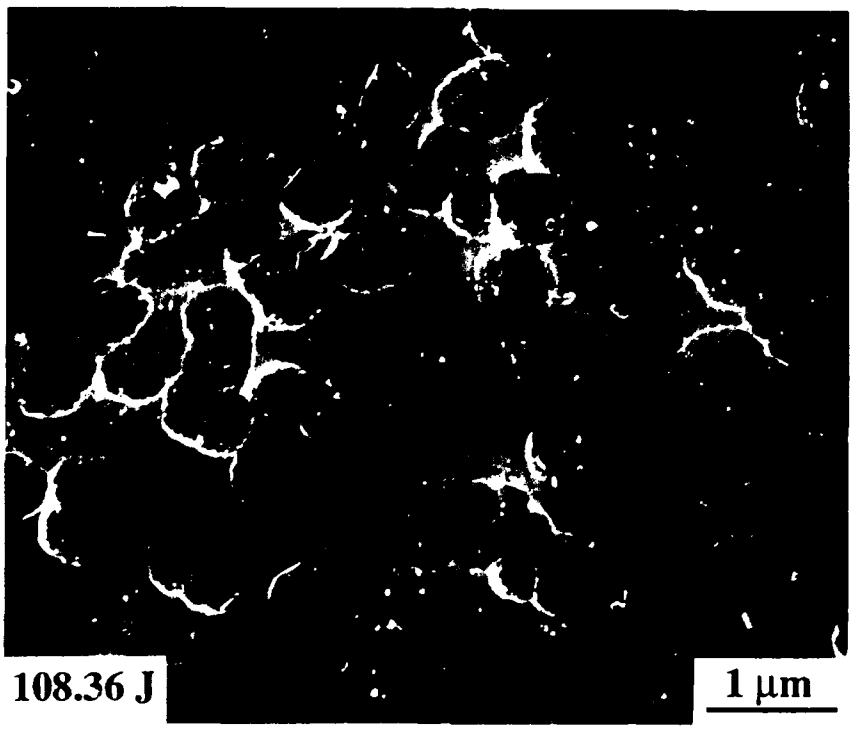

Figure 4-20 SEM micrograph of an etched LSP low carbon steel specimen at high magnification from Figure 4-19.

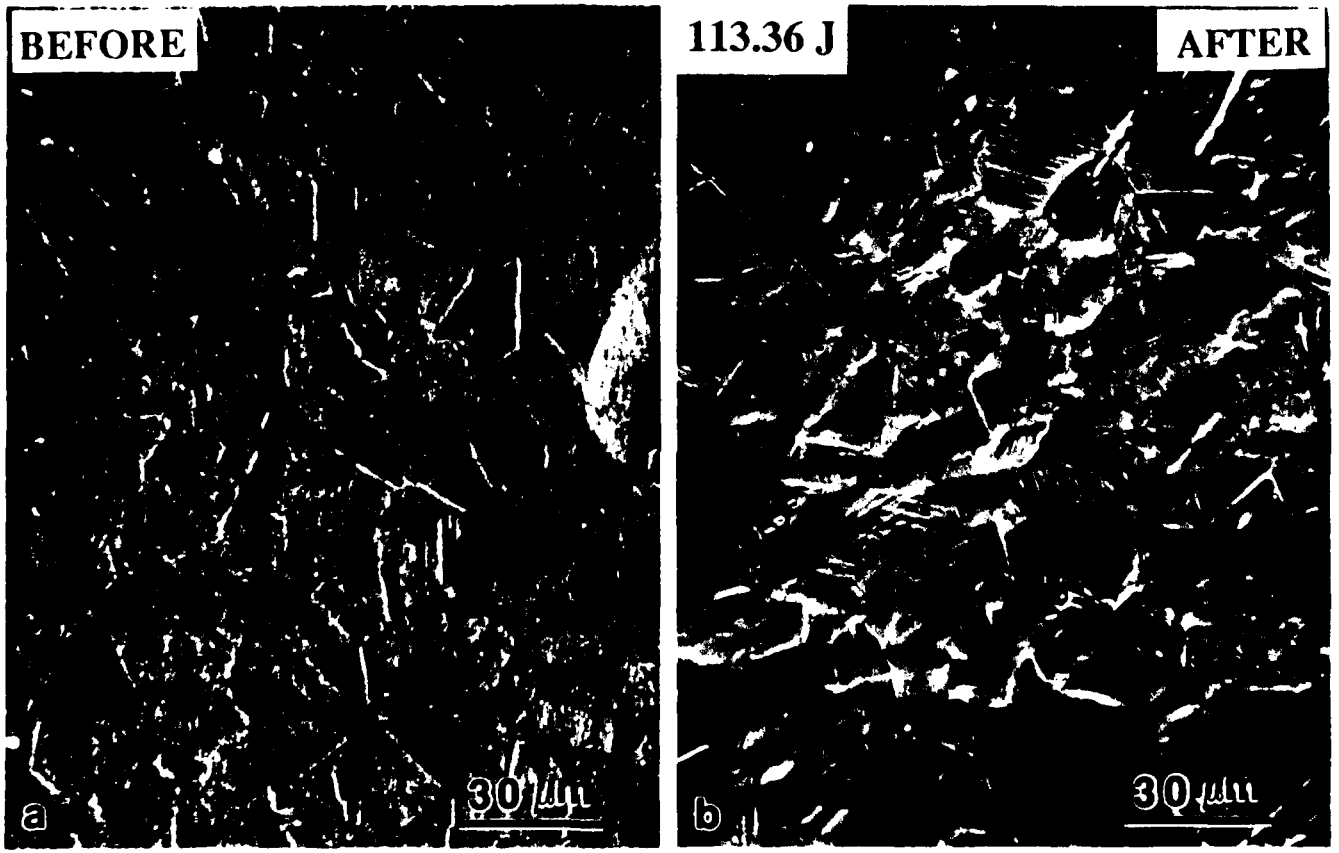

Figure 4-21 SEM micrographs of etched Hadfield steel specimens (a) Before LSP. (b) After LSP at an energy of 113 J with a thick BP coating and no overlay.

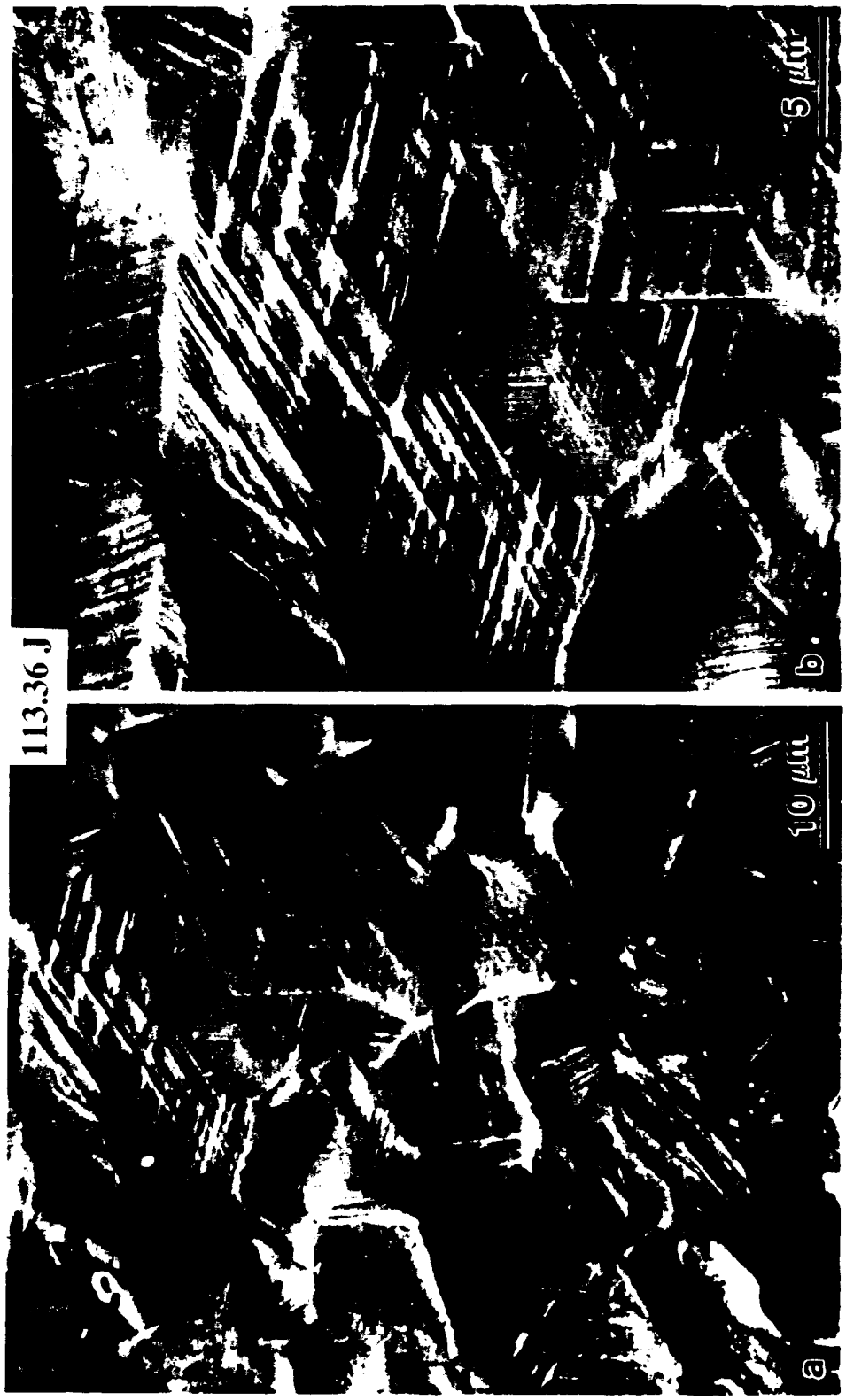

Figure 4-22 High magnification SEM micrographs of an etched Hadfield steel specimen after LSP at an energy of 113 J with a thick BP coating and no overlay.

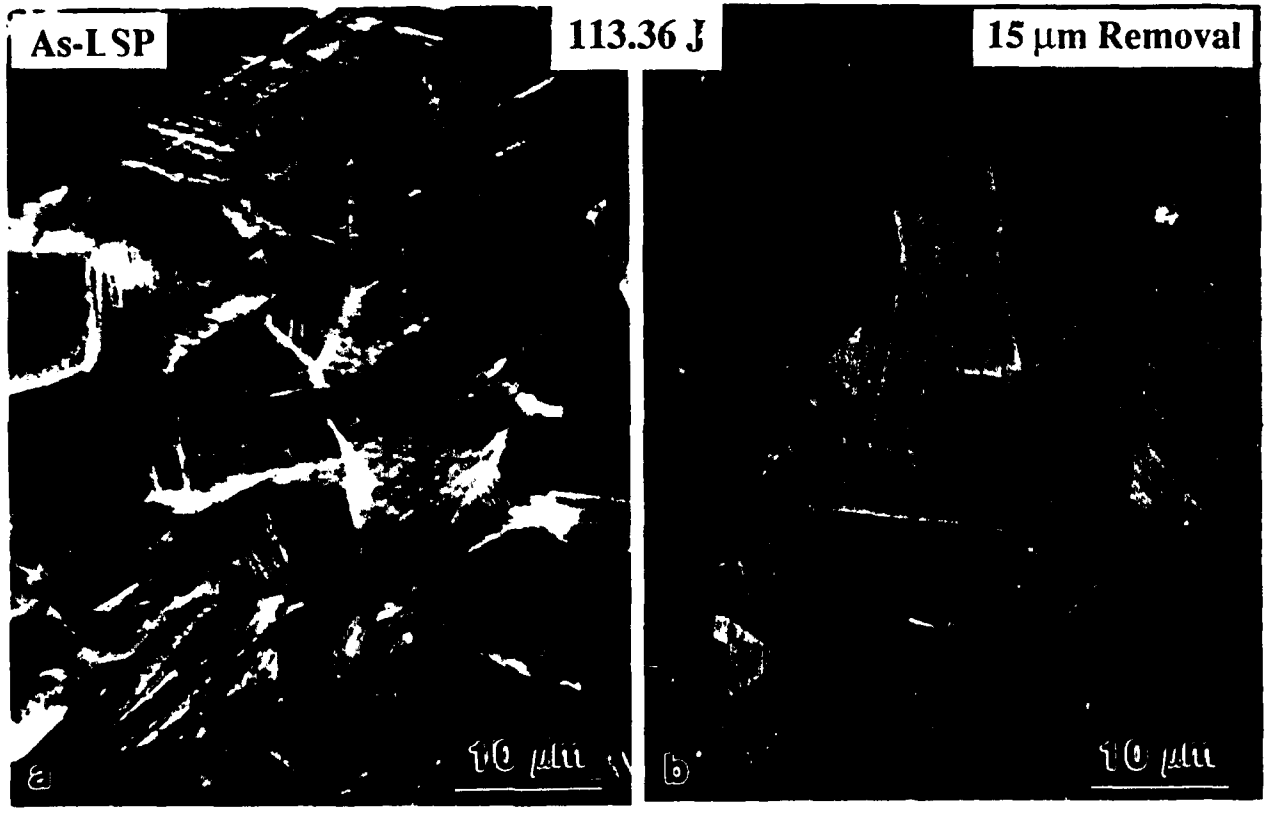

Figure 4-23 SEM micrographs of an etched Hadfield steel specimen (a) After LSP at an energy of 113 J with a thick BP coating and no overlay. (b) After 15 μm surface layer removal.

In the SEM micrographs at higher magnifications, features such as the slip lines in the grains and surface relief are clearly revealed, as seen in Figure 4-22. In both micrographs, the grain boundaries were not distinct, presumably due to a macroscopic surface relief. The slip lines, however, were apparent all over the examined area (Figure 4-22a). Again, there was no surface melting observed in the region. In Figure 4-22b, a higher magnification micrograph shows more than one type of slip line present within the same grain. For example, at the center of the micrograph two types (directions) of slip lines are seen in one grain. In the right bottom corner, three types of slip lines are revealed within a grain. As a result, ledge-like morphologies are found in those regions.

Existence of slip lines at 15 μm below the surface is shown in Figure 4-23 for an electropolished LSP Hadfield steel specimen which was BP coated and treated at an energy of 113 J. The LSP surface morphology is given in Figure 4-23a for comparison, while the surface after 15 μm removal is in Figure 4-23b. The macroscopic surface relief was clearly revealed in the as-LSP surface micrograph (Figure 4-23a), while the removed surface did not have any macroscopic relief visible and grains were clearly seen (Figure 4-23b). Since there is no macroscopic surface relief found 15 μm below the LSP surface, it is confirmed that the plastic deformation on the LSP surface was responsible for the macroscopic surface relief. Furthermore, since slip lines were apparent in both micrographs, the deformation was substantial enough to induce slip lines in the region about 15 μm from the LSP surface.

For comparison, Figure 4-24 shows SEM micrographs obtained from a shot peened low carbon specimen. These micrographs reveal some features (such as craters and dimples) as an evidence of surface damages from the impact loading of the shot.

d. Summary of Surface Morphology

From the above SEM observations, it is noted that the LSP surface conditions play an important role in altering the surface morphology; melting at different extents, as well as partial and even no melting could be obtained. When a quartz overlay with no BP coating was used, the most severely melted surface resulted. A bare specimen without an overlay or BP coating actually had less melting due to LSP. For these two LSP surface conditions, the melted features most observed were craters, holes, solidified droplets, splash-like spills and molten flowing layers. Further, it is found that the laser intensity variation within the treated region generated different surface morphologies on the specimen. That is, the center surface suffered more melting than the periphery.

The BP coating appeared to protect the LSP surface from melting. A thin BP coating (10 - 15 μm) resulted in scattered surface melting. This melting was completely eliminated by applying a thick BP coating (40 - 50 μm). In the absence of melting, microstructural changes due to plastic deformation were clearly revealed. For the LSP low carbon steel specimens, numerous dislocation etch pits were observed on the surface, while for the LSP Hadfield steel specimens macroscopic surface relief lines and numerous slip lines within grains were found. The slip lines still existed even after 15 μm of the surface layer was removed. For the shot peened specimen, the surface appeared to have craters and dimples resulting from the shot loading.

4.2.3. Microstructure and Phase Transformation

LSP effects on the microstructure were examined by TEM for the low carbon and Hadfield steel specimens. Examination of the surface and the near surface were performed. For comparison, specimens of both steels were examined after shot peening and cold rolling.

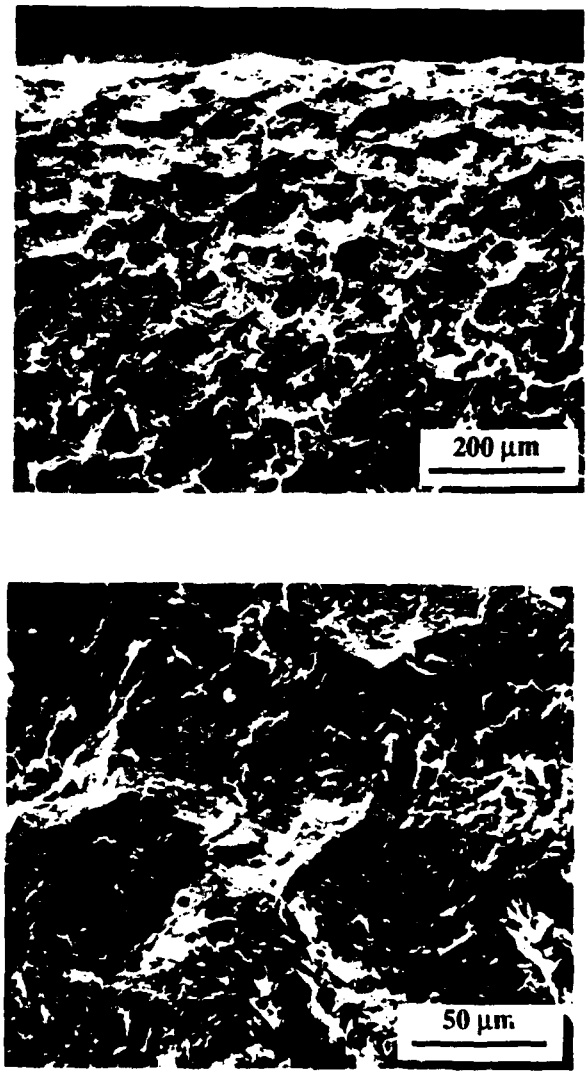

Figure 4-24 SEM micrographs of a shot peened low carbon steel specimen.

a. LSP Effects

Low Carbon Steel

The prominent TEM feature of the LSP low carbon steel specimens was high density dislocations. Figure 4-25 shows a TEM bright field image from near-surface (<1 μm) region of a LSP low carbon steel specimen coated with BP prior to LSP and treated with a laser energy of 111 J. This micrograph shows a very high density of dislocations in a random tangled arrangement. The dislocation density was calculated to be $2.6 \times 10^{11}/cm^2$ based on a method given by Hirsch et al. *[127]*, assuming specimen thickness of 500Å. The high dislocation density was a direct result of laser shock wave deformation.

Cross-sectional TEM microstructure studies revealed high dislocation densities as deep as 50 μm from the LSP surface. In Figure 4-26 (BP coated specimen treated with a laser energy of 177 J) the bright field micrograph of a region about 50 μm below the LSP surface shows dense arrays of dislocations both in the grain matrix and near the grain boundary regions. In the region away from grain boundary, dislocation density was estimated to be 1 to $1.8 \times 10^{11}/cm^2$. This value was still high compared with a unshocked specimen ($<1 \times 10^{10}/cm^2$), although it was not as high as that at LSP surface.

Hadfield Steel

Extensive formation of ε-hcp martensite and generation of a high density of dislocations was observed for LSP Hadfield steel. In Figure 4-27, a bright field micrograph from the indentation region of Hadfield specimen that was BP coated and treated with a laser energy of 113 J. This micrograph shows several grains each of which contains several variants of ε-hcp martensite, stacking faults, and dislocations in a γ-fcc austenite matrix. The thin ε-hcp martensite plates are the region of the slip lines visible in the SEM micrograph of the same specimen in Figure 4-22b.

Figure 4-28a is a dark field micrograph of the ε-hcp martensite plates using the $1\bar{1}1$-fcc reflection. This micrograph shows that ε-hcp martensite plates consist of multiple overlapped stacking faults. The irregular patchy contrast indicates faults in the stacking arrangement of the stacking faults making up individual ε-hcp martensite plates *[128]*. A selected area diffraction pattern taken from this region is shown in Figure 4-28b. Streaks of γ-fcc diffraction spots are seen. As the TEM foil was tilted (~10°) from the $[\bar{1}12]$ orientation of Figure 4-28b to the $[\bar{1}23]$ orientation of 4-28c, the diffraction pattern had a streak clearly along the $[1\bar{1}1]$ direction, indicating that the stacking faults were formed on the {111} γ-fcc matrix planes. As shown in Figure 4-29, in some areas all of four ε-hcp martensite variants was clearly visible. These four types of faults were believed to be on four {111} γ-fcc matrix planes, since they were at different orientations and thicknesses.

In the bright field micrograph of Figure 4-30a, an area showing overlapping stacking faults and dislocations is presented. The specimen was BP coated for LSP and treated with a laser energy of 104 J. In addition to the ε-hcp martensite plates imaged as stacking faults bound by partial dislocations, this region had a high density of dislocations, estimated to be $6.2 \times 10^{10}/cm^2$. As seen in this micrograph, some of the dislocations appeared in a tangled

arrangement. Point defects present in this micrograph were attributed to ion damaging from atom milling. It is noted that neither deformation twins nor α'-bcc martensite were evident in this region. The diffraction pattern, Figure 4-30b, from this region shows the presence of both the γ-fcc austenite matrix and ε-hcp martensite phase.

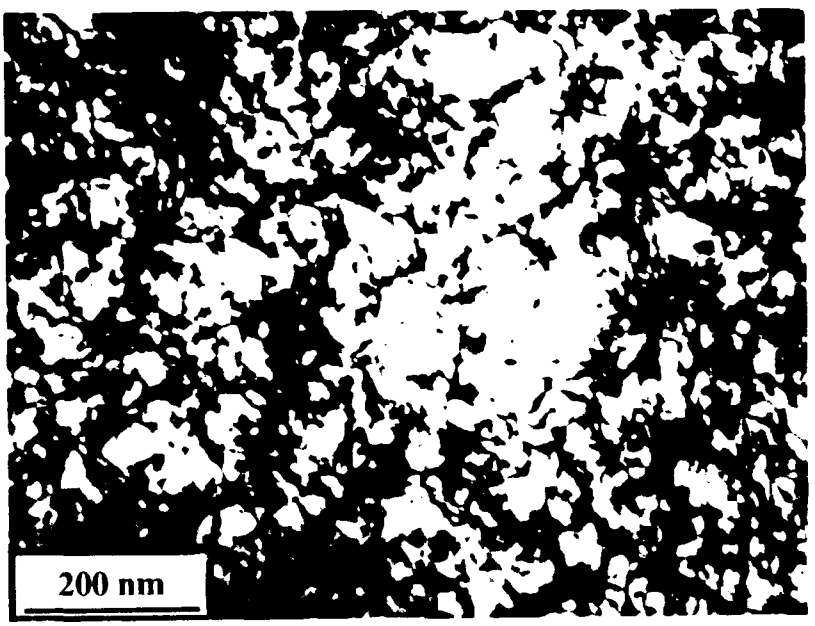

Figure 4-25 TEM micrograph of a low carbon steel specimen after LSP at an energy of 111 J with a thick BP coating and no overlay.

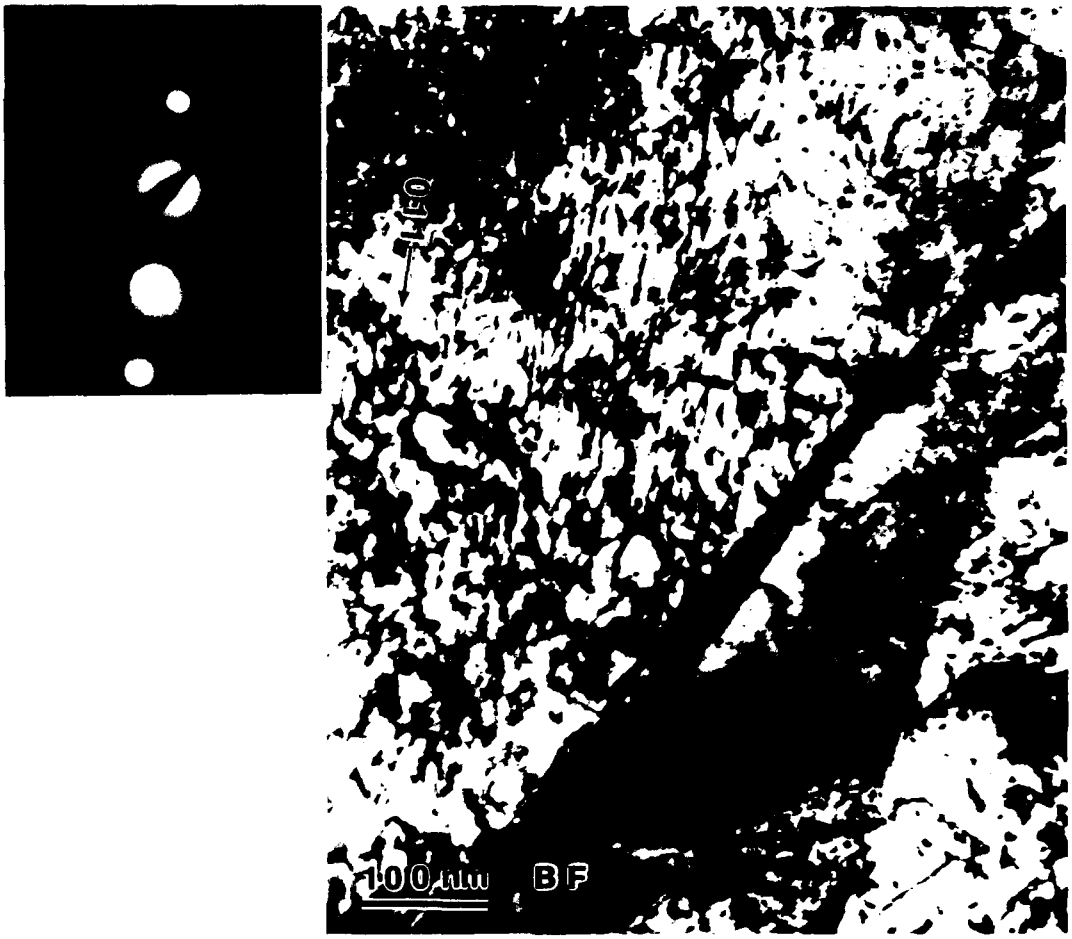

Figure 4-26 Cross-sectional TEM micrograph of a low carbon steel specimen after LSP at an energy of 177 J with a thick BP coating and no overlay.

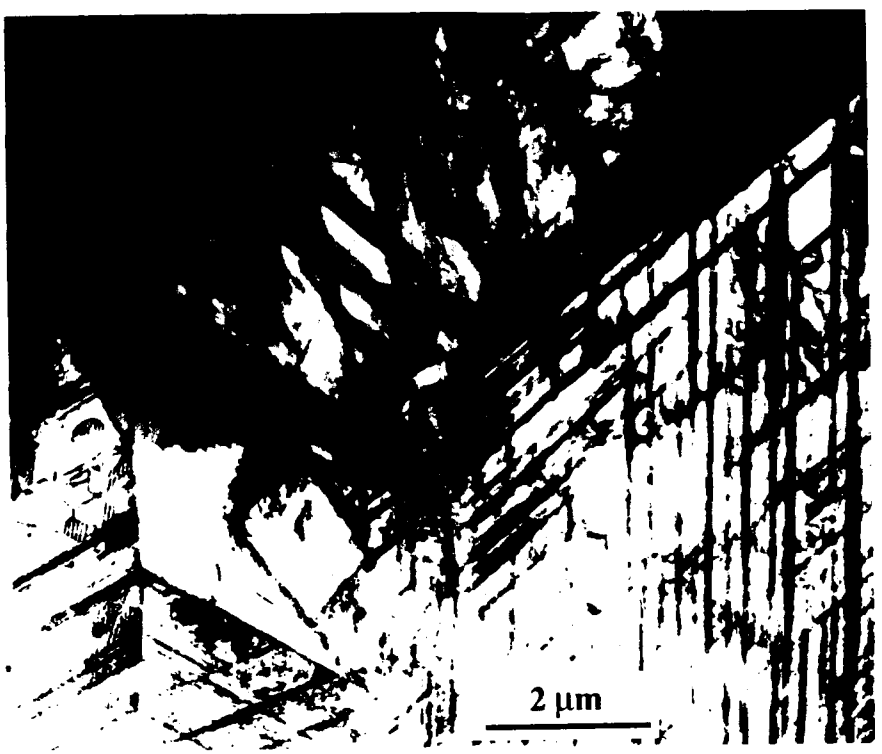

Figure 4-27 TEM micrograph of Hadfield steel specimen after LSP at an energy of 113 J with a thick BP coating and no overlay.

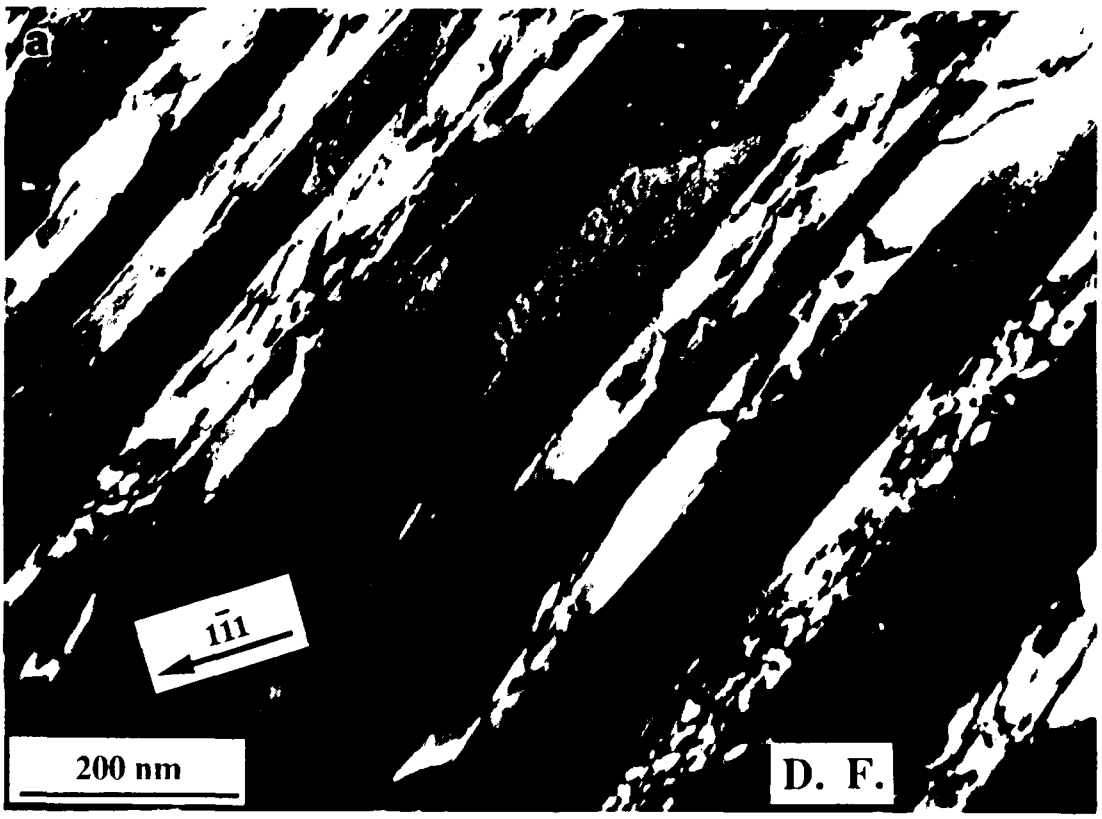

Figure 4-28 (a) TEM micrograph of Hadfield steel specimen after LSP at an energy of 113 J with a thick BP coating and no overlay.

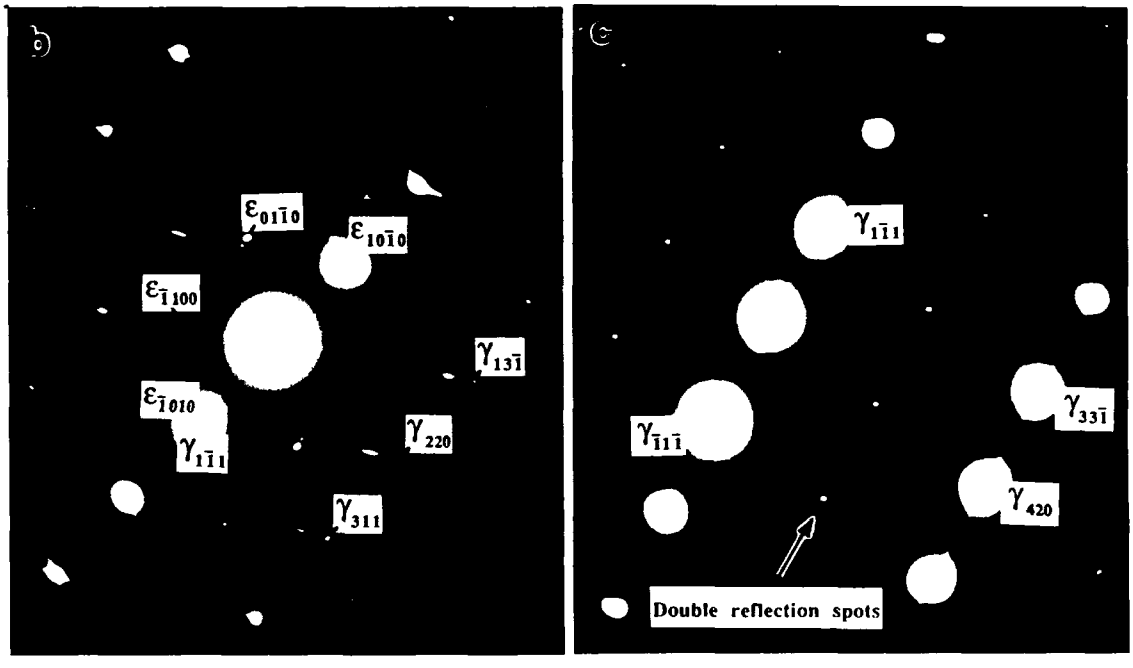

F.O.≈ $[\bar{1}12]$ F.O.≈ $[\bar{1}23]$

Figure 4-28 (continued) Selected area diffraction patterns: (b) from Figure 4-28(a) and (c) after tilting (~10°).

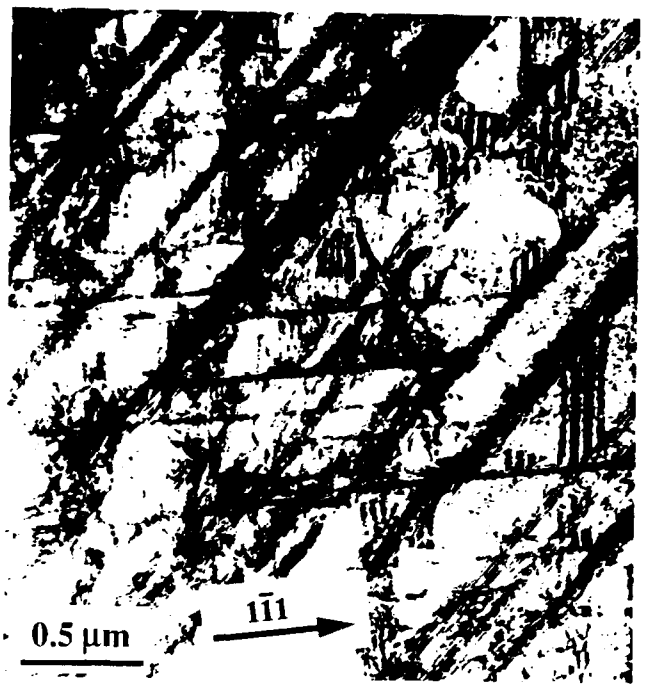

Figure 4-29 TEM micrograph of Hadfield steel specimen after LSP at an energy of 113 J with a thick BP coating and no overlay.

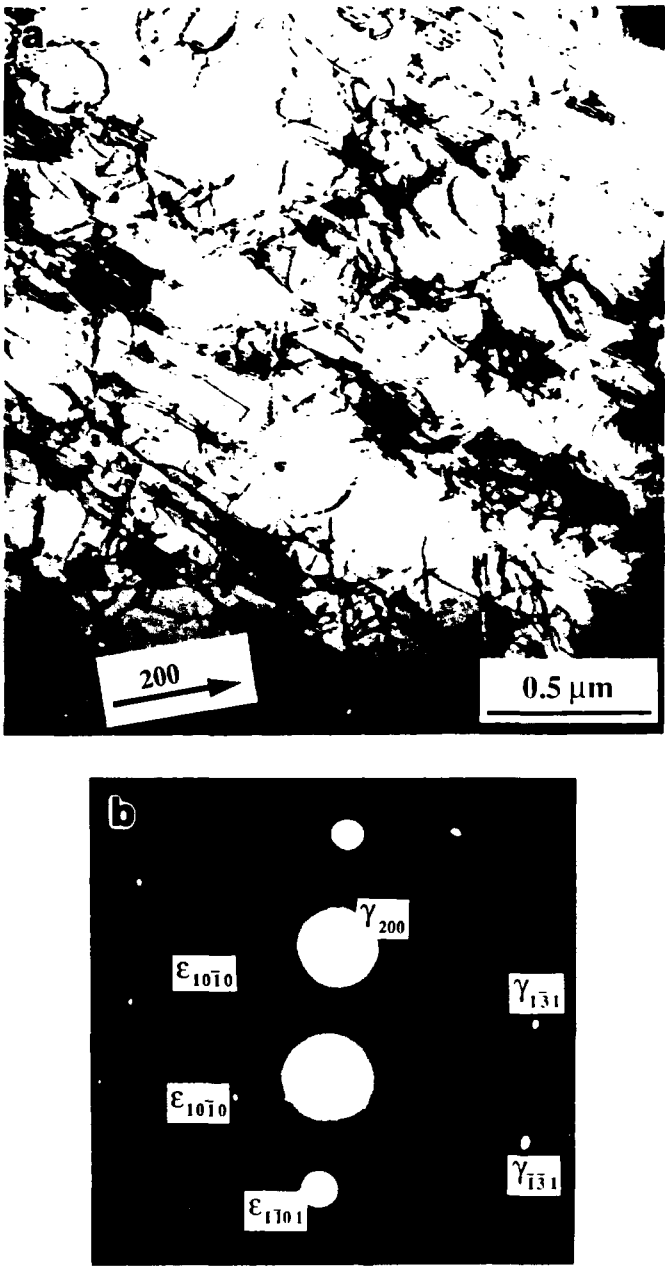

Figure 4-30 (a) TEM micrograph and (b) a selected area diffraction pattern of Hadfield steel specimen after LSP at an energy of 104 J with a thick BP coating and no overlay.

b. Cold Rolling and Shot Peening Effects

Low Carbon Steel

A low magnification bright field image is shown in Figure 4-31a for the shot peened low carbon steel specimen. This micrograph reveals a dense dislocation cell structure. In the selected area diffraction pattern from this region, a well-defined ring pattern was present; see Figure 4-31b. This indicates that the region was highly deformed and consisted of subgrains. Using Figure 4-32, the dislocation density was calculated to be $\geq 2 \times 10^{11}/cm^2$, again assuming the specimen thickness of 500Å. This value was of the same order of magnitude as was that found in the LSP specimen surface.

Figure 4-33a, a bright field image micrograph of a low carbon steel specimen cold rolled 63%, reveals a high density of dislocations. The arcs visible in the selected area diffraction pattern (Figure 4-33b) from this region indicates that a cell-like substructure has been produced. At higher magnification micrograph in Figure 4-34, dense dislocation regions are clearly shown. The dislocation density for this region was calculated to be at least $1 \times 10^{12}/cm^2$, again assuming a 500Å thick TEM specimen.

Hadfield Steel

Figures 4-35 and 4-36 show the microstructure of a shot peened Hadfield steel. The lath-like substructures seen in Figure 4-35a are shown by the diffraction pattern of Figure 4-35b to consist of mainly austenite with some ε-hcp martensite. As shown in Figure 4-36, shot peening resulted in extensive deformation twin formation, in addition to high dislocation densities. In the diffraction pattern in Figure 4-36b, a γ-fcc pattern and a twin pattern were identified. Note the streaks along the γ-fcc $[\bar{1}1\bar{1}]$ direction. From this [110] foil orientation, the twin plane (K_1) and the shear direction (η_1) were identified to be $(1\bar{1}1)$ and $[\bar{1}12]$, respectively *[129]*. The matrix and twin diffraction patterns were mirror reflections across the $(\bar{1}1)$ plane *[129]*. To image the deformation twinnings, the dark field image shown in Figure 4-36c was obtained using a 002 twin spot.

Figures 4-37 and 4-38 show the microstructure from a region near the surface (~1 μm) of a Hadfield steel specimen cold rolled 51%. The bright field images reveal an abundance of dislocations in a lath-like substructure. The dislocations were too dense to be clearly resolved. The diffraction pattern in Figure 4-38b shows nearly continuous rings consist with a microstructure of mainly ε-hcp martensite with minor amounts of γ-fcc austenite and no α'-bcc martensite.

c. Summary of Microstructure and Phase Transformation

The results of the TEM studies are summarized in Table 4-1 for both steel specimens after LSP, shot peening, and cold rolling.

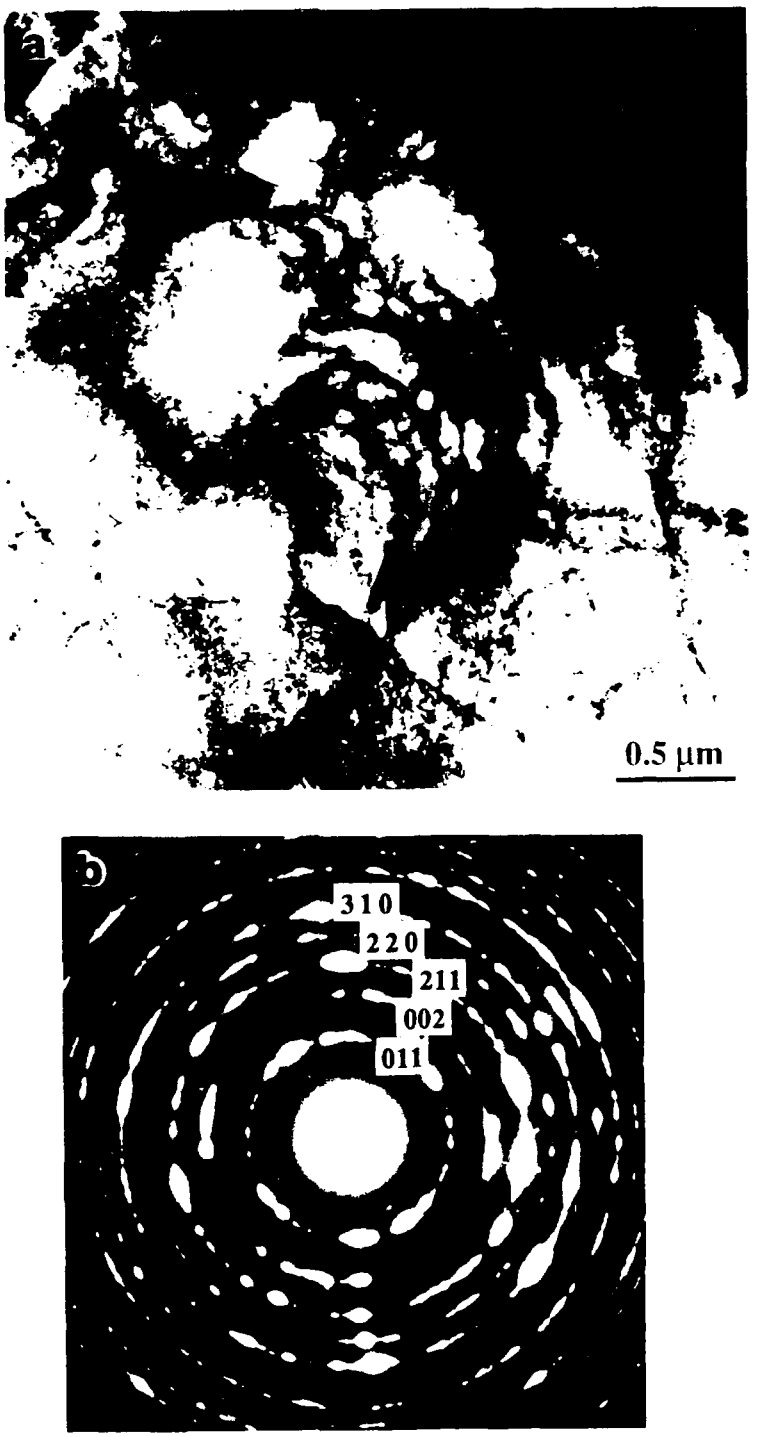

Figure 4-31 (a) TEM micrograph and (b) a selected area diffraction pattern of a shot peened low carbon steel specimen.

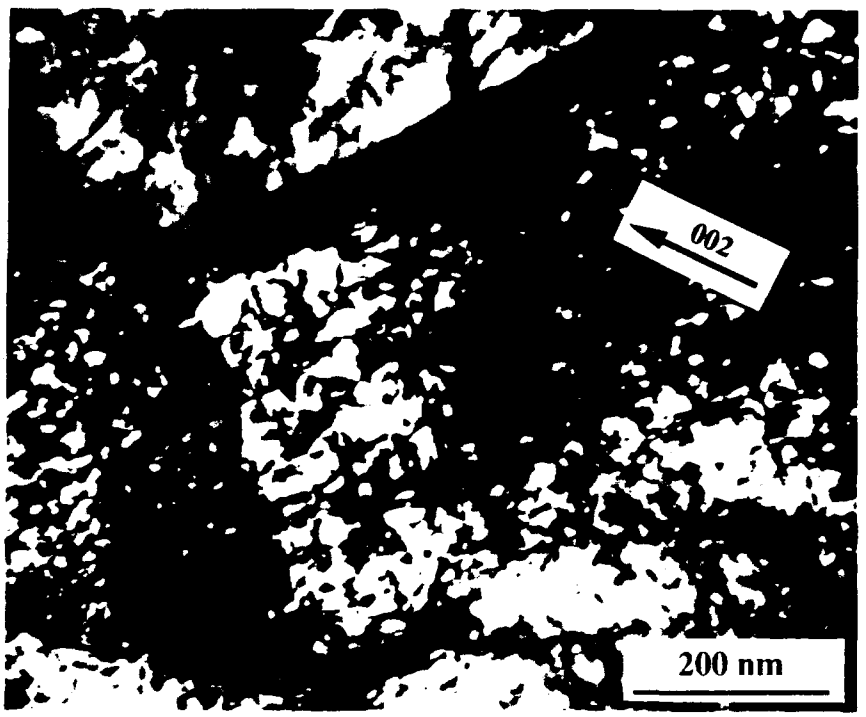

Figure 4-32 TEM micrograph of a shot peened low carbon steel specimen.

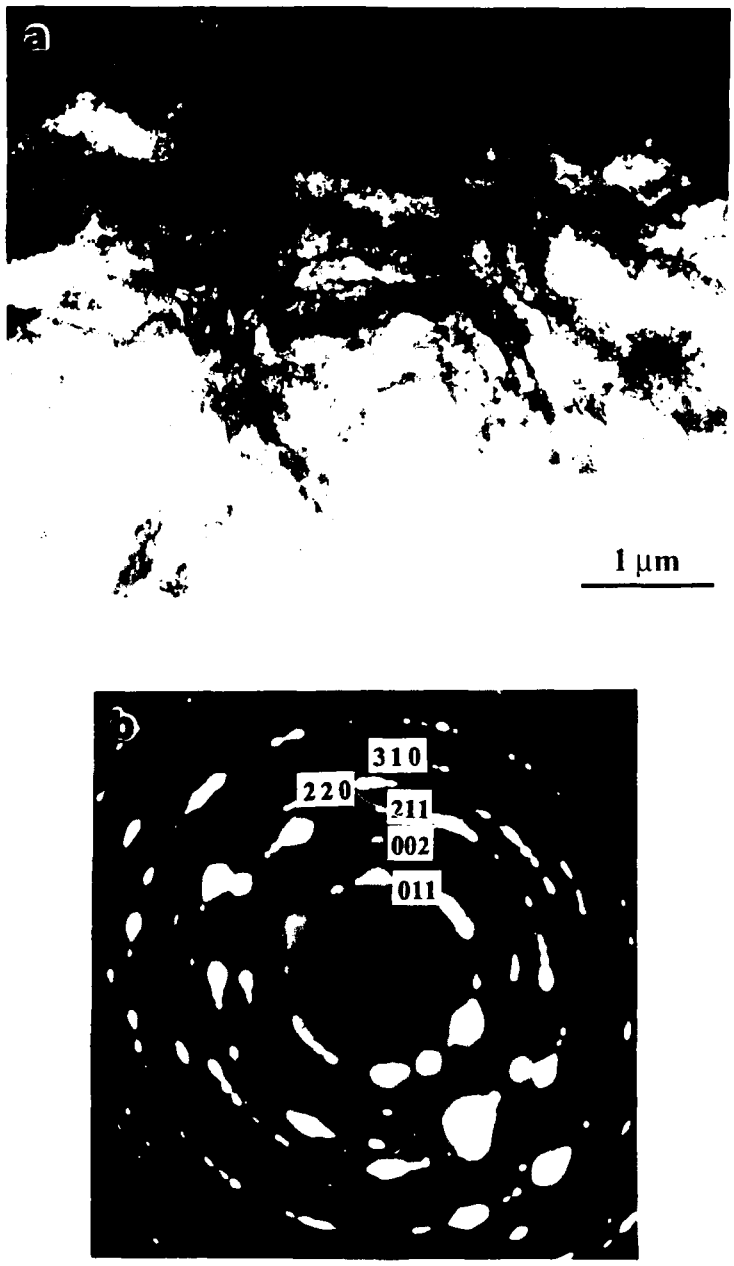

Figure 4-33 (a) TEM micrograph and (b) a selected area diffraction pattern of a cold rolled low carbon steel specimen.

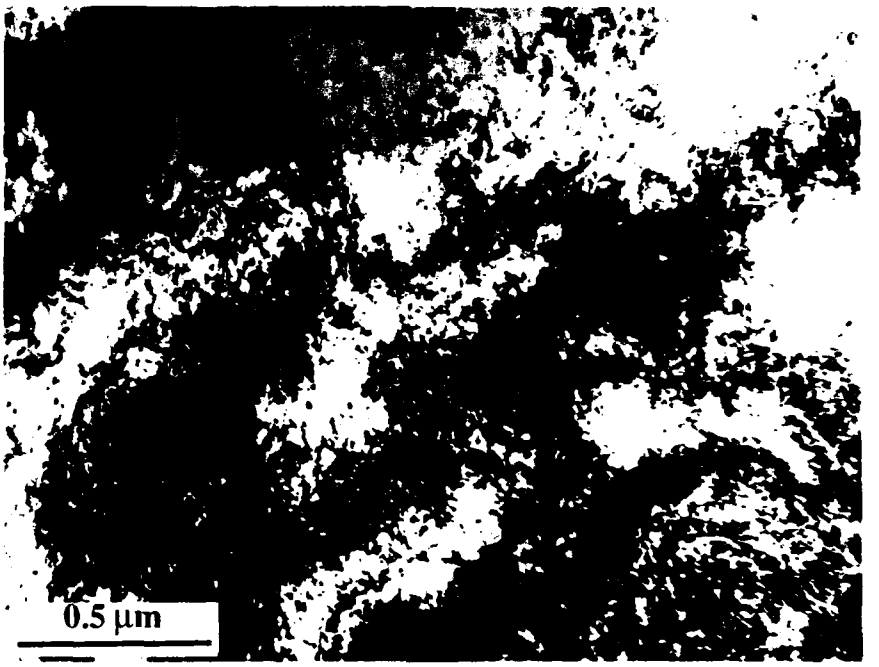

Figure 4-34 TEM micrograph of a cold rolled low carbon steel specimen.

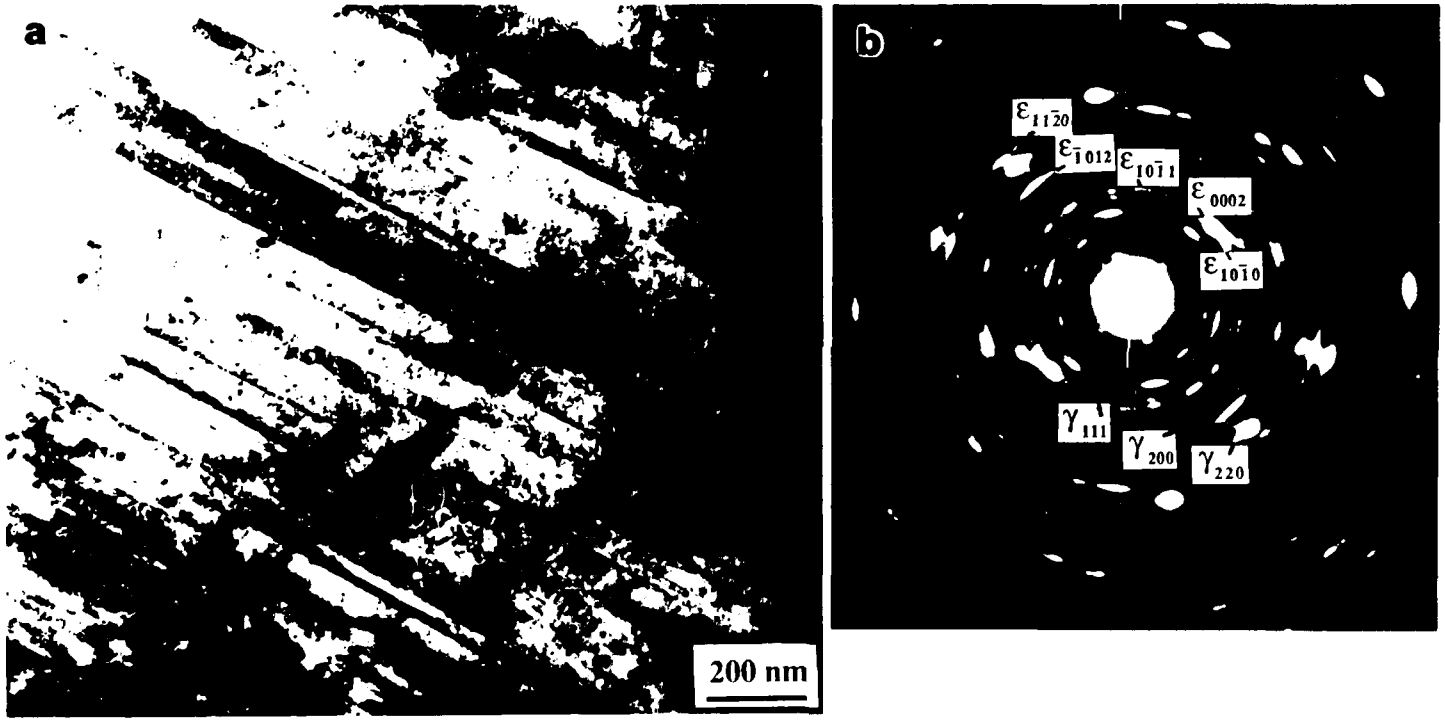

Figure 4-35 (a) TEM micrograph and (b) a selected area diffraction pattern of a shot peened Hadfield steel specimen.

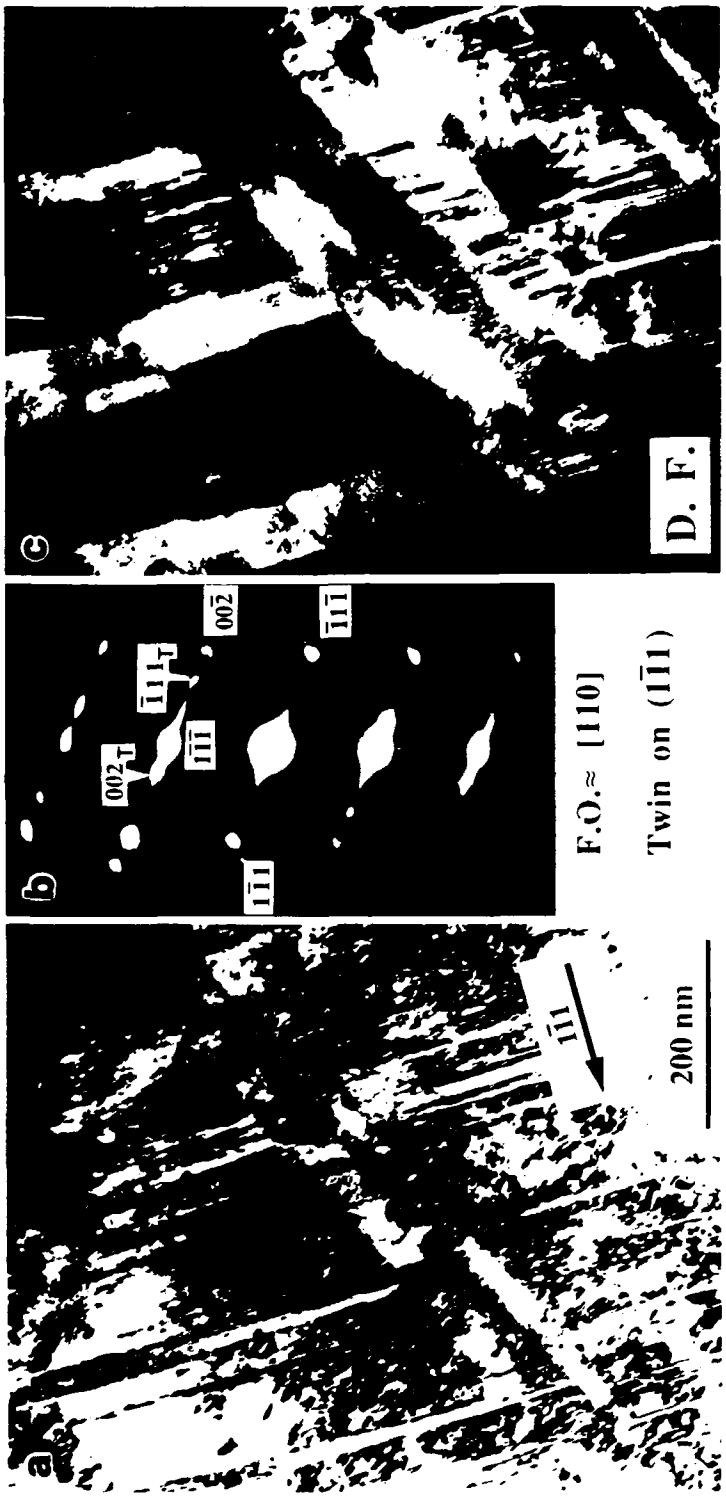

Figure 4-36 (a) TEM micrograph and (b) a selected area diffraction pattern of a shot peened Hadfield steel specimen. (c) A dark field micrograph from 002 reflection twin spot.

4.2.4. Evolution of Phase Transformation by X-ray Diffraction

No phase transformations were found for LSP, shot peened, or cold rolled low carbon steel specimens. Therefore, the X-ray diffraction results discussed in the following sections are exclusively for Hadfield steel specimens under different experimental conditions (LSP, shot peening, and cold rolling).

a. Semi-quantitative Analysis

LSP Laser Energy Effects

Figure 4-39 shows X-ray diffraction results from as-annealed and two BP coated Hadfield steel specimens laser treated with energies of 9.4 and 102 J. As seen in the figure, the (111) and (200) γ-fcc austenite are the major peaks and the ε-hcp martensite $(10\bar{1}1)$ peak evolves with increasing laser energy. Comparing the laser treated and annealed results, no significant change was evident in the ε-hcp (0002) peak intensity. The appearance of new ε-hcp $(10\bar{1}1)$ peak suggests that more ε-hcp martensite has formed due to LSP.

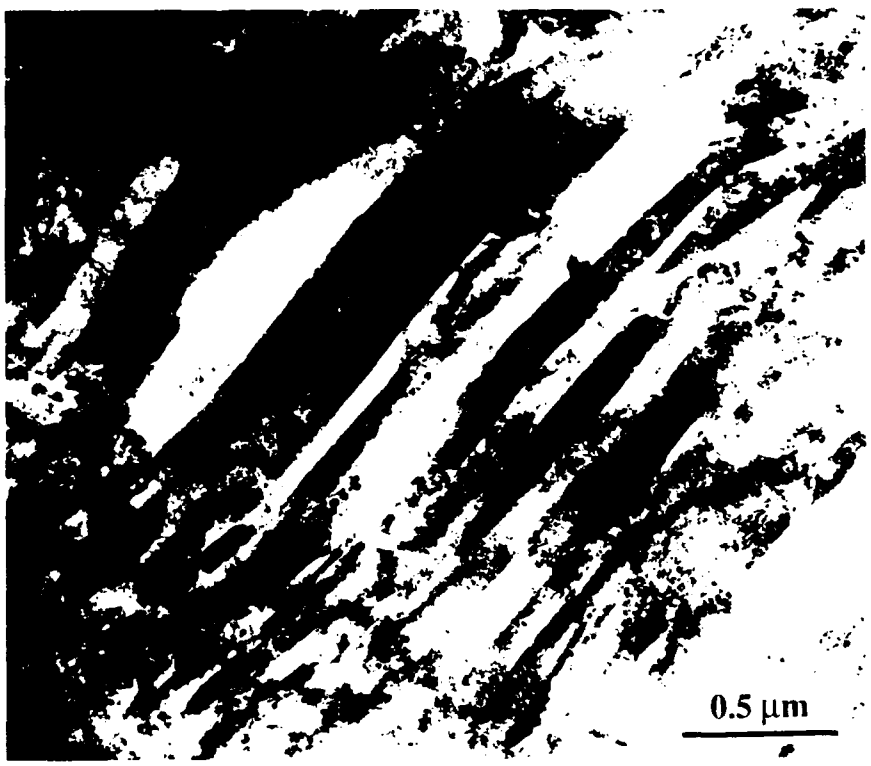

Figure 4-37 TEM micrograph of a cold rolled Hadfield steel specimen.

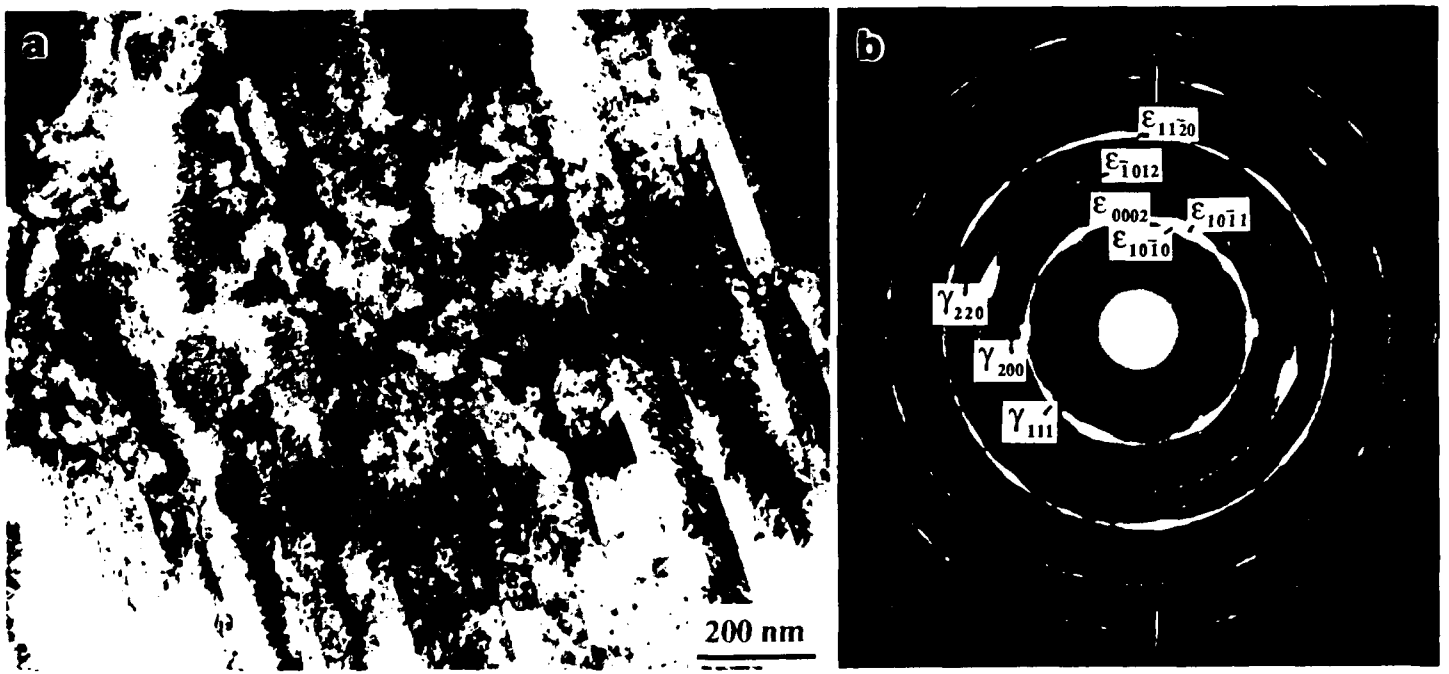

Figure 4-38 (a) TEM micrograph and (b) a selected area diffraction pattern of a cold rolled Hadfield steel specimen.

Table 4-1. Summary of TEM surface observations in the low carbon steel and Hadfield steel after LSP, cold rolling, and shot peening.

Processing	Low carbon steel	Hadfield steel
LSP‡	Dense arrays of tangle dislocations ($2.6 \times 10^{11}/cm^2$); no martensite phase found	γ-fcc austenite a major phase and extensive formation of ε-hcp martensite; dense arrays of dislocations
Shot peening*	Dislocation cell substructures and dislocation densities $\geq 2 \times 10^{11}/cm^2$; well-defined ring diffraction pattern	γ-fcc austenite as a major phase with deformation twins; dense arrays of dislocations in a lath-like substructure and not well-defined ring pattern
Cold rolling#	Dislocation cell substructures and dislocation densities $>1 \times 10^{12}/cm^2$; not well-defined ring diffraction pattern	ε-hcp martensite as a major phase and little γ-fcc; dense arrays of dislocations in a lath-like substructure and well-defined ring pattern

‡ The specimens were black paint coated for the LSP and treated with laser energy at 100 to 120 J.

* The shot peening was done on 100% surface coverage for both steels.

The low carbon steel specimen was cold rolled to 63% reduction in thickness, while the reduction for the Hadfield steel specimen was 51%.

Laser Overlay Effects

Figure 4-40 shows the effects of the quartz overlay used during LSP on the phase transformations of Hadfield specimens. Data from the as-annealed specimen is again included for comparison. The specimens were BP coated and treated with laser energies of 5.5 J and 108 J. The Hadfield steel specimen treated with 5.5 J exhibited the presence of an ε-hcp $(10\bar{1}1)$ peak, while the annealed and the 108 J laser treated specimens showed no noticeable presence of the ε-hcp $(10\bar{1}1)$ peak. This evidence is consistent with the previously presented data showing absorption of the laser energy by overlay plasma formation when high laser powers are used for LSP.

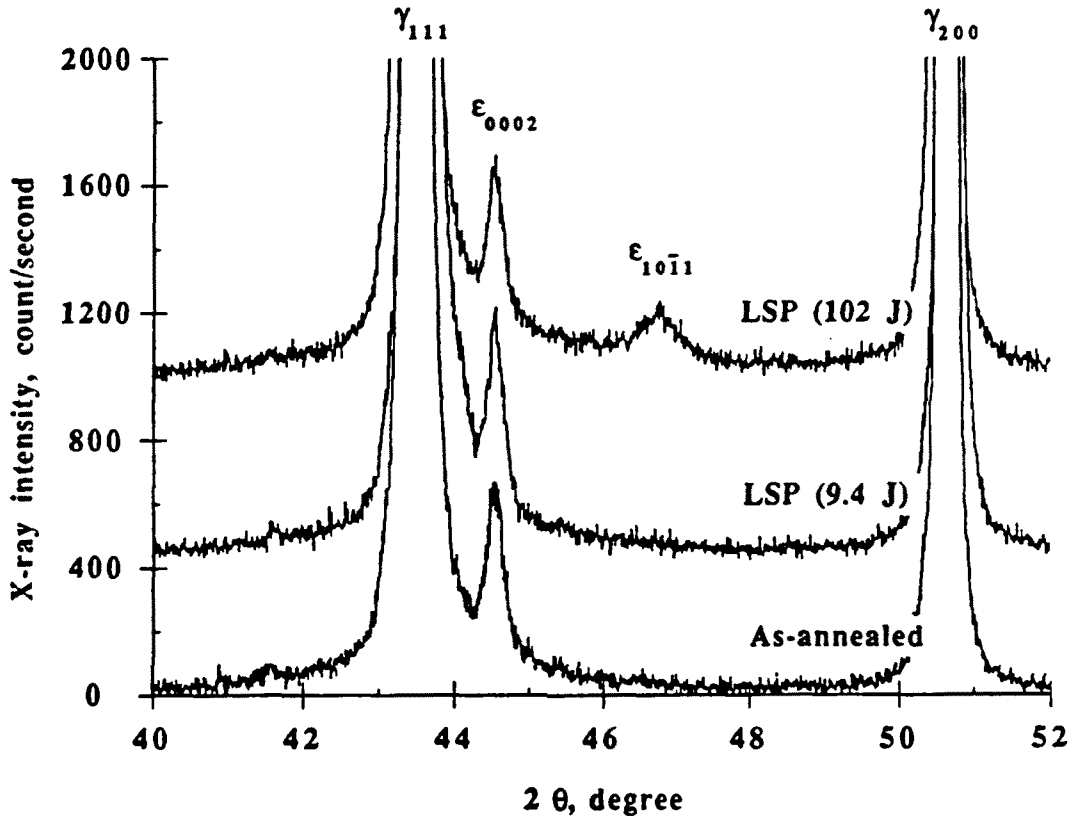

Figure 4-39 X-ray diffraction patterns of as-annealed and LSP Hadfield steel specimens at energies of 9.4 J and 102 J with a thick BP coating and no overlay.

Comparisons of LSP, Cold Rolling, and Shot Peening

To examine the effect of different processing methods on the phase transformation of Hadfield steel, Figure 4-41 shows results from as-annealed, cold rolled, shot peened, and LSP specimens. Since the measured areas for these four specimens were not the same, the results allow only qualitative comparisons. The ε-hcp martensite was the only phase detected in the 51% cold rolled specimen, suggesting that nearly total transformation of the γ-fcc austenite. The single, strong (0002) peak indicates development of a preferred orientation, as pointed out by Collette et al. *[130]*. Line broadening of the (0002) peak is due to heavy deformation by the cold rolling. For the shot peened specimen, the γ-fcc austenite was still a major phase along with the small ε-(0002) peak. LSP produced far less ε-hcp martensite than did cold rolling. Since the LSP area was small (~6%) as compared to the whole specimen surface area analyzed by X-ray, the contribution by LSP to the line broadening of the γ-fcc peaks was not noticed. The presence of ε-$(10\bar{1}1)$ peak is a result of the LSP induced γ→ε phase transformation.

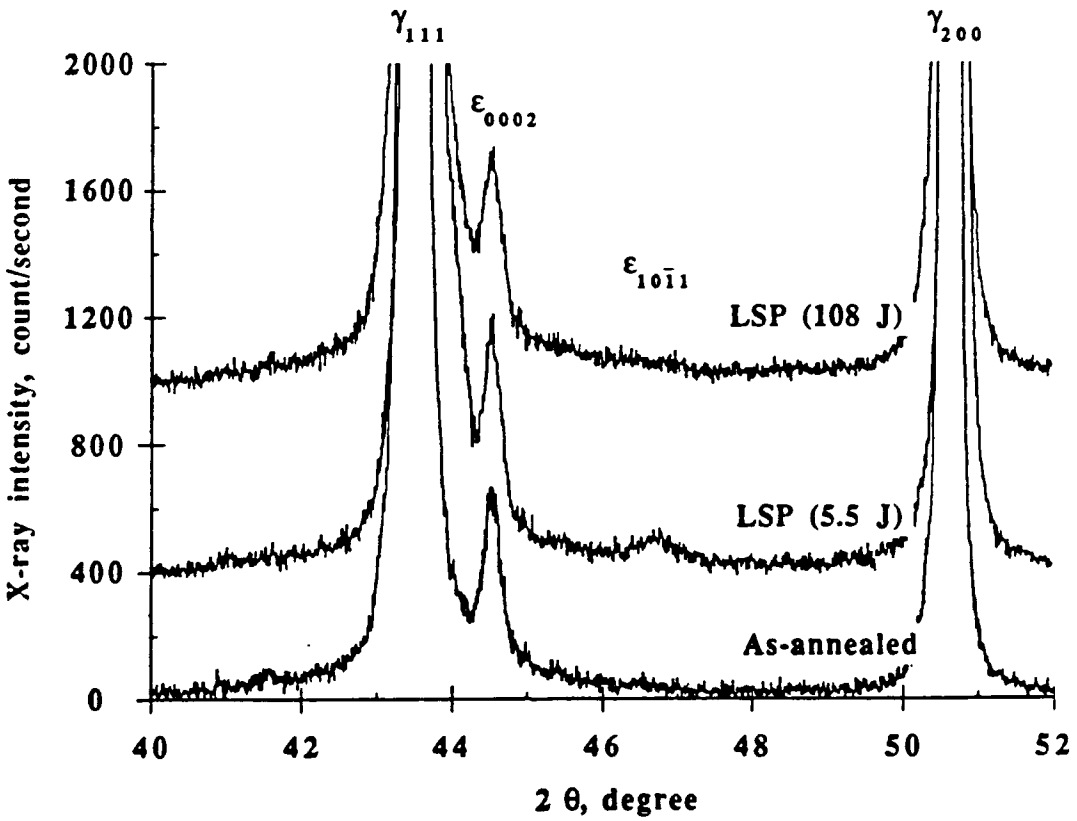

Figure 4-40 X-ray diffraction patterns of as-annealed and LSP Hadfield steel specimens at energies of 5.5 J and 108 J with a thick BP coating and an overlay.

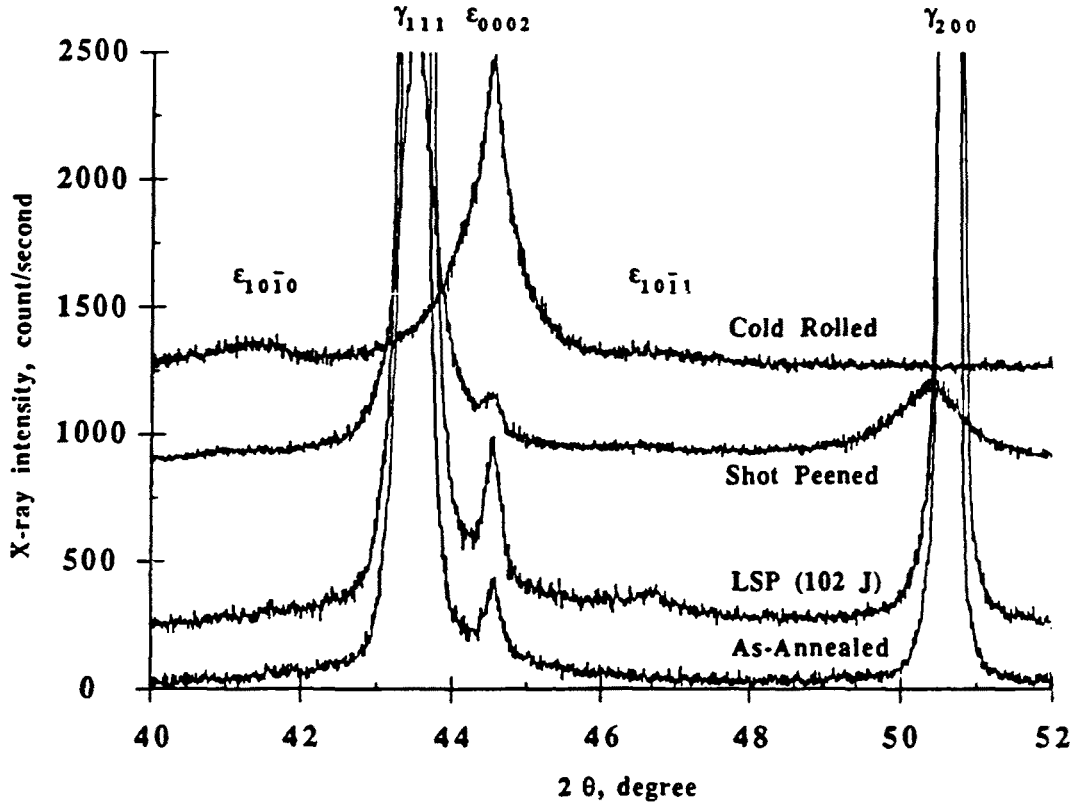

Figure 4-41 X-ray diffraction patterns of as-annealed, LSP, shot peened, and cold rolled Hadfield steel specimens.

b. Quantitative Analysis -- Overall Effects

To quantitatively analyze the effects of laser energy, quartz overlay, and different processing methods, Tables 4-2 to 4-4 list the ε-hcp martensite volume fraction results calculated by the peak integrated intensity ratio method. Since preferred orientations were found in both γ-fcc austenite and ε-hcp martensite for the as-annealed and as-processed specimens, a method given by Dickson *[131]* was used to average the integrated peak intensities for γ-(111) and (200) as well as ε-(0002) and (10$\bar{1}$1). The results were calculated after background intensity was subtracted and $K_{\alpha 2}$ peaks were stripped from the raw data files. Because the LSP area was only ~6% of the specimen surface area analyzed by X-ray, the results were corrected by a geometry factor. Due to the limited number of peaks available to correct for preferred orientations, the results should be used to show an overall trend and not absolute values.

Table 4-2 shows LSP-induced ε-hcp martensite values as high as 35 vol.% for 102 J, and as low as 6.5 vol.% for 9.4 J. This major increase in ε-hcp martensite volume fraction is consistent with the surface profilometry results where the higher energies produced indentations deeper than those of the lower energies. Nevertheless, even at 9.4 J it is evident that LSP created martensite at levels in excess to that found in the as-annealed material.

Considering the effects of the quartz overlay, Table 4-3 shows that at 5.5 J the martensite transformation increased to nearly 12 vol.% (an 8.7 vol.% net increase) whereas at 108 J essentially no measurable amount of ε-hcp martensite produced above that found in the as-annealed material. Again, this result is consistent with the surface profilometry results where when a quartz overlay is used the low laser energies resulted in deeper indentations than did high laser energies.

For the different processing methods, Table 4-4 shows that the cold rolled specimen consisted of nearly 100% ε-hcp martensite. The shot peened specimen had more than 8 vol.% of ε-hcp martensite produced during processing. Moreover, an increase of 32 vol.% was measured in the LSP specimen. These results are consistent with TEM observations in which twins were found in the shot peened specimen and extensive formation of ε-hcp martensite was observed in LSP specimens. By cold rolling, the most significant amount (~100 vol.%) of ε-hcp martensite was measured, also in agreement with TEM observations.

Table 4-2 X-ray phase analysis results of LSP Hadfield steel -- Energy effects.

Laser energy, J @	Volume % of ε-hcp martensite	
	Total	Net increase
102	35.3±4.8	32.0±6.5
9.4	6.5±1.0	3.3±2.7
As-annealed	3.5±1.5	--

@ The specimens were black paint coated during the LSP and without any overlay.

Table 4-3 X-ray phase analysis results of LSP Hadfield steel -- Overlay effects.

Laser energy, J ©	Volume % of ε-hcp martensite	
	Total	Net increase
108	3.5±1.0	~0
5.5	11.9±1.8	8.7±3.5
As-annealed	3.5±1.5	--

© The specimens were black paint coated and covered with overlay during the LSP.

Table 4-4 X-ray phase analysis results of Hadfield steel -- Effects of cold rolling, shot peening, and LSP.

Processing	Volume % of ε-hcp martensite	
	Total	Net increase
Cold rolling§	~100*	> 96
Shot peening#	11.7±2.0	8.4±3.7
LSP‡	35.3±4.8	32.0±6.5
As-annealed	3.5±1.5	--

§ The specimen was cold rolled to 51% reduction in thickness.

The shot peening was done on 100% surface coverage.

‡ The specimen was black paint coated for the LSP and treated with energy at 102 J.

* This volume fraction was estimated based on no measurable γ-fcc austenite peaks.

c. In-depth Measurement

The extent of LSP-induced phase transformation as a function of depth was measured on a Hadfield steel specimen and is shown in Figure 4-42 for a BP coated specimen treated with a laser energy of 102 J. The surface was removed incrementally using the electropolishing procedure given previously. Figure 4-42 compares X-ray diffraction results obtained at various depths from the LSP surface with that of an as-annealed specimen. At the LSP surface, noticeable peak intensities for ε-(0002) and $(10\bar{1}1)$ were measured. As the surface layer was removed, the intensity of ε-$(10\bar{1}1)$ peak decreased and was negligible at 50 μm below the LSP surface. The ε-(0002) peak intensity is also decreased with depth. As expected, the calculated volume fractions of LSP-induced ε-hcp martensite decreased with depth and these results are shown in Figure 4-43. The volume fractions were calculated from the diffraction patterns shown in Figure 4-42 using the same method described previously. As seen in Figure 4-43, the ε-hcp martensite value of 35 vol.% at surface dropped to 18 vol.% 20 μm below the surface. At ~50 μm, the volume fraction reached the as-annealed specimen value (~3 vol.%).

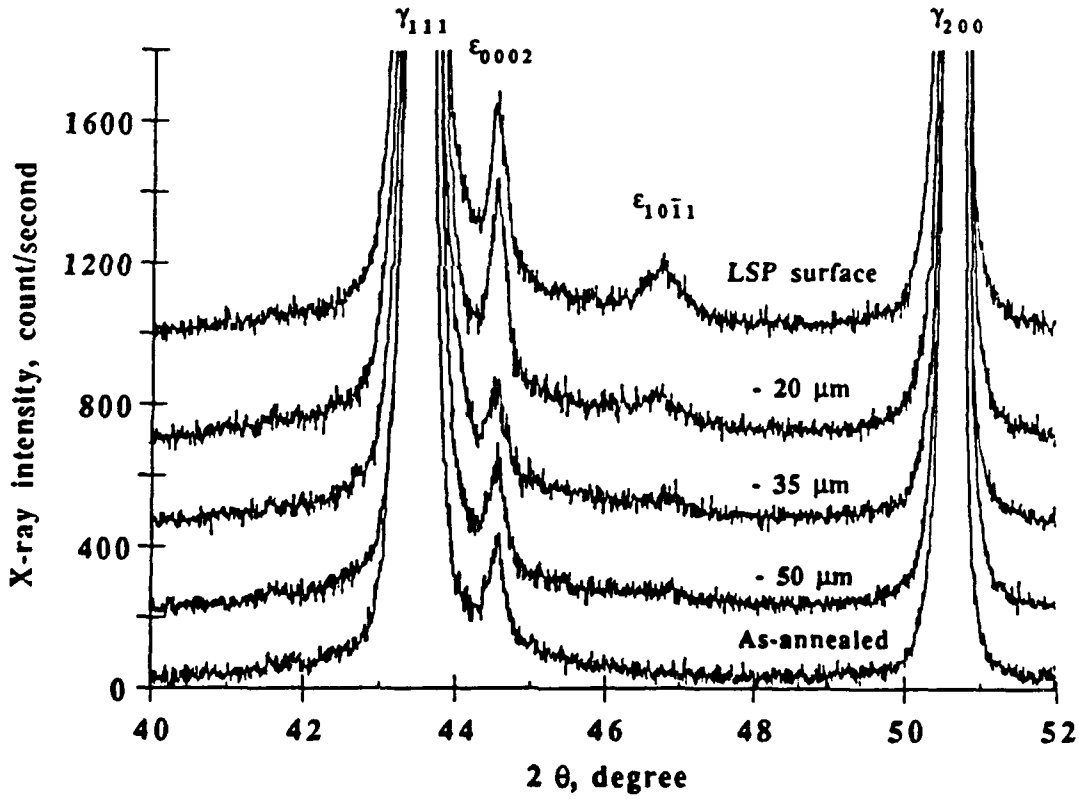

Figure 4-42 X-ray diffraction patterns of as-annealed and LSP Hadfield steel specimens (from the LSP surface to 50 μm below) at an energy of 102 J with a thick BP coating and no overlay.

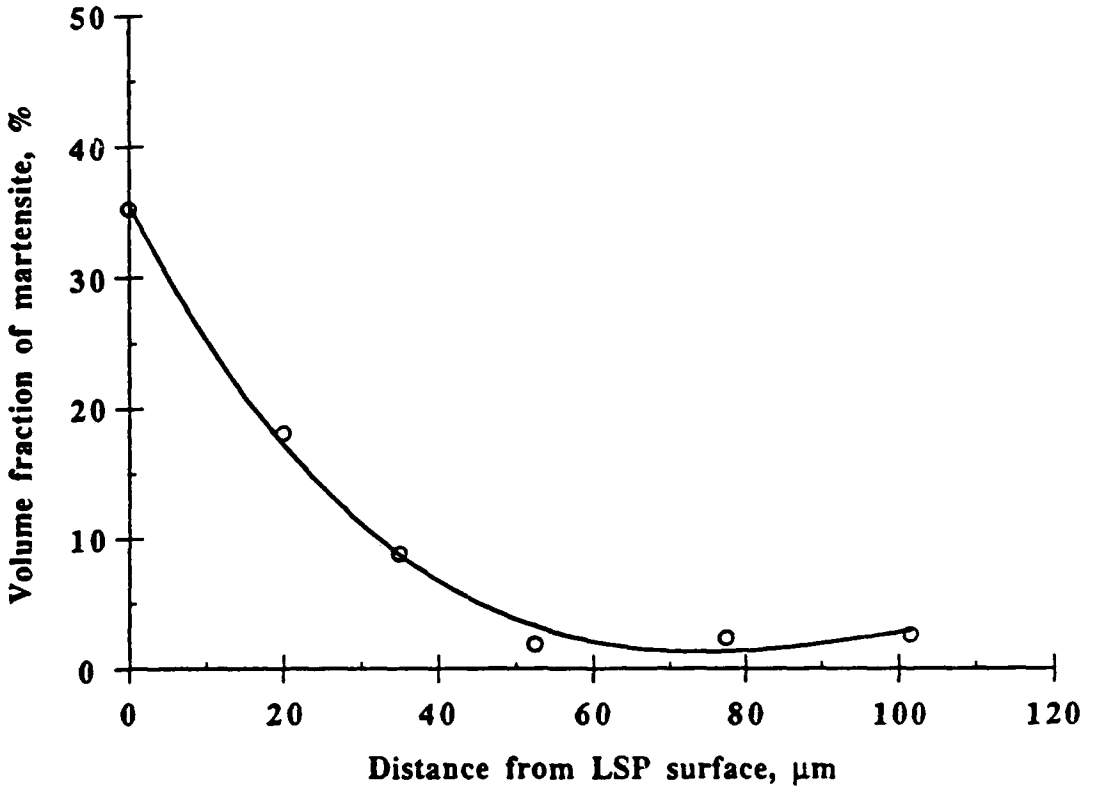

Figure 4-43 Volume fraction of ε-hcp martensite as a function of depth in a LSP Hadfield steel specimen at an energy of 102 J with a thick BP coating and no overlay.

4.3. Mechanical Properties

4.3.1. Residual Stresses -- X-ray Diffraction

Residual stress measurements were conducted on both low carbon and Hadfield steel specimens after subjecting them to LSP, cold rolling and shot peening. Stresses were measured for the as-processed surfaces as a function of depth.

a. Comparisons of LSP, Cold Rolling, and Shot Peening

In Figure 4-44, a summary of the surface residual stress measurements is shown for the LSP low carbon steel specimens. In this bar figure, results of cold rolled, shot peened, and as-annealed specimens are compared. For LSP overlay, bare, and overlay plus BP coated specimens, residual tensile stresses were measured in the specimen surfaces, while the BP coated specimen had a compressive residual stress. Among the tensile surface stress specimens, the bare specimen showed the highest stress value, followed by that of the overlay only specimen. These high surface residual stresses are attributed to the severe melting as observed in the SEM micrographs of Figures 4-13 to 4-16. As BP was used in addition to the overlay during LSP, the extent of the surface melting was substantially reduced, decreasing the tensile residual stress.

When the overlay was not used, the BP coated specimen had a compressive residual surface stress; the result of an unmelted, shock wave deformed surface. However, the LSP specimen showed a smaller compressive stress than for the cold rolled and shot peened specimens. The shot peened specimen showed an unusually high stress level (about twice the as-annealed material's yield strength).

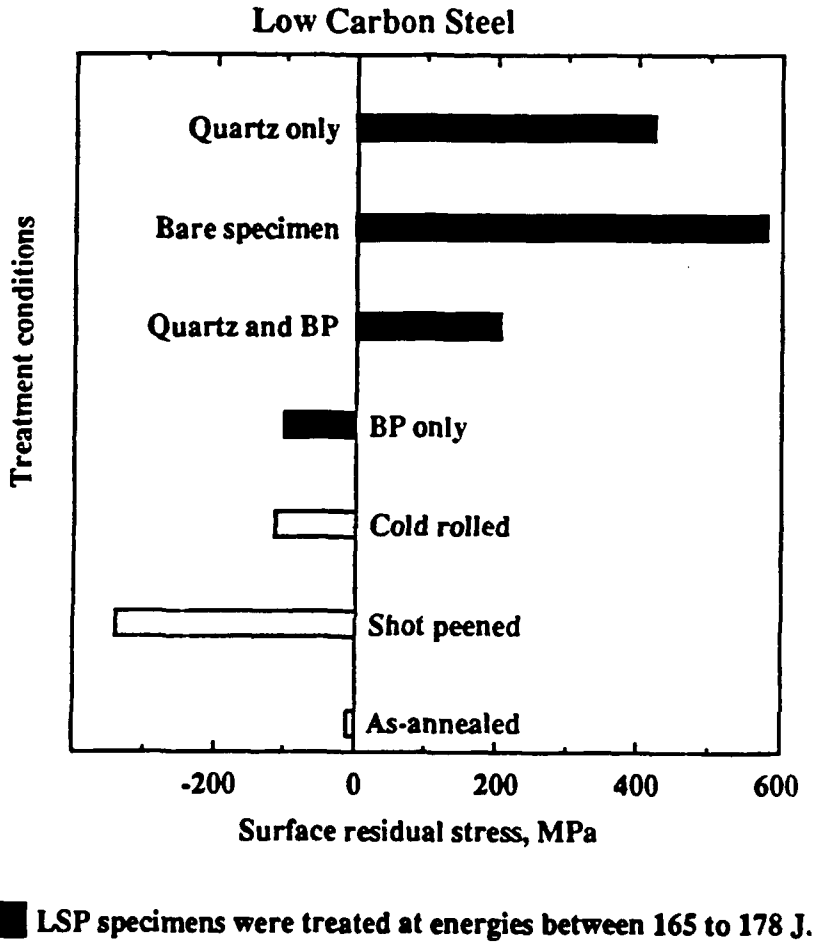

Figure 4-44 A summary of the surface residual stress measurements for LSP, cold rolled, shot peened, and as-annealed low carbon steel specimens.

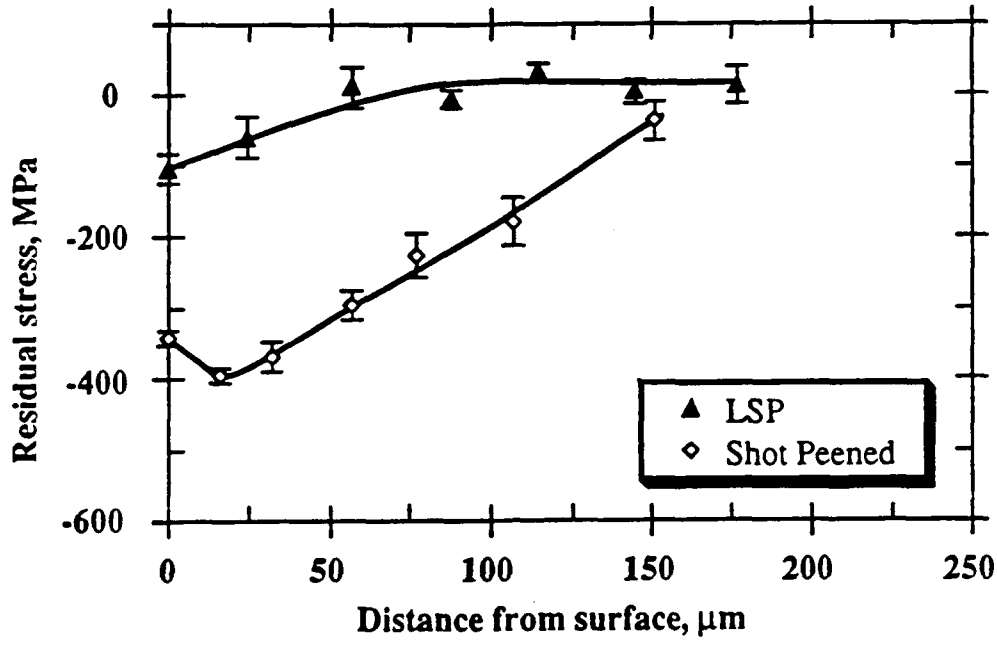

Figure 4-45 Residual stress in-depth profiles for LSP and shot peened low carbon steel specimens.

b. In-Depth Measurement

For stress measurement as a function of depth, low carbon and Hadfield steel specimens were examined after LSP and shot peening. Surface material removal was done by the electropolishing method described previously.

Low Carbon Steel

Figure 4-45 shows the in-depth residual stresses for shot peened and LSP low carbon steel specimens. The LSP specimen was thick BP coated and treated with a laser energy of 108 J. As seen in this figure, the surface stresses of these two specimens are distinctly different; the shot peened specimen had more than twice the compressive stress of the LSP specimen. As the surface layers were removed, the residual stress of LSP specimen leveled off within 100 μm of the surface. The shot peened specimen increased to a maximum compressive value at ~20 μm and then declined with depth, reaching a neutral stress level at 150 - 200 μm.

Hadfield Steel

Figure 4-46 shows the results of the in-depth residual stress measurement for shot peened and LSP Hadfield steel specimens. The LSP specimen was BP coated and treated with a laser energy of 102 J. As seen in this figure, a trend similar to that of the low carbon steel specimen was found. The LSP specimen surface stress was slightly compressive while that of the shot peened specimen showed a much greater compressive stress. Although starting at a low level of compressive stress at the surface, the LSP specimen showed a noticeable increase in compressive stress with increasing depth, reaching a maximum at ~50 μm depth and thereafter decreasing with increasing depth. Following a trend similar to that observed in the shot peened low carbon steel, the shot peened Hadfield steel exhibited a maximum stress value at ~20 μm depth which then decreased monotonically with increasing depth. This stress was extrapolated to zero at about 200 μm depth, which is about twice as deep as that after LSP. As was the case for low carbon steel, the shot peened Hadfield steel specimen had a higher compressive residual stress throughout the specimen.

4.3.2. Microhardness Measurement

Microhardness was measured using Knoop microhardness tester for both low carbon and Hadfield steel specimens after LSP, cold rolling or shot peening. Surface microhardness results were obtained for the LSP and cold rolled specimens. Because of surface roughness, surface microhardness results for the shot peened specimens were extrapolated from the transverse hardness results.

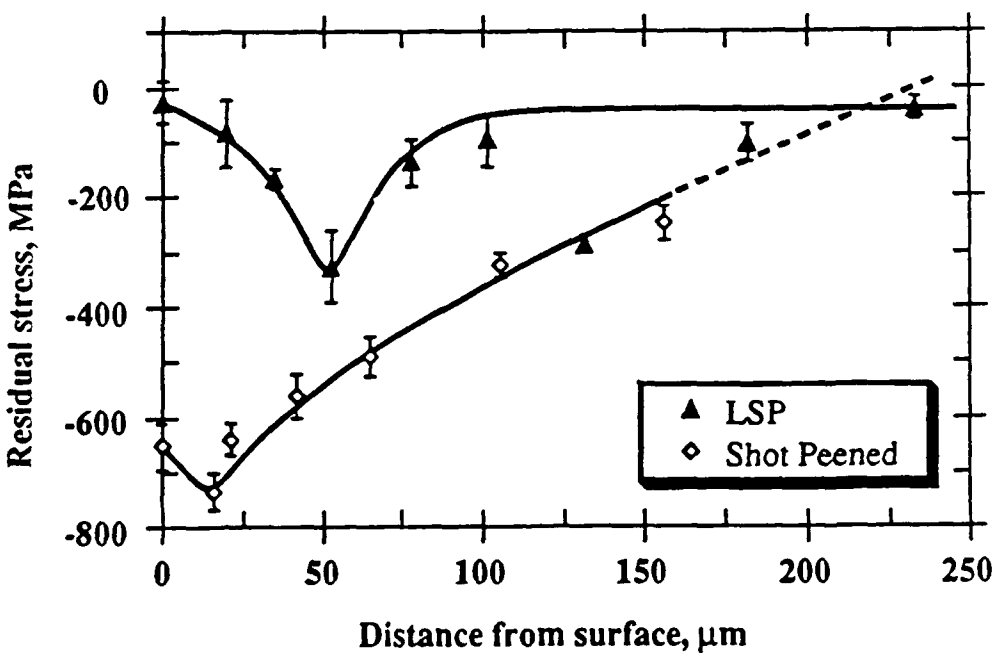

Figure 4-46 Residual stress in-depth profiles for LSP and shot peened Hadfield steel specimens.

a. Low Carbon Steel

Figure 4-47 shows an example of a LSP surface hardness profile obtained from a BP coated low carbon steel specimen treated with a laser energy of 108 J. The normalized hardness profile revealed a pattern similar to the surface profile shown in Figure 4-10. In the hardness profile, the 3 mm region of increased hardness agreed with the 3 mm wide laser beam. The hardness within the LSP region was 30 to 80% higher than that of the untreated region. Scatter in the measured hardness values is attributed to inhomogeneity of the laser beam energy. The measured hardness drop at the center of LSP region coincided with the center protrusion in the LSP surface profile of Figure 4-10.

To examine the hardness as a function of depth into the specimen, Figure 4-48 shows an example of a normalized transverse hardness profile obtained from a BP coated LSP specimen treated with a laser energy of 108 J. In this figure, results from the cold rolled (63% reduction in thickness) and shot peened specimens are also included for comparison. For the LSP transverse profile, the increased hardness (~60% higher than the untreated value) rapidly decayed and reached the untreated value within 50 μm of the depth. In general, the measured hardness fell to the untreated level within 50 to 100 μm below the LSP surface. The cold rolled specimen, on the other hand, showed a high hardness (nearly a 70% increase) at the surface, leveling off at about 100 to 150 μm of depth. This flat level of hardness was still 40% higher than the untreated value because cold rolling resulted in significant deformation throughout <0.6 mm thick specimen. For the shot peened specimen, the surface hardness was extrapolated to be about 30 to 50% greater than the bulk and the increased hardness dropped to the untreated value at about 100 μm from the surface.

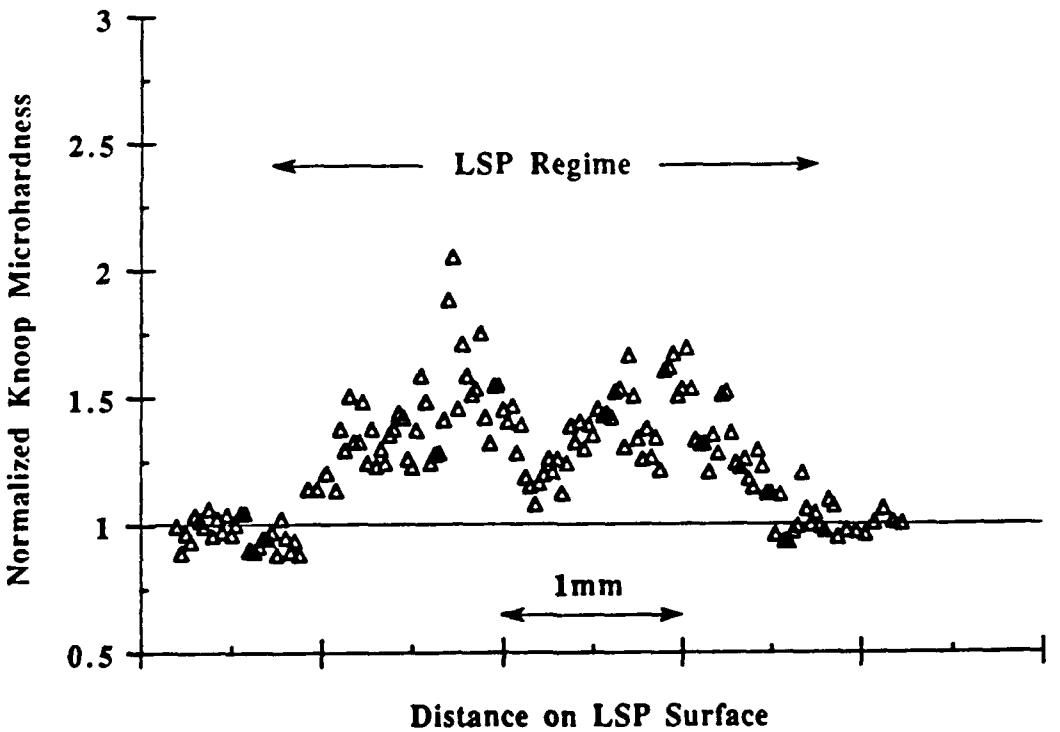

Figure 4-47 Normalized surface hardness profile for a low carbon steel specimen after LSP at an energy of 108 J with a thick BP coating and no overlay.

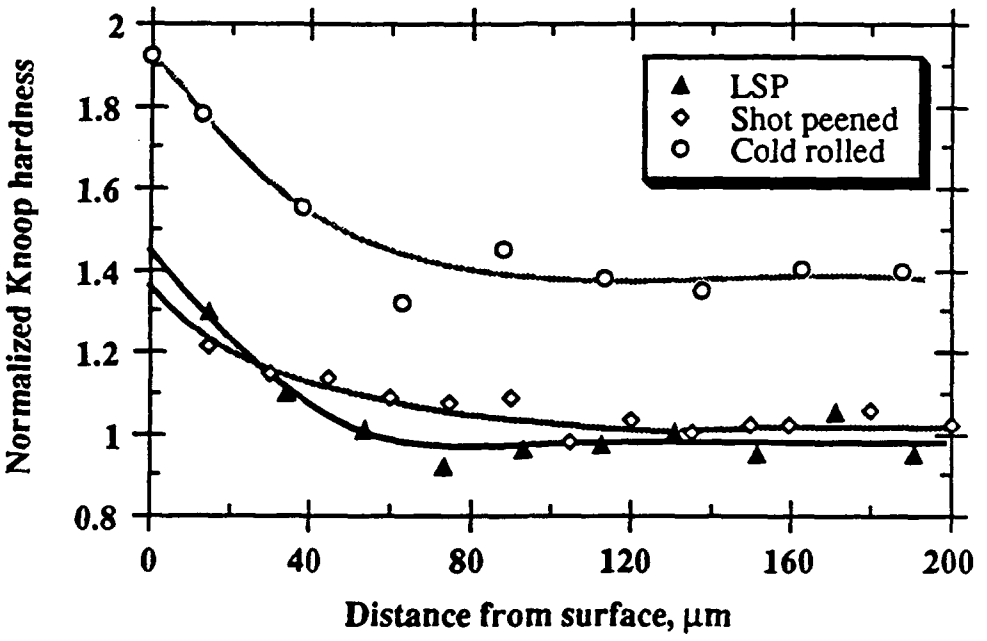

Figure 4-48 Normalized transverse hardness profiles for LSP, shot peened and cold rolled low carbon steel specimens. LSP was done at an energy of 108 J with a thick BP coating and no overlay.

b. Hadfield Steel

Figure 4-49 shows an example of a LSP surface hardness profile of a BP Hadfield steel specimen treated with a laser energy of 102 J. This normalized hardness profile demonstrates that the hardness increases 50 to 130% within the LSP region. Again, laser beam inhomogeneity can explain the scattered values of measured hardness. It should be noted that the hardness increase is much higher than that of the LSP low carbon steel specimen because of the presence of ε-hcp martensite. At the center of the LSP region of this profile, there was a plateau containing some lower hardness values that may be reflected to the protrusion at center of the surface profile shown in Figure 4-11.

For the transverse hardness profile, Figure 4-50 compares the LSP results with results from the 51% cold rolled and shot peened specimens. The hardness versus depth curves are quite similar in appearance and are within a reasonable degree of scatter of being identical. The increased hardness values decrease to bulk values about 100 μm from the surface. For the cold rolled specimen, the surface hardnesses were measured about 60% higher than the untreated value. This value was lower than those measured on the LSP surface (Figure 4-49). For the shot peened specimen, scattered hardness values were measured near the surface, and the range of increased surface hardness was estimated to be between 40 to 60%. These values are in the same

magnitude of that measured for cold rolled specimens and lower than those of LSP surface values.

4.4. Laser Shock Pressure

Figure 4.51 shows the response of a PVDF gauge from the laser-shock experiment in which the transducer was covered by 35 μm thick layer of black paint. Since the transducer was used in the negative current orientation, the first peak in the Fig. 4.51a should be negative. If it were positive, it would mean that the PVDF was responding to penetrating infra-red radiation (created by the plasma formation). According to the measurements, there was a positive response apparently to the infra-red radiation, and this event lasted for approximately 15 ns. The first major negative peak (presumably due to the mechanical shock wave) followed. The mechanical-shock wave pressure reached a maximum of 2.24 GPa (Fig. 4.51c) after approximately 12 ns (rise time t_r). The mechanical shock wave decayed after approximately 140 ns.

Figure 4.52 shows the response of a PVDF gauge from the laser-shock experiment in which the transducer was not protected by black paint. The first peak in Fig. 4.52a is negative implying that a mechanical shock wave was the first event apparent in this experiment (any response to the infra-red radiation was probably obscured). The laser-shock pressure reached its maximum of 1.89 GPa (Fig. 4.52c) after approximately 8 ns (rise time t_r). The mechanical shock wave decayed after approximately 90 ns.

These two experiments show the importance of the black paint. Since it reduced the reflection of the incident laser beam energy, the maximum pressure of mechanical-shock wave was higher when black paint layer was present.

4.5. Fatigue Test Results

Figures 4.53 and 4.54 show fatigue test results for both low carbon steel and Hadfield steel respectively. The maximum local stress at the notch root was plotted versus fatigue life. Stress concentration factors were calculated for each specimen using charts and relations from *[174]*. Experimental data was approximated using linear regression analysis. Results did not show any difference in a fatigue performance of LSP and shot-peened specimens for low carbon steel. For Hadfield steel, however, there was a slight difference: LSP specimens showed longer fatigue lives in the range $N < 10^5$ cycles.

The reason for the small improvement in fatigue life for the LSP and shot peened specimens is to be attributed to the presumed residual stress distribution in specimens tested. During fatigue testing, the fatigue crack initiated in the center of the ≈1 mm thickness specimens at the notch root. These regions could not be treated by either shot peening or LSP. Only the faces of the of the specimen could be treated by LSP or shot peening. The compressive residual stresses induced by these surface treatments at the specimen surface were balanced by tensile stresses at notch root and at the mid thickness of the specimen (Fig. 4.55) which could, in fact, slightly accelerate crack initiation and early growth in that location.

Thus, the experiments performed using the time and funds at our disposal do not reflect any benefit of LSP. However, we do not feel that these experiments correctly reflect the potential benefits of LSP due to the experimental difficulties discussed above.

4.6. Summary of Results

The important results can be summarized below into two categories -- (1) LSP optimization and (2) effects on microstructure and mechanical properties.

4.6.1. LSP Optimization

a) The direct LSP plasma observations showed the BP coating produced a less intense plasma plume than that of the bare specimen, suggesting the BP coating protected the specimen from melting and vaporization.

b) The role of the BP coating for surface protection was demonstrated by LSP surface features such as smooth profiles and compressive residual stresses.

c) When no overlay was used, the plasma that formed on the coated surface intensified with increased laser energy, resulting in more shock wave intensity and thus more specimen deformation. Such increased deformation with increasing laser energy was illustrated on the LSP specimens by deeper surface indentations and more ε-hcp martensite formed in the Hadfield steel specimen at higher laser energy.

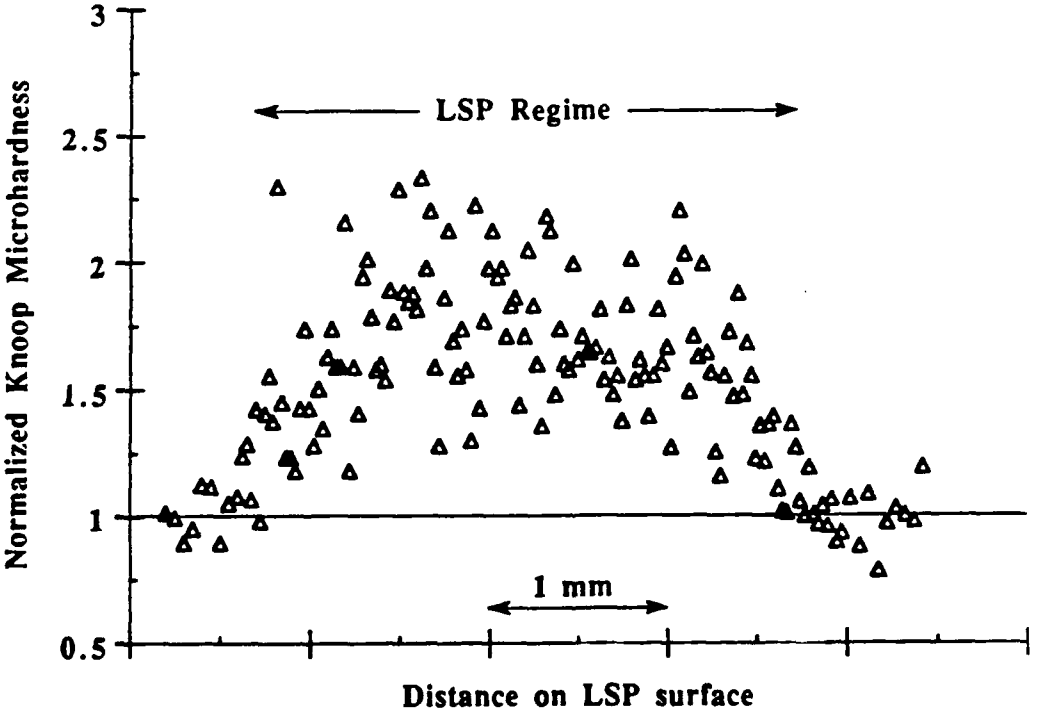

Figure 4-49 Normalized surface hardness profile for Hadfield steel specimen after LSP at an energy of 102 J with a thick BP coating and no overlay.

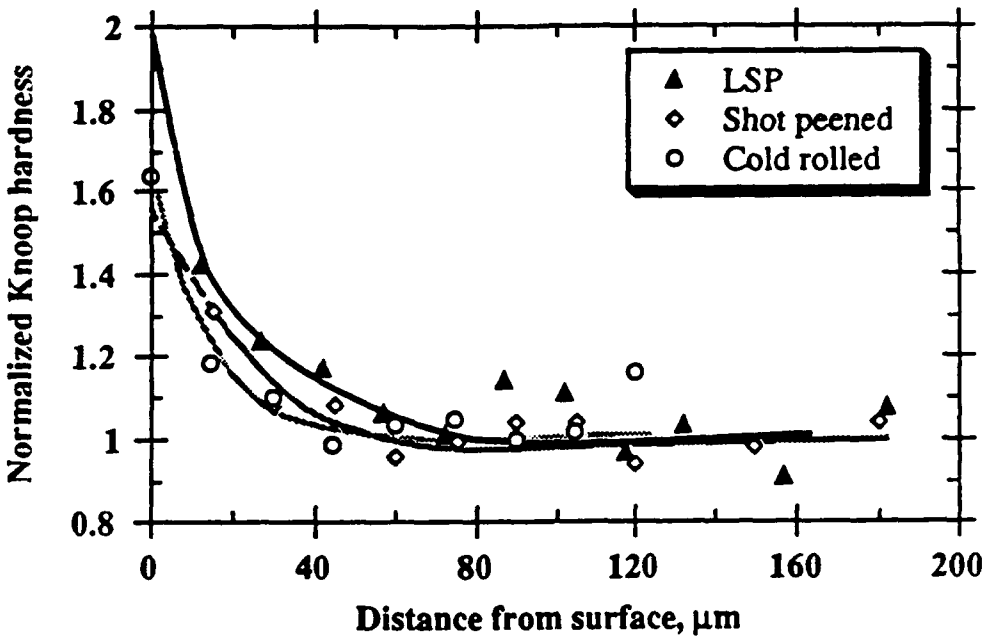

Figure 4-50 Normalized transverse hardness profiles for LSP, shot peened and cold rolled Hadfield steel specimens. LSP was done at an energy of 102 J with a thick BP coating and no overlay.

d) When a quartz overlay was used, plasma plumes formed on both overlay surfaces, resulting in a loss of effective laser energy and thereby a loss of shock wave pressure (as demonstrated by the extent of deformation measurements).

4.6.2. Effects on Microstructure and Mechanical Properties

a) For the low carbon steel, evidence of LSP-induced plastic deformation included dislocation etch pits in the SEM micrographs and dense arrays of dislocations in the TEM observations. Dislocation densities were calculated to be ~$3x10^{11}/cm^2$ and no martensite nor twin was found. At 50 μm below the surface, microstructure with dislocation density of ~$1.4x10^{11}/cm^2$ was observed.

b) For the LSP-induced deformation in the Hadfield steel, SEM micrographs showed macroscopic surface relieves and slip line markings and these slip lines were found ~15 μm below the surface. TEM examinations revealed extensive formation of ε-hcp martensite as well as dense dislocation arrays. The dislocation density was calculated to be ~$6x10^{10}/cm^2$ and no deformation twins nor α'-bcc martensite was found.

a) Current versus time

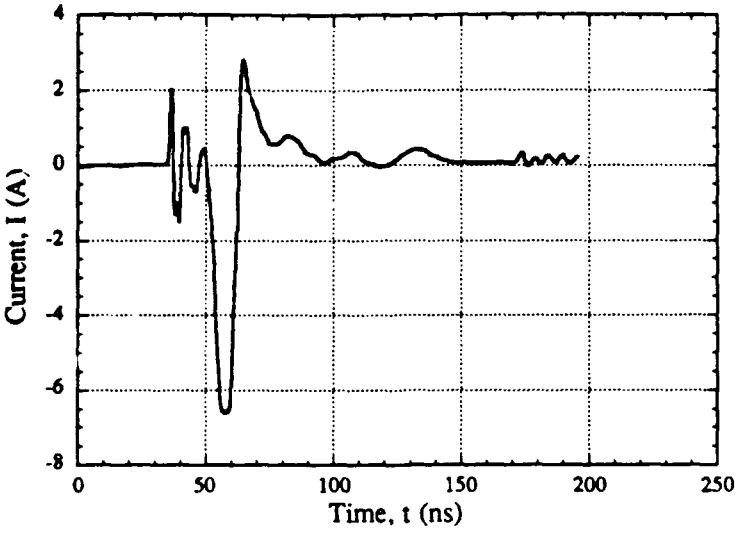

b) Charge versus time

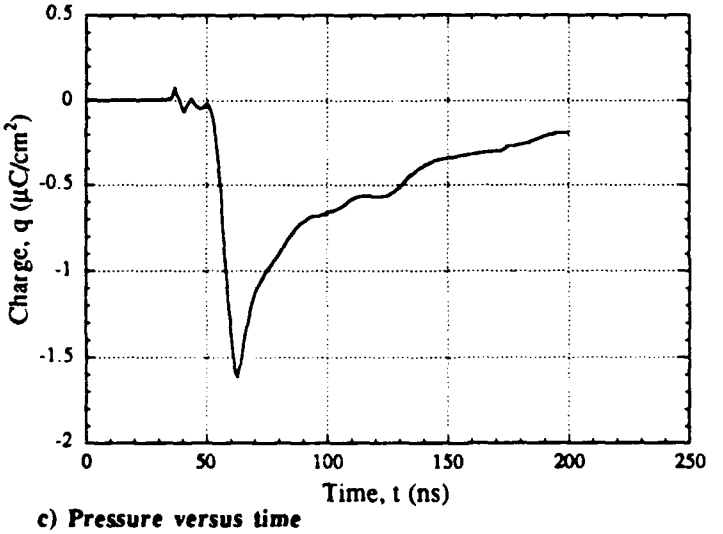

c) Pressure versus time

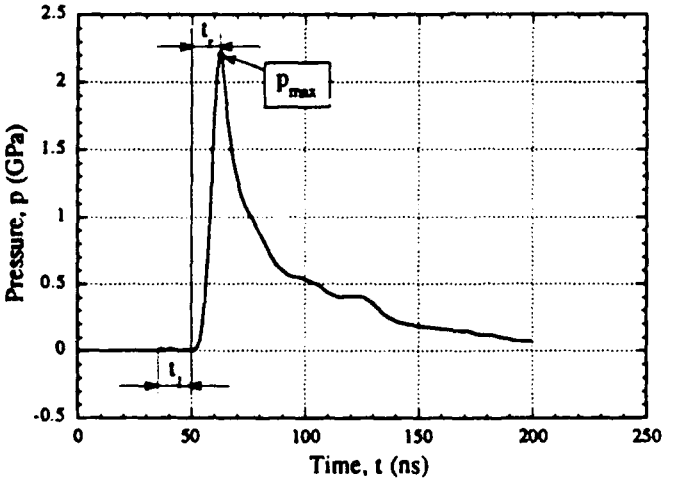

Fig. 4-51 PVDF response from the laser-shock experiment: E = 78.53 J, t_1 = 15 ns, t_r = 12 ns, p_{max} = 2.24 GPa, ~35 μm of BP.

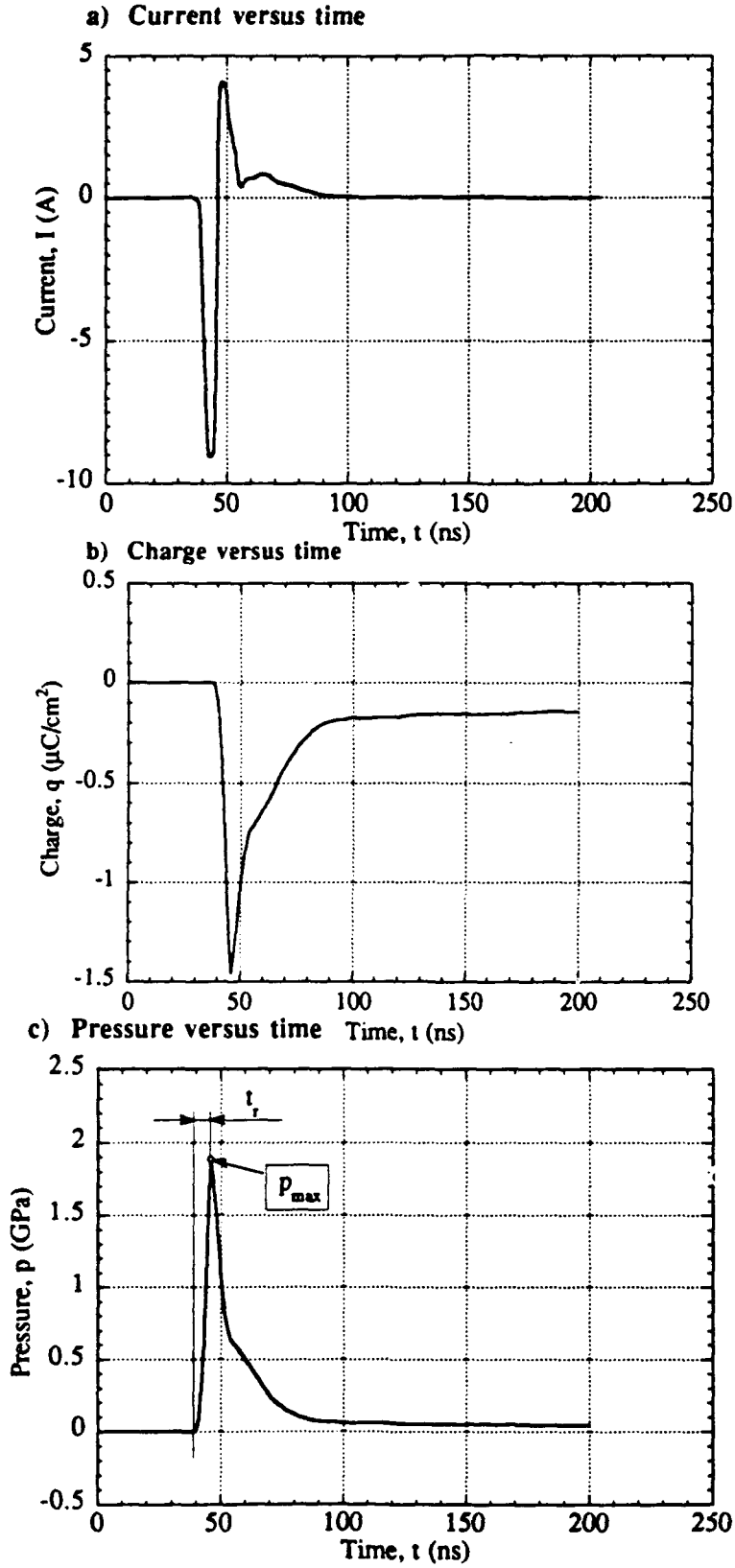

Fig. 4-52 PVDF response from laser-shock experiment: E = 72.43 J, $t_1 = 0$, $t_r = 8$ ns, $p_{max} = 1.89$ GPa, no BP.

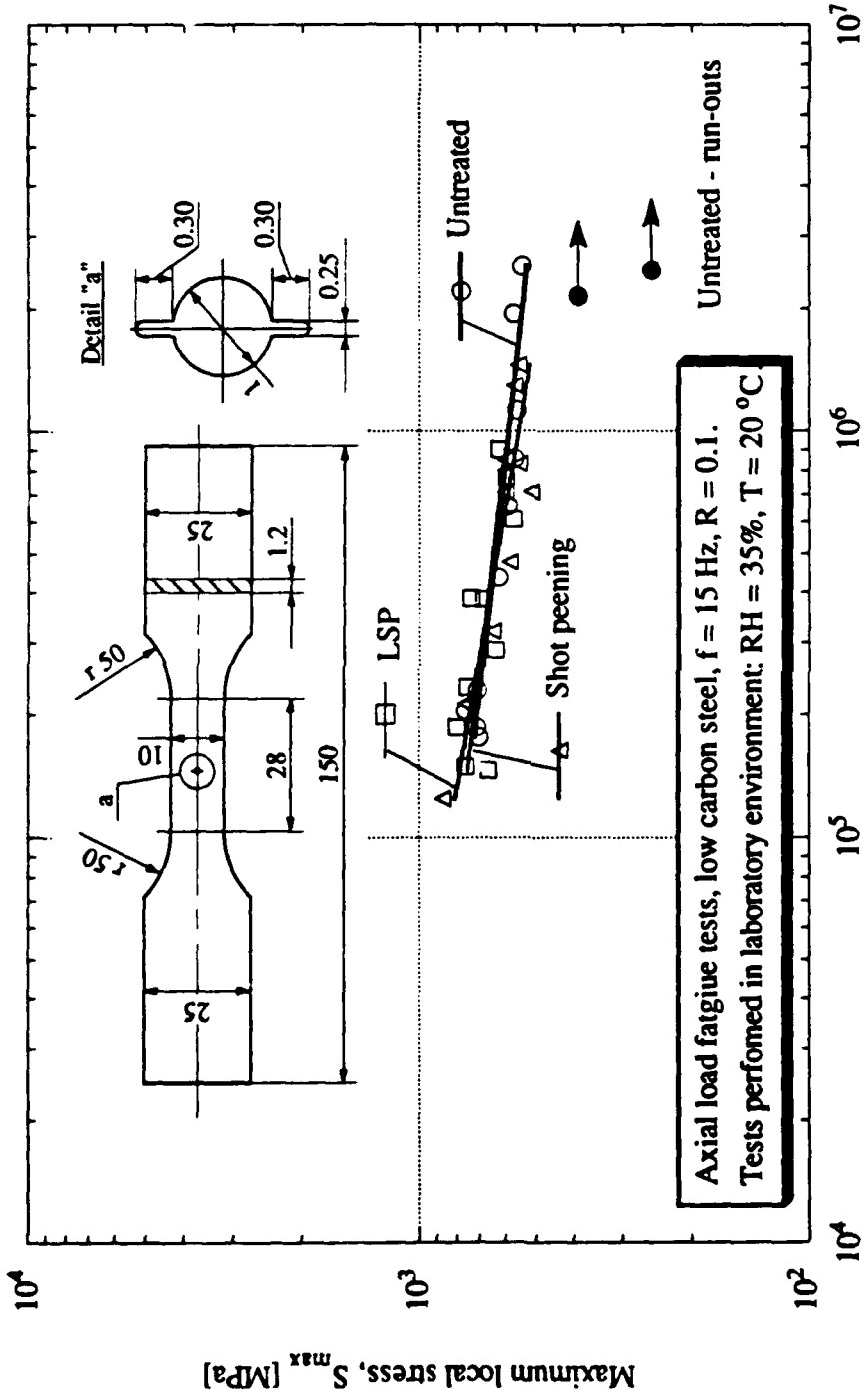

Fig. 4-53 Fatigue test results for untreated, LSP, and shot peened low carbon steel specimens.

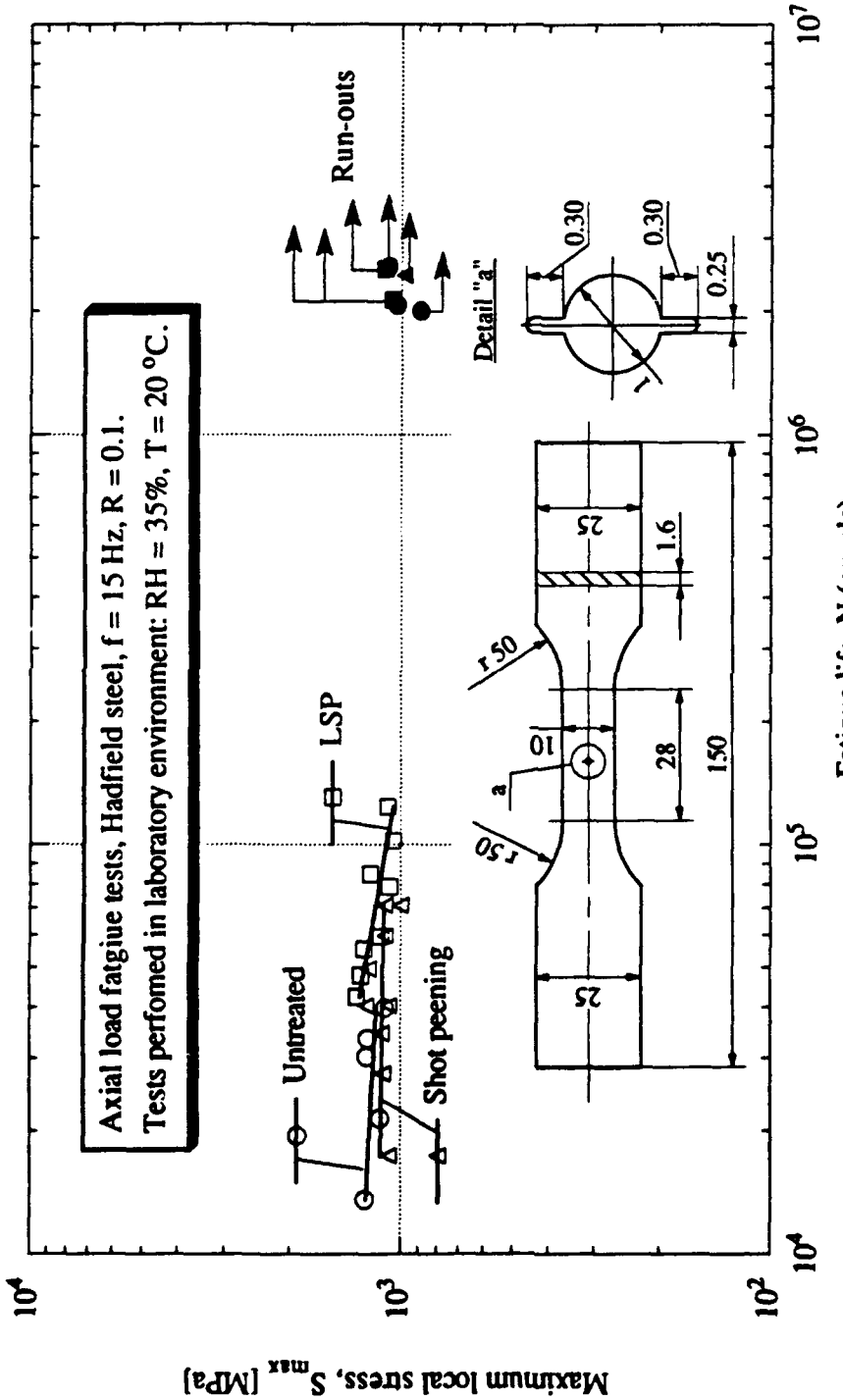

Fig. 4-54 Fatigue test results for untreated, LSP, and shot peened Hadfield steel specimens.

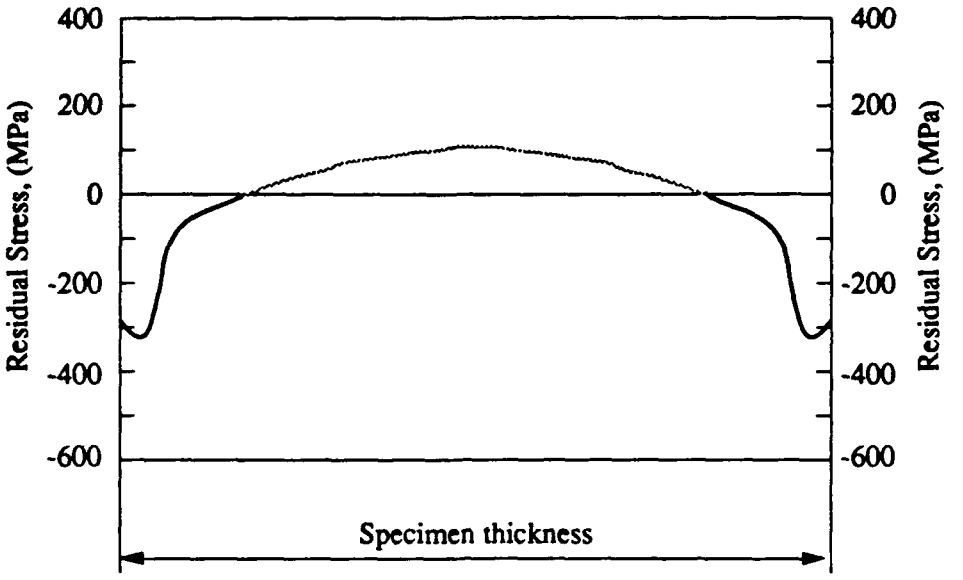

Fig. 4-55 Hypothetical residual stress distribution through the thickness of the specimen.

c) The X-ray results indicated that the volume fraction of ε-hcp martensite increased from <4 vol.% in the annealed material to >35 vol.% in the LSP Hadfield steel. Depth profiles of martensite volume fraction showed a drop to the untreated value at depth of about 50 μm.

d) For the cold rolled and shot peened specimens, both steels exhibited microstructures very different from those of the LSP specimens. For cold rolling, the low carbon steel had dislocation cell structures with a high dislocation density ($>1x10^{12}/cm^2$), while the Hadfield steel showed ε-hcp martensite as the major phase. The shot peened low carbon steel, dislocation densities were $\geq 2x10^{11}/cm^2$, while the similarly processed Hadfield steel contained dislocations, deformation twins and some ε-hcp martensite.

e) LSP low carbon steel showed maximum compressive residual stresses on the surface, while Hadfield steel had maximum stress below the surface. For both steels, these stresses decayed to a saturated level at about 100 μm below the surface. Compared with LSP, shot peening generated higher and deeper compressive stresses for both steels. For both steels after shot peening, the maximum stresses measured ~20 μm below the surface and they fell to the neutral value at 150 - 200 μm of depth.

f) Surface hardness profiles of both LSP steels exhibited a hardness drop at the center of LSP region, coinciding with the center protrusion region in the LSP surface profile. The hardness increases, which varied significantly in the LSP region due to inhomogeneity of laser beam distribution, ranged from a 30 - 80% increase for the low carbon steel to a 50 - 130% for the

Hadfield steel specimen. The transverse hardness profiles of both LSP steels showed a rapid decrease in hardness at between 50 to 100 μm of the depth.

g) For the cold rolling, high surface hardness (~70% increase for the low carbon steel and ~60% for the Hadfield steel) fell to the plateau level at about 100 to 150 μm for the low carbon steel and ~100 μm for the Hadfield steel. The plateau level for the cold rolled low carbon steel was still 40% higher than the untreated value. For shot peening, the scattered surface hardness values were extrapolated to show a 30 to 50% increase for low carbon steel and a 40 to 60 % increase for Hadfield steel. These surface hardnesses dropped to the untreated value within 100 μm of the depth in the low carbon steel and 75 μm in the Hadfield steel.

4.6.3. Effects on Laser Shock Pressure

Laser shock pressure was measured using PVDF gauges. The maximum magnitude of laser shock pressure was obtained for the specimen covered by black paint (2.24 GPa). The pressure reached its peak after approximately 12 ns (rise time t_r). When no black paint was applied, the maximum pressure was 1.89 GPa and the rise time was t_r = 8 ns.

4.6.4. Effects on Fatigue Performance

Fatigue test results did not show significant improvement of LSP and shot peened specimens in comparison to untreated specimens. The reason for little or no improvement could be attributed to the residual stress distribution at the notch root of specimen tested. If the crack initiation sites of specimens tested had been treated by either LSP or shot peening, the effects would have been much better.

5. DISCUSSION

Surface conditions have been shown to play an important role in achieving large surface deformation and in protecting the specimen surface from melting. To understand the surface-related phenomena (for example, breakdown of the quartz overlay), a model is presented and evaluated in light of plasma image results. In this section, overlay breakdown and optimized LSP conditions are discussed and a physical model that describes the formation of plasma pressure is proposed. The shock wave pressure is then calculated according to an existing model and experimental results. For the LSP effects on the microstructure, discussions and comparisons are made with the other shock and conventional processing results. Then, strengthening mechanisms are described according to the observed microstructures of the low carbon and Hadfield steels. LSP and shot peening effects on the near and sub-surface residual stresses are discussed.

5.1 Laser Shock Processing

5.1.1. Use of Overlay

The use of an overlay was found to be very important in other LSP studies for enhancing shock wave pressure. However, in this study the overlay was found to be detrimental in shock wave generation because even in high vacuum the overlay became a source for the development of an energy absorbing plasma. The discrepancy is discussed. Then, early published overlay breakdown results are given and a model is proposed to describe the evolution of plasma formation observed in this study.

a. Role of Overlay in LSP Studies

As indicated by several studies *[5-10, 49-55]*, high shock wave pressures have been achieved by the use of a plasma-confining overlay. The desired overlay function is illustrated in Figure 5-1. As seen in this figure, when the plasma is formed on the laser-irradiated specimen surface, expansion of the plasma volume is confined within the overlay-specimen interface region. Thus, the shock wave created by the plasma volume expansion is enhanced in the specimen direction. The magnitude of shock pressure subsequently increases, for instance, from 47 MPa without an overlay to 790 MPa with an overlay on an aluminum foil at ~10^9 W/cm^2 laser power density *[53]*. Nevertheless, in this study, the role of pressure enhancement by the overlay is not realized, especially when the high laser energy is applied. This is supported by the observations of much less deformation to the specimens and no detectable ε-hcp martensite formed in Hadfield steel.

To understand the contradiction between this and other LSP studies, some experimental parameters may be considered. These include, for example, type of overlay materials, laser pulse duration, wavelength, and laser power density. While the experimental parameters may vary, the most important factor is the laser power density. This is because almost all the studies that showed pressure enhancements by the overlay were at power densities between 10^8 to 10^9 W/cm^2 *[1-10, 51-54]* until a recent study at power densities up to 10^{12} W/cm^2 by Fabbro et al. *[55]*. They found that a decline of shock wave intensity occurred above 2.8×10^9 W/cm^2 for a 3-ns pulse duration and 1.06-μm wavelength laser. This intensity decline was accompanied by some visible damage of a BK-7 overlay when it was irradiated alone. This damage was shown to be attributed to the laser-induced breakdown of the overlay *[55]*. Once the breakdown took place, most of the laser energy was absorbed by the overlay for the damaging, resulting in a laser energy loss. Further, such energy loss was shown to become more significant as the laser energy

increased *[55]*. Therefore, they concluded that the laser-induced breakdown of overlay was the main mechanism limiting shock wave generation at high power laser densities.

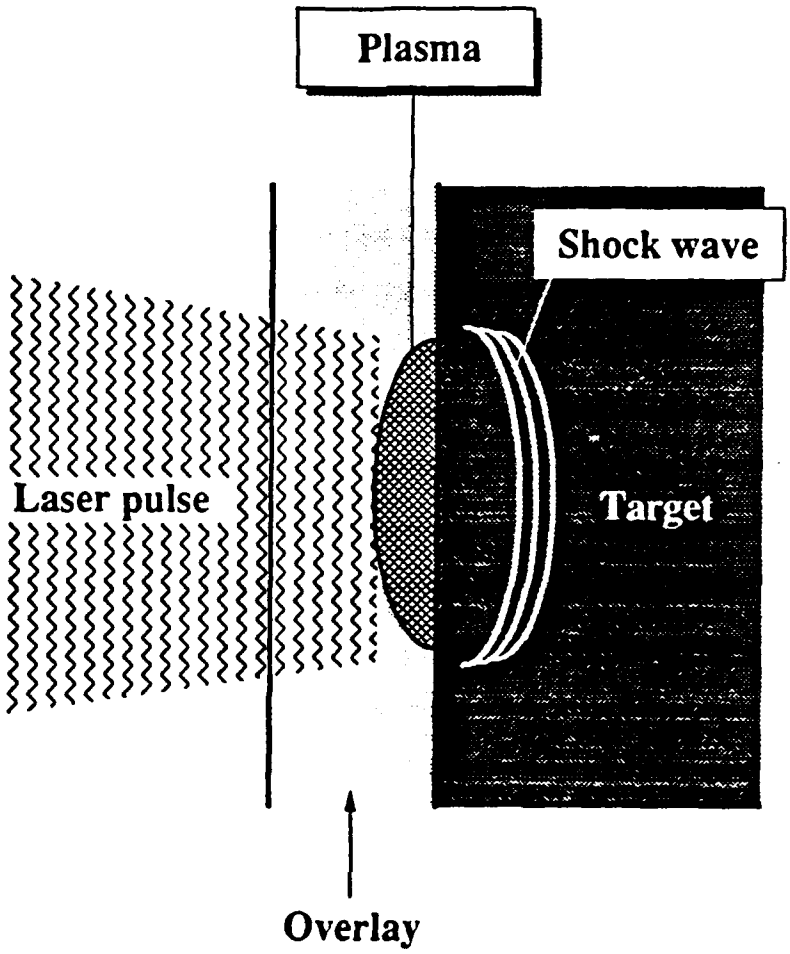

Figure 5-1 Desired overlay function in LSP.

b. Breakdown in Overlay

In this study at power densities between 1.2×10^{11} to 4.7×10^{12} W/cm^2, a similar laser-induced breakdown was observed on both the quartz and BK-7 overlays. The first evidence is seen in the in-situ laser plasma imaging in which the LSP-produced plasma plumes were shown to form on the overlay surfaces. As a result of overlay plasma formation, the visual surface and internal damage were observed in the overlay after being irradiated alone. The extent of damage appeared to be laser energy dependent. This is because with the increased laser energy the plasma became intensified. Expectedly, a significant energy loss occurred in the high laser energy LSP due to the increased energy absorption by the intensified overlay plasma. Evidence of this significant energy loss was confirmed by the results of surface indentation profiles, foil deformation measurements, Auger and X-ray analyses. The phenomena [overlay plasma and subsequent energy loss] are definitely attributed to the laser-induced breakdown of the overlay. With the evidence shown in this study and in the study by Fabbro et al. *[55]*, the laser-induced breakdown of the overlay is confirmed experimentally when the high power laser density of LSP is over 10^9 W/cm^2.

Breakdown Thresholds

In the literature, the breakdown threshold information for the selected overlay material are not always consistent. For instance, the BK-7 glass breakdown threshold is quoted as ranging from 0.2 to 710×10^9 W/cm^2 *[55, 132, 133]*. The threshold value given by Fabbro et al. *[55]* is in the lower limit of this range. The broad spread in the breakdown threshold values may come from the large variation of experimental parameters such as the state of surface and internal perfection of the material, laser focal area, wavelength, and pulse duration. Therefore, the values cited can not be accepted as exact, absolute numbers. Experimental measurement is needed for the breakdown threshold determination of a given overlay material. In this study the breakdown threshold for the quartz overlay used was estimated to be 5.2×10^{10} W/cm^2 by the plasma imaging method and visual examination of laser-treated quartz *[134]*. This is about an order of magnitude lower than the power density range used in this study. To eliminate the overlay breakdown problem, the laser power density therefore has to be decreased by increasing the irradiated area or lowering the laser pulse energy.

Furthermore, as indicated by Milam in his breakdown measurement study at different pulse durations [wavelength of 1.06 μm] *[135]*, the threshold values were shown consistently higher on the laser side (front surface) than the target side (rear surface) of a given thickness of overlay; see Figure 5-2. This finding can explain why the overlay damages always started to appear at the rear surface in this and the Fabbro et al. *[55]* study. Although the breakdown ratios are not always consistent with the ratio of calculated intensities at the front and rear surfaces *[135]*, it is adequate to consider at the same laser energy the power density at the rear surface to be somewhat higher than that of the front surface since the laser beam is converged to the focus point. As the energy increases the power density at the rear surface reaches the threshold value first. At even high laser energy, the front surface power density is over the threshold value and the breakdown occurs. Since the breakdown of an overlay surface takes place at lower threshold values than volume breakdown *[133]*, in this study damage was consistently observed to start from the rear and front surfaces of overlay.

Proposed Model

A comprehensive, detailed discussion of physical breakdown mechanisms is beyond the scope of this study. However, a model is introduced in light of understanding the evolution of overlay plasma formation in this study. As shown by several studies, the breakdown in the

transparent overlay materials is associated with mechanisms such as multiphoton ionization of host atom, heating and thermal explosion of absorbing inclusions, and etc *[133, 136]*. These mechanisms all are laser energy dependent; i.e., the laser energy plays an important role not only in generating these mechanisms, but in sustaining them once formed. Therefore, it is reasonable to expect that the rear surface plasma on overlay is not able to expand or intensify like the front surface plasma does. Since the front surface plasma is located ahead of the rear surface plasma, the former always receives laser energy before the latter, although the latter forms prior to the former one. The following is a model to explain the plasma formations in Figs. 4-4 and 4-5.

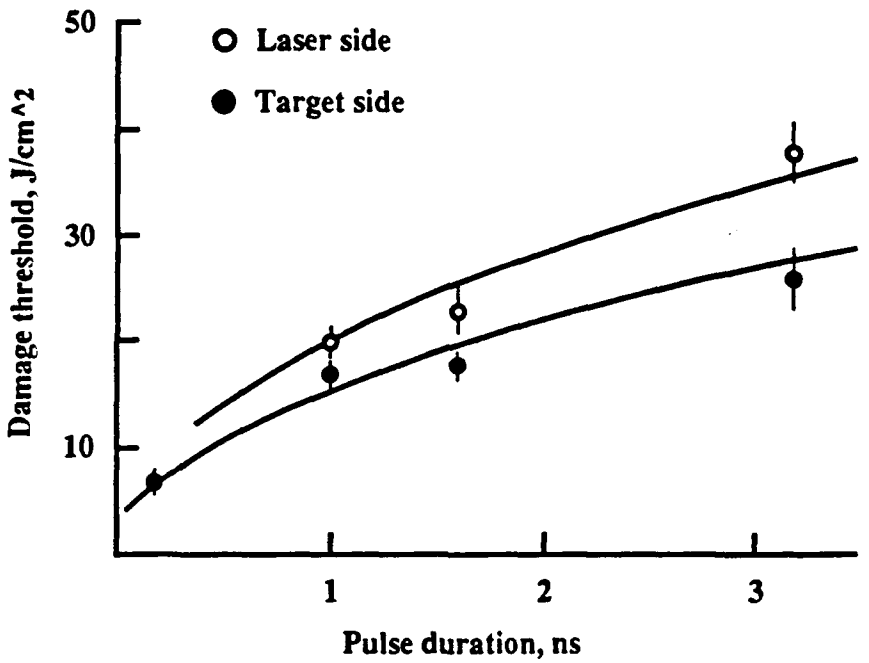

Figure 5-2 Damage threshold of BK-7 overlay as a function of pulse duration *[135]*.

Consider the delivered laser pulse as a Gaussian pulse form which illustratively consists of three segments: the first is a low energy segment, followed by the peak energy segment as the second and then ended with the third segment of low energy; see Figure 5-3. When the overlay is irradiated with low laser energy, the first segment of laser pulse creates some plasma on the rear surface as a result of breakdown, provided this segment energy is higher than the rear surface breakdown threshold but lower than that of the front surface. This target is illuminated by the laser before an intense plasma is formed. Also, this illumination may result from some of later laser segments passing through the plasma as long as the plasma absorption is not significant. As the second segment of laser arrives at the front overlay surface the plasma forms, provided that the second energy segment is higher than the front surface breakdown threshold value. Once this plasma forms, most of the laser energy is consumed for front surface plasma formation and only a fraction of this second pulse segment will pass to the rear surface plasma.

When the third pulse segment reaches the front surface plasma, the laser energy may be absorbed and no significant portion of laser energy will reach the rear surface or even the specimen. Therefore, once the plasma has formed on the front overlay surface, the rear surface plasma and specimen will receive little or even no laser energy, depending upon the degree of laser absorption by the front surface plasma. Figure 4-4c demonstrates the extreme case of this model. At this laser energy level, which was much higher than the front surface breakdown threshold value, the front surface plasma formed in the very early stage of the first pulse segment. As a result, the rest of the laser pulse segments were not able to get through because the formed front surface plasma consumed the ensuing laser energy for expansion and intensification. Subsequently, there is no detectable plasma on the rear overlay surface nor illumination on the specimen. According to this model, the results obtained at high laser energy with the overlay can be explained. These results included no detectable surface indentation, significant laser energy loss measured by the deformed foil surface profiles, much less surface contamination (see Auger results in Appendix B) and no measurable ε-hcp martensite phase in X-ray results.

Nevertheless, this proposed model can not thoroughly explain the plasma behavior shown in Figure 4-5 for the quartz overlay. It showed that while the front surface overlay plasma intensified at high laser energy, the rear surface plasma and specimen illumination also showed a noticeable increase. Still, the intensified front surface plasma is in agreement with the model proposed. The specimen illumination increased in this case due to the extremely bright plasma formed on the rear overlay surface, not due to increased absorption of laser energy by the specimen. This is because the specimen did not exhibit any increased deformation on the surface under this condition. The behavior of the rear overlay surface plasma may be attributed to a strong laser-plasma interaction. To understand this some additional experiments are needed.

In the conclusion of this section, a model is presented to explain the plasma formation observed on the overlay surfaces as a result of breakdown induced by the laser. This proposed model is developed based upon the existing breakdown mechanisms and plasma image results of this study. It is shown that once the plasmas form on the overlay surfaces the specimen receives little or no laser energy. In the extreme case at high laser energy, the front surface plasma forms at the early stage of laser pulse and such formed plasma absorbed almost all of the incoming laser energy, resulting in no noticeable energy to irradiate the specimen or to form the rear overlay surface plasma. With this proposed model describing the overlay breakdown and plasma formations during LSP, all the material characterization results can be explained based on the lack of improved LSP effects from the overlay. Yet, due to strong laser-plasma interaction, the proposed model can not explain an exceptional rear surface plasma phenomenon that showed the enlarged plasma size at high laser energy.

5.1.2. Plasma Formation -- Optimized LSP Conditions

In this study, the optimized conditions for LSP are shown to be the use of a black paint coating for specimen surface protection and application of high laser energy to produce intense plasma on the surface to achieve high shock wave intensity. So, understanding of plasma formation is important and its effects on the melted and unmelted surface morphologies observed on the specimens are first discussed. The shock pressure then is calculated and compared with other early results.

a. Effects on Surface Morphologies

It is shown in the plasma images of Figures 4-2 and 4-3 that the plasma plume formed on the bare and black paint coated specimens when no overlay was used. The plasma formed on the black paint became intensified as the laser energy increased, resulting in increased deformation

of the specimen. To understand the formation of plasma, some vivid SEM surface features of bare specimens shown in Figures 4-13 and 4-14 are used. The surfaces shown have distinct

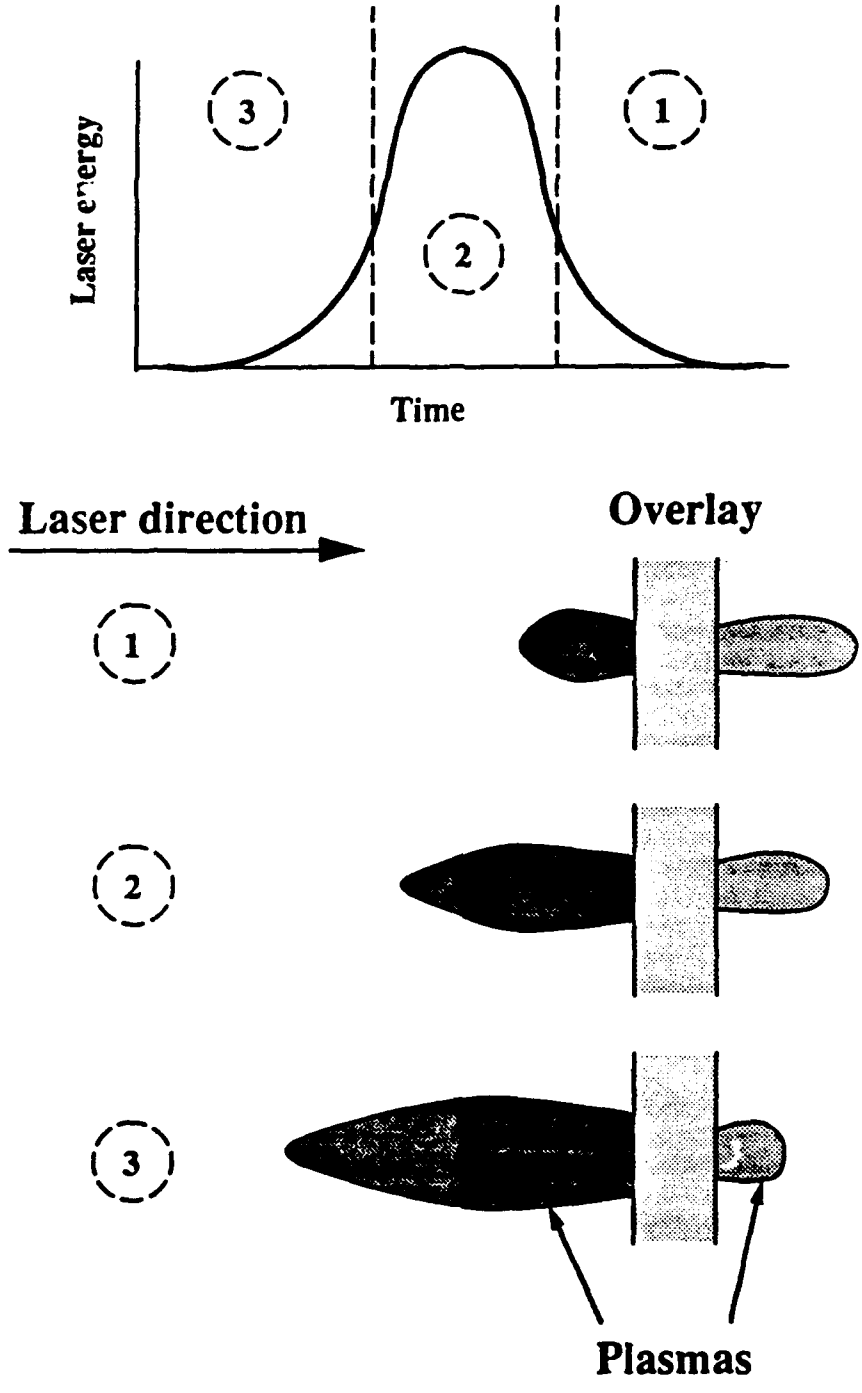

Figure 5-3 Schematic of overlay plasma evolution during LSP.

features between the center and outer regions: solidified droplets, craters and holes at the center region whereas splash-like droplets exist in the outer region. As these solidified surfaces gave strong evidences of severe, explosion-like melting during LSP, it is indicated that there was a pressure exerting on the melted surface and pushing the melted material out of melted pool. Similar SEM surface morphologies are also observed by the other LSP studies. These include, for example, solidified droplets, craters and holes by Clauer and Fairand in Fe-Si alloy *[4]* and Al alloy *[5]*, and splash-like features by Bournot et al. *[12]* and Phipps et al. *[59]* in Al, Hoffman in Au *[137]*, and Vohra et al. in Si *[138]*. For the surface indentations on the LSP specimens, similar features were also found in iron by Cottet et al. *[11, 72]*, and in aluminum by Bournot et al. *[12]*. However, none of these studies explained in detail how the observed surface morphology was formed during LSP.

Radial Plasma Expansion

The pressure exerting on the surface during LSP is caused by the sudden volume expansion of plasma formed on the melted surface. The following is a qualitative plasma formation model describing the observed surface morphologies. While the bare surface morphologies are used for this model, the plasma formation mechanism proposed is valid for both bare and coated specimens. The expanding plasma is illustrated schematically in Figure 5-4a, which is originally presented in *[47, 139]*. This scheme is a modified picture of Figure 2-2. It shows that after the target is laser irradiated some important features are created within the pulse duration and these must be considered to describe the effects of plasma on the target surface morphologies. The features are the shock, absorption plasma zone, and plasma left behind the propagating region. As seen in this figure, the shock and absorption plasma zone are propagating away from the target surface, whereas the plasma behind them is expanding radially and accompanying with another shock that is propagating in the same direction. While the absorption plasma zone consumes most of the incoming laser energy, some of it passes through and is expended by the plasma behind. With this supplied laser energy the plasma left behind expands radially until its energy is exhausted by this volume expansion. So it is expected that this expansion will last for some period of time after the laser is switched off.

This type of plasma radial expansion is reported to start at about the middle of the laser pulse *[30, 41]*, and therefore it is reasonable to expect that it would not be a significant effect at low laser energy. It is because once the plasma forms it will quickly expand axially to absorb the still-incoming laser energy, and the low laser energy will be consumed mostly by the absorption plasma zone, resulting in insufficient energy for the plasma behind to expand radially. In fact, this phenomenon is demonstrated by the plasma images of Figures 4-3a and b taken from the coated specimens at relatively low laser energies. At low energies of 6.40 and 27.70 J , only low intensity plasmas were observed predominantly near the coated surface and no noticeable radial plasma expansion was seen, whereas at the high energy of 67.85 J the red plasma began to appear outer region due to the radial plasma expansion. At an even higher energy this red plasma became more intense, indicating a greater radial expansion.

Axial Plasma Expansion

While this radial plasma expansion mainly occurs on the surface beginning at the middle of pulse, the absorption plasma zone launches its volume expansion axially opposite to the laser direction at a relatively early stage. The time relative to the laser pulse for the plasma expanding axially is dependent on the laser energy: for instance, for a 200-ns pulse the expansion may start within 20-ns for 700 J/cm^2 and at 60-ns for 70 J/cm^2 *[41]*. The center melted region of the specimen experiences a recoil force due to the absorption plasma expanding axially, and as a result the melted surface is subjected to a shock wave pressure. While the center melted region

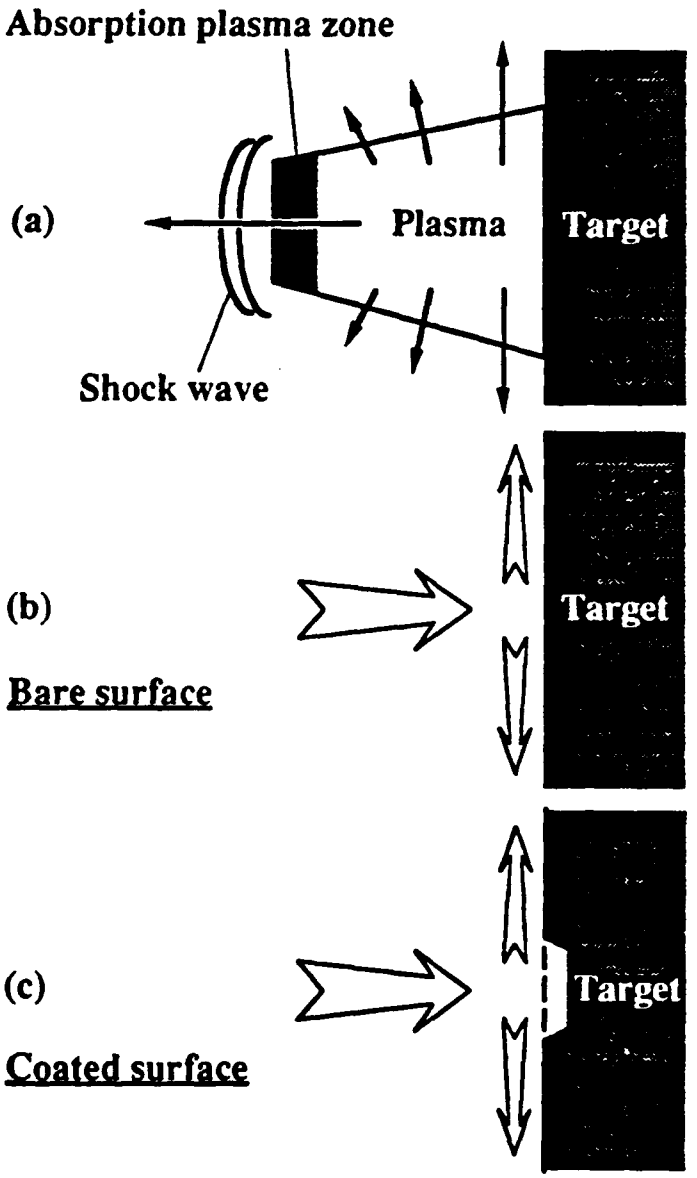

Figure 5-4 (a) Plasma volume expansion *[47, 139]*. (b) Pressure exerting on a bare surface, and (c) on a coated surface.

may be pushed away radially due to this recoil pressure, the hot plasma is still in contact with the specimen and therefore the specimen surface remains melted as long as the plasma exists. [In the case of coated specimens, the coating is melted during LSP and the specimen substrate is only

subjected to the shock-induced deformation.] Subsequently, the center retains some features (craters and holes) that resulted from the melting under the high pressure.

Overall, Figure 5-4b shows a qualitative model describing the uncoated surface morphologies resulting from different types of plasma pressure exerting on the melted surface. The radial plasma expansion is shown pushing the melted material out of melted pool and a splash-like solidified feature is finally seen in the outside region. On the other hand, the center region mainly suffers from the high recoil pressure due to the plasma expanding axially. In this center region, surface features such as solidified droplets and spheroids are seen. These droplets and spheroids are first ejected from the surface during melting and later return to the surface either by gravitational or electrostatic attraction, and then are solidified as spheroid or droplets *[140]*. The proposed model can be readily examined by placing an aperture on the bare specimen surface. The aperture has an opening cut off on the side so that the plasma expands radially into the opening direction; expectedly the melted surface flows toward the same direction and eventually solidifies *[134]*. Another example is when the overlay was placed on the specimen. The more extensive splash-like surface morphologies were observed due to the greatly enhanced radial expansion of plasma; see Figure 4-15.

In the case of surface indentations observed on coated specimens (Figures 4-10 and 11), the effects of both axial and radial plasma expansions are also seen. As illustrated in Figure 5-4c, the bottom of the indent is narrower than the top. This large opening on the top of surface is a direct result of the radial plasma expansion. Very similar shapes of surface indentations were observed on an aluminum specimen in the study by Bournot et al. *[12]* at 10^9 W/cm^2 power density and 25-ns pulse. In that study, the Al specimen was confined with a transparent overlay. The size of indentation was about 6 mm in diameter and 2 mm in depth. It is also noted that a protrusion at the center of the indent was similar to those found in this study. This protrusion is presumably a characteristic feature resulting from the laser shock-induced deformation. Another example of indentation was observed on an iron specimen in the study by Cottet and Romain *[11]* at 10^{14} W/cm^2 power density and 3.5-ns pulse. The cross-section optical micrograph indicated the size of the indent was 340 μm in diameter and 140 μm in depth, while the laser beam size was about 100 μm in diameter. Nevertheless, the indent's shape was not of flat-bottom, rather it was hemispherical and showed no protrusion at the center of indent. This hemispherical indentation was reported to be attributed to the melting caused by 800 GPa shock pressure at the surface. For the melting in the iron it needs at least 250 GPa shock pressure to generate shock heating effects *[12]*. Since the shock pressure reached in this study was about 2 GPa, the shock heating effect is negligible.

b. Some Other Effects of Plasma Formation

While the shock wave pressure is mainly generated by the axial plasma expansion, the radial plasma expansion reduces the overall shock pressure created by the plasma, as pointed out by Root *[47]*. This can be seen from the fact that the recoil pressure due to the plasma expanded axially not only exerts on the specimen surface but also assists the radial expansion of the near surface plasma. As a result, the pressure on the specimen from the axially expanding plasma is reduced. To enhance the shock wave pressure, a constraint on the radial plasma expansion may be needed.

To examine thermal effects of plasma formation on the specimen substrate, it is necessary to consider the heat penetration equation of (2-3). For the black paint coating material used in this study, the thermal diffusivity (κ) is on the order of 0.004 cm^2/sec *[20]* and time for LSP was estimated to be about 150 ns *[134]*. Accordingly, the depth of heat penetration is ~0.5 μm at the end of LSP. This is negligible as compared to the whole thickness of black paint coating (40 to 50 μm) applied to the specimen substrate. Therefore, the thermal effects on the specimen are

considered to be insignificant. This, in fact, is confirmed by the Auger results (see Appendix B) where no contamination from the black paint coating was detected on the unmelted specimen surface.

As an approximation of some properties of the observed plasma, results are quoted from the studies that were performed in the same power density range and on similar materials. The temperature of plasma is 10 to 100 ev for the 10^{11} - 10^{12} W/cm^2 power density *[41]*, and maximum velocity of the axial plasma expansion is approaching to 2×10^7 cm/sec at 10^{12} W/cm^2 *[41, 141, 142]*. In the plasma image photo of Figure 4-3, the observed plasma emission from the coated specimen extended to be about 1.5 cm long, although the actual plasma emission may be longer than this value. Taking an average plasma expansion velocity of 6×10^6 cm/sec *[41]*, the lifetime for this plasma is about 250 ns, a time much longer than the laser pulse (0.6 ns), but consistent with *[134]* and other results *[41]*.

c. Estimation of Shock Wave Pressure

To estimate the shock wave pressure generated by the plasma formation and expansion on the surface, it is necessary to consider the empirical equation given by Fabbro et al. *[55]* and Phipps et al. *[59]* for the C-H type materials, as described previously in Eqn. (2-9):

$$P = \frac{0.786\, I^{0.7}}{t\, \lambda^{0.3}\, \tau^{0.85}} \qquad (2\text{-}9)$$

Here the P, I, t, λ, and τ are, respectively, the shock pressure (GPa), the laser power density (GW/cm^2), the pressure duration (ns), the wavelength (μm), and the pulse duration (ns). Since the coating used in this study is a carbon-rich material, the above equation may be safe to use for the shock pressure estimation. Knowing the laser parameters that were used in this study, as listed below,

Laser power density (at 3-mm diameter, 100 J), (GW/cm^2)	$I = 2.4 \times 10^3$
Pressure duration from *[134]*, (ns)	$t = 150$
Wavelength, (μm)	$\lambda = 1.054$
Pulse duration, (ns)	$\tau = 0.6$

the surface shock pressure is then calculated to be 1.85 GPa. This value is very close to the measured pressure (~2 GPa) in *[134]* and is comparable to values from other LSP studies. Consider the work by Fabbro et al. *[55]* at the same laser wavelength, pulse duration, and power density (2×10^3 GW/cm^2). The pressure value is extrapolated to be about 4 GPa for the confined plasma configuration. Since it is not feasible to achieve much higher pressure with the confined plasma configuration because of the overlay breakdown problem, the extrapolated pressure may also be used for the unconfined plasma case such as the one in this study. Therefore, the calculated pressure in this study is the same magnitude as other pressure measurement results.

For the shear stress calculation, taking this pressure value into Eqn. (2-17) *[77]*,

$$\tau_{max} = \frac{3(1 - 2\nu)}{2(1 + \nu)} P \qquad (2\text{-}17)$$

a maximum shear stress is less than 1 GPa for LSP. Since the maximum shear stress calculated for the shot peening is above 8 GPa (see details in Appendix B), the shear stress produced by LSP is about one magnitude lower than that by the shot peeing. Such stress difference can also be seen from the surface profiles of both specimens shown in Figures 4-11b and e; the shot peening produced relatively deeper indentations than those of LSP, indicating the former generated more stress than the latter. This significant stress difference plays an important role in explaining some distinct microstructure generated by LSP and shot peening.

5.2 Laser Shock Processing Effects

In this section, the LSP effects on the microstructure of both steels are discussed along with results from the shot peened and cold rolled specimens. For the effects on mechanical properties, strengthening mechanisms for both steels are addressed. A model that is used from studies is discussed for effects of LSP and shot peening on the near and sub-surface residual stresses.

5.2.1. Effects on Microstructure

Since the two steels exhibited distinct processing effects on the microstructure, this discussion section is segmented into two sections. For the low carbon steel, it is found that the strain rate of deformation plays an important role in altering the microstructure, whereas for the Hadfield steel the microstructure is seen as a function of applied stress magnitude. For both cases, results from the explosive shock studies and conventional deformation processing studies are compared.

a. Low Carbon Steel

LSP Effects

From the surface indentation results measured on the LSP specimens, it indicates that the shock-induced plastic deformation has occurred. The surface has been recessed by about 1.5 μm due to this plastic deformation. The dislocation etch pits were found in SEM and high density dislocation microstructure was observed in TEM micrographs. These are in agreement with the surface profile results qualitatively. Neither ε-hcp phase nor deformation twins was observed in this study, which is consistent with the calculated pressure results.

In this study, observation of neither twins nor ε-hcp phase in LSP specimens is believed to be mainly due to the relatively low shock pressure achieved (<2 GPa). For the twins to form it is required critical resolved shear stress. In other LSP studies at different levels of shock pressure, twinning was found in iron and iron-based alloys, but no study reported on the formation of ε-hcp phase. The LSP study on pure iron (99.95% pure) by Cottet and Romain *[72]* at 10^{14} W/cm^2 power density and 3.5 ns pulse showed the extensive formation of deformation twins under an indented crater up to 870 μm deep based on optical metallographic observations. Although no other supporting evidence was presented, ε-hcp phase may be present, because the shock pressure in that study was derived to be approximately 800 GPa *[72]* and was far above the pressure threshold (13 to 16 GPa) for the ε-hcp phase to form, as reported in explosive shock studies *[90-92]*. Yet, due to such high shock pressure, a considerable amount of twins was formed and this is qualitatively consistent with the results from explosive studies on iron *[74, 101]*. Further, twin formation was observed in Fe-3 wt.% Si alloys at relatively low shock pressure (0.9 GPa) in a study by Clauer et al. *[4]*. The power density used was between 10^8 to 10^9 W/cm^2. Observed twin formation at such low shock pressure is believed to be attributed to

the addition of silicon. It is known that the addition of silicon to iron causes twinning to be more prominent during deformation *[143]*.

Comparisons with Conventional Deformation and Other Shock Processing

In addition to the shock pressure, the strain rate of deformation has to be considered when evaluating the shock-induced microstructural changes. Since the pressure duration measured from *[134]* is about 150 ns, the strain rate is expected to be higher than 10^6 sec^{-1}. Twinning in iron is reported to form more readily as the strain rate is increased *[143]*. For example, the pure iron will deform at 4K by twinning in a tensile test [decreasing temperature is equivalent to increasing strain rate] and deformation by impact at room temperature will also cause twinning. Although this study has achieved a high strain rate, the shock pressure may not be sufficient to induce the twinning.

Another effect that needs to be considered is the pulse duration. It has been found in AISI 1008 carbon steel *[120]*, AISI 304 stainless steel *[119]* and Hadfield steel *[86]* that the explosive deformation induced twins are pulse duration dependent. For the stainless steel the twin density increased during the 0.5 - 2 μs range and beyond 2 μs the twin density became constant, while for the Hadfield steel twinning was observed only above a 0.065 μs pulse. For the 1008 carbon steel, the twin density increased with the pulse duration from 0.5 to 1.0 μs. Thus, it is tentatively proposed that there should be a threshold time for twin formation in this low carbon steel and in this study the 0.15 μs pressure pulse *[134]* may be below such required threshold time.

In regard to the dense dislocation structure observed in this steel after LSP, discussion and comparison will be made with results from the explosive shock studies by Leslie et al. *[144, 145]*, as there is no available TEM results on the similar steel from other LSP studies. In the study by Leslie et al., the iron specimen was shock-loaded at room temperature to 7 GPa for an unspecified pulse duration. The dislocation microstructure was characterized by arrays of straight and parallel screws dislocations in the grains. No twins were reported by Leslie *[144, 145]* at this pressure (7 GPa), which is consistent with this study for the LSP specimen.

A similar straight, parallel dislocation structure was also observed in iron rolled to 2% reduction at 77K *[144, 145]*. In bcc metals, the shock-loaded substructures tend to resemble the low-temperature substructures generated by conventional low strain rate deformation *[73, 100, 144, 145]*. Under deformation at high strain rates or at low temperatures, the edge components of dislocations can move at higher rates than the screw components, and these screw components are unable to cross-slip, resulting in elongated segments of the latter in the structure *[73, 100]*. Because of this lack of cross-slip, it is not possible to see the cell structure which is common to conventionally deformed iron at low strain rates *[144, 146]*. In this study, the dislocation cell substructures are seen to be developed in both shot peened and cold rolled low carbon steel specimens. This cell substructure with high dislocation densities is a pronounced microstructural example of α-bcc irons deformed at low strain rates *[144, 146]*.

The high dislocation density structures that were frequently observed in this study [refer to Figure 4-25] have not been reported elsewhere in explosively shock-loaded studies of the similar material. Yet, explosively shock loaded molybdenum (which is a bcc structure) at 15 GPa for 2 μs exhibited a similar dislocation microstructure *[147]*. In that study, the density of dislocations was approximately $1 \times 10^{10}/cm^2$ which is about an order of magnitude lower than that of this study ($2.6 \times 10^{11}/cm^2$). Since there is no noticeable formation of cell structure in this study, the dislocations generated by LSP are not expected to cross-slip or move some distance for such cell substructure formation. Also, lack of cell substructure formation indicates that both edge and screw components of dislocations remain in the structure. Therefore, it is tentatively

suggested that LSP deformation was made rather fast and insufficient time was available for events such as dislocation cross-slipping and long-range movements of dislocations. Conclusively, the strain rate dependence of microstructure is found in this low carbon steel where the high strain rate LSP deformation generates mostly tangled high density dislocations and the conventional low strain rate deformations of shot peening and cold rolling in this study produced dislocation cell substructures.

b. Hadfield Steel

For the Hadfield steel specimens, distinctly different microstructure is produced after LSP, shot peening and cold rolling. Since various microstructures were also reported elsewhere when the Hadfield steel was deformed, the microstructural observations obtained from this study are discussed and compared with those from other explosive shock and conventional deformation studies. An explanation is proposed for the formation of ε-hcp martensite in LSP specimens.

LSP Effects

For the LSP specimens, the results from SEM and TEM micrographs and X-rays diffraction patterns consistently showed the extensive formation of ε-hcp martensite. The diffraction patterns obtained from X-ray and TEM confirmed the presence of the ε-hcp martensite phase in the LSP, shot peened and cold rolled specimens. The calculated lattice parameters are a = 3.61 Å for γ-fcc austenite matrix and a = 2.55 Å and c = 4.10 Å for ε-hcp martensite, in agreement with early results *[111, 113, 130]*. Crystallographically, the LSP-induced ε-hcp martensite phase has been shown to be identical to that in Hadfield steel *[105, 112-114, 118, 148]*, as well as to that in austenitic stainless steels induced by deformation *[149-151]* and by hydrogen *[152]*. The evidence of faults within the ε-hcp martensite plates, together with the apparent randomness of matrix dislocations bounded by the existing faults, indicates that the overlapping stacking fault mechanism for the fcc to hcp transformation is irregular, in agreement with a detailed study of deformation-induced ε-hcp martensite in austenitic stainless steel *[153]*.

Comparisons with Conventional Deformation

Observation of slip line surface markings, as seen in SEM micrographs of Figures 4-21 and 4-22, is one of the few evidences among deformation studies of Hadfield steels showing formation of ε-hcp martensite. Although such slip line surface markings and surface relieves have been reported in steels of similar composition that are conventionally deformed at low temperatures, it has never been confirmed as ε-hcp martensite, instead most of the features observed were interpreted as deformation twins. For Hadfield steels, which have compositions in a range of 11 - 13% Mn and 1 - 1.4% C, conventional deformation studies by Doepken *[103]* at 77K, Adler *[107]* at 173K, Dastur and Leslie *[106]* at 223K, and Zuidema et al. *[108]* at 297K, showed the surface slip line markings all resulted from deformation twins, since most of them found no ε-hcp martensite phase in X-ray or TEM observations. Only the study by Ottet *[104]* at 4K explained the surface slip lines as possible stacking faults because streaks due to the stacking faults were observed on the X-ray photograph obtained from a specimen deformed 5.7% by hammering at 4K and no streaks were found when the specimen was compressively deformed to fracture at 77K. Deformation by hammering at room temperature is also shown to generate the ε-hcp martensite for the similar composition of Hadfield steels, as indicated in the TEM studies by Nishiyama *[112]* and Roberts *[105]*; the former used TEM to prove the surface markings as martensite, but the latter found twins as the major product phase. Further, this kind of surface feature was also reported in specimens deformed 10% in tension at room temperature

by Collette et al. *[130]*. Using X-ray and replica TEM, the evidences of stacking faults, ε-hcp martensite, and α'-bcc martensite were found.

Moreover, the results from several studies *[110, 111, 148, 154, 155]* indicate that composition plays a role in alteration of microstructure: typically, the high manganese (>15%) and low carbon (<0.06%) steel will result in a greater tendency for the formation of ε-hcp martensite upon deformation at room temperature. In fact, not only composition but also temperature affects the deformation-induced microstructure in the Hadfield steel. This is because the austenitic stacking fault energy (SFE) decreases with decreasing temperature or decreasing carbon content, but the reverse is true for increasing Mn content *[155-157]*. Such a reduced SFE promotes the generation of widely extended and densely populated faults which are then favorable for the formation of ε-hcp martensite *[153]*. Therefore, when the manganese steel is strained, the ε-hcp martensite is likely to form either at low temperatures or at high temperatures through modifying its composition. Likewise, with the normal Hadfield steel composition (10 - 14% Mn and 1.0 - 1.4% C) *[106]*, the deformation twins are predominant when the deformation is made at room temperature or higher.

In Figure 5-5, the deformation-induced microstructures that have been observed by a number of studies are summarized as a function of the austenite SFE. A similar deformation structure as a function of SFE and temperature is also suggested in the Fe-Mn-Cr-C system by Remy and Pineau *[158]*. In this figure, the SFE for each study is estimated based on the composition and temperature of steel used, according to the relationship given by *[157]*. It is seen that as the SFE increases the induced phase changes from α'-bcc to ε-hcp martensite and twins. The transition from α'-bcc to ε-hcp martensite may be explained by a kinetics model described by Holden et al. *[110]*, in which the applied stress for $\gamma \rightarrow \alpha'$ is somewhat lower than that required for the $\gamma \rightarrow \varepsilon$ when the austenite SFE approaches zero. The transition from ε-hcp martensite to twins is not as clearly defined, simply because the twins form in a large range of SFE. However, the twins are shown to be the only microstructural product found at higher SFE's ($\geq$50 erg/cm^2).

In this study, the Hadfield steel (13.83% Mn and 0.97% C) used has about 45 erg/cm^2 stacking fault energy at room temperature, according to *[157]*. Thus, both the ε-hcp martensite and twins may form when the specimen is deformed at room temperature, as indicated by Figure 5-5. However, the question remains: why did the LSP generate ε-hcp martensite, shot peening produce deformation twins and ε-hcp martensite and, yet, cold rolling resulted in ε-hcp martensite? As suggested in some TEM studies by Nishiyama et al. *[112, 113]* and Raghavan et al. *[114]*, the applied deformation stress might have a great influence on the type of microstructure formed. Using the TEM, Raghavan et al. *[114]* found in Hadfield steel (12.5% Mn and 1.13% C) that by bending the specimen back and forth at a small applied stress numerous individual stacking faults were induced. With increased stress, widely dissociated dislocations and lath-like twins were found in the lightly compressed (10%) specimen and the neighboring twins were connected by the stacking faults. As the compressive stress increased to produce 57% strain, the observed stacking faults thickened into twin lamellae which in turn subdivided the austenite matrix into smaller domains *[114]*. For comparable steel compositions, similar stress-dependent microstructure was found in other studies by Nishiyama et al. *[112, 113]* and Roberts *[105]*. The studies by Nishiyama et al. *[112, 113]* showed that applied stress by hammering induced ε-hcp martensite, while cold rolling to 30% reduction produced both ε-hcp martensite and twins. Roberts *[105]* revealed that hammering caused more twinning than ε-hcp martensite in the specimen. Further, only dislocations and twins were found in the specimens deformed by 2% and 20%, respectively, in tension *[105]*.

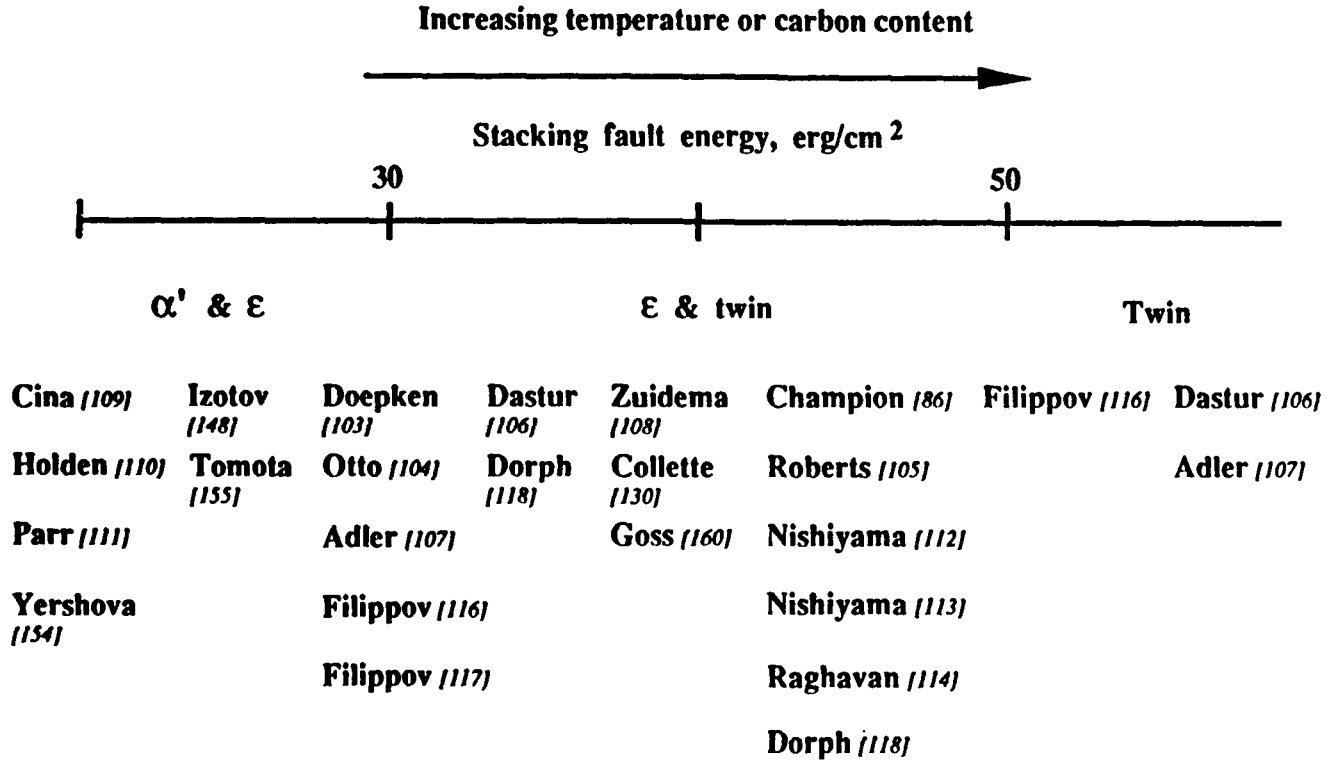

Figure 5-5 A summary of deformation-induced microstructure observed in Hadfield steel.

Since microscopic slip appears to be a prerequisite for the nucleation of twins *[159]*, it is not surprising that the critical resolved shear stress (CRSS) values for twinning reported in the literature for Hadfield steel shows such a large scatter. In general, however, the overall deformation stress dependence of microstructure is held in this steel composition (~12% Mn and ~1% C). To examine this dependence in detail, Figure 5-6 schematically illustrates the applied stress for the formation of the α'-bcc, ε-hcp martensites, and twinning as a function of SFE. Since the CRSS for twinning is interpreted as having a linear relationship with SFE in the Fe-Mn-Cr-C system *[158]*, it is reasonable to expect the applied stress for twinning to behave linearly with SFE. The applied stress for α'-bcc martensite is extrapolated from *[110]*. As seen in this figure, the SFE used in this study is favorable for the formation of ε-hcp martensite when the applied

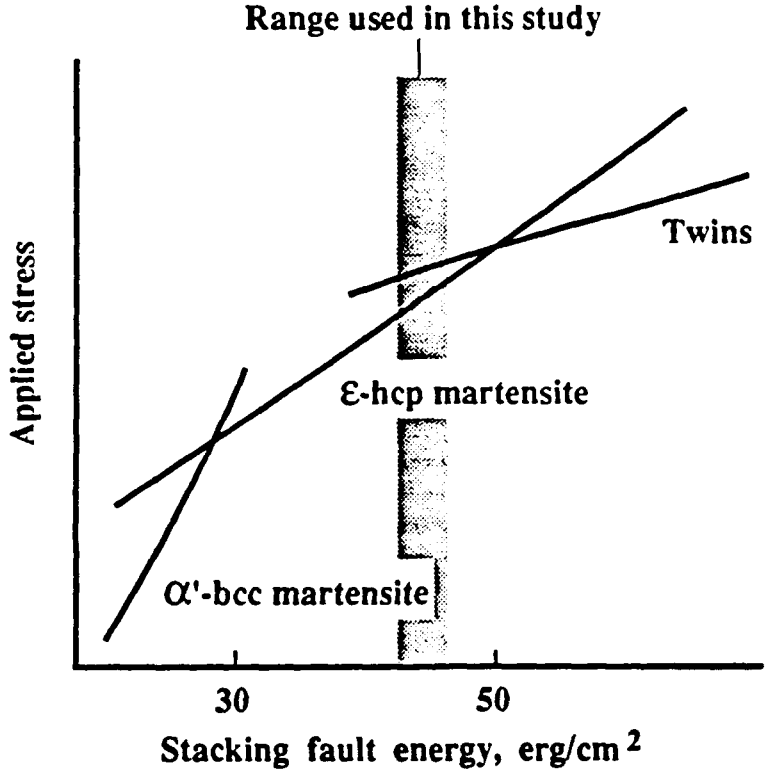

Figure 5-6 A summary of deformation-induced microstructure observed in Hadfield steel.

stress is not high enough for twinning to form. This is the case for LSP in this study. With applied stress higher than the CRSS for twinning, the specimen is then favorable for the formation of twins. This is the case for the shot peening in this study. As a proof of the above postulate, the same situation should also be applied for the low SFE (<30 erg/cm^2) manganese steels where the ε-hcp martensite is likely to form when a stress is applied; see Figure 5-6. Indeed, this has been demonstrated by several previous studies *[110, 111, 148, 154, 155]*.

In this study, the TEM and X-ray results of the LSP and shot peened specimens are qualitatively in good agreement with the mentioned stress dependence of microstructure. As mentioned before, the shear stress produced by LSP is about one magnitude lower than that by the shot peening. Thus, according to the postulate in Figure 5-6, it is expected that shot peening has a greater possibility to generate twins than does LSP.

Nevertheless, in the cold rolling process the TEM and X-ray results showed that almost complete transformation to ε-hcp martensite, which seems contrary to the mentioned stress dependence of microstructure. Yet, this feature may stem from severe deformation caused by cold rolling that induced the ε-hcp martensite from the twins formed early in the rolling. This can be seen from the fact that the interspacing of ε-hcp martensite in rolled specimens and that of twins in peened specimen are almost the same (200 - 300 nm), as seen in TEM micrographs of Figures 4-35 and 37. Further, the ε-hcp martensite has a relatively compact atom stacking that may accommodate the severe deformation caused by rolling. While the mechanism of this twin to ε-hcp martensite transformation is not well understood, in literature there are some similar findings. As an example, in the low SFE manganese steels (i.e., >15% Mn and <0.06% C of composition), upon cold rolling, several studies have observed different extents of increase in ε-hcp martensite volume fraction *[110, 111, 148, 154, 155]*. For instance, Gordon Parr *[111]* found ε-hcp martensite increased from 55 to 80 vol.%, while Yershova et al. *[154]* observed a volume increase from 33 to 80% after cold rolling. In fact, for steel compositions comparable to that of this study, there is an early study by Goss *[160]* that showed some features similar to the X-ray result in Figure 4-41. The Hadfield steel used in that study contained 14.0% Mn and 1.3% C and was cold rolled to 87% in reduction (the reduction was 51% in this study). After cold rolling, X-ray diffraction photographs showed that the γ-(200) line was missing and a line near γ-(111) position became broadened, though Goss claimed this line was still γ-(111) *[160]*. With closer examination, such a broadened line should be indexed as ε-(0002) since it was overlapping with the γ-(111) and appeared in relatively strong intensity due to preferred orientation, same as that shown in Figure 4-41. Hence, Goss revealed X-ray results qualitatively in good accordance with those of this study for the cold rolled Hadfield steel specimen; that is line broadening of ε-(0002) and disappearance of γ-(111) and (200).

Comparisons with Other Shock Processing

As compared with conventional explosive shock studies on the Hadfield steel, results from this study showed some similarity as well as contradiction. In an early work by Holtzman and Cowan *[115]* on Hadfield steel with 13.7% Mn and 1.2% C, shock pressure at 7 GPa was found to induce surface slip line markings similar to those observed in this study. Since this pressure also generated a noticeable strengthening in hardness and tensile strength, they suspected the surface markings to be due to structural changes and such changes that were not accessible to their optical microscope technique might have accompanied the shock deformation. For a comparable steel composition (12.5% Mn and 1% C) to this study, Champion and Rohde *[86]* and Roberts *[105]*, using TEM, observed twins and dislocations at shock pressures ranging from 2 to 39.5 GPa, while the latter found the threshold pressure pulses for twinning were

between 2.2 μs and 65 ns. Numerous deformation twins have developed for the longer pulse (2.2 μs) and no twins were found in the shorter pulse (65 ns). In this study, the shock pressure pulse was estimated to be at most 150 ns *[134]*, which is between the threshold time range. However, while the pressure pulse may play a role in the formation of twins, the pressure magnitude is believed to be more important, since the formation of twins is a diffusionless process and the formation is commenced as soon as a sufficient external stress is applied.

In fact, a TEM study by Dorph *[118]* demonstrated the principle of Figure 5-6 on an explosively shock loaded Hadfield steel (13% Mn and 1% C). In that work, an unspecified shock pressure produced dense dislocations and twins at the top surface of the specimen, whereas at the bottom (2 cm away from the top) ε-hcp martensite was found to be the major microstructural product. These two different types of microstructure can be explained qualitatively according to the proposed stress dependence of microstructure and Figure 5-6. That is, the top surface received a much higher pressure than the bottom. Hence, twin formation was more favorable to form on the top than the bottom and the reverse was true for the ε-hcp martensite. This is consistent with the results of this study. In addition, Dorph *[118]* observed the ε-hcp martensite phase on the top surface of a low carbon content (0.5%) specimen that was shocked at a pressure assumed to be the same as the 1% carbon specimen. This is also in full agreement with the proposed stress dependence model; i.e., the SFE is lowered due to a decrease in carbon content and a difference in the applied stresses for twinning and ε-hcp martensite is thus increased; see Figure 5-6. Thus, the twins need more applied stress to form, as compared to that of previous high carbon (1.0%) content specimen. In other works by Filippov et al. *[116, 117]*, X-ray phase analysis results showed explosively shock-induced formation of ε-hcp martensite on low carbon (0.4%) Hadfield steel, also confirming the above postulate. Therefore, the proposed stress dependent microstructure model is valid for the explosively shocked Hadfield steel.

As a comparison with other fcc metals, a work by Murr *[75]* is considered in which deformation-induced microstructures of brass, 304 stainless steel, Inconel nickel alloys, copper, and nickel were studied at different shock pressures. In that work, critical twinning pressure was found to be a linearly increasing function of metal stacking fault energy. This linear relationship between the twinning pressure and stacking fault energy for several metals *[75]* is similar to that of Figure 5-6 for the Hadfield steel. According to this relationship *[75]*, the Hadfield steel used in this study (SFE ~45 erg/cm^2) will have stacking fault microstructure at pressures below 10 to 20 GPa, whereas the twins and stacking faults are dominant above these pressures. This is in good agreement with results of this study.

5.2.2. Effects on Mechanical Properties

In this section, a plastic deformation anomaly due to LSP is discussed. The LSP effects on mechanical properties of both steels are addressed and compared with results from other studies. To understand the relationship between microstructure and mechanical properties after processing, the existing strengthening mechanisms are used and evaluated in light of the results found in this study.

a. Plastic Deformation Anomaly

Under the same LSP conditions, different extents of indentations on the Hadfield steel and low carbon steel are noticed in the surface profilometry results; see Figures 4-10 and 4-11. Although a difference is expected since the two steels have different mechanical properties (such as yield strength and work hardening), a plastic deformation anomaly is seen. While the static deformation mode is different from the dynamic deformation mode, it is instructive to see stress-

strain curves of Figure 5-7 for both steels *[161]*. Because the low carbon steel has a lower yield strength and smaller work hardening rate as compared with those of the Hadfield steel, it is expected, under the same LSP conditions, that the former should be plastically yielded more than the latter. However, the reverse situation is found; the measured surface indentation for the low carbon steel is about 1.5 μm deep and that for the Hadfield steel is 3 μm at laser energies between 100 to 110 J, as depicted in Figures 4-10 and 4-11.

This plastic deformation anomaly is believed to be related to the LSP-induced phase transformation occurring in the Hadfield steel. In an early work by Bogachev et al. *[162]*, this plastic deformation anomaly was observed in a series of Mn-Cr and Mn-Ni austenitic steels that were treated by an explosive shock loading. They found that when considerable α'-bcc martensite was formed during shock loading the dynamic plastic deformation increased to 27% from 9% of that deformed by the conventional tensile testing. The volume fraction of martensite was about 50% for the shock loading steel, and that of tensile tested steel was 12%. In contrast, when the steels did not undergo phase transformation, the extent of plastic deformation was not increased upon shock loading. Therefore, under the high strain-rate deformation, the martensite phase transformation in the material somewhat improves the ductility. Cause of such ductility improvement may be attributed to the stress relaxation that is associated with the phase transformation induced by the high strain-rate deformation *[162]*. However, a fundamental understanding of this ductility improvement is not well established.

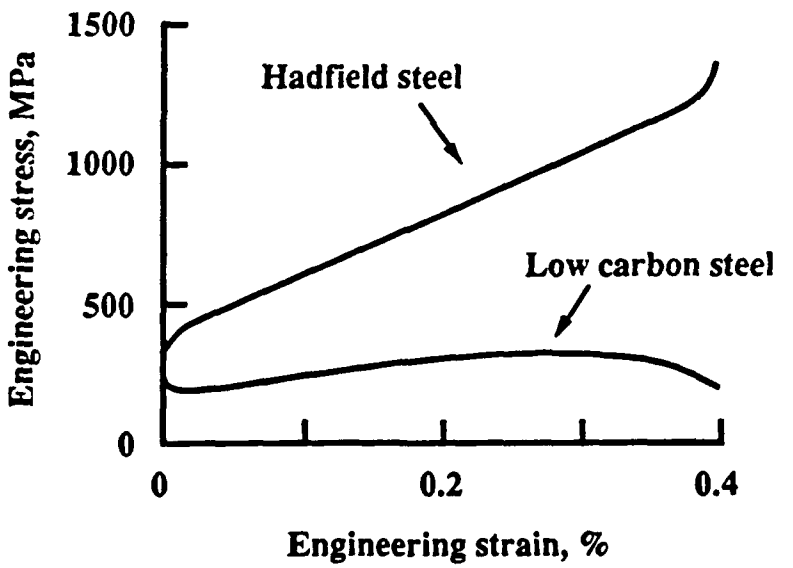

Figure 5-7 Stress strain curves of low carbon and Hadfield steels *[161]*.

b. Residual Stress

Surface Melting

In the case when no energy-absorbing coating was used during LSP, the specimen surface melting were found and surface tensile residual stresses were measured; see Figure 4-44. Similar surface tensile residual stresses were also reported in other laser processing-related studies, such as Fournier's study on LSP nickel-based alloys *[13]* and Speck et al. on the laser heated graphite *[140]*. These tensile residual stresses are formed as a direct result of surface melting and solidification during LSP. As seen in a schematic of Figure 5-8 *[140]*, the melting on the surface, due to laser heating, produces a volume expansion of melt pool. However, the substrate outside the irradiated area acts as a rigid barrier to thermal expansion of the melt pool. After the laser is off, the melt pool subsequently solidifies and a thermal contraction is formed due to its volume shrinkage. Such thermal contraction generates a tensile stress resulting from the constraint of its surrounding rigid regions. As a result, a surface tensile residual stress is produced on the solidified LSP bare surface. The formation of this type of residual stress is very similar to that due to thermal shock by rapid heating and quenching of bulk material *[163]*.

No Surface Melting

For the unmelted LSP coated surface, both the low carbon and Hadfield steels showed compressive residual stresses; see Figures 4-45 and 4-46. These compressive residual stresses are indicative of shock pressure exerted on the specimen surface during LSP. Such compressive residual stresses are in agreement with the surface indentation results, TEM and SEM microstructure observations, that resulted from the compression of the specimens and generation of the defects such as dislocations. In other LSP studies, the compressive residual stresses are widely reported since these are the most significant contribution to the improvement of fatigue properties *[7-10, 13, 14, 70]*.

In regard to stress magnitude, the shot peened surfaces exhibited stresses much higher than those of LSP surfaces for both steels; see Figures 4-45 and 4-46. This is attributed to the greater applied stress relative to LSP. As indicated by Cullity *[164]* these high compressive stresses may also result from false interpretation of X-ray diffraction reading from surface roughness. High points of rough surface are not stressed in the same manner as the bulk material is, but these points contribute to most of the diffraction pattern. This is particularly evident when the specimen is tilted at high angle for the stress measurement *[164]*. Nevertheless, the overall residual stress magnitudes measured on the peened specimens are believed higher than those of LSP specimens. This interpretation is consistent with the fact that shot peened specimens have applied stresses greater than LSP.

For the compressive residual stresses presented by other LSP studies *[8, 10, 13, 70, 72]*, the shapes of in-depth stress profiles are similar to those of Figures 4-45 and 4-46. The depth of stress is different because of different applied shock pressures. For the LSP Hadfield steel, the compressive stress was small at the surface, but it reached a maximum in some sections of subsurface (50 μm of depth) before it gradually decreased with depth. For the low carbon steel the stress monotonically decreased with depth. To understand the presence of a stress peak under the LSP surface for Hadfield steel it is necessary to correlate the X-ray in-depth phase analysis results of Figure 4-43. The ε-hcp martensite in the Hadfield steel has more compact stacking of atom layers than that for γ-fcc austenite since the d-spacing of ε-(0002) is smaller than that of γ-(111). The LSP surface consisted of two competitive stresses: the tensile stress due to the extensive formation of ε-hcp martensite and the compressive stress due to the compressed lattice strain. The LSP surface contained 35 vol.% of ε-hcp martensite. Therefore the tensile stress at

this position is expected to be larger than at positions under the surface where the amount of ε-hcp martensite diminished, as indicated in the X-ray results of Figure 4-43. So, as the surface layer was removed, the tensile stress decreased and the compressive stress became dominant. Compressive stress eventually reached a peak value where the ε-hcp martensite was minimized. Under the LSP surface, a peak was not observed in the in-depth stress profile for the low carbon steel which did not undergo a phase transformation. The formation of ε-hcp martensite in the Hadfield steel plays a role in the stress distribution of LSP specimen. The stress in-depth measurement for the LSP Hadfield steel is in full agreement with X-ray phase analysis results; see Figures 4-43 and 4-46.

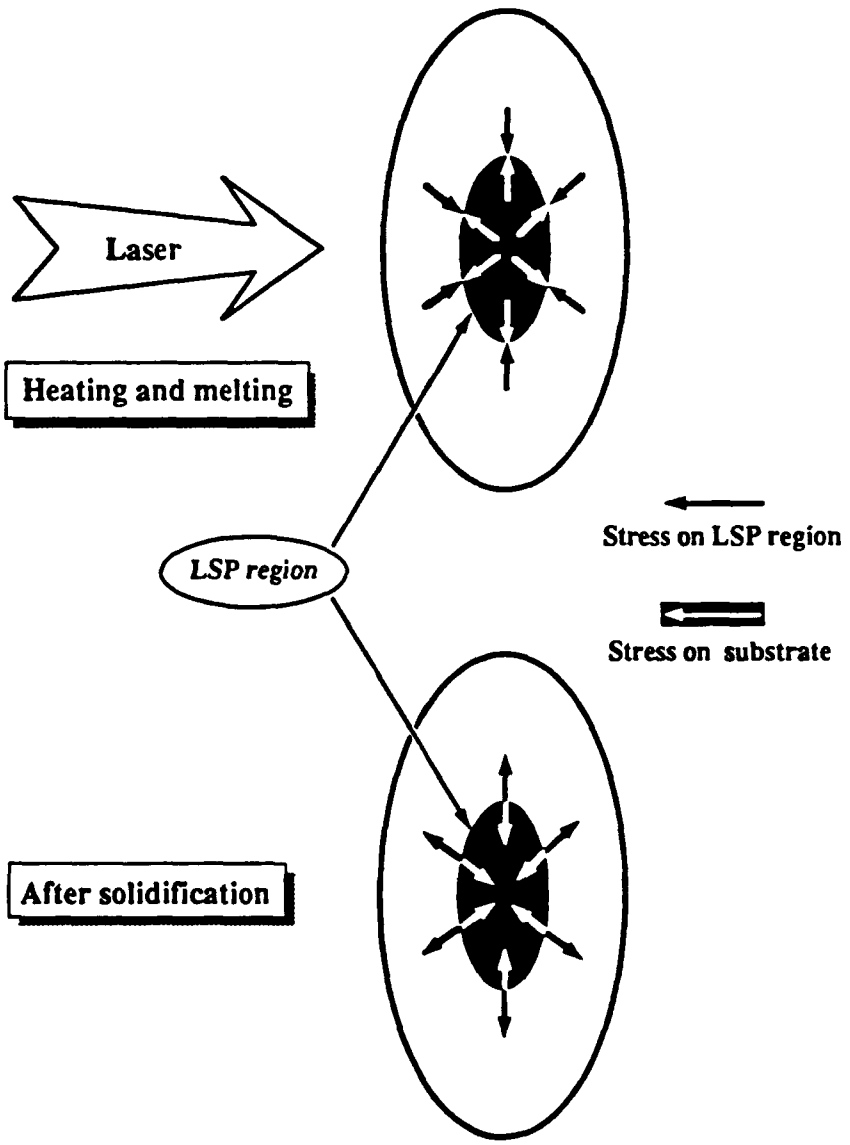

Figure 5-8 Formation of tensile residual stress on LSP specimen surface *[140]*.

For the shot peened specimens, both steels showed peak stress under the surface of the in-depth stress profiles; see Figures 4-45 and 4-46. This arises from the fact that peening-induced shear stress reached a maximum value below the surface. As described by Wohlfahrt *[165]*, the distribution of residual stress depends upon the direct plastic surface elongation in y-direction and the shear stress that is generated below the surface. In Figure 5-9 *[165]*, schematically illustrated are both effects on the stress in-depth distribution. The direct plastic elongation of surface layers is a consequence of tangential force applied to the surface. Such plastic elongation of surface layer results in the maximum lattice strain, and therefore maximum compressive residual stress at the surface, as seen in Figure 5-9a. This process is comparable to hammering of the surface. The stress situation generated by the LSP in this study is analogous to Figure 5-9a, resulting from the relatively flat LSP surface compared to the shot peening case.

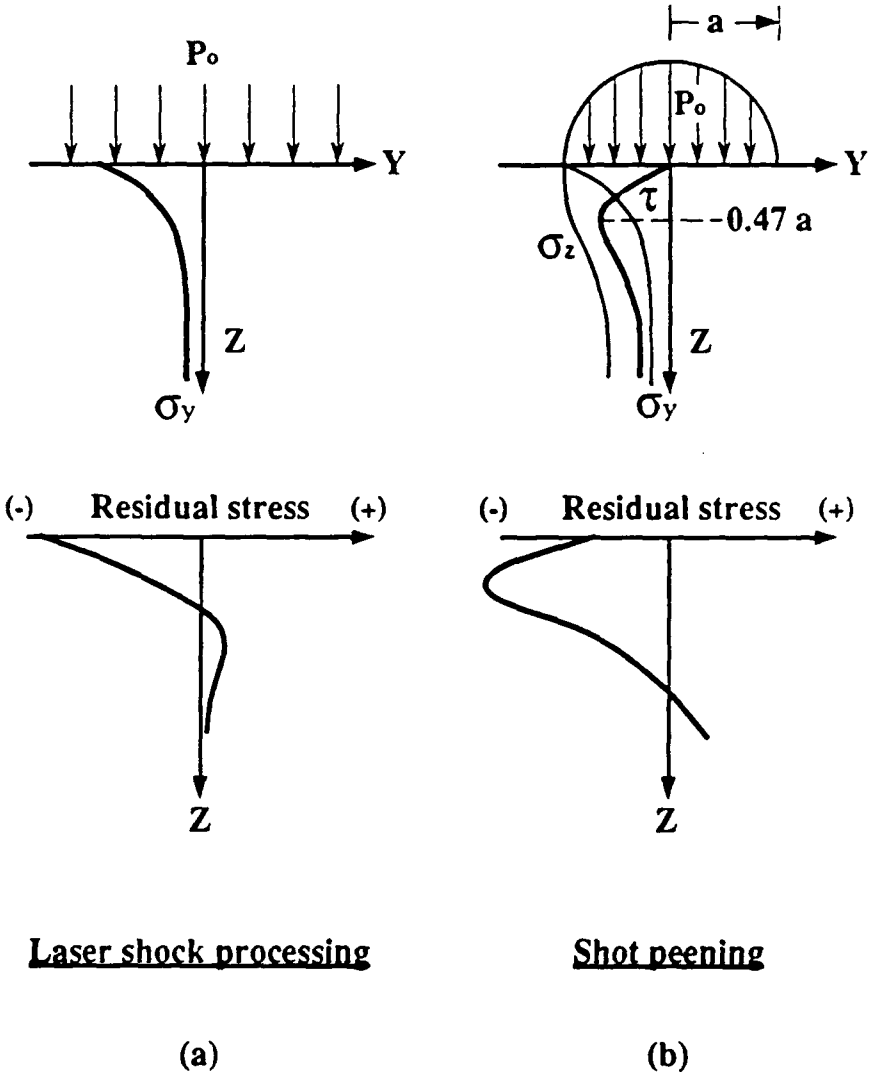

Figure 5-9 Schematic of residual stress in-depth profiles as a result of (a) LSP and (b) shot peening *[165]*.

For the shot peening, the residual stress generating process is mainly due to Hertzian pressure which is a consequence of vertical force, F, with the impact of each shot ball peen *[165]*. The Hertzian pressure statically acting on the indented surface is illustrated in Figure 5-9b. The figure shows that the on surface has maximum residual stresses along y- and z-directions. Stresses along y- and z- directions decrease in magnitude with depth, similar to that in Figure 5-9a. According to the theory of Hertz *[165]*, the shear stress also results and it has the maximum value at a distance, $Z_{\tau_{max}}$, below surface, which is

$$Z_{\tau_{max}} = 0.47\ a \tag{5.1}$$

where (a) is the radius of contact zone. If the Hertzian pressure becomes high enough, the maximum shear stress can exceed the flow stress at the depth of 0.47a, resulting in a peak compressive residual stress at this depth. Furthermore, Wohlfahrt *[165]* calculated the depth of maximum shear stress by assuming that the depth of contact zone, h, is nearly equal to the measured surface roughness:

$$a = \sqrt{2hr - h^2} \tag{5.2}$$

where (r) is radius of the shot ball peen. With this approach, Wohlfahrt *[165]* was able to compare the calculated depth of maximum residual stress with the measured depth. It was concluded that the difference between these two is within the accuracy of measurement or at least within the order of magnitude. In fact, the $Z_{\tau_{max}}$ are 11 and 21 μm for the shot peened low carbon and Hadfield steels, respectively, as calculated in Appendix C. The calculated values are in agreement with the measured depths, as seen in Figures 4-45 and 4-46.

The LSP stress results are also consistent with the model described by Wohlfahrt *[165]*. The actual distribution of compressive residual stress resulted from the combined effect of direct plastic surface deformation and plastic deformation of deeper layers due to the Hertzian pressure. As shown by the relatively flat surface profiles (Figures 4-10 and 4-11), it is obvious that LSP generated a macroscopic deformation mode by stretching the surface layer. The shot peened rough surface indicates the Hertzian pressure-induced deformation was dominant. When the effect of ε-hcp martensite was considered in the Hadfield steel, the LSP specimens showed maximum compressive residual stress on the surface which then monotonically decreased with depth.

c. Microhardness

Low Carbon Steel

The microhardness results are in accordance with those of TEM microstructure analysis and X-ray phase analysis. For low carbon steel, the microstructure observed is that of dislocations at different densities after LSP, shot peening, and cold rolling. The cold rolled specimen had highest surface hardness and also showed the highest dislocation density. The LSP and shot peened specimens both had comparable dislocation densities and microhardness. It is reasonable to conclude that the processing-induced strengthening in the low carbon steel is due to the presence of dislocations. To quantitatively correlate the microhardness results with the observed microstructure, the calculated dislocation densities are used for the low carbon steel. According to an early work on an explosively shock loaded iron by Ganin et al. *[122]* and a cold rolled iron by *[166]*, the mechanical properties such as hardness and yield stress can be expressed in terms of the microstructure such as dislocation density and twin spacing. In this study, the dislocation substructure is the only feature observed in the low carbon steel for all

three types of processing. The measured microhardness value, H, should fit into the following equation:

$$H = H_0 + a G b \sqrt{\rho} \qquad (5\text{-}3)$$

where (ρ) is the average dislocation density, and (H_0), (a), (G), and (b) are the material's constants. H_0 is hardness in an ideal material without any defects, G the shear modulus, and b the scalar value of Burgers vector. As an approximation, the material's constants of H_0, a, G, and b are calculated based upon the results from the study by Ganin et al. *[122]*. In that study, the iron was explosively shock loaded at 17 GPa and Vickers hardness values were taken on the transverse section of shocked specimens. Although deformation twins were found in that study *[122]*, a relationship between hardness and dislocation density was obtained. The relationship holds since the twin spacing was a function of dislocation density. For this study, the empirical equation is comparable with that seen in *[122]* which describes the dislocation density and microhardness is

$$H = 145 + 2.1 \times 10^{-4} \sqrt{\rho} \qquad (5\text{-}4)$$

To verify this equation, dislocation densities calculated in the TEM micrographs are used. A comparison is listed in Table 5-1 for the calculated and measured surface hardness values. This table shows that the calculated values correlate with the measured data, within the experimental error, for all three processed specimens. While both the LSP and shot peened surface exhibited scattered hardness values, but the calculated data are seen reasonable and consistent with those quoted by Ganin et al. *[122]*. It is therefore concluded that the strengthening of low carbon steel is mainly due to the presence of high density dislocations. Although no dislocation density data is available for the subsurface hardness calculation of cold rolled specimen, an average 40% increase of hardness at center of rolled specimen (see Figure 4-48) is also reported in a study by Dieter *[121]*. The Vickers hardness data shown in Figure 2-9 is from his study for a cold rolled iron which are converted to Knoop hardness values. It is found that at an equivalent true strain (114%) produced by the cold rolling in 63% thickness reduction the hardness increase approximately 40%.

Hadfield Steel

For the processing-induced strengthening of Hadfield steel, the microstructure also contributes in a similar, but complex, fashion. The complexity arises from the variety of the processing-produced microstructure. The microstructure include dislocations, stacking faults, twins and ε-hcp martensite. The interaction among these is considered important for strengthening effects. The surface hardness increase is given as 50-130% for the LSP specimens, 40-60% for the shot peened specimen, and about 60% for the cold rolled specimen. Strengthening results from the combination effects of dislocation and ε-hcp martensite for the highest hardness found in the LSP specimen. Strengthening is a result of ε-hcp martensite and twin with dislocations effects, respectively, for the cold rolled and shot peened specimens.

As seen in the TEM micrograph of Figure 4-30a, presence of widely separated partial dislocations bounded with the stacking fault is seen for the LSP specimens. Such widely dissociated dislocations are of importance in many aspects of plastic deformation. An increase in strength results from the difficulty of dissociated dislocation cross slip under the applied stress. Furthermore, with the wide separation by the stacking fault, the dislocations have a difficulty in intersecting each other, giving rise to one source of work-hardening *[167]*. This dislocation intersecting process and subsequent crossing of stacking faults lead to a complex fault in the plane of intersection. Such an intersecting process leads to a decrease in the dislocation mobility

under an applied stress *[167, 168]*. Further, there is a possible solid solution effect arising from the diffusion of carbon atoms to interact and "lock" the stacking faults from moving -- namely Suzuki effect as described in *[169, 170]*. While this Suzuki effect is not a long-range interaction, it may present a barrier to the motion of dissociated dislocations *[170]*. In addition to these strengthening mechanisms, for the LSP specimens, the LSP-induced ε-hcp martensite also contribute a strengthening effect in the LSP specimens. This strengthening effect is a different mechanism, as will be discussed in the following section. For the LSP specimens the strengthening is the combined effects of slow dislocation mobility, complex interaction of stacking faults, locking of stacking faults by the solute atoms, and the presence of ε-hcp martensite.

Table 5-1 Comparison of measured and calculated hardnesses for low carbon steel.

Processing	Surface dislocation density, cm^{-2}, ρ	Surface Knoop hardness number	
		Calculated*	Measured
Cold rolling§	$>1x10^{12}$	>355	339
Shot peening#	$\sim 2x10^{11}$	~239	230-270
LSP‡	$2\text{-}6x10^{11}$	239-308	243-303
As-annealed	$\sim 1x10^{10}$@	166	178

§ The specimen was cold rolled to 63% reduction in thickness.

The shot peening was done on 100% surface coverage.

‡ The specimen was black paint coated for the LSP and treated with energy at 111 J.

* Calculations are based on the equation: $H = 145 + 2.1x10^{-4}\sqrt{\rho}$.

@ As-annealed dislocation density was measured in this study and is comparable with that found by Ganin et al *[122]*.

Widely dissociated dislocations were not observed in the shot peened and cold rolled specimens. Instead, microstructure in these two specimens were high density dislocation substructures. In addition to the high density dislocation effect, the strengthening is also due to subdivision of the matrix grains by the twins in the shot peened specimen and by the ε-hcp martensite in the cold rolled specimen. The subdivided grains in these specimens increased the number of boundaries and therefore increased barriers to the dislocation movements. When

considering both the dislocations and grain-subdividing effects, the material hardness, H, is described by the Eqn. (2-18) given previously *[122]*;

$$H = H_o + \frac{k}{\sqrt{\Lambda}} + a\,G\,b\sqrt{\rho} \qquad (2\text{-}18)$$

where (Λ) is the average inter-spacing of twin or ε-hcp martensite, (ρ) is the average dislocation density, and (H_o), (a), (G), and (b) are the material's constants. H_o is hardness in an ideal material without any defects, G the shear modulus, and b the scalar value of Burgers vector. The "locking parameter", k, measures the relative hardness contribution of the subdivision of grain "boundaries" by the twins and ε-hcp martensite *[171]*. This k value may be different for the twin and ε-hcp martensite. Thus, the second term is a contribution from the twins and/or ε-hcp martensite, while the third term results from the dislocation effect. TEM micrographs of Figures 4-35 to 4-38 show the lath-like twins and ε-hcp martensite which have approximately the same inter-spacing 200 to 300 nm. The dislocation density is not accessible for the comparison purposes since they can not be resolved. Therefore, to evaluate the above postulate, other explosive shock results for the same material are compared.

In a work by Roberts *[105]*, an explosively shock loaded Hadfield steel at 43 GPa showed a hardness increase comparable with that of a specimen deformed by hammering,. The former consisted only of twins and the latter had both the twin and ε-hcp martensite. This implies the k values in Eqn. (2-18) are about the same, or at least in the same order of magnitude, for the twin and ε-hcp martensite assuming the dislocation densities are about the same. Qualitatively, this is consistent with this study's results; the spacing of twin in shot peened and that of the ε-hcp martensite in cold rolled specimens were about 200 to 300 nm and the hardnesses of these specimens were approximately the same. Roberts *[105]* also found the twins in a specimen deformed in tension by 30% elongation. However, this specimen had a twin spacing 200 nm (it was about 50 nm for the shocked specimen), and its hardness was not as high as those of shock loaded and hammered specimens -- only about two thirds of those values. This result follows the trend of the above equation, in which the finer twin spacing results in higher strengthening effects, provided the dislocation contribution is constant. Roberts *[105]* concluded the presence of dislocations contributes the most to the strengthening mechanism relative to twin or ε-hcp martensite alone. This is because the latter does not significantly improve the material hardness *[105]*. This view is later supported by studies of Champion and Rohde *[86]* and Dorph *[118]*.

Champion and Rohde *[86]* showed that strengthening of the explosively shock loaded Hadfield steels is a function of dislocation density and stacking fault volume fraction. They found the dislocation densities and stacking fault volume fraction for the shocked specimens correlated well with the hardness data when the only microstructural feature observed was dislocation, whereas the twins they found had a negligible effect on the hardness. In summary, the explosive shock wave studies on this steel by Roberts *[105]*, Champion and Rohde *[86]*, and Dorph *[118]* came to the same conclusion. The conclusion that the high density dislocation microstructure is the most important strengthening mechanism in the Hadfield steel and the combination of twins and dislocations is of only secondary importance. In the case of conventional deformation processing, Dastur and Leslie *[106]* also reported a similar result. When numerous twins were produced by deformation, the work hardening rate was not significant, whereas no twins were found the work hardening was high.

In this study, the strengthening mechanism in the LSP Hadfield steel was due to the combined effects of widely separated partial dislocations bounded with stacking faults and

subdivision of the matrix grains by ε-hcp martensite plates. High strengthening effect by LSP is consistent with other explosive shock studies. Strengthening effects resulting from the subdivision of the matrix grains by twins and ε-hcp martensite plates were approximately identical and both were important in shot peened and cold rolled specimens.

Comparisons with Other LSP Studies

Scattered surface hardnesses measured on the LSP low carbon and Hadfield steels are indicative of inhomogeneity of laser beam energy on the shock area; see a laser energy spatial distribution plot in Figure 3-2b. While this inhomogeneity may be a characteristic of the optic used in this study, similar scattered surface hardness results are also seen in Al alloys by Clauer et al. *[8]* and by Bournot *[12]*, and in stainless steels by Fairland and Clauer *[7]*. In these studies, the laser power densities used were about 10^9 to 10^{10} W/cm^2, and pressures were between 4 to 5 GPa. The increase in the surface hardness was 15 to 20% for Al alloys *[8, 12]* and 40% for stainless steels *[7]*. Such hardness increases were results of the dislocation density increases, as indicated in the Clauer at al. TEM studies *[7, 8]*. This is consistent with results of this study. The low carbon steel in this study showed an increased dislocation density and increased surface hardness by about 30-80%. The surface hardness increased more for the Hadfield steel, about 50-130%, and was caused by the presence of widely dissociated dislocations and ε-hcp martensite. Furthermore, this study showed a surface hardness drop in the center of LSP region similar to those of Fairand et al. *[7, 8]* and by Bournot *[12]* in Al alloys, and Romain et al. *[72]* in iron. Even after five multiple LSP treatments on the same area in the stainless steel, Fairand and Clauer *[7]* still revealed this hardness drop in the center LSP region. Therefore, this type of hardness profiles is characteristic of LSP.

For LSP in-depth hardness profile results, this study showed the hardening caused by LSP is superficial. This also can be seen from the LSP-induced ε-hcp martensite in the Hadfield steel which diminished at ~50 μm of the depth, suggesting LSP is a surface treatment processing. This result is in agreement with other LSP studies. In the studies by Clauer et al. *[8]* and Banaś *[14]*, the Al alloys and maraging steel after LSP exhibited that hardness leveled off within 100 μm of surface. The strengthening effects of LSP are therefore observed near the surface and do not extend into the bulk. Accordingly, surface-related mechanical properties such as fatigue strength can be improved by LSP *[7-10, 13, 70, 14]*, but the properties such as yield strength are often not greatly enhanced *[1, 5]*.

6. CONCLUSIONS

The effects of laser shock processing on the microstructure and mechanical properties of the low carbon and Hadfield manganese steels have been studied. The following conclusions are drawn from this study.

(1) Processing optimization: In the laser power density range of $1x10^{11}$ to $5x10^{12}$ W/cm^2, maximum shock wave intensities were obtained when a plasma-confining overlay was not used. Absorption of an overlay plasma resulted in laser energy loss when an overlay was used, and such laser absorption increased with increasing power density. The specimen surface yielded LSP-induced indentation only when an energy-absorbing black paint coating was used, and the indentation depth increased as the laser power density increased. Shock pressures of about 2 GPa were calculated for a power density of $2.4x10^{12}$ W/cm^2. This pressure was about one magnitude lower than that of shot peening.

(2) Low Carbon Steel Microstructure: A strain rate dependence of microstructure was seen in this steel. High density dislocation arrays were induced by LSP due to high strain-rate deformation, whereas dislocation cell substructures were generated by the lower strain rate processes of shot peening and cold rolling.

(3) Hadfield Steel Microstructure: A stress magnitude dependence of microstructure was seen in this steel. LSP induced extensive formation of ε-hcp martensite as a result of insufficient pressure to allow the twin formation, while high pressure shot peening produced both twins and ε-hcp martensite. The LSP-induced ε-hcp martensite (35 vol.%) on the surface decreased with the depth, reaching nominal bulk values (<4%) at 50 μm. Severe deformation by cold rolling was responsible for the almost complete ε-hcp martensite microstructure.

(4) Residual Stress: Uncoated LSP surfaces showed tensile residual stresses because of melting, while coated surfaces had compressive stresses due to deformation by the applied pressures. As compared to LSP, shot peening resulted in relatively higher and deeper compressive stress. Due to a difference in applied pressure geometry, shot peening produced a peak compressive stress under the surface for both steels, whereas LSP induced the maximum compressive stress on the surface for low carbon steel. For the LSP Hadfield steel, a maximum compressive stress below the surface resulted from diminishing of LSP-induced ε-hcp martensite.

(5) Ductility and Microhardness: A plastic deformation anomaly was found in LSP Hadfield steel because it exhibited deeper indentation than that of the low carbon steel for the same LSP conditions. This may be related to the LSP-induced phase transformation in the Hadfield steel, as suggested by other explosive shock wave studies. For the strengthening effects, the microhardness of low carbon steel was shown to be a function of dislocation density. The highest hardness was obtained from the highest dislocation density microstructure in the cold rolled specimen. For the Hadfield steel, LSP resulted in a surface hardness greater than that for shot peening and cold rolling. Strengthening of the LSP Hadfield steel was due to the combined effects of widely separated partial dislocations bounded with stacking faults and subdivision of the matrix grains by ε-hcp martensite plates. High strengthening effect by LSP is consistent with other explosive shock studies. Subdivision of the matrix grains by twins and ε-hcp martensite plates was the major strengthening mechanism for the shot peened and cold rolled Hadfield steel. The near surface strengthening effects due to LSP were observed for both steels.

APPENDIX

A. Volume Fraction Analysis by X-ray Diffractometer

The diffracted X-ray intensity in a single-phase specimen may be expressed as *[123]*

$$I = \frac{R}{2\mu} K \qquad \text{(A-1)}$$

where K is a constant which is independent of the nature of the specimen and μ is the linear absorption coefficient of the specimen, while R is a factor which depends on θ, the reflecting set of planes and the crystal structure of the specimen:

$$R = \frac{1}{v^2} [|F|^2 p \left(\frac{1 + \cos^2 2\theta}{\sin^2\theta \cos\theta} \right)] e^{-2M} \qquad \text{(A-2)}$$

where V = volume of unit cell, F = structure factor, p = multiplicity factor, θ = Bragg angle, e^{-2M} = temperature factor.

In the case of this study, a mixture of two phases (γ and ε) in Hadfield steel, the diffracted X-ray intensity is, according to the direct comparison method *[123]*,

$$I_{\gamma_{hkl}} = \frac{R_{\gamma_{hkl}} C_\gamma}{2\mu_m} K, \quad \text{and} \quad I_{\varepsilon_{hkl}} = \frac{R_{\varepsilon_{hkl}} C_\varepsilon}{2\mu_m} K \qquad \text{(A-3)}$$

where C_γ and C_ε are volume fractions of γ and ε phase, respectively, $I_{\gamma_{hkl}}$ and $I_{\varepsilon_{hkl}}$ are their measured integrated intensities, and μ_m is the linear absorption coefficient of the mixture.

$$C_\gamma = \frac{2\mu_m I_{\gamma_{hkl}}}{K R_{\gamma_{hkl}}} = K' \left(\frac{I_{\gamma_{hkl}}}{R_{\gamma_{hkl}}} \right), \qquad \text{and}$$

$$C_\varepsilon = \frac{2\mu_m I_{\varepsilon_{hkl}}}{K R_{\varepsilon_{hkl}}} = K' \left(\frac{I_{\varepsilon_{hkl}}}{R_{\varepsilon_{hkl}}} \right) \qquad \text{(A-4)}$$

In the case of preferred orientation in the specimen, the correct equation for summation of intensity ratios from a number of reflections may be deduced as follows: *[131]*

$$C_\varepsilon = K' \frac{1}{n_\varepsilon} \sum_{0}^{n_\varepsilon} \left(\frac{I_\varepsilon}{R_\varepsilon} \right) \qquad \text{(A-5)}$$

where n_ε is number of ε peaks considered. Hence,

$$\frac{C_\gamma}{C_\varepsilon} = \frac{\frac{1}{n_\gamma}\sum_{0}^{n_\gamma}\left(\frac{I_\gamma}{R_\gamma}\right)}{\frac{1}{n_\varepsilon}\sum_{0}^{n_\varepsilon}\left(\frac{I_\varepsilon}{R_\varepsilon}\right)} \qquad \text{(A-6)}$$

and the values of C_γ and C_ε can be obtained from the additional relationship:

$$C_\gamma + C_\varepsilon = 1 \qquad \text{(A-7)}$$

The unit cell volumes for γ and ε phases used in Eqn (A-2) are listed below:

$$V_\gamma = 4.67\text{x}10^{-29}\ \text{m}^3$$

$$V_\varepsilon = 2.31\text{x}10^{-29}\ \text{m}^3$$

B. Surface Chemical Analysis

For specimens melted during LSP, their surfaces may have been contaminated by the coating and/or overlay materials. Thus the chemical compositions of LSP specimens were examined by Auger microprobe analysis. In Figures A-1 and A-2, two Auger in-depth profiles are presented. The profiles shown are plots of the atomic percentages (A.C.%) of the elements as function of sputter time (in minute). The profiles were obtained from the same specimen using different areas: Figure A-1 was from the matrix area that showed no melting, while Figure A-2 was from the melted region. The specimen analyzed was low carbon steel coated with the black paint during LSP (no overlay) and treated at energy of 83 J. To examine a possible post-LSP surface absorption effect, the oxygen concentration was also included for both profiles. No detectable overlay contamination was found on the LSP specimens, therefore, no results will be presented.

As shown in Figure A-1, the iron concentration reached a saturated value within a few minutes of sputtering. The carbon concentration diminished to the noise level within the same period of time and oxygen remained at a noise level throughout the sputtering and was considered negligible. For the melted region, Figure A-2 shows the iron concentration slowly increased with sputter time, while the carbon decreased at the same rate; eventually both reached their saturation values after 25 minutes of sputtering. In this case, the oxygen concentration was initially significant and then reduced to a noise level after two minutes of sputtering. The quick reduction in oxygen suggested that the post-LSP absorption effect was limited and that the high carbon concentration near the surface was not formed after LSP but during LSP. Thus, differences in carbon concentration between the two profiles (Figures A-1 and A-2) can be seen: as high as 40 at.% carbon concentration on the LSP melted surface. This concentration profile may be result of the melting of the very low carbon-content iron («1 at.%) specimen surface and then the mixing with the carbon from the black paint coating during LSP.

To study the effects of energy and surface condition (overlay and coating), Figures A-3 and A-4 summarize the Auger in-depth profiling results obtained from a number of LSP specimens. In order to eliminate experimental variation on the results, the elemental peak-to-peak ratios were used in both figures and these ratios are considered tc be proportionally related to atomic concentration. One of the peak-to-peak depth profiles is shown in Figure A-5. To plot profiles such as Figure A-3 or A-4, the carbon peak-to-peak profile was normalized against that of the iron profile and then the carbon to iron ratio (peak heights) was plotted versus the sputter time. The results shown in Figure A-3 were from the melted regions of five different LSP specimens (energy and overlay effects), while those in Figure A-4 were from the unmelted regions of two specimens (overlay effect). The specimens analyzed were low carbon steel and all were coated with a thin (10 - 15 μm) layer of black paint prior to LSP. For the sake of comparison, both figures include results from an unshocked specimen .

To demonstrate pulse energy effect, Figure A-3 shows a set of results from the melted regions of overlay specimens treated with several different energies (2.6, 35, 83, and 126 J). It is clearly shown that the specimen treated with the lowest energy (2.6 J) exhibited the highest carbon concentration throughout the depth (~1.7 μm) profile analysis. With the same surface condition, it is apparent that as the laser energy increased, the surface concentration and depth of residual carbon decreased. It is also consistent that as the surface carbon concentration was higher, the carbon diffused deeper. Therefore, the melted region of the LSP specimen underwent a diffusional process during which the carbon from the black paint coating diffused into melted specimen. Low laser energy resulting in higher carbon concentration suggests that at higher laser energy less melting as well as intermixing, occurred on the specimen because of energy absorption by the overlay plasma.

Furthermore, as seen in Figure A-3, with using approximately the same laser energy (about 84 J), the overlay plus black paint coated specimen showed a higher surface carbon concentration (about twice) and approximately 50% deeper residual carbon diffusion depth than that of the black paint coated specimen. This is because the use of overlay enhanced the melting and thus the carbon diffusion became greater than the one without it. Compared with that of untreated specimen, the melted regions of LSP specimens all had increases in the carbon concentration on and near the LSP surface. On the other hand, for the unmelted region in-depth profiles, Figure A-4 shows results from two LSP specimens and an unshocked specimen. This figure shows that the carbon concentration remained at a very low level throughout analysis. This low level of concentration is considered to be spectrum noise as the lower limit on carbon detection is ~3 at.%. Therefore, it is apparent that the unmelted regions had no detectable carbon contamination in bulk, and either on or near the LSP surface, the carbon concentrations were much less than those of the melted regions.

The results of Auger in-depth chemical analysis are summarized as follows: (1) Compared with an unshocked specimen, carbon contamination from the black paint coating was found on and near melted surface for different LSP conditions. The most pronounced contamination was found when the coated specimen was covered with an overlay and subjected to a low energy laser pulse. The carbon concentration at the surface was more than 45 at.% and was significant to a depth of 1.7 μm. (2) Carbon contamination decreased as the laser energy increased due to the overlay plasma energy absorption, resulting in energy loss. Overall, the higher the surface carbon concentration, the deeper the carbon penetrated into the specimen. (3) The use of an overlay also enhanced the carbon contamination; specimens treated with an overlay had twice the surface concentration and 50% greater carbon penetration than specimens shocked at the same energy without an overlay. (4) When no surface melting occurred, carbon contamination was not detected on either LSP surface or in the bulk.

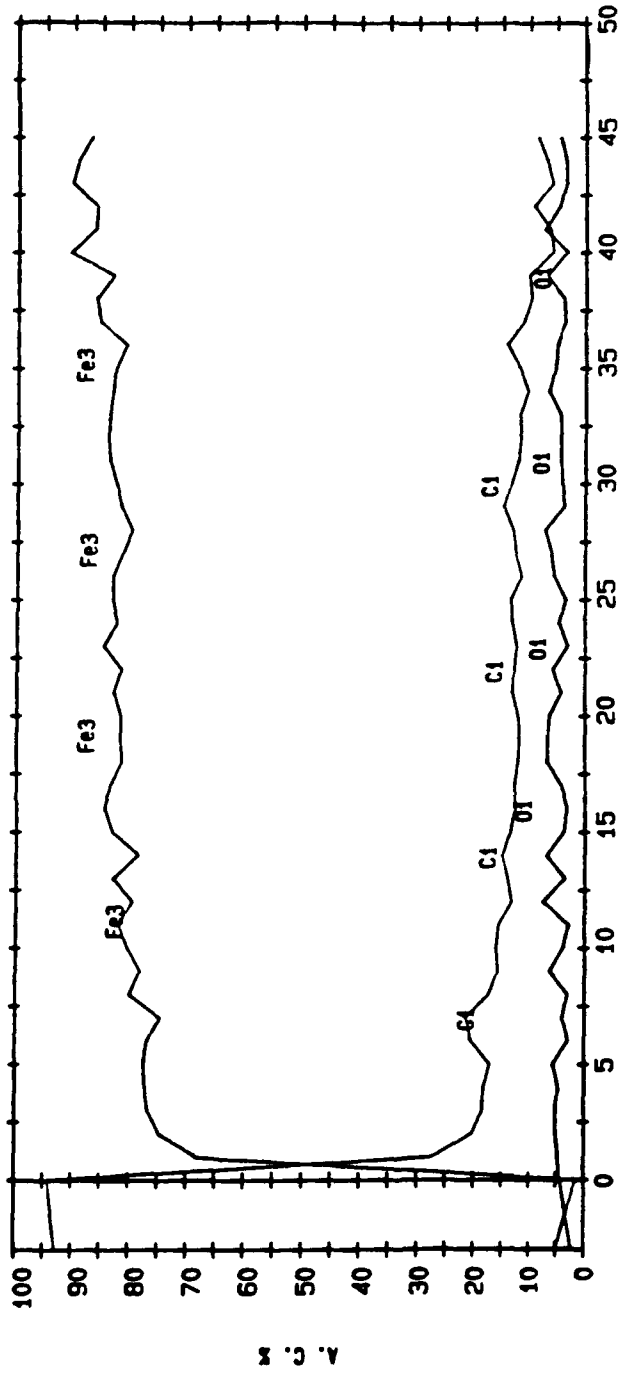

Figure A-1 Auger depth profile (in atomic percentage) of LSP low carbon steel at the unmelted matrix region. The specimen was treated at an energy of 83 J with a BP coating and an overlay.

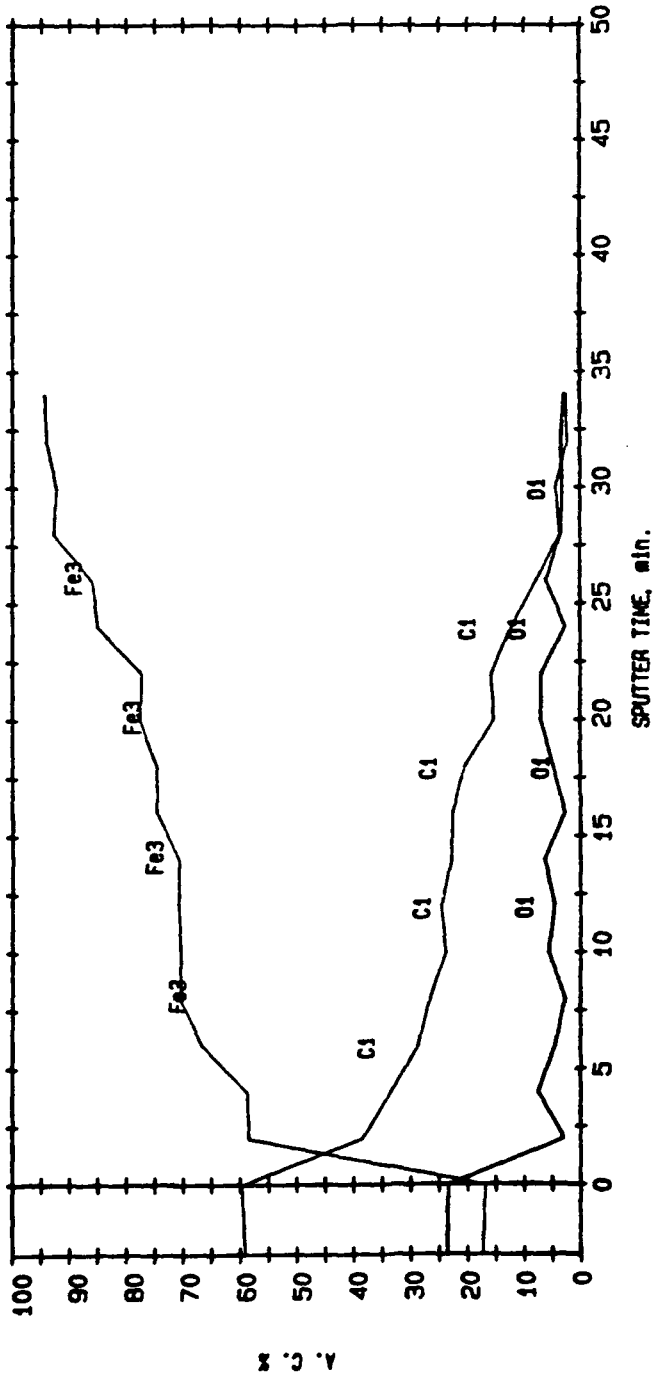

Figure A-2 Auger depth profile (in atomic percentage) of LSP low carbon steel at the melted region. The specimen was treated at an energy of 83 J with a BP coating and an overlay.

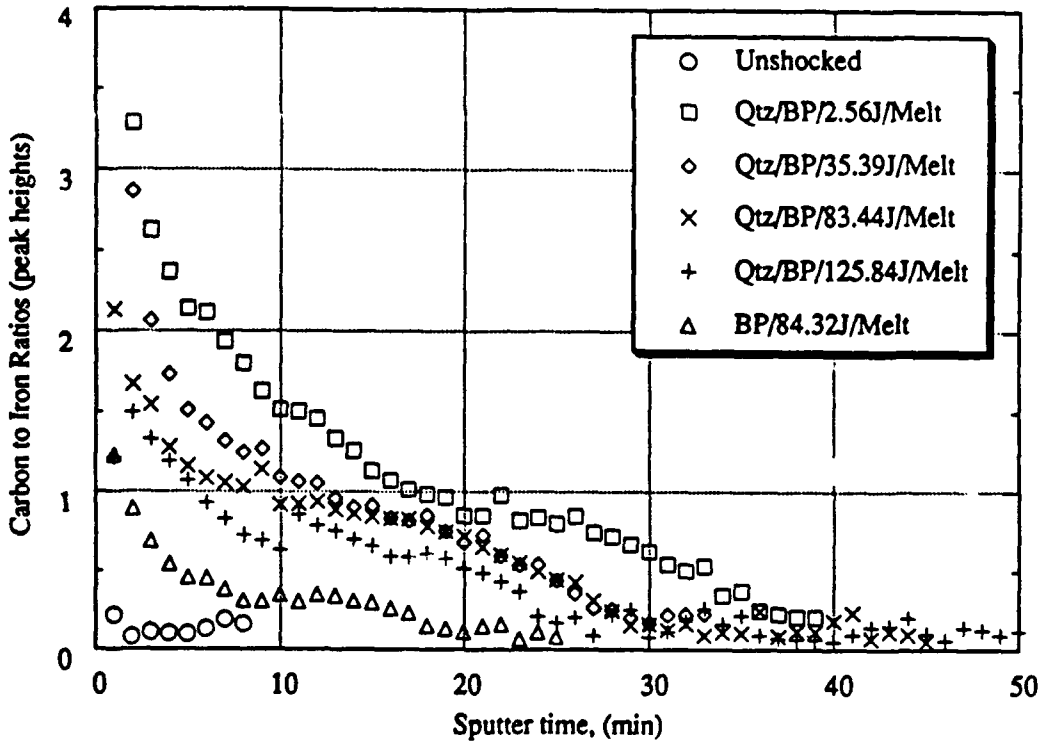

Figure A-3 Summary of Auger depth profiles at melted regions for different energies and surface conditions.

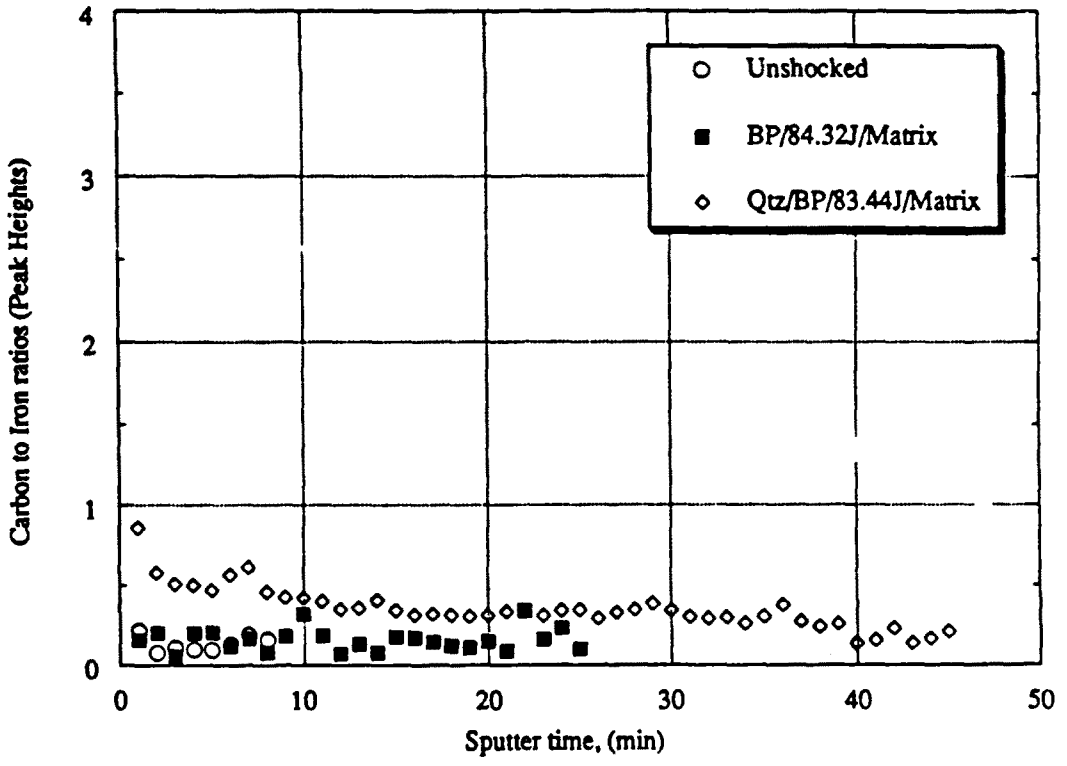

Figure A-4 Summary of Auger depth profiles at unmelted matrix regions for different energies and surface conditions.

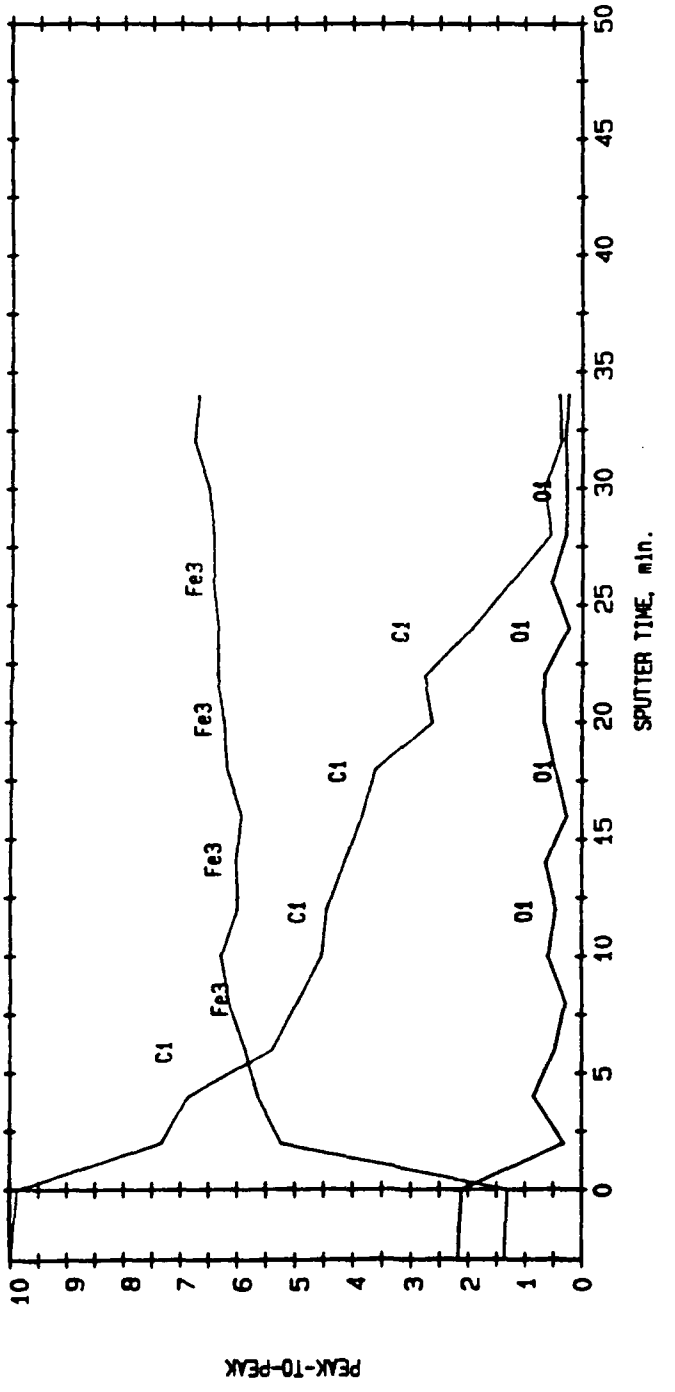

Figure A-5 Auger depth profile (peak-to-peak) of LSP low carbon steel at the melted region. The specimen was treated at an energy of 83 J with a BP coating and an overlay.

C. Estimation of Pressure Generated by Shot Peening

The pressure generated by the shot peening is estimated based on the works by Wohlfahrt *[165]* and Shaw *[172]*. As an approximation, the materials are assumed to behave linearly when they are plastically deformed. The Hertz equation then gives the load, F, in terms of spherical shot ball peen diameter, D, and indentation diameter, d, *[172]*

$$F = \frac{4}{9}\frac{E d^3}{D} \qquad \text{(A-8)}$$

where E is the elastic constant of material. The vertical pressure, P, in Figure 5-9b is given by *[165]*

$$P = \frac{6}{\pi}\frac{F}{d^2} \qquad \text{(A-9)}$$

To estimate indentation diameter, d, it is assumed that the contact depth, h, of shot ball peen is nearly equal to the measured surface roughness and thus d can be obtained from *[165]*

$$d = 2a = 2\sqrt{2hr - h^2} \qquad \text{(A-10)}$$

where r is the radius of the shot ball peen. The maximum shear stress, τ_{max}, is equal to *[165]*

$$\tau_{max} = 0.31\,P \qquad \text{(A-11)}$$

The average measured surface roughness, h, of the low carbon steel and Hadfield steel was obtained and listed in the table below, along with average calculated indentation diameter, d, and calculated pressure, P, as well as maximum shear stress, τ_{max}. The shot ball diameters are listed in Table 3-4, and the elastic constants used are 210 GPa and 203 GPa for the low carbon steel and Hadfield steel, respectively.

Material	Roughness h, μm	Indentation diameter d, μm	Pressure P, GPa	Maximum shear stress τ_{max}, GPa
Low carbon	2.56 - 3.51	42.4 - 49.5	42.4 - 49.6	13.1 - 15.4
Hadfield	3.01 - 3.57	91.4 - 94	24.6 - 26.8	7.6 - 8.3

For the calculation of depth at which the shear stress is maximum, the following is used *[165]*

$$Z_{\tau_{max}} = 0.47\,a = 0.235\,d \qquad \text{(A-12)}$$

$Z_{\tau_{max}}$ is therefore 10 - 12 μm for low carbon steel, and 21 - 22 μm for Hadfield steel.

ACKNOWLEDGMENTS

Authors thank Doctor Spencer Wu from the Air Force for his help in making this research program happen and his invaluable suggestions during first two years of this study. Doctor John Botsis from the Air Force is thanked for his help during third year of this research program. The Air Force Office of Scientific Research is acknowledged for the financial support through the contract AFOSR-90-0185.

The Center for Microanalysis of Materials and the Center for Electron Microscopy at the University of Illinois, the Materials Engineering Research Laboratory at the University of Illinois, and the Laboratory for Laser Energetics at the University of Rochester are acknowledged for access to their equipment. The personnel of these facilities, particularly Mr. William Beich from the Laboratory for Laser Energetics, is acknowledged for help in conducting the experiments and solving great deal of problems related the this research program.

REFERENCES

1 B. P. Fairand, B. A. Wilcox, W. J. Gallagher, and D. N. Williams, *J. Appl. Phy.*, 1972, Vol. 43, p. 3893-5.

2 B. P. Fairand, A. H. Clauer, R. G. Jung, and B. A. Wilcox, *Appl. Phy. Lett.*, 1974, Vol. 25, p. 431-3.

3 B. P. Fairand and A. H. Clauer, *Optics Communications*, Vol. 18, 1976, 588-91.

4 A. H. Clauer, B. P. Fairand, and B. A. Wilcox, *Metall. Trans. A*, 1977, Vol. 8A, p. 119-125.

5 A. H. Clauer, B. P. Fairand, and B. A. Wilcox, *Metall. Trans. A*, 1977, Vol. 8A, p. 1871-f.

6 B. P. Fairand and A. H. Clauer, *J. Appl. Phy.*, 1979, Vol. 50, p. 1497-1502.

7 B. P. Fairand and A. H. Clauer, in *Laser-Solid Interactions and Laser Processing*, 1979, p. 27-42.

8 A. H. Clauer, J. H. Holbrook, and B. P. Fairand, in *Shock Waves and High-Strain-Rate Phenomena in Metals: Concepts and Applications*, Ed. by M. A. Meyers and L. E. Murr, 1981, p. 675-702.

9 S. C. Ford, B. P. Fairand, A. H. Clauer, and R. D. Galliher, *Technical Report AFWAL-TR-80-3001*, 1980, Vol. 1, p. 268-278.

10 A. H. Clauer, C. T. Walters, and S. C. Ford, in *Laser in Materials Processing*, Ed. by M. Bass, 1983, p. 7-22.

11 F. Cottet and J. P. Romain, in *Shock Waves in Condensed Matters-1981*, Ed. by W. J. Nellis, L. Seaman, and R. A. Graham, 1981, p. 130-4.

12 Ph. Bournot, D. Dufresne, M. Autric, P. Giovanneschi-Testud, and C. Coquerelle, in *SPIE-High Power Lasers*, Vol. 801, 1987, p. 308-313.

13 J. Fournier, *Ph. D. Dissertation* (in French), 1989.

14 G. Banaś, H. E. Elsayed-Ali, F. V. Lawrence, Jr., and J. M. Rigsbee, *J. Appl. Phy.*, 1990, Vol. 67, p. 2380-4.

15 Shock wave-related proceeding publications: *Metallurgical Effects At High Strain Rates*, Ed. by R. W. Rohde, B. M. Butcher, J. R. Holland, and C. H. Karnes, 1973, *Shock Waves and High-Strain-Rate Phenomena in Metals: Concepts and Applications*, Ed. by M. A. Meyers and L. E. Murr, 1981, and *Metallurgical Applications of Shock-Wave and High-Strain-Rate Phenomena*, Ed. by L. E. Murr, K. P. Staudhammer, and M. A. Meyers, 1986.

16 B. Steverding and H. P. Dudel, *J. Appl. Phy.*, 1976, Vol. 47, p. 1940-5.

17 D. Salzmann, I. Gilath, and B. Arad, *Appl. Phy. Lett.*, 1988, Vol. 52, p. 1128-9.

18 F. Cottet and M. Boustie, *J. Appl. Phy.*, 1989, Vol. 66, p. 4067-73.

19 S. Eliezer, I. Gilath, and T. Bar-Noy, *J. Appl. Phy.*, 1990, Vol. 67, p. 715-724.

20 W. T. Silfvast, in *Encyclopedia of Physical Science and Technology*, Ed. by R. A. Meyers, 1987, Vol. 7, p. 146.

21 R. Allan, *IEEE Spectrum*, 1979, Vol. 16, p. 42-49.

22 E. M. Breinan and B. H. Kear, in *Laser Materials Processing*, Ed. by M. Bass, 1983, p. 235.

23 *Source Book on Applications of the Laser in Metalworking*, Ed. by E. A. Metzbower, 1981, and *Laser Materials Processing*, Ed. by M. Bass, 1983.

24 A. Clauer, B. P. Fairand, S. C. Ford, and C. T. Walters, U. S. Patent 4,401,477, 1983.

25 R. M. White, *J. Appl. Phy.*, 1963, Vol. 34, p. 2123-24.

26 G. A. Askar'yan and E. M. Moroz, *Soviet Physics JETP*, 1963, Vol. 16, p. 1638-39.

27 L. Davison and R. A. Graham, *Phy. Report*, 1979, Vol. 55, p. 255-379.

28 L.E. Murr, *Shock Waves for Industrial Applications*, 1988, p.14.

29 J. F. Ready, in *Proceedings of the First International Laser Processing Conference*, Anahem, California, November, 1981.

30 T.P. Hughes, *Plasmas and Laser Light*, 1975, p.274.

31 N. Bloembergen, in *Laser-Solid Interactions and Laser Processing-1978*, Ed. by S. D. Ferris, H. J. Leamy, and J. M. Poate, p. 1-11.

32 R. K. Singh, *Appl. Phy. Lett.*, 1991, Vol. 59, p. 2215-17.

33 *CRC Handbook of Chemistry and Physics*, Ed. by R. C. Weast, 1984-1985, 65th edition, p. F-65.

34 M. Bass, in *Encyclopedia of Physical Science and Technology*, Ed. by R. A. Meyers, 1987, Vol. 7, p. 129-145.

35 H. S. Carslaw and J. C. Jaeger, *Conduction of Heat in Solids*, 2nd ed., 1959, p. 75.

36 F. Spaepen and C. Lin, in *Amorphous Metals and Non-equilibrium Processing*, Ed. by M. von Allmen, 1984, p. 65-72.

37 M. C. Downer, R. L. Fork, and C. V. Shank, in *Ultrafast Phenomena IV*, 1984, p. 106-110.

38 Y. W. Kim, in *Laser-Induced Plasma and Applications*, Ed. by L. J. Radziemski and D. A. Cremers, 1989, p. 327-346.

39 J. H. Eberly and P. Lambropoulous, *Multiphoton Processes*, 1978.

40 N. G. Basov, V. A. Boiko, O. N. Krohin, O. G. Semenov, and G. V. Sklizkov, *Soviet Phy.-Technical Phy.*, 1969, Vol. 13, p. 1581-82.

41 J. F. Ready, *Effects of High-Power Laser Radiation*, 1971, p. 161-175.

42 E. Archbold and T. P. Hughes, *Nature*, 1964, Vol. 204, p. 670.

43 J. Sneddon, P. G. Mitchell, and N. S. Nogar, in *Laser-Induced Plasma and Applications*, Ed. by L. J. Radziemski and D. A. Cremers, 1989, p. 347-383.

44 J. F. Ready, *Appl. Phy. Lett.*, 1963, Vol. 3, p. 11-3.

45 H. Weichel and P. V. Avizonis, *Appl. Phy. Lett.*, 1966, Vol. 9, p. 334-7.

46 L. R. Veeser and J. C. Solem, *Phy. Rev. Lett.*, 1978, Vol. 40, p. 1391-4.

47 R. G. Root, in *Laser-Induced Plasma and Applications*, Ed. by L. J. Radziemski and D. A. Cremers, 1989, p. 69-103.

48 J. F. Ready, *J. Appl. Phy.*, 1965, Vol. 36, p. 462-68.

49 N. C. Anderholm, *Bull. Am. Phy. Soc.*, 1968, Vol. 13, p. 338.

50 N. C. Anderholm, *Appl. Phy. Lett.*, 1970, Vol. 16, p. 113-5.

51 L. C. Yang and V. J. Menichelli, *Appl. Phy. Lett.*, 1971, Vol.19, p. 473-5.

52 L. C. Yang, *J. Appl. Phy.*, 1974, Vol. 45, p. 2601-8.

53 J. D. O'Keefe and C. H. Skeen, *Appl. Phy. Lett.*, 1972, Vol.21, p. 464-6.

54 J. D. O'Keefe, C. H. Skeen, and C. M. York, *J. Appl. Phy.*, 1973, Vol. 44, p. 4622-26.

55 R. Fabbro, J. Fournier, P. Ballard, D. Devaux, and J. Virmont, *J. Appl. Phy.*, 1990, Vol.68, p. 775-784.

56 J. A. Fox, *Appl. Phy. Lett.*, 1972, Vol.24, p. 461-4.

57 D. W. Gregg and S. J. Thomas, *J. Appl. Phy.*, 1966, Vol. 37, p. 2787-89.

58 B. Arad, S. Eliezer, Y. Gazit, H. M. Loebenstein, A. Zmora, and S. Zweigenbaum, *J. Appl. Phy.*, 1979, Vol. 50, p. 6817-21.

59 C. R. Phipps, Jr., T. P. Turner, R. F. Harrison, G. W. York, W. Z. Osborne, G. K. Anderson, X. F. Corlis, L. C. Haynes, H. S. Steele, K. C. Spicochi, and T. R. King, *J. Appl. Phy.*, 1988, Vol. 64, p. 1083-96.

60 H. Schoeffmann, H. Schmidt-Kleiber, and E. Reichel, *J. Appl. Phy.*, 1988, Vol. 63, p. 46-51.

61 A. Ng, in *Shock Waves in Condensed Matter-1987*, Ed. by S. C. Schmidt and N. C. Holmes, p. 767-72.

62 P. E. Schoen and A. J. Campillo, *Appl. Phy. Lett.*, 1984, Vol. 45, p. 1049-51.

63 A. J. Campillo, R. D. Griffin, and P. E. Schoen, *Optical Comm.*, 1986, Vol. 57, p. 301-6.

64 F. Bauer, in *Shock Waves in Condensed Matters-1983*, Ed. by J. R. Asay, R. A. Graham, and G. K. Straub, 1984, p. 225-8.

65 L. M. Lee, R. A. Graham, F. Bauer, and R. P. Reed, *J. De Physique*, Colloque C3, Supplement, 1988, p. C3-651-657.

66 V. B. Braginskii, I. I. Minakova, and V. N. Rudenko, *Soviet Phy.-Technical Phy.*, 1967, Vol. 12, p. 753-57.

67 J. Fournier, R. Fabbro, and R. Fabbro, *C. R. Acad. Sci. Paris*, Series II, 1987, p. 1051-54.

68 J. Fournier, R. Fabbro, P. Ballard, and J. Virmont, in *Laser Interaction with Matter*, Ed. by G. Velarde, E. Minguez, and J. M. Perlado, 1989, p. 259-262.

69 S. A. Metz and F. A. Smidt, Jr., *Appl. Phy. Lett.*, 1971, Vol.19, p. 207-8.

70 P. Ballard, J. Fournier, R. Fabbro, J. Frelat, and L. Castex, *J. De Physique*, Colloque C3, Supplement, 1988, p. C3-401-406.

71 D. Ayrault, R. Fabbro, J. Fournier, and J. L. Strudel, *C. R. Acad. Sci. Paris*, Series II, 1987, p. 353-358.

72 J. P. Romain, M. Hallouin, M. Gerland, F. Cottet, and L. Marty, *Shock Waves in Condensed Mater*, Ed. by S. C. Schmidt, N. C. Holmes, 1987, p.787-90.

73 W. C. Leslie, in *Metallurgical Effects at High Strain Rates*, Ed. by R. W. Rohde, B. M. Butcher, J. R. Holland, and C. H. Karnes, 1973, p. 571-586.

74 M. A. Meyers and L. E. Murr, in *Shock Waves and High-Strain-Rate Phenomena in Metals: Concepts and Applications*, Ed. by M. A. Meyers and L. E. Murr, 1981, p. 487-530.

75 L. E. Murr, in *Shock Waves and High-Strain-Rate Phenomena in Metals: Concepts and Applications*, Ed. by M. A. Meyers and L. E. Murr, 1981, p. 607-673.

76 D. B. Hayes, *Introduction to Stress Wave Phenomena*, Sandia National Laboratory Report, SLA-73-0801, 1973.

77 M. A. Meyers and K. K. Chawla, *Mechanical Metallurgy*, 1984, p.571.

78 A. Ng, D. Parfeniuk, and L. DaSilva, *Phy. Rev. Lett.*, 1985, Vol. 54, p. 2604-7.

79 *CRC Handbook of Chemistry and Physics*, Ed. by R. C. Weast, 1984-1985, 65th edition, p. E-43.

80 V. E. Fortov, V. V. Kostin, and S. Eliezer, *J. Appl. Phy.*, 1991, Vol. 70, p. 4524-31.

81 H. Kressel and N. Brown, *J. Appl. Phy.*, 1967, Vol. 38, p. 1618-25.

82 C. S. Smith, *Trans. AIME*, 1958, Vol. 212, p. 574-589.

83 M. A. Meyers and J. R. C. Guimaraes, *Mat. Sci. and Eng.*, 1976, Vol. 24, 289-92.

84 H.-J. Kestenbach and M. A. Meyers, *Metall. Trans. A*, 1976, Vol. 7A, p. 1943-50.

85 D. C. Brillhart, R. J. DeAngelis, A. G. Preban, J. B. Cohen, and P. Gordon, *Trans. AIME*, 1967, Vol. 239, p. 836-43.

86 A. R. Champion and R. W. Rohde, *J. Appl. Phy.*, 1970, Vol. 41, p. 2213-23.

87 C. S. Smith, *Trans. AIME*, 1958, Vol 212, p. 574.

88 J. Weertman, in *Shock Waves and High-Strain-Rate Phenomena in Metals*, Ed. by M. A. Meyers and L.E. Murr, 1981, p. 469-84.

89 M. A. Meyers, in *Strength of Metals and Alloys*, Ed. by P. Hassen, V. Gerold, and G. Kostorz, 1979, p. 547-52.

90 F. S. Minshall, *Bull. APS*, 1954, Vol. 29, p. 23.

91 D. Bancroft, E. L. Perterson, and F. S. Minshall, *J. App. Phys.*, 1956, Vol. 27, p. 291-8.

92 P. C. Johnson, B. A. Stein, and R. S. Davis, *J. App. Phys.*, 1962, Vol. 33, p. 557-61.

93 R. N. Keeler and A. C. Mitchell, *Solid State Communications*, 1969, Vol. 7, p. 271-4.

94 E. G. Zukas, C. M. Fowler, F. S. Minshall, and J. O'Rourke, *Trans. AIME*, 1963, Vol. 227, p. 746.

95 T. R. Loree, C. M. Fowler, E. G. Zukas, and F. S. Minshall, *J. App. Phys.*, 1966, Vol. 37, p. 1918.

96 A. Christou and N. Brown, *Met. Trans.*, 1972, Vol. 3, p. 867.

97 W. C. Leslie, D. W. Stevens, and M. Cohen, in *High Strength Materials*, Ed. by V. F. Zackay, 1965, p. 382.

98 W. C. Leslie, E. Hornbogen, and G. E. Dieter, *J. Iron and Steel Inst.*, 1962, Vol. 200, p. 622-33.

99 E. Hornbogen, *Acta Met.*, 1962, Vol. 10, p. 978-80.

100 R. E. Smallman, *Modern Physical Metallurgy*, 1985, p. 253.

101 J. N. Johnson and R. W. Rohde, *J. Appl. Phys.*, 1971, Vol. 42, p. 4171-82.

102 S. Mahajan, *Phy. Stat. Sol.*, 1969, Vol. 33, p. 291.

103 H. C. Doepken, *Trans. AIME*, 1952, Vol. 194, p. 166-70.

104 H. M. Otte, *Acta Met.*, 1957, Vol. 5, p. 614-27.

105 W. N. Roberts, *Trans. AIME*, 1964, Vol. 230, p. 372-7.

106 Y. N. Dastur and W. C. Leslie, *Metall. Trans. A.*, 1981, Vol. 12A, p. 749-59.

107 P. H. Adler, G. B. Olson, W. S. Owen, *Metall. Trans. A.*, 1986, Vol. 17A, p. 1725-37.

108 B. K. Zuidema, D. K. Subramanyam, and W. C. Leslie, *Metall. Trans. A.*, 1987, Vol. 18A, p. 1629-39.

109 B. Cina, *Acta Met.*, 1958, Vol. 6, p. 748-61.

110 A. Holden, J. D. Bolton, and E. R. Petty, *J. the Iron and Steel Inst.*, 1971, Sept., p.721-28.

111 J. Gordon Parr, *J. the Iron and Steel Inst.*, 1952, June, p. 137-141.

112 Z. Nishiyama and K. Simizu, *J. Phy. Soc. Japan*, 1960, Vol. 15, p. 1963-69.

113 Z. Nishiyama and K. Simizu, *Trans. Japan Inst. Metals*, 1965, Vol. 6, p. 88-92.

114 K. S. Raghavan, A. S. Sastri, and M. J. Marcinkowski, *Trans. AIME*, 1969, Vol. 245, p. 1569-75.

115 A. H. Holtzman and G. R. Cowan, in *Response of Metals to High Velocity Deformation*, Ed. by P. G. Shewmon and V. F. Zackay, 1960, p. 447-82.

116 M. A. Filippov and I. N. Bogachev, *Phy. of Metals and Metall*, 1965, Vol. 20, p. 83-90.

117 M. A. Filippov and B. N. Kodes, *Phy. of Metals and Metall*, 1973, Vol. 31, p. 171-5.

118 K. Dorph, *Scand. J. of Metallurgy*, 1977, Vol. 6, p. 38-9.

119 L. E. Murr and K. P. Staudhammer, *Mat. Sci. and Eng.*, 1975, Vol. 20, p. 9

120 G. A. Stone, R. N. Orava, G. T. Gray, and A. R. Pelton, *Final Technical Report* , U. S. Army Research Office, Grant No. DAA629-76-0181, 1978, p. 30.

121 G. E. Dieter, *Response of Metals to High Velocity Deformation*, Ed. by P. G. Shewmon and V. F. Zackay, 1960, p. 429.

122 E. Ganin, Y. Komem, and A. Rosen, *Materials Sci. and Eng.*, 1978, Vol. 33, p. 1-4.

123 B. D. Cullity, *Elements of X-ray Diffraction*, p. 411-5.

124 K. C. Thompson-Russell and J. W. Edington, *Electron Microscope Specimen Preparation Techniques in Materials Science*, 1975, p. 6.

125 I. C. Noyan and J. B. Cohen, *Residual Stress*, p. 207.

126 G. F. Vander Voort, *Metallography: Principles and Practice*, 1984, p. 538-9.

127 P. B. Hirsch, A. Howie, R. B. Nicholson, D. W. Pashley, and M. J. Whelan, *Electron Microscopy of Thin Crystals*, 1965, p. 422.

128 P. B. Hirsch, A. Howie, R. B. Nicholson, D. W. Pashley, and M. J. Whelan, *Electron Microscopy of Thin Crystals*, 1965, p. 244.

129 J. W. Edington, *Electron Diffraction in the Electron Microscope, 2*, 1975, p.45-46.

130 G. Collette, C. Crussard, A. Kohn, J. Plateau, G. Pomey, and M. Weisz, *Revue De Metallurgie*, 1957, Vol. 54, p. 433-486.

131 M. J. Dickson, *J. Appl. Cryst.*, 1969, Vol. 2, p. 176-180.

132 K. Yoshida, H. Yoshida, T. Noda and S. Nakai, *Laser-Induced Damage in Optical Materials:1990*, SPIE Vol.1441, p. 9.

133 J. F. Ready, *Effects of High-Power Laser Radiation*, 1971, p. 288-303.

134 G. Banaś, J. P. Chu, H. E. Elsayed-Ali, F. V. Lawrence, Jr., and J. M. Rigsbee, unpublished work.

135 D. Milam, *Laser-Induced Damage in Optical Materials:1978*, NBS Special Publication 541, p. 164.

136 A. A. Manenkov, *Laser-Induced Damage in Optical Materials:1988*, NIST Special Publication 775, p. 486.

137 C. G. Hoffman, *J. Appl. Phy.*, 1974, Vol. 45, p. 2125-28.

138 A. Vohra, S. K. Bansal, R. K. Sharma, G. P. Srivastava, C. L. Grag, and R. P. Mull, *J. Phy. D: Apply. Phy*, 1990, Vol. 23, p. 56-66.

139 A. N. Pirri, *Phy. Fluids*, 1973, Vol. 16, p. 1435-40.

140 J. S. Speck, J. Steinbeck, and M. S. Dresselhaus, *J. Mater. Res.*, 1990, Vol. 5, p. 980-88.

141 J. Grun, R. Decoste, B. H. Ripin, and J. Gardner, *Appl. Phy. Lett.* , 1981, Vol. 39, p. 545-47.

142 P. D. Gupta, P. A. Naik, and H. C. Pant, *Appl. Phy. Lett.* , 1983, Vol. 43, p. 754-56.

143 R. W. K. Honeycombe, *The Plastic Deformation of Metals*, 1982, p. 212.

144 W. C. Leslie, J. T. Michalak, and F. W. Aul, in *Iron and Its Dilute Solid Solutions*, Ed. by C. W. Spencer and F. E. Werner, 1961, p. 119.

145 W. C. Leslie, E. Hornbogen, and G. E. Dieter, *J. of Iron and Steel Inst.*, 1962, p. 622-33.

146 J. D. Embury, A. S. Keh, and R. M. Fisher, *Trans. Met. Soc. AIME*, 1966, Vol. 236, p. 1252-60.

147 L. E. Murr, O. T. Inal, and A. A. Morales, *Acta Metall.*, 1976, Vol. 24, p. 261-70.

148 V. I. Izotov and P. A. Khandarov, *Phy. of Metals and Metall.*, 1971, Vol. 32, p. 138-144.

149 J. A. Venables, *Phil. Mag.*, 1962, Vol. 7, p. 35-44.

150 R. Lagneborg, *Acta Met.*, 1964, Vol. 12, p. 823-43.

151 P. M. Kelly, *Acta Met.*, 1965, Vol. 13, p. 635-46.

152 J. M. Rigsbee, *Metallography*, 1978, Vol. 11, p. 493-8.

153 H. Fujita and S. Ueda, *Acta Met.*, 1972, Vol. 20, p. 759.

154 L. S. Yershova, I. N. Bogachev, and R. S. Shklyar, *Phy. of Metals and Metall.*, 1961, Vol. 12, p. 40-47.

155 Y. Tomota, M. Strum, and J. W. Morris, Jr., *Metall. Trans. A.* , 1986, Vol. 17A, p. 537-47.

156 Dj. Drobnjak and J. Gordon Parr, *Metall. Trans.*, 1970, Vol. 1, p. 759-65.

157 P. Yu. Volosevich, V. N. Gridnev, and Yu. N. Petrov, *Phy. of Metals and Metall.*, 1975, Vol. 40, p. 90-94.

158 L. Remy and A. Pineau, *Mat. Sci. and Eng.*, 1977, Vol. 28, p. 99-107.

159 S. Mahajan and D. F. Williams, *International Metall. Rev.*, 1973, Vol. 18, p. 43-61.

160 N. P. Goss, *Trans. ASM*, 1945, Vol. 34, p. 630-44.

161 *Metals Handbook, Vol. 1*, 1988, p. 576.

162 I. N. Bogachev, M. A. Filippov, and B. A. Potekhin, *Phy. of Metals and Metall.*, 1966, Vol. 21, p. 162-4.

163 F. A. McClintock, in *Mechanical Behavior of Materials*, Ed. by F. A. McClintock and A. S. Argon, 1966, p. 426-7.

164 B. D. Cullity, *Elements of X-Ray Diffraction*, 1978, p. 464.

165 H. Wohlfahrt, *Proceedings of the Second International Conference on Shot Peening, ICSP-2*, Ed. by H. O. Fuchs, 1984, p. 316-331.

166 A. S. Keh, *Direct Observation of Imperfections in Crystals*, Ed. by J. B. Newkirk and J. H. Wernick, 1961, p. 213-238.

167 R. E. Smallman, *Modern Physical Metallurgy*, 1985, p. 217.

168 D. Hull and D. J. Bacon, *Introduction to Dislocations*, 1986, p. 153.

169 R. E. Smallman, *Modern Physical Metallurgy*, 1985, p. 271.

170 D. Hull and D. J. Bacon, *Introduction to Dislocations*, 1986, p. 224.

171 G. E. Dieter, *Mechanical Metallurgy*, 1986, P. 189-190.

172 M. C. Shaw, in *Mechanical Behavior of Materials*, Ed. by F. A. McClintock and A. S. Argon, 1966, p. 457.

173 Anderson, M.U. and Wackerbarth, D.E., (1988). "Technique and Data Analysis for Impact-loaded Piezoelectric Polymers (PVDF)." Prepared by Sandia National Laboratories, Report No. SAND88-2327 • UC - 13.

174 Peterson, R. E. "Stress Concentration Factors." A Wiley-Interscience Publication, John Wiley & Sons, Figs. 137 and 138.